A comprehensive study of surface and space charge effects at an operating water splitting iron oxide photoanode

Dissertation zur Erlangung des Grades

Doktor der Naturwissenschaften

am Fachbereich Physik
der Freien Universität Berlin

vorgelegt von

Julius Plescher

Berlin, 2024

Erstgutachter:	Prof. Dr. Martin Wolf
Zweitgutachter:	Prof. Dr. Holger Dau
Tag der Disputation:	18. Oktober 2024

Die experimentellen Arbeiten zu diesem Promotionsvorhaben wurden zwischen April 2016 und Juni 2020 am Fritz-Haber-Institut der Max-Planck-Gesellschaft in den Abteilungen Physikalische Chemie und Anorganische Chemie durchgeführt.

Zusammenfassung

Die vorliegende Arbeit beschreibt eine grundlegende Charakterisierung der Ladungsverteilung entlang einer wasserspaltenden α-Fe_2O_3-Photoanode unter Reaktionsbedingungen. Die Studie bedient alle experimentellen Arbeiten, von der Herstellung eines repräsentativen Probensystems, über die Entwicklung geeigneter Messzellen bis hin zur Messung des statischen elektrischen Feldes an der Elektroden-Grenzfläche mittels optischer Frequenzverdopplung (SHG) in Kombination mit klassischen photoelektrochemischen Methoden. Alle Ergebnisse werden fortlaufend durch Kontrollexperimente überprüft und bestätigt.
Es wird gezeigt, wie die elektrochemische Abscheidung von FeO_xH_y mit Hilfe des angelegten Potentials und des resultierenden Stroms gesteuert bzw. überwacht werden kann. Die Dichte an Oberflächenzuständen und -ladungen der α-Fe_2O_3-Photoanoden wird anhand eines kleinen Stromsignals in guter Übereinstimmung mit Literaturwerten bestimmt. Auf Grundlage einer kinetischen Analyse von Photostrom-Transienten wird ein Reaktions-Zeitgesetz dritter Ordnung abgeleitet. Unter Zuhilfenahme von Dichte-Funktional-Simulationen wird ein entsprechender Mechanismus für die photo-elektrochemische Sauerstoff-Entwicklung vorgeschlagen und mit der Ladungsakkumulation an der Elektrodenoberfläche verglichen.
Ein SHG-Signal wird gemessen, das mit dem angelegten Potential sowohl entlang der Intensität, als auch der Frequenz-Achse verändert und sicher der α-Fe_2O_3-Schicht zugeordnet werden kann. Die Potentialabhängigkeit der SHG-Antwort wird im Sinne einer elektrischen Feldverstärkung (EFISH) in der Raumladungszone interpretiert und mittels komplementärer elektrochemischer Methoden bestätigt.
Dadurch wird eine direkte Beobachtung der potentialabhängigen Bandverbiegung ermöglicht. Eine Diskussion der Ladungsdichte im Halbleiter-Elektrodenmaterial belegt eine vollständige Erschöpfung freier Ladungsträger ab einem bestimmten Potential in guter Übereinstimmung mit Ergebnissen aus Elektronenmikroskopie und Röntgenbeugung. Der einhergehende Übergang von quadratischer zu linearer Potentialabhängigkeit des SHG-Signals wird im Sinne einer Änderung von halbleitender hin zu dielektrischer Polarisierung des Elektrodenmaterials modelliert. Eine Verschiebung des spektralen Schwerpunktes des SHG Signals mit dem Potential wird analog interpretiert und einer zusätzlichen Bandstruktur innerhalb elektronischen Struktur der α-Fe_2O_3-Schicht zugeordnet.

Abstract

This work presents an investigation of the charge distribution across an operating, water splitting α-Fe_2O_3 photoanode from bottom up. The study covers the entire experimental framework from the preparation of a representative sample system via the construction of an appropriate sampling environment up to the direct detection and analysis of surface- and space charge at the electrode surface using second harmonic generation (SHG) spectroscopy in combination with photo-electrochemical standards. All results are constantly validated by a range of control measurements. It is shown how the electrodeposition of FeO_xH_y films can be modified and monitored by the deposition potential and current, respectively. During alkaline water photo-electrolysis, a small current signal is detected from the α-Fe_2O_3 photoanodes and discussed in terms of electronic surface state charging in good agreement with literature values. On the base of a kinetic analysis of photocurrent transients, a third order water oxidation rate law is inferred. By means of complementary density functional theory calculations, a photo-electrochemical oxygen evolution reaction mechanism is suggested and compared with surface charge accumulation processes. An SHG signal is measured and ascribed to the α-Fe_2O_3 photoanode material that can be modified by the external bias potential along both the intensity and spectral dimensions. The SHG response is shown to correlate with the band bending at the electrode surface according to the electric field induced second harmonic theory in good agreement with electrochemical analyses of the sample system.
With this, it is possible to directly map and analyse surface the band-bending as function of the applied potential. The charge density in the semiconductor electrode material is discussed and a complete majority carrier depletion of the bulk semiconductor material at higher potentials is inferred in good accordance with electron microscopy and X-Ray diffraction experiments. The concomitant transition from a quadratic to linear potential dependence of the SHG response is modelled in terms of a transition from purely depletive to dielectric electrode polarization in series with a semi-conductive back contact. Spectral changes of the potential dependent SHG response are interpreted analogously and considered an indication of an additional band-component to the semiconductor electronic structure.

Für Mama, Papa und Martin

Acknowledgements

The author wishes to acknowledge the following persons who supported the preparation and realization of this thesis in various ways.
Martin Wolf and R. Kramer Campen for scientific supervision, funding and the opportunity to prepare a PhD thesis at the Fritz-Haber-Institute of the Max-Planck-Society (FHI), Department of Physical Chemistry (PC).
The excellent technical support at the FHI that substantially helped to meet the experimental demands of these works. In particular Sabine Wasle for the evaporation of metal films and lab support. Reinhard Franke for technical drawings and construction of mechanical parts. Sven Kubala for evaporation of metal films. Daniel Wegkamp for a software solution to spectrally scan the laser output. The FHI workshop for their fabrication of challenging mechanical parts, often also on short notice. The FHI E-Lab for the construction of several electric devices. And also Glasbläserei Müller for the manufacturing of demanding glass equipment.
Martin Thämer and Yujin Tong for scientific and technical discussions and instruction to optical non-linear spectroscopy. Manuel Krüger and Ines Bressel from the FHI PC Deparment secretary's office for formal and administrative support. My fellow PhD candidates Tobias Garling, Christopher Winta, Thomas Vasileiadis, Ivana Lapšanská and Stefano Calati for uplifting extrascientific conversations during doctoral students' lifes.
The generous experimental support from the Department of Inorganic Chemistry. In particular Franz Schmidt, Adnan Hammud and Thomas Lunkenbein for electron microscopy; Jutta Kröhnert for UV-Vis-Spectroscopy; Yuanquing Wang, Gregory Huff and Annette Trunschke for Raman-Spectroscopy and Frank Girgsdies for XRD-measurements.
The efforts and contributions by Detre Teschner and Simone Piccinin to the surface chemical analysis which could be published in the Nature Catalysis journal.
Sebastian Fiechter and Klaus Rademann for academic advice and education. Patricia Dombrowsky and Gerhard Stockheim for their excellent scholar tuition – likely thereby also forming one nucleus for this doctoral endeavour.

„Wernstrom ... !!!"

Prof. Hubert J. Farnsworth
Mars University

Contents

Part I

Introduction

1 Motivation

1.1 Anthropogenic climate change

A constantly increasing amount of theoretical and empirical studies give evidence that our world is undergoing severe changes of multiple ecological parameters which are crucial for the biosphere of the entire planet.[1–9] Following scientific reason, there is a broad consent within the United Nations that a continued temperature increase in the earth atmosphere will cause dramatic impacts on the ecosystem we live in and that instant and resolute political action is necessary in order to sustain a habitable planet for the human kind and other living creatures.[1, 2]

Several indicators show that the balance of physical, chemical and biological equilibria of our planet is endangered. The progress of some of these indicators is presented in Fig. 1.1. It shows the combined land-surface air and sea-surface water temperature as deviation from the 1951 to 1980 mean,[10–12] the sea level rise with respect to the 1993 to 2008 average,[13, 14] the change of the Antarctic ice mass relative to 2002[16] and the sea water pH from the ALOHA station in Hawaii.[15] As we can see, our world is subjected to a constantly increasing global temperature, a rising sea level, a melting polar ice shield and an acidification of the oceans, just to mention a few severe effects.

All of these metrics in Fig. 1.1 are typical indicators of global warming[3, 6, 7] and there is broad consensus about the need to limit the global warming and concomitant climate change in order to prevent an uncontrollable increase of natural disasters such as flooding, droughts, violent storms, heat waves or mass extinction.[1, 2]

It is known from both empirical and theoretical considerations that global warming and the aforementioned consequences are caused by the so called greenhouse effect – the conservation of heat within atmospheric gases' degrees of freedom.[2, 4, 5] An increasing amount of anthropogenic emissions causes an accumulation of greenhouse gases such as CO_2, CH_4 and N_2O in the atmosphere which are absorbing heat irradiation that would otherwise be emitted back into space. Thereby, the increasing

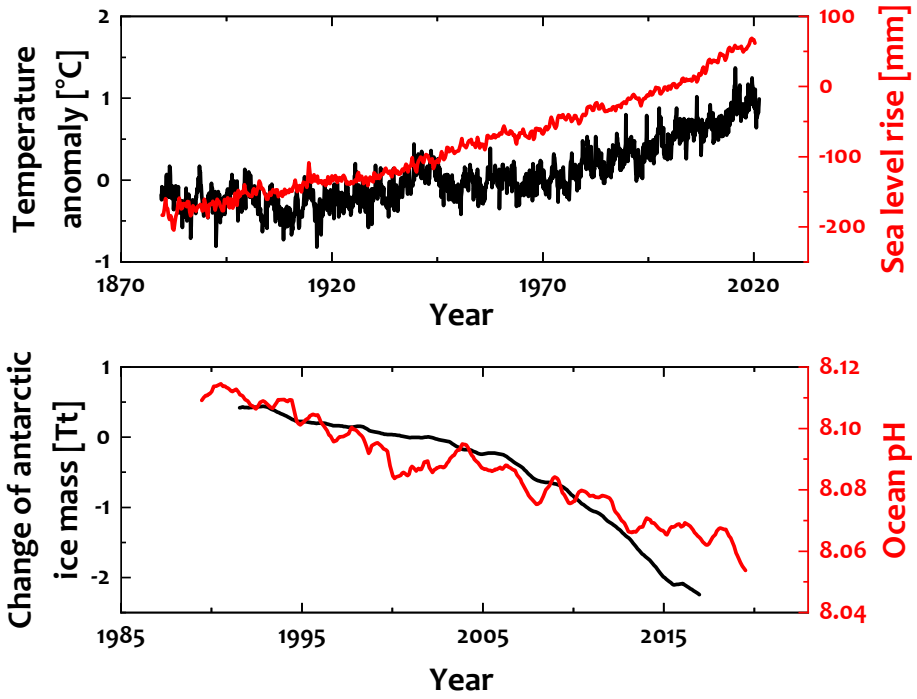

Figure 1.1: Indicators of global warming: Increasing earth surface temperature,[10–12] rising sea level,[13, 14] acidification of oceans[15] and decreasing Antarctic ice mass[16]. Data from [17].

concentrations of these gases causes a net increase of the atmosphere heat capacity and global warming.

Besides the first order effects as apparent in Fig. 1.1, a range of self accelerating processes will have even more catastrophic consequences. As for instance, a melting of permafrost soils would release vast amounts of CH_4 into the atmosphere causing a feedback loop of further global warming. Also, increasing amounts of forest fires will raise the atmospheric CO_2 concentration with a simultaneous loss of capability to chemically fix this greenhouse gas.[1, 2]

An empirical manifestation of this effect is shown in Fig. 1.2. This graph shows the atmospheric concentrations of CO_2, CH_4 and N_2O over the last centuries combined with the measured change of atmospheric temperature with respect to the pre-industrial average.[17, 18] We can see that global warming is clearly accompanied by an increase of CO_2, CH_4 and N_2O anthropogenic emissions and that this effect has an accelerating tendency.

Therefore, both theoretical and empirical evidence shows the urge to dramatically

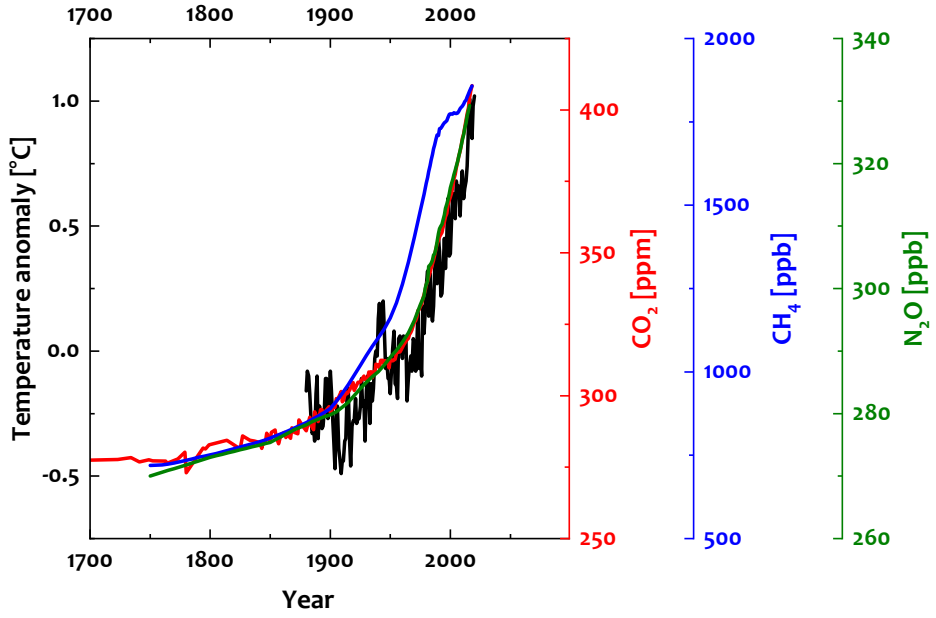

Figure 1.2: Climate change and anthropogenic emissions: Increase of earth surface temperature[10] compared with atmospheric concentrations of greenhouse gases CO_2, CH_4, N_2O.[18]

reduce the anthropogenic emissions of greenhouse gases in order to maintain a habitable planet for future generations of human and other living beings.

The largest source of anthropogenic emissions is the consumption of fossil fuels such as coal, mineral oil and natural gas which inherently produces vast amounts of CO_2 and also leads to the emission of further climate damaging compounds.[1–5] In 2020 85 % of the global energy consumption was supplied by the combustion of fossil fuels coal (28 %), oil (32 %) and gas (25 %).[19] This has lead to a world wide CO_2 emission of 34.81×10^9 t from fossil fuels which is the vast majority of the 38.02×10^9 t total global CO_2 emission.[20] If we compare these amounts with pre-industrial values of 2.73×10^9 t total emitted CO_2 of which only 196.9×10^6 t stem from fossil fuels in 1850,[20] we see that the large energy demand during the industrialization has caused the main part of the anthropogenic CO_2 emission and concomitant climate change.

Therefore, the global energy supply, which is strongly based on the combustion of fossil fuels, needs to be transformed towards more sustainable energy carriers in order to reduce the emission of greenhouse gases and keep the global warming at an acceptable level.[1, 2]

1.2 Energy transformation

1.2.1 Hydrogen as energy carrier

A range of renewable energy technologies is already available in order to avoid the environmentally harmful combustion of fossil fuels. While purely electricity based techniques such as solar cells, wind turbines or hydroelectric power systems are already well established and capable of power supply on the TW scale,[21] there is still demand for a clean and sustainable chemical fuel in order to offset fluctuations of wind and solar power and to provide a convenient low mass energy carrier for the transport sector.[22–25]
The most promising chemical fuel for a sustainable energy economy is hydrogen H_2. This gas is a particularly clean and sustainable energy vector as it only leaves water as reaction product. It provides a range of advantages such as relatively simple and clean access from water electrolysis and a well established re-conversion into electrical energy by fuel cell technologies. H_2 is also a base chemical for a range of industrial processes and could be utilized to synthesize more complex chemical fuels in Fischer-Tropsch processes including a fixation and conversion of atmospheric CO_2.[23–26]

1.2.2 Photoelectrochemical water splitting

$$H_2O \longrightarrow H_2 + \frac{1}{2}O_2 \qquad \Delta_R G^\circ = +237\,\mathrm{kJ\,mol^{-1}} \tag{1.1}$$

H_2 production from renewable energies – so called green hydrogen – is first of all provided by water splitting Eq. 1.1. In this endergonic reaction the water molecule is disproportionated into H_2 and oxygen O_2. The most convenient approach to split the water molecule is the electrolytic dissociation. Water electrolysis is a redox-reaction driven by ubiquitarian electric power between two electrodes – an anode and a cathode – and therefore conveniently yielding H_2 and O_2 as separate products at both half cells.[23, 25, 26]

$$4\,H_2O + 4\,e^- \longrightarrow 2\,H_2 + 4\,OH^- \quad (1.2)$$

$$4\,OH^- + 4\,h^+ \longrightarrow 2\,H_2O + O_2 \quad (1.3)$$

$$2\,H_2O \longrightarrow 2\,H_2 + O_2 \quad (1.4)$$

The two half reactions of electrolytic water splitting are shown in the equation system above, where negative charge is indicated as electrons e^- and positive charge is displayed by holes h^+. Hydroxide ions OH^- indicate that the process is conducted in an alkaline medium. If a sufficiently large voltage is applied across two electrodes in an aqueous electrolyte, excess negative charge at the cathode drives the water reduction to form hydrogen i.e. Eq. 1.2, the hydrogen evolution reaction (HER). Excess positive charge at the anode drives the water oxidation reaction to form oxygen, Eq. 1.3, OER.[26, 27] The sum of both electrode reactions is identical with the net water splitting reaction Eq. 1.4 and Eq. 1.1 where the thermodynamic costs for this process are given by a net Gibbs free energy of +237 kJ per mole H_2 corresponding to an electromotive force of 1.23 V, while several hundreds of mV are typically required to overcome the activation barrier of the OER.[26–28]

In order to produce sustainable electrolytic hydrogen, the energetic costs for Eq. 1.1 must be provided from renewable energies. Several projects are already running, for instance, where wind turbines are coupled with electrolysers in order to convert wind power into hydrogen.[29–32] Another method to provide the thermodynamic costs for the water splitting reaction is the direct utilization of solar energy by a semiconductor photoelectrode system in a photoelectrochemical (PEC) process.[26, 33] In contrast to wind or solar power coupled dark electrolysers that are already in pre-industrial stages,[29–32] the PEC approach combines power harvest and electrolysis compartments in one unit and therefore perspectively provides both lower production costs and larger energy conversion efficiencies.[26] It may also provide advantages under conditions of limited space such as astronautics and it is argued that an integrated PEC cell system provides room for efficiency improvements by concentrated irradiation and heat management.[34, 35]

PEC water splitting – a form of artificial photosynthesis – was first described by Fujishima and Honda in the early 1970s.[37, 38] Fig. 1.3 schematically shows an energy scheme of this effect using the standard example of an n-type photoanode and a metal cathode.[26, 36] This serves as prototypical illustration for the principle

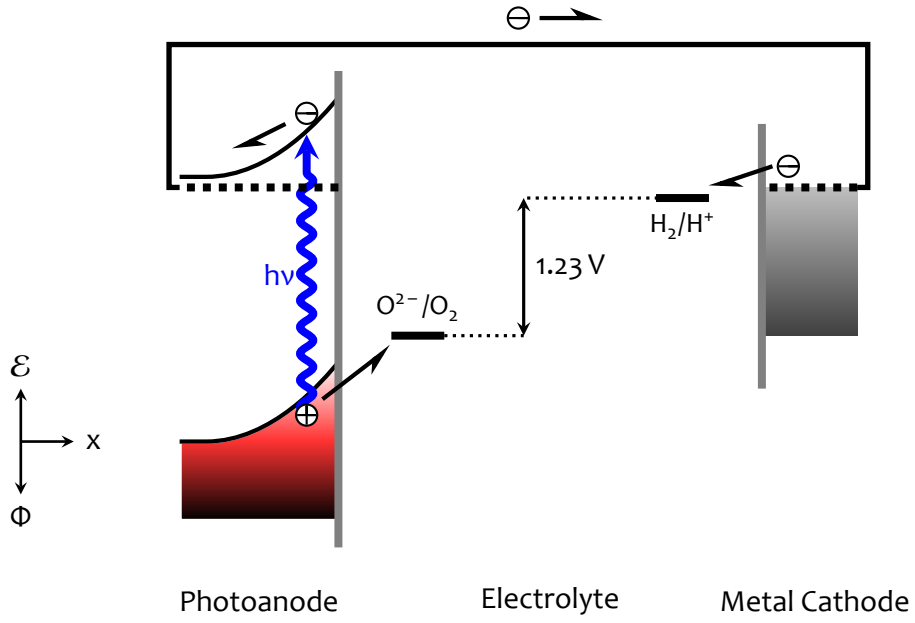

Figure 1.3: The principle of PEC water splitting illustrated using the standard example of an n-type semiconductor photoanode [26, 36]

of semiconductor-electrochemical water splitting, and also for the system we are going to explore in this thesis, while a range of different device-configurations are possible, as well.[39]

On the left-hand side of Fig. 1.3 we see an n-type semiconductor photoanode in contact with an aqueous electrolyte. Illumination of the photoanode with photon energies above the material's band-gap causes carrier excitation and forms a photoexcited electron hole pair. The built-in electric field at the semiconductor-liquid junction (see Section 2.1) drives the dissociation of the electron hole pair in such a way that the conduction band electron migrates towards the bulk photoanode material whereas the valence band hole is accelerated towards the electrode surface. Such surface valence band holes will then drive the water oxidation and form molecular oxygen (Eq. 1.3) – provided that a range of thermodynamic and kinetic requirements are fulfilled. The remaining electron is accelerated towards the back-contact and driving the water reduction and hydrogen evolution (Eq. 1.2) at the cathode to complete the mass and electronic balance of the process.[26, 33, 36, 40]

From Fig. 1.3 we already see that the photoanode/electrolyte interface plays a crucial role in the process of PEC water splitting. It enables light harvesting, charge separation and chemical charge transfer to drive the OER. This thesis will develop a detailed examination of the charge distribution across an operational water split-

ting photoanode surface under working conditions. However, first it is necessary to gather a base of fundamental knowledge in order to increase our understanding of all relevant electronic effects at the micro- and nanoscopic scale.

1.3 Prospects and drawbacks of α-Fe_2O_3 photoanodes

There has been a long quest for a suitable PEC water splitting material and a broad range of semiconductors has been suggested for the technical realization of a commercial device. An ideal semiconductor photoanode material needs to meet a range of requirements in order to fulfil the demands for an economically compatible industrial scale hydrogen production process and simultaneously provide an ecological advantage. The most important criteria are:[26, 41, 42]

i Suitable energetic band positions. Depending on the actual device configuration, a photoanode should at least possess a valence band-edge well below the water oxidation redox potential in order to provide a thermodynamic driving force and to overcome the kinetic barrier. The band-gap should be preferably small to harvest a large amount of the solar spectrum but also large enough to provide sufficient overpotential to drive the OER reaction.[43]

ii Stability. An economic and sustainable photoanode system should ideally withstand the abrasive OER conditions, due to electrolyte pH-values far from neutral[26] and the presence of highly reactive intermediates over years.[44–46]

iii Sustainability. In order to gain an ecological advantage from PEC water splitting, the device should be made of harmless materials and production processes.

iv Efficiency. Any commercial PEC water splitting cell system will be eventually assessed by its solar to hydrogen (STH) conversion efficiency.[47]

v Low cost. Besides stability and efficiency, the economic balance also favours abundant materials that are available on industrial scales.[26]

A range of materials in various combinations were shown to be in principle capable to facilitate STH energy conversion[26, 41] comprising manifold metal oxides such as TiO_2,[38, 48] $BiVO_4$,[49] WO_3[50] and also classical semiconductors such as Si[49, 51, 52] and III-V materials like GaP and GaAs.[51, 53]

One material that meets many of the requirements is hematite α-Fe_2O_3.[42, 54, 55] α-Fe_2O_3 is an earth abundant, non-toxic mineral with an outstandingly high stability under alkaline OER conditions that can be synthesized by a range of plain methods.[42, 55] Its band-gap of ≈2.1 eV allows to harvest an appropriate portion of the solar spectrum and the valence band position is low enough to generate high energy holes for the OER (Eq. 1.3).[42, 55] On the other hand, the energetic conduction band position below the water reduction redox potential would require the implementation in a tandem device. The intrinsic properties of the material also require improvements in order to reach economic STH efficiencies.[42, 55]
Nevertheless, the prospects of an earth abundant, low cost, non-toxic and OER-resistant photoanode material prevail in such a way that α-Fe_2O_3 has been studied as both model system and candidate for commercial applications for solar H_2 production over decades.[26, 42, 54, 55]
Besides the striking cost, sustainability and stability advantages, pristine α-Fe_2O_3 photoanodes suffer from low energy conversion efficiencies due to high carrier recombination rates, a limiting light absorption coefficient and poor catalytic properties.[26, 42, 55, 56] The small hole conductivity causes charge carriers to recombine instead of forming long-lived surface holes of sufficient energy and concentration to drive the OER reaction whereas a small absorption coefficient provokes large hole diffusion path lengths. Sluggish OER charge transfer kinetics further decrease the STH efficiency of α-Fe_2O_3 photoanodes.[26, 57–60]

A lot of improvements on the efficiency of water splitting α-Fe_2O_3 photoanodes have been made. The application of nanostructured architectures has combined two advantages – an increase of the chemically active surface area with simultaneous decrease of the distance that photogenerated holes need to traverse to reach the electrode surface.[26, 61, 62]
Doping with several metal cations was shown to improve the PEC performance.[42, 55, 56, 63, 64] However, the introduction of dopant atoms is accompanied by two obstacles. First, an increase of the majority carrier concentration decreases the absorption path length available to harvest PEC convertible light and a minority carrier doping might hamper the material's electric conductivity.[26, 56] Second, there is an interplay between extrinsic donor atoms and the presence of surface states which may affect the properties of OER active surface holes in an unknown fashion.[57, 59, 60, 63, 65]
Pristine α-Fe_2O_3 photoanodes suffer from poor OER catalytic properties. This has

been demonstrated by the application of so-called hole scavengers, i.e. the addition of reducing agents such as CH_3OH or H_2O_2 to the electrolyte. In presence of such reactants, the OER surface charge transfer is no longer limiting the formation of photocurrents and much faster transfer rates are observed under such conditions.[66, 67]

Finally, it was shown that the catalytic performance can be enhanced by deposition of overlayers and surface modifications.[42, 55] A range of oxides was deposited on top of α-Fe_2O_3 photoanodes and showed significant acceleration of the surface charge transfer rates. Conventional OER catalysis such as IrO_x or $Ni_{1-x}Fe_xO_y$ were shown to enhance the PEC conversion efficiency of α-Fe_2O_3 photoanodes.[68–71] Besides these classical electro-catalysts a range of further oxides have also increased the catalytic performance such as Al_2O_3, Ga_2O_3 and some cobalt phosphate compounds "CoPi".[59, 72, 73] It is argued that these overlayers promote a different mechanistic route by passivation of electronic surface states and thereby catalytically favouring the interfacial charge transfer over a surface charge accumulation.[55, 59, 74]

1.4 In situ characterization of electrode interfaces

All the above-mentioned improvements on a photoelectrode performance can be shown by simple current-voltage (IV) measurements – a voltage is imposed to the electrode while the cell current is recorded. An increase of photocurrent and a decrease of the bias voltage necessary to drive it will indicate an improvement of the photoanode efficiency.[26, 36] While this approach – combined with a couple of further parameters – already provides a solid basis for the development of a functional photoelectrode system, there are only scarce methods to comprehensively characterise interfacial electronic structures and processes of electrode systems *in situ*.

The most common approach to investigate charge transfer processes is electrochemical impedance spectroscopy (EIS) (see Section 3.3). In a typical EIS experiment, a sinusoidal perturbation is modulated around a baseline potential and imposed to the electrode, while the amplitude and phase shift of the resulting current is measured. This frequency dependent response at different bias potentials can be used to infer information on charge transfer and accumulation processes across the working electrode half cell.[26, 75] However, most electrode systems are quite complex and often a particular set of impedance spectra can be explained by multiple different electronic

structures.[76] The interpretation of impedance spectra often requires a considerable amount of presumptions so that conclusions from EIS are typically biased by the models used for the interpretation.[26, 76] One manifestation of this lack of validity are the strongly differing reported flat-band potentials of α-Fe_2O_3 photoanodes, for instance.[77]

Another method to investigate charge transfer processes across semiconductor electrodes which has gained particular attention in the past decade is transient absorption spectroscopy (TAS). In this method, the time dependent light absorption of a photoelectrode is measured upon initiation of charge excitation by a short light pulse. These works, mainly elaborated in the group of Durrant, contributed several new findings on the charge carrier dynamics in α-Fe_2O_3 photoanodes at ultrafast timescales.[58, 60, 66, 78] Although this method doubtlessly provides precious insight into charge carrier transfer and accumulation processes, it should be mentioned that TAS delivers an integral signal of relative energies over the whole system that can not be spatially resolved normal to the electrode surface. Thus, it is not possible to assess whether transient absorption takes place in the electrode bulk or surface or which amounts of charge are exchanged. While carrier dynamics can be tracked well, the electrostatic information from EIS on interfacial field distributions, dopant concentrations and flat-band potential remain obscured.

Therefore, it would be desirable to develop a novel route to investigate an α-Fe_2O_3 photoanode surface that combines the advantages of both techniques – access to the interfacial field distribution with an unbiased method that is independent from presumptions and offers an option for ultrafast time resolution.

One technique that is in principle capable to provide both types of experimental information is second harmonic generation (SHG) spectroscopy. SHG is a nonlinear optical process that is capable of delivering a purely interface specific signal. Besides the sensitivity to interfacial electric fields it can also be employed for time resolved characterisation of electronic processes on ultrafast time scales (see Section 3.2). SHG has been already applied to TiO_2 and n-Si semiconductor electrode systems, where, however a range of methodical and scientific questions have remained (see also Section 9.2).[79–81]

1.5 Objective

The goal of this thesis is to investigate an operating α-Fe_2O_3 photoanode using inherently surface specific second harmonic generation (SHG) spectroscopy in order to conduct a comprising characterization of interfacial electronic structures and processes.
For this, a functional and realistic electrode system needs to be developed that provides reliable information which can be compared well with literature standards. The electrode system needs to meet common PEC characteristics and has to be thoroughly characterized with respect to its electronic, morphologic and crystallographic properties and compared with sample systems from literature. A sampling environment has to be developed that enables SHG measurements under full control over all vital PEC parameters – potential, current and electrode illumination with time resolution. SHG experiments will then be conducted under variation of the respective PEC parameters. Continuous control measurements need to be taken in order to confirm stability and repeatability of the developed experiment. All results from SHG spectroscopy will be complemented by conventional PEC standard methods such as EIS and IV measurements and verified by continuous comparison between both fundamentally different techniques. The findings will be discussed in terms of particular properties of the α-Fe_2O_3 electrode system and also applied to commonly known PEC models.

2 Models

Since this work aims to gather new information on the α-Fe_2O_3 photoanode/electrolyte interface, we now want to briefly found a scientific base with all relevant physical models to describe the semiconductor liquid junction. For further details the author highly recommends lecture of *Photoelectrochemical Hydrogen Production*, (Eds.: R. van de Krol, M. Grätzel), Springer US, Boston, MA, **2012** which has been an essential source of fundamental knowledge through the whole thesis.
It might be worth noting, that in semiconductor photoelectrochemistry one-dimensional pictures of semiconductor band structures are typically employed to describe relevant materials properties rather than detailed solid state physical phenomena such as lattice anisotropy, spin, phonon and coupling effects. This is in so far valid as the sample systems are far from perfect crystallites and fundamental, ultrafast effects are often summed up to observables that can be tracked on chemical time scales.[44, 82]

2.1 The n-type semiconductor/liquid junction

An illustration of the common description of an n-type semiconductor in junction with an alkaline electrolyte is illustrated in Fig. 2.1.[26, 36] It shows the energetic distribution of charge carriers across the interface – from the bulk electrode towards bulk electrolyte. As a convention through this thesis and elsewhere, the electron energy $\mathcal{E}(e^{\ominus})$ is plotted along the positive vertical scale whereas the potential Φ is referred to a positive test charge and scales in the opposite direction according to $\mathcal{E}(e^{\ominus}) = -(\Phi * e_0)$.
The semiconductor electrode interface is typically described by three different, spatially separated layers of charge. Proceeding from the bulk photoelectrode towards the electrolyte the first compartment is a layer of *space charge* Q_{SC} beneath the electrode surface, that is composed of ionized lattice defects and forming a potential drop Φ_{SC} with respect to the surface, which will be explained in more detail hereafter

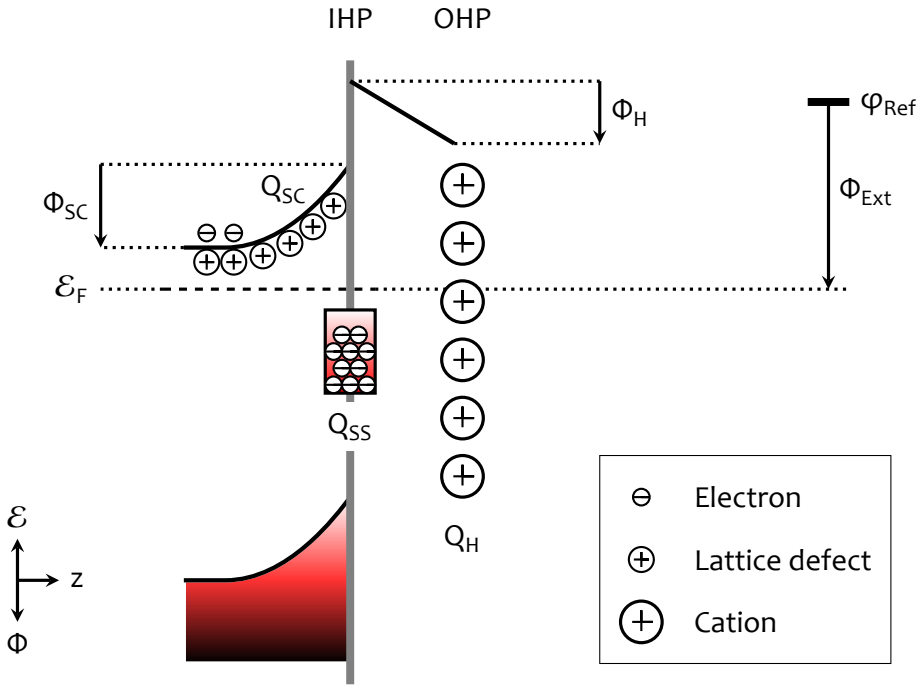

Figure 2.1: Conventional description of the charge and potential distribution across the n-type semiconductor photoanode interface. Charges Q which are hosted in the space charge region (SC), in surface states (SS) and the Helmholtz layers (H) are forming different compartments of the electrode system.[26]

(see Section 2.2 and Section 2.3). A second compartment is a sheet of surface states that may act as host for the accumulation of surface charge Q_{SS}. These two layers are balanced by adjacent ions from the liquid Q_H, which would be composed of positive charge for a fully deprotonated oxide electrode surface in an alkaline electrolyte. This countercharge forms a potential difference between the electrode surface, the inner Helmholtz-plane (IHP), and the closest electrolyte ions, the outer Helmholtz-plane (OHP), the so-called Helmholtz-potential Φ_H.[83, 84] This Helmholtz or *double layer* is typically described by two planar sheets of charge in analogy to a plate capacitor for electrolytes with sufficiently high ionic strength to instantly compensate for any electric effects within the electrode system without undergoing significant changes itself.[26, 33, 36]

The Fermi-level of the electrode system can be altered by application of an external bias potential Φ_{Ext} that is measured as difference to a reference electrode potential φ_{Ref}. Φ_{Ext} provides a powerful tool to control and monitor charging processes across the electrode system. The distribution of this external bias over the com-

partments of the different electrode system is an essential subject of semiconductor electrochemistry research and so of the thesis at hand.[26, 33, 36]

2.2 The depletion layer

One main feature of semiconducting materials in general is the phenomenon of so-called *carrier depletion*, *band-bending* or a *space charge region* SCR, which may be considered equivalent terms for a depletion of majority carriers at the semiconductor surface. The formation of a depletion layer is an essential aspect of most semiconductor technologies, regardless of whether the surface is in junction with air, metals, other semiconductors or – as described here – with an aqueous liquid. In regard to this thesis, the SCR plays a crucial role for the light harvest, charge separation and transfer processes as already shown in Fig. 1.3.[26, 40]

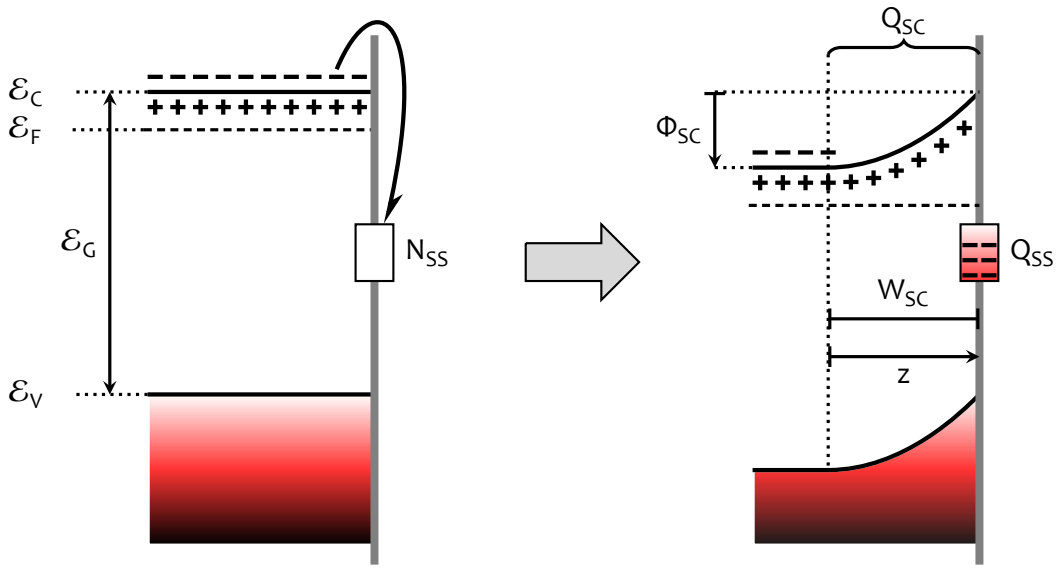

Figure 2.2: The formation of a depletion layer beneath the n-type semiconductor surface due to charge transfer from the bulk material into surface states [26, 40]

The formation of space charge is commonly explained by a depletion of bulk majority carriers into surface states as shown in Fig. 2.2. In the left-hand side we see an energy diagram of a hypothetical infinitely extended n-type semiconductor material crystal of universally balanced charge. The electronic states of this phase form a valence

band and a conduction band at the energies $\mathcal{E}_{\mathrm{V}}$ and $\mathcal{E}_{\mathrm{C}}$, respectively. Both bands are energetically separated by a band-gap $\mathcal{E}_{\mathrm{G}}$.
The n-type semiconducting properties of the material are constituted by an excess of donor type defects (+) later on described by their volume concentration N_{D} in cm^{-3}, which donate electrons (−) into the conduction band. This gives rise to an increased concentration of free negative charge which is reflected by a Fermi-energy E_{F} above mid band-gap. This excess charge promotes electrons as majority carriers and constitutes the n-type semiconducting properties of the material. The spatial coordinate x in this one-dimensional model is projected onto the distance from the electrode surface, where the electro-neutral bulk is conveniently chosen as zero.[26, 40]
The right-hand side of Fig. 2.2 shows the re-distribution of charge under ambient conditions. Any real semiconductor crystal will undergo a transfer of majority charge carriers from the bulk material into a set of surface states N_{SS} while ionic donor type lattice defects remain fixed in the solid matrix. This process causes a lowering of the Fermi-level due to a decreased concentration of free electrons thereby leaving a layer of unbalanced charge from ionized donor atoms beneath the semiconductor surface. This lattice charge forms the so-called space charge region (SCR) which is composed of a total amount of positive charge Q_{SC} forming a static electric field, built-in beneath the electrode surface. The lowered Fermi-level causes a band bending and a potential drop to an extent of Φ_{SC} beneath the electrode surface. Since this layer is depleted of majority charge carriers in all cases considered here and lowering the bulk conduction band energy, the term *depletion layer* may be used equivalently. Depending on the concentration of donors and Fermi-level, the SCR may extend a from few to several hundreds of nm into the bulk, this distance between the electro-neutral bulk and electrode surface is the so-called *space charge width* W_{SC}, which is a function of the lattice defect and carrier concentration, dielectric constant and the electrode potential.[26, 40]
In Fig. 1.3 in Section 1.2.2 we already saw that the SCR is of crucial importance for PEC water splitting as it facilitates the separation of excited electron-hole pairs and thereby enables the photo-electric energy conversion. Therefore, we now want to further review the physical description of this essential compartment of the PEC cell.

2.3 The MOTT-SCHOTTKY approximation

Two mutually dependent physical parameters describe the SCR of a given material system – the space charge width W_{SC} and the potential drop Φ_{SC} (see Fig. 2.2). Qualitatively spoken, the imposition of an external potential Φ_{Ext} is effectively altering the system's FERMI-level. This often allows to externally control the amount of band bending Φ_{SC} which inherently spans an associated space charge width W_{SC}. The volume charge density in the SCR is given by a constant, homogeneous distribution of donor-type defects. With this in mind we want to see how we can quantify this relationship.

The fundament for a quantitative description of the SCR is POISSON's equation Eq. 2.1 stating a proportional dependence between the potential curvature, electric field gradient and charge density ρ at some point z, where ϵ_0 and ϵ_{r} are the absolute and relative electric permittivities, respectively.[26, 40]

$$\frac{\mathrm{d}^2\Phi}{\mathrm{d}z^2} = \frac{\mathrm{d}\mathbf{E}}{\mathrm{d}z} = -\frac{\rho(z)}{\epsilon_0\epsilon_{\mathrm{r}}} \tag{2.1}$$

This implies that the net static electric field $\mathbf{E}_{\mathrm{DC}}$ at any position z in the SCR can be calculated by integration of the charge density over the distance from the electroneutral bulk:

$$\mathbf{E}_{\mathrm{DC}}(z) = -\frac{1}{\epsilon_0\epsilon_{\mathrm{r}}}\int_{\mathrm{z}=0}^{z}\rho(z)\,\mathrm{d}z \quad . \tag{2.2}$$

As we saw in the previous section, the space charge is composed of ionized donor atoms. To be more precise, we want to follow two principles. The first is given by GAUß's law which states that the built-in field in the SCR solely depends on the enclosed charge – and is independent of any external charges as in surface states, for instance.[26, 40]

The second principle the so called SCHOTTKY approximation.[85] These assumptions state i), as already mentioned above, that the SCR is solely composed of immobile charges from donor type defects which are constrained and evenly distributed in a solid matrix. ii) The minority charge carrier density is negligible. And iii) all donor type defects are fully ionized so that we can express the SCR volume charge density ρ by the concentration of donor type defects N_{D}.[26, 40]

$$\rho = e_0 * N_\mathrm{D} \tag{2.3}$$

Since we assumed a constantly distributed donor density, we can combine the two equations above, solve the integral and obtain for a zero distance z_0 from the electro-neutral bulk (see also Section 2.2):[40]

$$\mathbf{E}_\mathrm{DC}(x) = -\frac{e_0}{\epsilon_0 \epsilon_\mathrm{r}} * N_\mathrm{D} * (z_0 - z) = \frac{e_0}{\epsilon_0 \epsilon_\mathrm{r}} * N_\mathrm{D} * z \quad . \tag{2.4}$$

According to Eq. 2.1, a further integration over the SCR distance from electro-neutral bulk yields the expression Eq. 2.5 for the potential drop in the SCR Φ_SC at any point z.

$$\Phi_\mathrm{SC}(z) = \frac{e_0}{2\epsilon_0 \epsilon_\mathrm{r}} * N_\mathrm{D} * z^2 \tag{2.5}$$

Since we are usually dealing with the entire potential drop across the SCR as a whole, we find that Φ_SC is proportional to the squared space charge width which also demonstrates the quadratic slope of surface band bending in Fig. 2.2:

$$\Phi_\mathrm{SC} = \frac{e_0}{2\epsilon_0 \epsilon_\mathrm{r}} * N_\mathrm{D} * W_\mathrm{SC}^2 \quad . \tag{2.6}$$

In this picture, the depletion layer is composed of homogeneously distributed, electronically uncompensated ionized donor type defects extending to a distance W_SC into the bulk material. Thus, the SCR volume as given by depth W_SC, and surface S provides access to the absolute amount of space charge Q_SC according to:[26]

$$Q_\mathrm{SC} = e_0 * N_\mathrm{D} * S * W_\mathrm{SC} \quad . \tag{2.7}$$

Combining Eq. 2.6 and Eq. 2.7 delivers an expression Eq. 2.8 that relates the amount of space charge Q_SC with the potential drop Φ_SC.[40]

$$\boxed{Q_{\mathrm{SC}} = S * \sqrt{2\epsilon_0\epsilon_{\mathrm{r}}e_0N_{\mathrm{D}} * \Phi_{\mathrm{SC}}}} \tag{2.8}$$

Eq. 2.8 postulates an inverse-square law dependence between potential drop and space charge. Another, more common form of this relation can be obtained if we introduce a space charge capacitance $C_{\mathrm{SC}} = \mathrm{d}Q_{\mathrm{SC}}/\mathrm{d}\Phi_{\mathrm{SC}}$ which allows to electronically detect SCR parameters under certain conditions. So if we take the derivative of Eq. 2.8 with respect to Φ_{SC} and solve for ${C_{\mathrm{SC}}}^{-2}$, we obtain a linear expression Eq. 2.9, the MOTT-SCHOTTKY equation.[26, 40]

$$\frac{1}{{C_{\mathrm{SC}}}^2} = \left(\frac{\mathrm{d}\Phi_{\mathrm{SC}}}{\mathrm{d}Q_{\mathrm{SC}}}\right)^2 = \frac{2}{\epsilon_0\epsilon_{\mathrm{r}}e_0N_{\mathrm{D}}S^2} * \Phi_{\mathrm{SC}} \tag{2.9}$$

To be more precise, we want to further consider the thermal distribution of electrons due to the finite temperatures in laboratory conditions. This will lead to an effective de-ionization of donor type defect states up to an energy of $k_{\mathrm{B}}T/e_0$ above the FERMI-level. Correspondingly, this value of ≈25 meV at room temperature slightly offsets the potential drop Φ_{SC} cathodic from the FERMI-level.[26, 40] Finally, we also want to express the sample inherent quantity Φ_{SC} by the experimentally accessible external bias potential Φ_{Ext} and a flat-band potential φ_{FB} according to $\Phi_{\mathrm{SC}} = \Phi_{\mathrm{Ext}} - \varphi_{\mathrm{FB}}$. This delivers the following, most common formulation of the MOTT-SCHOTTKY-equation.

$$\boxed{\frac{1}{{C_{\mathrm{SC}}}^2} = \frac{2}{\epsilon_0\epsilon_{\mathrm{r}}e_0N_{\mathrm{D}}S^2} * \left(\Phi_{\mathrm{Ext}} - \varphi_{\mathrm{FB}} - \frac{k_{\mathrm{B}}T}{e_0}\right)} \tag{2.10}$$

From Eq. 2.10 we see that a plot of ${C_{\mathrm{SC}}}^{-2}$ over the external potential axis would form a straight line that intersects the x-axis at $\varphi_{\mathrm{FB}} - k_{\mathrm{B}}T/e_0$. The flat-band potential φ_{FB} is a characteristic value of an electrode system that reflects zero band bending and the maximum electron energy available for a reduction reaction at the electrode.[26] Knowing the electrochemically active electrode surface and relative permittivity of the electrode material allows to determine its donor density N_{D}. Later on, we will use this quite common approach in order to verify the experimental results obtained from SHG spectroscopy.

It should be noted that the Mott-Schottky model as introduced above is a quite strong simplification of the semiconductor electronic structure, where lattice anisotropy, symmetry and electrodynamic effects or point defects were neglected, for instance.[86] However, this model has been successfully applied to a range of photo-electrochemical and further semiconductor applications and will also hold for a range of considerations in the results of this thesis.[26, 87, 88]

2.4 Surface states and Fermi-level-pinning

As already shown in Section 2.2, the presence of surface or interface states is a prerequirement for bulk carrier depletion and thus for a light-driven charge separation and photo-electric energy conversion. On the downside, such electronic states are also suspected to mediate loss processes such as charge accumulation and carrier recombination.[26, 57, 89–91]
The actual chemical nature of surface or interface states remains enigmatic. While the presence of surface states is postulated also for ideal crystal systems,[40, 92] their formation was also assumed to arise from surface hydroxylation of metal oxides,[26] or to be induced by the contact of semiconductors with other semiconductors or metals.[26, 40, 92] In fact, the presence of α-Fe_2O_3 photoanode surface states has been demonstrated by a range of modulated electrochemical experiments,[59, 65, 76, 91] whereas the catalytic role of these states remains unclear.[58, 59, 65, 76]
One particular phenomenon that should be mentioned in the context of surface states at the semiconductor/electrolyte interface is so-called Fermi-level-pinning. It was found, that under certain conditions the Schottky barrier height at semiconductor-metal contacts is not affected or incompletely biased by the external electrode potential. Since this effect first manifested as a fixed work-function in photoemission experiments it was called Fermi-level-pinning.[40, 93–96] This constraint to the surface band bending is a deviation of an ideal Mott-Schottky-behaviour and therefore of particular interest for semiconductor electrodes. Thus, Fermi-level-pinning in the context of semiconductor photo-electrochemistry should be explained in a bit more detail here.[63, 65, 97–99]
Fig. 2.3 schematically illustrates Fermi-level-pinning at an n-type semiconductor photoanode interface. We see the depletion layer and a distribution of surface states under three different degrees of externally applied bias potential.[40, 65, 98] On the left-hand side, the Fermi-level is set in a way that no band bending occurs. This

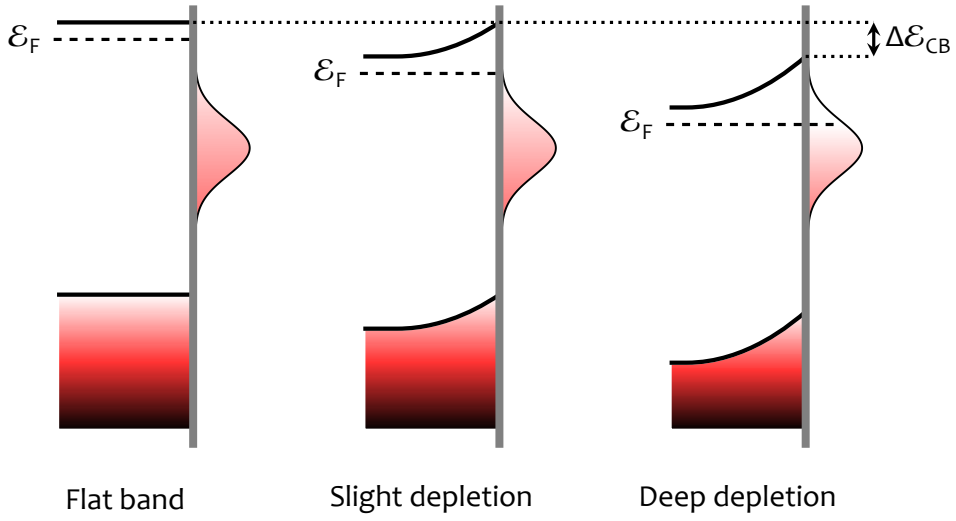

Figure 2.3: The concept of FERMI-level-pinning due to an overlap between the FERMI-level and a high density of surface states

flat-band condition implies that $\Phi_{\mathrm{Ext}} = \varphi_{\mathrm{FB}} - k_{\mathrm{B}}T/e_0$, $\Phi_{\mathrm{SC}} = 0$, $Q_{\mathrm{SC}} = 0$ and $W_{\mathrm{SC}} = 0$ (see Eq. 2.6, Eq. 2.8 and Eq. 2.10).

In the middle of Fig. 2.3, we see the semiconductor surface under gentle depletion conditions. While the conduction band-edge remains pinned at the same energetic position, the semiconductor material is depleted of electrons and a classical space charge layer forms. Under such conditions, an external bias would completely fall across the SCR and fully correspond to the built-in field. The MOTT-SCHOTTKY approximation is fulfilled.[26, 33]

The right-hand side of Fig. 2.3 shows the case of FERMI-level-pinning for a strongly depleted n-type semiconductor photoanode surface. Here, the FERMI-level has a significant energetic overlap with a high density of surface states so that the external bias is distributed over two different electronic layers. Under such conditions, a shift of the conduction band-edge $\Delta\mathcal{E}_{\mathrm{CB}}$ is observed which limits the amount of band bending and consequently the maximum photovoltage and -current of the semiconductor device.[65, 98] In this case, the external bias is distributed over the SCR and HELMHOLTZ layer,[33, 98] so that the one-to-one correspondence between Φ_{Ext} and Φ_{SC} would be discontinued over the surface states energetic distribution. In fact, a plateau of semiconductor electrode MOTT-SCHOTTKY-plots in conjunction with an increased surface state density has been measured and interpreted in terms of FERMI-level-pinning.[33, 65]

This example in Fig. 2.3 explains a model of a potential distribution due to a parallel arrangement of surface and space charge layer, where the total capacitance C_{T} is composed of a space and a surface charge capacitance $C_{\mathrm{T}} = C_{\mathrm{SC}} + C_{\mathrm{SS}}$. For a large surface state capacitance, the applied bias would be mostly compensated within the surface state charge distribution to cause a plateau in the Mott-Schottky plots.[33, 36, 98]
Another case of Fermi-level-pinning can be observed when a capacitance is arranged in series with the space charge layer, as for instance the Helmholtz or double layer capacitance C_{H}, which is similar or even smaller than the space charge capacitance, so that the effect gains influence on the applied bias according to ${C_{\mathrm{T}}}^{-1} = {C_{\mathrm{SC}}}^{-1} + {C_{\mathrm{H}}}^{-1}$. Under such conditions, the external potential is also not entirely acting on the band bending and distributed over the space charge and double layer.[36, 100] Therefore, particular attention on the arrangement of different capacitive layers is important to extract information on the space charge evolution with the applied bias potential.
So far, the presence of α-Fe_2O_3 photoanode surface state densities have been mostly inferred from EIS techniques that can be used to calculate a surface density of states (DOS).[63, 65, 101] Later on, we will see how comparable results can be obtained from IV and transient photovoltage measurements showing good agreement with literature values from different electrochemical techniques.[63, 65, 101]

2.5 Quasi-Fermi-levels

At this point, we have elaborated a description of an n-type semiconductor electrode system in the dark – i.e. for equilibrium carrier distribution. However, electrode illumination and carrier excitation is a basic element of PEC water splitting. Therefore, we want to have a look at some energetic aspects of the irradiated electrode.
Fig. 2.4 shows energy schemes of a water splitting semiconductor electrode in the dark and under illumination. In the left-hand side, we see the formation of a dark OER current j_{Dark}, if sufficient overpotential η is provided. The right-hand side shows the situation for an illuminated electrode. In this case, the water oxidation reaction is driven by photogenerated valence band holes and a photocurrent j_{Photo} is observed. As a consequence, one would expect less bias potential at the working electrode in order to drive the same OER current. This is generally observed in PEC IV measurements: A cathodically shifted OER onset potential due to the formation of a photocurrent.[26, 57]

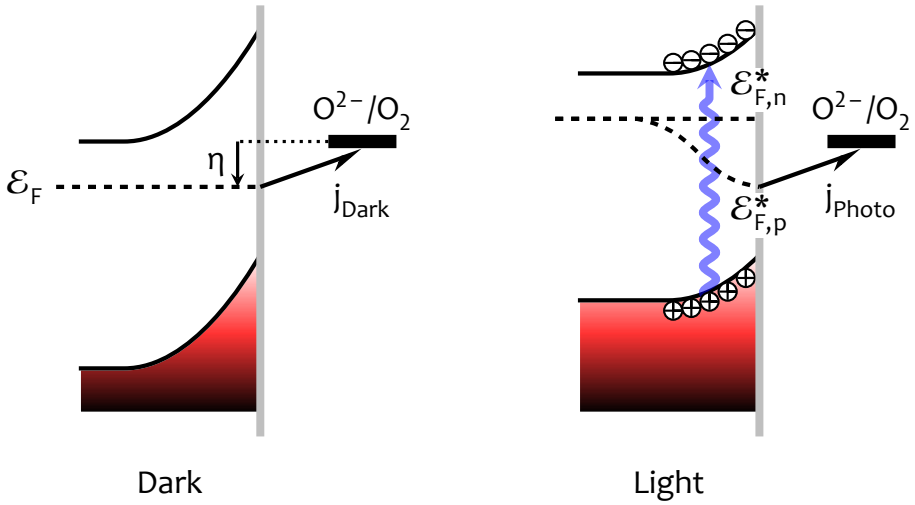

Figure 2.4: The concept of quasi-Fermi-levels for an n-type semiconductor electrode that is driving a water splitting OER current

In order to account for these thermodynamic considerations, one has introduced the concept of quasi-Fermi-levels.[26, 33] Unlike the n-type semiconductor electrode in the dark, the illuminated electrode will undergo a change of the free charge carrier concentration. This affects the concentration of both majority carriers n and minority carriers p and is therefore reflected by different Fermi-levels for electrons and holes, the so called quasi-Fermi-levels $\mathcal{E}^*_{F,n}$ and $\mathcal{E}^*_{F,p}$, respectively. As shown in the right-hand side of Fig. 2.4, the OER overpotential under illumination is provided by photo-excited holes which implies that less external bias potential is required to drive the same current. This deceased bias is reflected by a lowered SCR potential drop, called *band flattening*.[26, 79]

$$n = n_0 + \Delta n = N_C + \exp\left\{\frac{-(\mathcal{E}_C - \mathcal{E}^*_{F,n})}{k_B T}\right\} \tag{2.11}$$

$$p = p_0 + \Delta p = N_V + \exp\left\{\frac{-(\mathcal{E}^*_{F,p} - \mathcal{E}_V)}{k_B T}\right\} \tag{2.12}$$

The values for both quasi-Fermi-levels can be calculated via Eq. 2.11 and Eq. 2.12, respectively. In this model, N_C denotes the conduction band DOS. The symbols n_0, n and Δn denote the conduction band electron concentrations in the dark, under illumination and their absolute difference, respectively. Analogously, N_V, p_0, p and

Δp are the valence band DOS, dark and illuminated hole concentrations and the difference, respectively.[26, 33]
In our sample system, an n-type semiconductor electrode, the majority and the minority charge carriers are electrons and holes, respectively. With this, we can approximate a negligible change of the majority carrier concentration $n \approx n_0$ under illumination and a negligible concentration of minority carriers in the dark $p_0 \approx 0$. Thus, $\mathcal{E}^*_{\mathrm{F,n}}$ remains approximately constant while the illumination of an n-type semiconductor photoanode would mainly affect the concentration of photo-generated valence band holes.[26, 40]
To the author's knowledge, the physical validity of quasi-Fermi-levels is still under debate. First of all because this model is only based on net thermodynamic considerations while kinetic effects such as different lifetimes for electrons and holes or excitonic, phonoic or polaronic effects are not considered.[26, 86] A range of ultrafast processes, were shown to dramatic effects on the semiconductor lattice electronic structures.[102–104] Also, different resistive and capacitive losses within the semiconductor material are not reflected by this model.[105] However, the concept has been applied as a useful tool to describe the formation of photovoltage in semiconductor structures in particular equilibrated conditions.[106, 107] Later on, we will make use of the concept of quasi-Fermi-levels to describe the relation between photovoltage and photocurrent under static conditions.

3 Methods

3.1 Anodic electrodeposition

The method of choice for the preparation of α-Fe_2O_3 photoanode samples is an anodic electrodeposition (ED) film growth from an iron(II) ($Fe^{2\oplus}$) plating solution with subsequent thermal annealing. This simple route provides the advantages of a cheap and scalable process that avoids ecological, economical and scaling issues which are associated with gas phase deposition processes, for instance. In addition, ED is known to provide an option for a tailored growth of *iron oxide* FeO_x and *iron oxy-hydroxide* FeO_xH_y films with a broad range of morphological and crystallographic properties, depending on the process parameters such as precursor concentration, chelating agents, deposition potential, temperature and pH.[108–115]

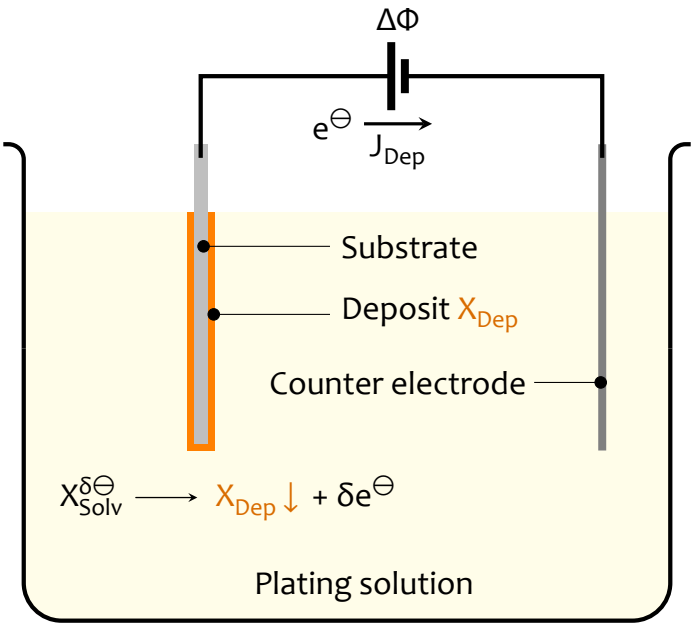

Figure 3.1: Anodic electrodeposition of a solvated precursor species $X_{Solv}^{\delta\ominus}$ that is oxidized in front of the substrate electrode to form a deposit film X_{Dep}

Electrodeposition (ED) refers to an electrolytically induced precipitation-deposition film growth process from a precursor solution onto a substrate electrode surface. Depending on the actual chemical redox process, the terms electroplating, galvanic deposition and electrophoretic deposition may be used equivalently.[116]
In our case, we aim to conduct an anodic ED film growth, that involves partial or complete oxidation of a precursor ion. Fig. 3.1 shows a scheme of this process in a general form. The simple but quite powerful principle is the oxidation of a reducible precursor ion or molecule $X_{Solv}^{\delta\ominus}$, that is solvated in an electrolyte plating solution, at the substrate electrode to form an adsorbed precipitate X_{Dep}. The driving force of the precursor oxidation is provided by a potential difference $\Delta\Phi$ between two electrodes to attract the ions to the respective electrodes of opposite charge. The potential difference will be later on more accurately measured as potential versus an external reference Φ_{Ext}. In order to drive a complete oxidation reaction, a standard redox potential of the precursor redox couple $\varphi^{\circ}(X_{Solv}^{\delta\ominus}/X_{Dep})$ must be exceeded.[27, 116, 117] A partial or complete oxidation of the precursor yields a positive deposition current J_{Dep}.[27, 116]

$$Fe^{2\oplus} + 2\,H_2O \xrightarrow{\Delta\Phi} FeOOH + 3\,H^{\oplus} + e^{\ominus} \tag{3.1}$$

The net chemical redox process that is relevant for the film growth of our samples is the electrolytic oxidation of $Fe^{2\oplus}$ to form an $Fe^{3\oplus}$-oxy-hydroxide FeO_xH_y, mostly FeOOH phases, according to Eq. 3.1,[109, 111, 112] whereas more mechanistic details will be discussed on the basis of electrochemical data in Chapter 8.
The as-deposited FeO_xH_y film will be thereafter converted to an α-Fe_2O_3 photoanode sample by thermal annealing in air according to Eq. 3.2.[111, 112]

$$2\,FeOOH \xrightarrow{\Delta T} \alpha\text{-}Fe_2O_3 + H_2O \tag{3.2}$$

3.2 Second harmonic generation

3.2.1 Non-linear polarization

The goal of this thesis is to investigate electronic structures and processes at the water splitting α-Fe_2O_3 photoanode interface under operating conditions using second

harmonic generation (SHG) spectroscopy. SHG is a second order non-linear optical process that can be considered as a conversion of two photons of angular frequency ω into one photon of doubled frequency 2ω.[118–120] As an outstanding feature, second order non-linear processes are prohibited in bulk centro-symmetric media such as the α-Fe_2O_3 lattice system, and therefore inherently specific to surfaces and interfaces.[119, 121, 122] Due to the photon energies of the sampling and probing light beams in the optical range, SHG provides the option to overcome the pressure gap and measure surface specific signals in realistic conditions at the operating electrode without costly vacuum demands. SHG also involves the utilization of high power pulsed ultrashort laser light which allows for time resolved investigation of electronic processes down to the ps scale.[123, 124] Since SHG is a special case of the sum frequency generation (SFG) process, where both incident electric photon energies are identical, the following theoretical considerations are partly adopted from a description of the SFG physics.[121]

SHG measurements, as any other optical spectroscopy, are probing the interaction of light with matter, i.e. the change of an electromagnetic wave upon interaction with the specimen. For our purpose, we want to consider light as a propagating electromagnetic wave that is sufficiently defined by an oscillating electric field $\widetilde{\mathbf{E}}(\omega, t)$ with an amplitude $\mathbf{E}_\omega$ and an angular frequency ω at any given time t.[121]

$$\widetilde{\mathbf{E}}(\omega, t) = \mathbf{E}_\omega * \cos \omega t \tag{3.3}$$

An electric field interacts with matter by relocation of charge and imposes a polarization to the respective medium. Consequently, the oscillating electromagnetic wave $\widetilde{\mathbf{E}}$ will induce a periodic polarization $\widetilde{\mathbf{P}}$ to the sample as given in Eq. 3.4.[121]

$$\begin{aligned} \widetilde{\mathbf{P}} = &\ \epsilon_0 \chi^{(1)} * \widetilde{\mathbf{E}} + \epsilon_0 \chi^{(2)} * \widetilde{\mathbf{E}}^2 + \epsilon_0 \chi^{(3)} * \widetilde{\mathbf{E}}^3 + \dots \\ = &\ \widetilde{\mathbf{P}}^{(1)} + \widetilde{\mathbf{P}}^{(2)} + \widetilde{\mathbf{P}}^{(3)} + \dots \end{aligned} \tag{3.4}$$

A materials property, the electric susceptibility χ, relates the induced polarization and the incident field. While classical linear optical processes are solely probing first order polarization $\widetilde{\mathbf{P}}^{(1)}$ effects, the total polarization of the material may contain

terms of higher order $\widetilde{\mathbf{P}}^{(2)}, \widetilde{\mathbf{P}}^{(3)}, \ldots$ which are also linked to the incident field via respective higher order susceptibilities $\chi^{(2)}, \chi^{(3)}, \ldots$ as given in Eq. 3.4.[119, 121]
If we insert Eq. 3.3 into Eq. 3.4 we obtain the following expressions for the second order polarization $\widetilde{\mathbf{P}}^{(2)}$.[121]

$$\widetilde{\mathbf{P}}^{(2)} = \epsilon_0 \chi^{(2)} \widetilde{\mathbf{E}}^2 = \epsilon_0 \chi^{(2)} {\mathbf{E}_\omega}^2 \cos^2 \omega t \tag{3.5}$$

$$= \frac{1}{2} \epsilon_0 \chi^{(2)} {\mathbf{E}_\omega}^2 (1 + \cos 2\omega t) \tag{3.6}$$

$$\widetilde{\mathbf{P}}^{(2)} = \frac{1}{2} \epsilon_0 \chi^{(2)} {\mathbf{E}_\omega}^2 + \frac{1}{2} \epsilon_0 \chi^{(2)} {\mathbf{E}_\omega}^2 * \cos 2\omega t \tag{3.7}$$

From Eq. 3.7 we see that $\widetilde{\mathbf{P}}^{(2)}$ is composed of two terms. First, there is one static component that scales with the squared amplitude of the incident field. This effect – the formation of a static field by large incident oscillating field strengths – is called *optical rectification*. The second term of Eq. 3.7 states that $\widetilde{\mathbf{P}}^{(2)}$ oscillates with the doubled frequency of the incident field 2ω.[119, 121]
Eq. 3.6 and Eq. 3.7 demonstrate the formation of a *second harmonic* (SH) signal – the imposition of a higher order polarization into the sample that contains a static term and one that oscillates with the doubled frequency 2ω of the incident field.[121] This 2ω oscillation will cause a re-emission of an SH electromagnetic wave $\widetilde{\mathbf{E}}(2\omega, t)$ with an amplitude $\mathbf{E}_{2\omega}$. Typical values of $\chi^{(2)}$ are twelve orders of magnitude smaller than $\chi^{(1)}$, which illustrates the huge light power densities required to drive SHG, that can only be provided by pulsed laser systems.[119]
From Eq. 3.7 we also find that the induced n^{th} order polarization depends on the $n+1$ dimensional tensors $\chi^{(n)}$. Analytical information from non-linear optical response is therefore derived from a description of the non-linear susceptibilities $\chi^{(n)}$, which may include molecular orientation [121, 125] or adsorption [126] at different interfaces, electronic transitions [124, 127, 128], rotational anisotropy [128, 129] or depth-dependent resolution of electronic properties[130].

$$\chi^{(2)}_{\mathrm{ijk}} = -\chi^{(2)}_{-\mathrm{i}-\mathrm{j}-\mathrm{k}} \tag{3.8}$$

The nature of $\chi^{(2)}$ implies that the incident fields cancel out due to negative interference in centrosymmetric media such as α-Fe_2O_3. Eq. 3.8 illustrates the third rank tensor $\chi^{(2)}_{\mathrm{ijk}}$ for an incident field strength in the jk plane propagating in a Poynting-

direction i. We see that SHG is only allowed at sites of broken symmetry such as the electrode surface or lattice defects in centro-symmetric media like α-Fe_2O_3, i.e. where $i \neq -i$, $j \neq -j$ or $k \neq -k$.[121, 131]
In order to provide energy conservation, for a loss free, thus parametric SHG process, the phase matching condition Eq. 3.9 must be fulfilled.[119, 121]

$$n(\omega) = n(2\omega) \tag{3.9}$$

For absorptive contributions the second order susceptibility one not just has to account for phase matching between incident and emitted fields but also for optical damping, phase mismatch, carrier lifetimes or population densities, for instance,[119, 127, 132, 133]. Such resonant contributions are reflected by a complex non-linear susceptibility, where $\chi^{(2)}$ is composed of a resonant and a non-resonant contribution according to Eq. 3.10.[121, 134]

$$\chi^{(2)} = \chi^{(2)}_{\mathrm{NR}} + i\chi^{(2)}_{\mathrm{R}} \tag{3.10}$$

One common description for a resonant susceptibility can be derived from the harmonic oscillator model as given in Eq. 3.11, with a resonance frequency ω_0 the fundamental frequency ω, a decay constant $i\Gamma$ and an oscillator strength B.[121, 134] Other models to describe imaginary contributions may employ the Drude model [119, 135] or exciton wave functions, for instance.[128, 133]

$$\chi^{(2)}_{\mathrm{R}} = \frac{B}{\omega_0 - \omega - i\Gamma} \tag{3.11}$$

The resonant part of the susceptibility also needs to account for optical absorption in z-direction for both, the fundamental and the SH fields. While this effect is further influenced by the coherence path length and the refractive index difference for both fields, the non-linear susceptibility often requires huge incident power densities so that the population ratio between excited state and ground state approaches unity.[119, 136] In literature, several studies have measured the SHG response from absorptive single crystal semiconductor photoanodes and evaluated the results from comparison with electrochemical measurements and concepts.[79–81, 137] Later

on, we will follow this approach but also experimentally compare the absorption coefficients of the sample system at the photon frequencies relevant to SHG in order to assess possible effects from optical absorption and analyse the SHG responses from comparisons with parallel electrochemistry (EC) and other experimental methods.

The induced second order polarization causes a re-emission of the two-photon electric field $\widetilde{\mathbf{E}}_{2\omega}$, where the relation between incident, transmitted and reflected fields as function of the incident angle, refractive indices and beam polarization combinations are given by the Fresnel-equations.[121, 138] In general, the emitted SHG field $\widetilde{\mathbf{E}}_{2\omega}$ in a direction i is given by the induced polarization amplitude $\mathbf{P}^{(2)}$ and a corresponding non-linear Fresnel- or L-factor according to Eq. 3.13.[121, 139] Thus, for constant probing geometry and phase relation of the participating fields, the emitted second harmonic electric field is directly proportional to the induced second order polarization.[125, 140]

$$\widetilde{\mathbf{E}}_{2\omega,\mathrm{i}} = L_{\mathrm{i}} * \widetilde{\mathbf{P}}^{(2)}_{\mathrm{i}} \tag{3.12}$$

$$\mathbf{E}_{2\omega} \propto \mathbf{P}^{(2)} \tag{3.13}$$

As outlined so far, a complete formulation of the relationship between incident fundamental and emitted SH is strongly model-based and involves a large space of optical, electronic, spatial and temporal parameters including contributions from phase relations, optical density, transition probabilities, path lengths, carrier lifetimes or electrodynamic effects in three different coordinate systems corresponding to the beam propagation, the sample system and surface molecular orientation.[119, 121] However, the experimental works in this thesis will track the SHG response from an operating, defective and nanostructured α-Fe_2O_3 photoanode and will be closely compared to electrochemical boundaries and other experimental methods. Therefore, a microscopic modelling of the non-linear effects will be omitted in order to avoid any speculative or model biased interpretations due to the multiplicity of degrees of freedom compared to single crystal or ultra high vacuum (UHV) conditions, for instance. Instead, we want to search for experimental confirmation and follow the approaches as published for different semiconductor electrode sample systems.[81, 137] The observed SHG response from the operating electrode will be evaluated in terms the macroscopic sample conditions, compared with common photo-electrochemical concepts and literature results and consecutively discussed and evaluated in combina-

tion with a range of additional methods in order to characterize electronic properties and processes of the sample system based on experimental reason.

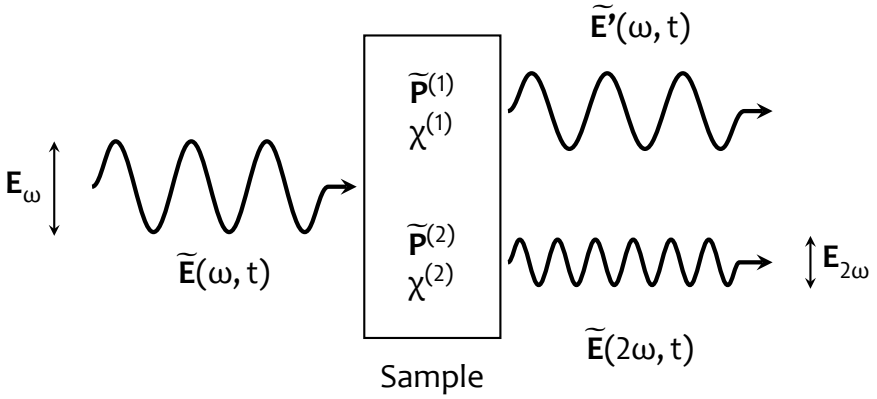

Figure 3.2: Schematic illustration of an SHG spectroscopy experiment.[119, 125] While linear spectroscopy is focused on first order changes of an incident field $\widetilde{\mathbf{E}}_{\omega}$ upon interaction with matter, SHG measurements are sensing the properties and physico-chemical origins of the emitted second harmonic signal $\widetilde{\mathbf{E}}_{2\omega}$.

A more intuitive illustration of an SHG experiment is illustrated in Fig. 3.2.[125] We see an incident field $\widetilde{\mathbf{E}}_{\omega}$ that oscillates with an amplitude $\mathbf{E}_{\omega}$. This fundamental field interacts with the sample and induces some first and second order periodic polarizations $\widetilde{\mathbf{P}}^{(1)}$ and $\widetilde{\mathbf{P}}^{(2)}$, respectively. Within a purely first order framework, this interaction might lead to changes of the intensity, colour or phase and leading to re-emission of some perturbed first order electric field $\widetilde{\mathbf{E}}'(\omega, t)$. Second harmonic generation (SHG), instead, is sensing the properties of the emitted SH field $\widetilde{\mathbf{E}}(2\omega, t)$, which oscillates with the twofold frequency of the incident field 2ω. The SHG measurements in this thesis will be performed under static conditions, where one constant incident fundamental field strength is upconverted at the sample system in reflection mode and the SHG intensity is measured. Therefore, the time domain effects are neglected, and all following analyses will be drawn from the amplitude $\mathbf{E}_{2\omega}$ of the emitted SHG field.[79, 81]

3.2.2 Electric field induced second harmonic

A range of SHG experiments have revealed an influence of electrode bias to the emitted SH intensity. The conventional explanation of this effect is an additional contribution to the induced polarization as given in Eq. 3.14. In this expression, the

induced polarization contains an additional third order component $\mathbf{P}^{(3)}$, where a static field of zero frequency $\mathbf{E}_{\mathrm{DC}}$ contributes to the induced polarization so that the emitted frequency is still 2ω. A qualitative picture of this effect is the introduction of additional asymmetry by a static field changing with distance from the interface to enhance the SHG response. [125, 141, 142]

$$\mathbf{P}_{2\omega} = \mathbf{P}^{(2)}_{2\omega} + \mathbf{P}^{(3)}_{2\omega} = \chi^{(2)}{\mathbf{E}_{\omega}}^2 + \chi^{(3)}\mathbf{E}_{\mathrm{DC}}{\mathbf{E}_{\omega}}^2 \tag{3.14}$$

As developed in Section 2.2, the static electric field is changing with distance from the semiconductor electrode surface. The third order polarization therefore is given by the integral over the probed surface region according to Eq. 3.15 and thus proportional to the voltage drop at the interface (see Fig. 3.3).[125, 142]

$$\mathbf{P}^{(3)}_{2\omega} = \chi^{(3)}{\mathbf{E}_{\omega}}^2 \int_0^z \mathbf{E}_{\mathrm{DC}}(z)\,\mathrm{d}z = \chi^{(3)}{\mathbf{E}_{\omega}}^2 * \Phi_{\mathrm{DC}} \tag{3.15}$$

Inserting Eq. 3.15 and Eq. 3.14 into Eq. 3.13 yields an expression for the emitted SH as function of the second and third order susceptibilities and the interfacial potential drop according to Eq. 3.16.[125, 142]

$$\boxed{\mathbf{E}_{2\omega} \propto \left(\chi^{(2)} + \chi^{(3)}\Phi_{\mathrm{DC}}\right){\mathbf{E}_{\omega}}^2} \tag{3.16}$$

As in any other spectroscopy, the experimentally accessible quantity of the SHG process is the light intensity which is given by the squared amplitude of the emitted field according to $I = \mathbf{E}^2$. With this we can express the measured SHG response as function of the non-linear susceptibilities and the incident field according to Eq. 3.17.[121]

$$\boxed{I_{2\omega} \propto \left|\chi^{(2)} + \chi^{(3)} * \Phi_{\mathrm{DC}}\right|^2 * {I_{\omega}}^2} \tag{3.17}$$

The expressions Eq. 3.17 and Eq. 3.16 provide a versatile relation to probe potential distributions across interfaces, i.e. the so-called electric field induced second harmonic (EFISH). This effect was first described by Lee and co-workers [141] and

has been used as probe for a range of surface and interfacial properties and processes.[142–144]

$$I_{2\omega} \propto \left| \left(\chi^{(2)}\right)^2 + 2 * \chi^{(2)}\chi^{(3)}\Phi_{\mathrm{DC}} + \left(\chi^{(3)} * \Phi_{\mathrm{DC}}\right)^2 \right| * {I_\omega}^2 \tag{3.18}$$

Due to squared modulus of the higher order susceptibilities in Eq. 3.18, an interpretation of the contributions from the static field is somewhat obscured. While an effect from the crossterm $2 * \chi^{(2)}\chi^{(3)}\Phi_{\mathrm{DC}}$ would result in a linear potential dependence, a purely third order polarization $(\chi^{(3)} * \Phi_{\mathrm{DC}})^2$ would cause a quadratic potential dependence. In any case, a minimum of the SHG response would indicate zero static field at the interface according to Eq. 3.19.

$$\left.\frac{\mathrm{d}I_{2\omega}}{\mathrm{d}\Phi_{\mathrm{DC}}}\right|_{\Phi_{\mathrm{Ext}}=\varphi_{\mathrm{FB}}} = 0 \tag{3.19}$$

A range of second order non-linear spectroscopy (SHG and SFG) studies on solid-liquid interfaces have shown that the magnitude of interface SHG or SFG responses can be modified by altering interfacial electric fields. This behaviour was observed for potential drops along both the solid and in the liquid side of the interface.[79, 81, 142, 145–148]
Most EFISH studies have focused on the potential drop into the liquid side of solid/liquid interfaces. In analogy to our considerations on the carrier density in the lattice (see Section 2.3), the distribution of ions in an electrolyte off of a solid surface can be tracked by EFISH measurements as well. With this, a range of works have inferred ionic distribution and polarization effects for a number of solids and ions.[140, 142, 149–152] These measurements are always performed in highly diluted electrolytes with very low ionic strengths from µmol to mmol which is necessary in order to provide a sufficiently long distance of the potential drop into the liquid (see Eq. 3.15).[142, 152] In contrast, a conventional concentrated 1 M KOH electrolyte will be applied in the following SHG measurements at the operating α-Fe_2O_3 photoanode which conveniently provides a better conductivity and also constrains the potential drop into the electrolyte to a few nm from the surface to suppress any manifestations of electrolyte polarization effects in the SHG signal formation.[26, 152]

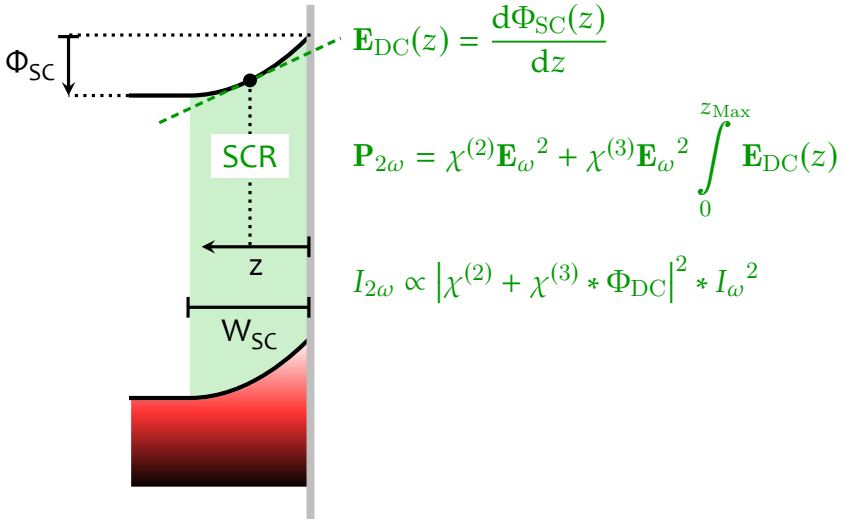

Figure 3.3: Application of the electric field induced second harmonic (EFISH) theory to the SCR potential drop of an n-type semiconductor surface [26, 79, 81, 125, 142]

Fig. 3.3 sketches the application of the EFISH effect to the SCR at the surface of an n-type semiconductor photoanode (see also Section 2.2).[26, 33] We see that the band bending causes a potential drop Φ_{SC} over a certain distance, called space charge width W_{SC}. In this one dimensional picture, the static electric field $\mathbf{E}_{DC}$ is a function of the distance from the electrode surface z, while the entire potential drop Φ_{SC} corresponds to the integral field $\mathbf{E}_{DC}$ over the whole depletion width W_{SC}.
As shown in Fig. 3.3, the integral static field is equal to the SCR potential drop Φ_{SC} which yields the expression Eq. 3.17 for the SHG response to a static electric field. Previous studies on potential dependent SHG from n-type semiconductor electrodes reported both quadratic and linear potential dependence.[79, 81] The works by Lantz and co-workers showed a purely linear relationship between the SHG response from a TiO_2 photoanode and the applied potential.[79, 80] Bian et al. measured a change from quadratic to linear potential dependence at a certain deflection potential. These works also pointed out that the change from quadratic to linear potential dependence is strongly affected by the azimuthal angle of a single crystal Si sample and thus by the lattice orientation with respect to the oscillating electric fields $\mathbf{E}_{\omega}$ and $\mathbf{E}_{2\omega}$.[81] In our nano-porous sample system, however, no crystallographic long range order is provided so that an azimuthal signal dependence can be neglected here. Both works eventually conclude that a linear SHG response to the external bias is caused by a limited optical path length in the single crystal semiconductor photoanodes.[79,

81] With this, these studies have confirmed the applicability of the EFISH effect to semiconductor electrode band bending and succeeded to determined flat-band potential, however, a comprising elaboration of the charge and potential distribution has not been achieved, yet.[79–81, 137]
This thesis will present an application of the EFISH effect to the SCR of a functional water splitting α-Fe_2O_3 photoanode (see Section 2.2). The experimental boundaries are carefully characterized considering and eliminating possible side effects or parasitic signal formation processes. We will see how the SHG response from the α-Fe_2O_3 photoanode reacts to external stimuli such as bias potential or electrode illumination. This effect will be referred to an enhancement of the SHG response by the electrode surface band-bending in very good correspondence with complementary electrochemical techniques. With this approach, a direct probe of the SCR potential drop is developed and applied to the α-Fe_2O_3 photoanode field distribution in particular.

3.2.3 Optical transitions

In analogy to Raman-scattering, the generation of SH light can be resonantly enhanced when the participating photon energies overlap with quantum state transitions of the sample system – i.e. mostly vibrational or electronic transitions.[119–121] The angular frequencies of the fundamental and SH waves are related to the electronic energy scale of the sample material according to $E = \hbar\omega$.[153, 154]

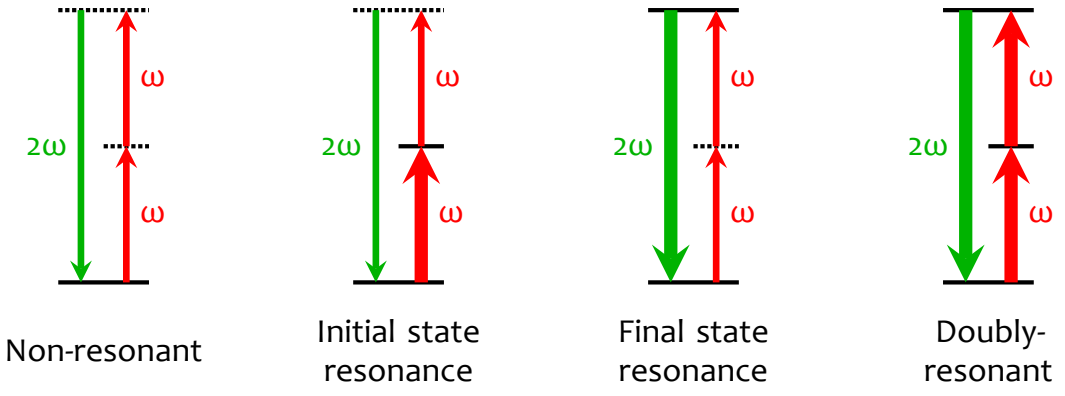

Figure 3.4: Optical resonances and electronic transitions in SHG spectroscopy

Different types of resonances are sketched in Fig. 3.4. A non- or off-resonant SHG process is shown on the left hand side, where none of the participating photon energies overlaps with electronic transitions of the material. A range of fundamental investigations of second order non-linear effects have focused on media that generate

pronounced non-resonant SH signals such as gold (Au) or quartz (SiO_2) due to their frequency-independent second order non-linear response.[130, 139, 155] The spectral shape of a purely non-resonant signal in absence of external fields solitarily depends on the incident field according to Eq. 3.17. Although an accurate description of the signal formation involves overlap matrices of incident and emitted fields, one might also think of non-resonant transitions in terms of virtual energy levels as indicated by dashed lines in Fig. 3.4.
If the fundamental frequency overlaps with a quantum transition of the sample system, the second order response can be enhanced around the respective photon energy.[120] While the most prominent application of this effect is utilized in vibrational SFG spectroscopies,[121, 139, 156] it might be also worth to consider such a initial state resonance with respect to the α-Fe_2O_3 band structure. Alternatively, the emitted SH might also be in resonance with an electronic transition energy difference leading to a signal enhancement at the respective SH photon, which would be classified as final state resonance.[120] Finally, it might also occur that both fundamental and SH overlap with electronic transitions of the sample system as shown on the right hand side in Fig. 3.4. This so called doubly resonant SHG is known to exhibit a strong enhancement of the SHG signal.[120, 157, 158]

One way to distinguish between resonant and non-resonant contributions is to normalize the second order spectral response of a non-resonant signal. This could eliminate the fundamental beam shape and yield a spectrum that provides information on resonant enhancements.[139, 156] Later on, we will apply these considerations to the SHG spectra obtained from the α-Fe_2O_3 sample and discuss them in terms of the electronic structure of the electrode system.
With regard to SHG investigations of an α-Fe_2O_3 semiconductor electrode, it seems sensible to tune the photon energies towards an electronic resonance with the electrode material. Therefore, the fundamental near infrared (NIR) light will be chosen in such a way, that the emitted SHG is in good overlap with the tail of material's band-gap around 2.1 eV in order to provide a possible resonance with shallow donor type defect states while still maintaining sufficient optical transmission for spatially unrestricted probing.

3.3 Electrochemical impedance spectroscopy

3.3.1 Equivalent circuits and quasi-capacitances

One common approach to model physico-chemical processes of electrode systems is to employ the concept of *quasi capacitances*. The idea behind this assumption is a description of electrode processes in analogy to an electric circuit, a so-called equivalent circuit. This allows to express charge accumulation processes by their analogues from electrical engineering – as capacitors – while charge transfer processes are represented as resistors. The physics of space charge and surface states in semiconductor electrode systems, for instance, have been mostly inferred from their capacitive behaviour within electric circuit systems (see Section 2.3 and Section 2.4). This reduction of multi-scale electrode processes down to a one dimensional electric capacitance is not always possible, but is has produced a range of valuable results for the α-Fe_2O_3 photoanode system[63, 65, 76, 159–161] and a broad range of further electrode materials.[88, 162]
If one compartment of the electrode system, such as the SCR or a set of surface states, exhibits a sufficiently pure charge accumulation behaviour, this compartment can be described by a quasi capacitance, i.e. by their ability to store a certain amount of charge per potential interval: $C_{\mathrm{Quasi}} = Q/\Phi$. Under these premises it would be possible, for instance, to derive a surface or volume charge density, $sigma = Q/S_{\mathrm{act}}$ or $\rho = Q/V$, respectively, from a capacitance measurement.[65, 163] The approximation is limited by the non-ideal behaviour of different electrode compartments. There are cases, where e.g. a hybrid resistive and capacitive behaviour is observed or where particle size distributions or diffusion processes in front of the electrode are preventing a reduction to a purely capacitive effect.[75, 160, 164] Therefore, any physico-chemical conclusion arising from a quasi-capacitance assumption should be carefully verified by additional arguments in order to exclude non-ideal effects that may distort a purely capacitive behaviour.[75, 163, 165]

Provided that an approximation of different electrode compartments by their capacitive properties is valid, these compartments can be analysed analogously to a set of capacitors in electrical engineering. Accordingly, a given arrangement of several capacitive electrode compartments may be considered as a set of parallel or serial capacitors.[26, 75] As illustrated in Fig. 3.5, an electrochemically observable total capacitive response of the integral electrode system C_{T} may be described by

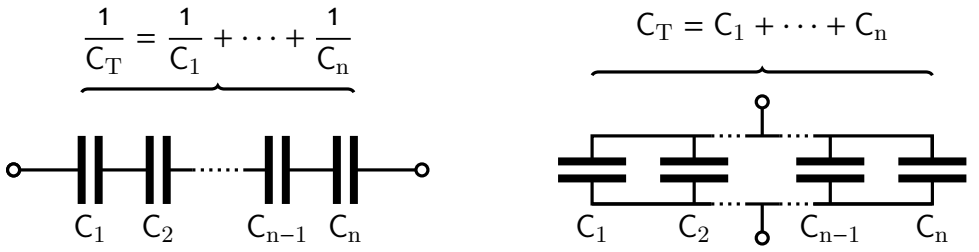

(a) Serial capacitors **(b)** Parallel capacitors

Figure 3.5: Description of capacitive effects by their equivalent circuits in parallel and in serial arrangement. Varying arrangements of capacitive compartments will lead to different capacitive responses C_T of the integral electrode system [26, 33, 75, 166]

an electric equivalent circuit. Thus, if two capacitors are arranged in series, the reciprocal resulting capacitive response of the electrode system is given by sum the single reciprocal capacitances as shown in Fig. 3.5(a).[75, 166]
This analogy serves as a common model to decouple the space charge capacitance C_{SC} from the Helmholtz capacitance C_H, for instance, as for concentrated electrolytes, C_H is typically much larger than C_{SC}.[26] Thus, with $C_H \gg C_{SC}$, we would find from Fig. 3.5(a), that $1/C_H \approx 0$ and the overall capacitive response C_T is governed by the space charge capacitance $C_T \approx C_{SC}$. This approximation is a common assumption to decouple EC contributions from different capacitive electrode compartments in series.[26, 159, 167]
Accordingly, the total capacitive response of parallel capacitive layers is given by the sum of the single capacitances as shown in Fig. 3.5(b). This arrangement is often employed in order to describe Fermi-level-pinning in the presence of surface states.[36, 65, 98]
In the following chapters, the different electrode compartments will be approximated as quasi-capacitances, while all of these analyses are confirmed by complementary techniques and multiple experimental or analytical arguments. We will encounter this picture several times and employ it to separate the space charge capacitance from further capacitive contributions of the electrode system and find good agreement between different methods and also with literature. The main analyses of the α-Fe_2O_3 photoanode system, for instance, will be performed at potentials below the OER reaction onset, so that capacitive effects will dominate over resistive processes, which are more relevant to significant net solid/liquid charge transfer processes.[63, 65,

160] The subsequent discussions will mainly focus on the assignment of particular electrode compartments to their corresponding capacitive features. Therefore, the terms *quasi-capacitance* and *capacitance* will used equivalently in the following sections due to their electrochemical manifestation as capacitive effects C.

3.3.2 Electric impedance

As mentioned before, range of electrochemical phenomena can be described in analogy to electric circuits. Particularly relevant is a measurement of the potential dependent space charge capacitance C_{SC}, which provides information on the flat-band potential and dopant densities of a semiconductor electrode (see Section 2.3). One prominent method to measure capacitive effects from electrode compartments such as C_{SC} or a surface state capacitance C_{SS} is electrochemical impedance spectroscopy (EIS).[63, 65] The electric impedance of a given electric system **Z** is a measure of its complex resistance to an alternating current. EIS is the frequency-resolved measurement of **Z** from an EC system which can provide information on electronic structures and processes.

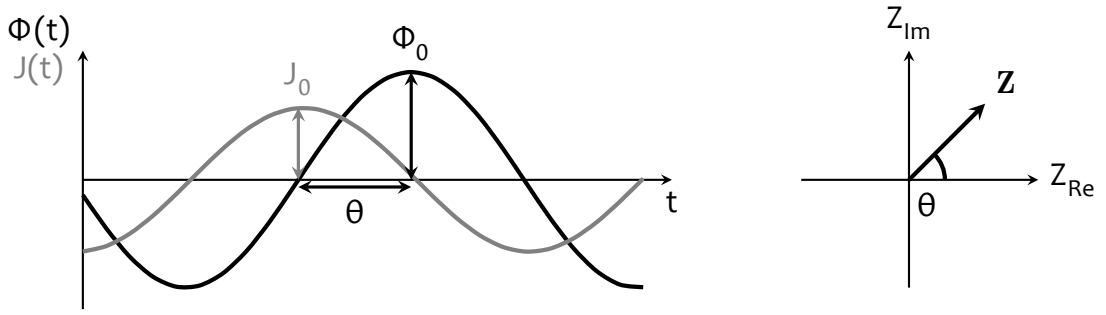

(a) Time domain sinusoidal potential perturbation and current response

(b) Frequency domain complex impedance

Figure 3.6: Electrical impedance illustrated by a sinusoidal potential perturbation and the current response [26, 75, 165]

Fig. 3.6 illustrates the principle of the electric impedance. In Fig. 3.6(a), we see a sinusoidal potential perturbation to an electric system with an amplitude Φ_0 as function of time t. The system response to this stimulus is a sine wave current with an amplitude J_0 that is shifted by a phase angle θ. Both waves oscillate with an angular frequency ω that is linked to the time domain and the ordinary frequency f

via $\omega = 2\pi f$ with $f = 1/t$. Thus, the time dependent potential $\Phi(t)$ and current $J(t)$ is given by Eq. 3.20 and Eq. 3.21, respectively.[165]

$$\Phi(t) = \Phi_0 * \sin(\omega t) = \Phi_0 * \exp(i\omega t) \tag{3.20}$$

$$J(t) = J_0 * \sin(\omega t + \theta) = J_0 * \exp(i\omega t - i\theta) \tag{3.21}$$

In analogy to the direct current resistance in Ohm's law, the complex impedance $\mathbf{Z}$ is defined as fraction of potential per current according to Eq. 3.22.[165]

$$\mathbf{Z} = \frac{\Phi(t)}{J(t)} \tag{3.22}$$

If we insert Eq. 3.20 and Eq. 3.21 into Eq. 3.22, we obtain a time-independent expression of $\mathbf{Z}$ with the magnitude of the impedance $|\mathbf{Z}| = \Phi_0/J_0$:[165]

$$\mathbf{Z} = |\mathbf{Z}| * \exp(i\theta) = |\mathbf{Z}| * (\cos\theta + i\sin\theta) \quad . \tag{3.23}$$

Eq. 3.23 can be separated into a real and an imaginary part and we obtain the most common representation for $\mathbf{Z}$, Eq. 3.24. Thus, as also shown in Fig. 3.6(b), the impedance can be represented as a vector in the complex plane with a length $|\mathbf{Z}|$, a real part Z_{Re} and an imaginary part Z_{Im} and a phase angle θ, where Z_{Re} represents resistive effects and Z_{Im} represents capacitive or phase related contributions to the frequency response of the electric system.[165]

$$\boxed{\mathbf{Z}(\omega) = Z_{\mathrm{Re}} + Z_{\mathrm{Im}}.} \tag{3.24}$$

3.3.3 Frequency response

As given in Eq. 3.24, the impedance is a characteristic of an electric system at any given frequency ω. An impedance spectrum is a plot of $\mathbf{Z}$ over the frequency-axis, where the two-dimensional nature of $\mathbf{Z}$ requires a separate representation of both ordinates (Bode-Plot) or the omission of an explicit frequency axis (Nyquist-Plot).[75] It is in principle possible to model the frequency response for any electric system

composed of the classical elements resistor, capacitor and inductor. The analysis of EC systems mainly follows the analysis of electric circuits, where capacitors and resistors are assumed to represent charge accumulation and transfer processes, respectively. Therefore, an equivalent circuit of an electrode system is typically applied as approximate model of charge storage and transport processes across the electrode. However, depending on the system's complexity, a the development of a global model of **Z** can become fairly involved. In addition, the application to EC systems is further complicated due to diffusion, adsorption and reaction steps or non-ideal behaviour of particular elements, for instance.[76] Therefore, it is often useful to make appropriate simplifications of the model.

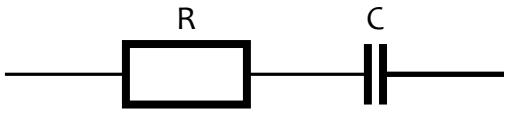

Figure 3.7: *RC*-circuit as convenient model of the space charge capacitance C_{SC} in series with a linear resistor [26]

One common simplification is an approximation of the frequency response in terms of a serial *RC*-circuit as shown in Fig. 3.7 which is just composed of a resistor *R* and a capacitor *C* in series.[26] Analogous to the Ohmic resistances, the total impedance $\mathbf{Z}_{\mathrm{T}}$ of two serial components is equal to the sum of the individual elements $\mathbf{Z}_{\mathrm{R}}$ and $\mathbf{Z}_{\mathrm{C}}$ according to

$$\mathbf{Z}_{\mathrm{T}}(\omega) = \mathbf{Z}_{\mathrm{R}} + \mathbf{Z}_{\mathrm{C}} \quad . \tag{3.25}$$

From basic electrical engineering it is known that resistors are changing the amplitude and capacitors are shifting the phase of an alternating current response, i.e. the total impedance of these elements conveniently contains just a real part for *R* and is purely imaginary for *C* (see Fig. 3.6 and Eq. 3.24).[166] In fact, both values are given by Eq. 3.26.[75, 165, 166]

$$\mathbf{Z}_{\mathrm{R}} = Z_{\mathrm{Re}} = R \qquad \text{and} \qquad \mathbf{Z}_{\mathrm{C}} = -Z_{\mathrm{Im}} = \frac{1}{\omega C}. \tag{3.26}$$

The latter expression allows us to determine the capacitance of a serial RC circuit by the imaginary part of the measured impedance and the angular frequency according to Eq. 3.27.[26, 166]

$$\boxed{C = \frac{1}{-\omega Z_{\mathrm{Im}}}} \tag{3.27}$$

One has to be cautious with such dramatic simplifications of PEC systems. However, later on we will see that this approach delivers reasonable values for the space charge capacitance over a frequency range as the results will show good correspondence with literature values, EFISH spectroscopy data and also with electron microscopy (EM) and XRD experiments.

Part II

Experimental

4 Experiments engineering

This chapter presents required engineering works in order to enable spectroscopic and photo-electrochemical experiments on an operating α-Fe_2O_3 photoanode for the thesis. As for that, three different cell systems were constructed in order to provide capabilities for film growth, in situ SHG experiments and PEC characterization, respectively. The latter served as experimental base for a reaction rate-law kinetic analysis from chronoamperometry measurements in the published article [44]. A preparation setup for an α-Fe_2O_3 thin film sample platform was developed, which provided a base for range of experiments from operando SHG spectroscopy to several static and dynamic amperometry and potentiometry measurements through the thesis. While the sample system itself provides good comparability with literature [42, 61, 110, 168, 169], the experimental development of the film growth setup showed some new aspects on the chemical electrodeposition process and provided the base sample system for one published article [44] and one manuscript that has been submitted for publication.[170]

4.1 Preparation of α-Fe_2O_3 photoanodes

The preparation of an α-Fe_2O_3 photoanode is conducted via a two-step process as shown in Fig. 4.1.[110, 111] First, an FeO_xH_y film of varying stoichiometric composition and crystallographic structure is grown by anodic electrodeposition from an aqueous $Fe^{2\oplus}$-solution.[109, 111, 112, 115] In a second step, thermal annealing in air converts the as-deposited FeO_xH_y film into α-Fe_2O_3. F:SnO_2, fluourine doped tin oxide (FTO) coated glass, is used as substrate through all studies in this work. F:SnO_2 is a widely used transparent conductive oxide (TCO) for photoanodes due to its low cost and good thermal and chemical stability.[26, 171] This sample system provides a wide-spread model for the PEC water oxidation with α-Fe_2O_3 photoanodes.[61, 111, 168]

The ED of FeO_xH_y occurs from an aqueous $Fe^{2\oplus}$ precursor solution at pH 7.5 (see

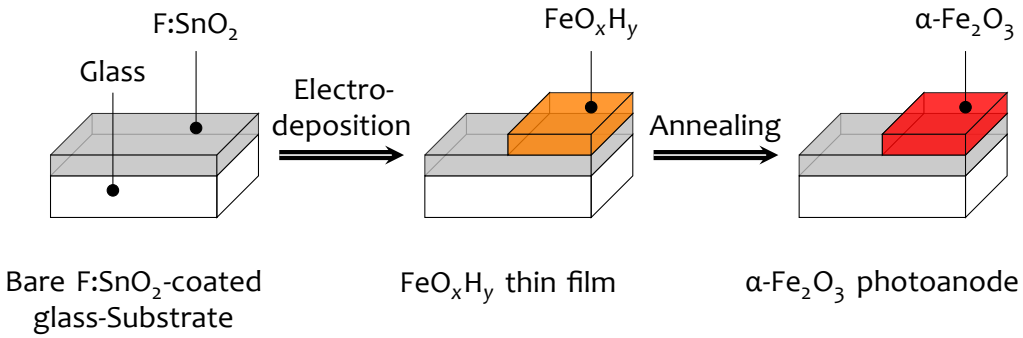

Figure 4.1: Two step preparation of a hematite photoanode sample: Anodic electrodeposition of an FeO_xH_y film onto an F:SnO_2-coated glass substrate and subsequent thermal annealing to form an α-Fe_2O_3 thin film photoanode

Section 3.1). Since $Fe^{2\oplus}$ is a strong reducing agent above pH 4, strict exclusion of air oxygen is required.[109, 172] Fig. 4.2 shows a scheme of an electrochemical cell which was developed for the film growth in order to provide control over a range of experimental parameters. For convenience, all relevant components are projected into the plane of view. The reactor cell provides a gas inlet, slots for a typical three-electrode configuration, a pH probe and an inlet for liquid injection and pH adjustment. The F:SnO_2-coated glass substrate is mounted in a PTFE holder and contacted as working electrode (WE). A Pt wire and a conventional Ag/AgCl electrode serve as counter electrode (CE) and reference electrode (RE), respectively. Permanent purging with 99.9999 % Ar that is further purified by an additional oxygen stripper is necessary to avoid precipitation processes in the precursor solution. The author wishes to acknowledge *Glasbläserei Müller* for manufacturing this six-necked glass-cell.

4.2 Photoelectrochemical characterization

In situ investigations on photoanodes for water splitting require a sample system that is capable of photo-driven water oxidation. Therefore, photoelectrodes are typically charactzerised in IV experiments under imposition of an external bias potential and illuminated with simulated solar irradiation while the measured photocurrent is used to assess the photoelectrochemical performance of the sample.[26] However, illumination with white light is not appropriate for SHG spectroscopy experiments. This is, on the one hand, due to the very low intensity of the second harmonic signal which can be easily contaminated by scattered photons from a solar simulator.[121,

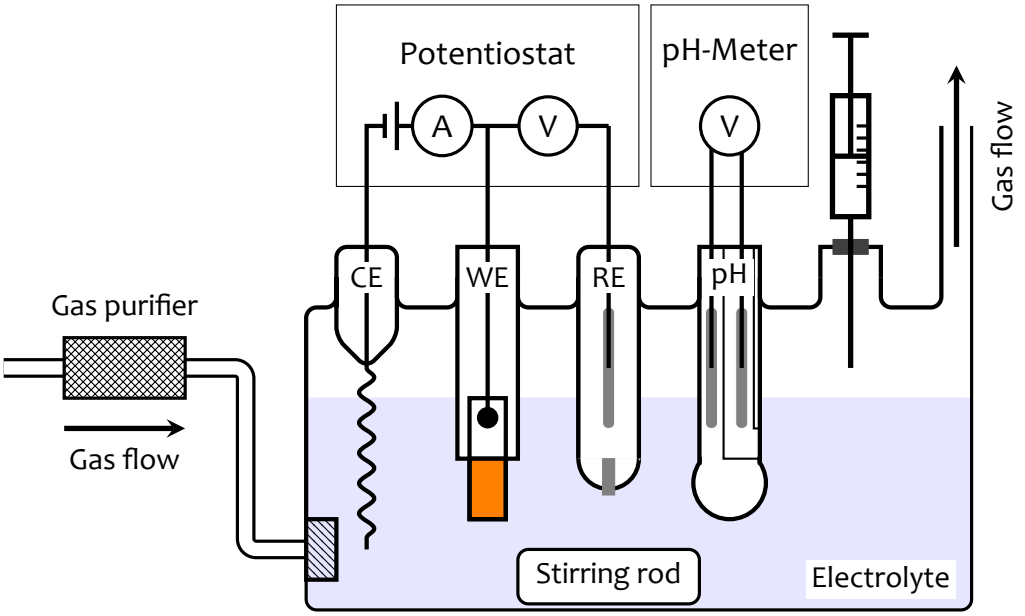

Figure 4.2: Electrochemical cell as reactor for the electrodeposition of thin films: Glass vessel with gas in- and outlet and slots for counter electrode (CE), working electrode (WE), reference electrode (RE), a pH-probe and a septum for liquid injection and pH adjustment

125, 142] On the other hand, several studies have found a strong wavelength dependence of carrier excitation and dynamics[58, 173–175] so that signals from broad band illumination would be more difficult to interpret than those which are excited using one single colour. Therefore, a monochromatic light source with a photon energy above the band-gap of α-Fe_2O_3 needs to be applied to illuminate the photoanode.

$$I_{\mathrm{Exc}} = \int_0^{E_{\mathrm{G}}} I'_{\mathrm{AM1.5}}\,\mathrm{d}\lambda = 32\,\mathrm{mW\,cm^{-2}}. \tag{4.1}$$

Thus, a 450 nm laser-diode has been selected and purchased as light source to investigate the photoanode system. Fig. 4.3 shows a comparison between the 450 nm laser-diode and the AM 1.5 solar spectrum at 1 sun (100 mW cm^{-2}) illumination. In order to provide a comparable pump intensity between solar irradiation and the laser-diode, we want to calculate the amount of the solar spectrum I_{Exc} that lays energetically above the band-gap of α-Fe_2O_3 ($E_{\mathrm{G}} = 2.1$ eV, see Section 5.2.2).[26, 61] Therefore, an integration of the 1 sun AM 1.5 solar spectrum over all photon energies E larger than the band-gap of α-Fe_2O_3 according to Eq. 4.1 should provide an estimation for the photon flux of the monochromatic laser-diode that compares to the pump power density of 1 sun of AM 1.5 conditions. A value of $I_{\mathrm{Exc}} = 32\,\mathrm{mW\,cm^{-2}}$ is

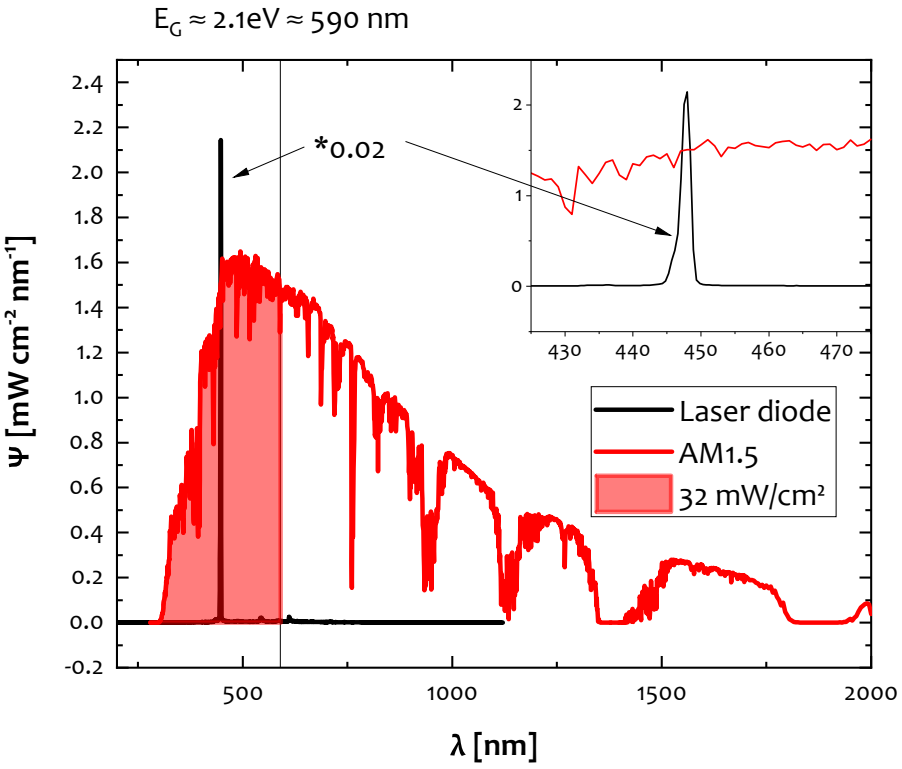

Figure 4.3: Comparison between solar irradiation and a monochromatic 450 nm laser-diode employed here for PEC experiments. The absorbable portion of the solar spectrum at a material's band-gap of 2.1 eV is used to estimate a pump power density comparable to 1 sun of AM1.5 solar irradiation

found to provide a comparable pump power density between the 450 nm laser-diode that and 1 sun of AM 1.5 solar irradiation. The photometrically detected incident illumination power density for the PEC characterization and in situ SHG experiments was 24.5 mW cm^{-2} and thus a bit below a 1 sun equivalent but well comparable, though.[101]

In order to assess the sample PEC properties, an appropriate setup was developed in the framework of this thesis as is shown in Fig. 4.4. The aforementioned 450 nm laser-diode is used as light source, where the laser-diode output is controlled by a current source (Driver) and a temperature controller (T-Control) is used to thermally stabilize the laser-diode. The collimated beam is guided through an optical shutter into the PEC cell in order to provide controllable, instant light exposure and blocking. The PTFE-cell is based on a device described in [26]. Both, a quartz glass window and the photoelectrode are pressed against the cell and sealed with a perfluoropolymer

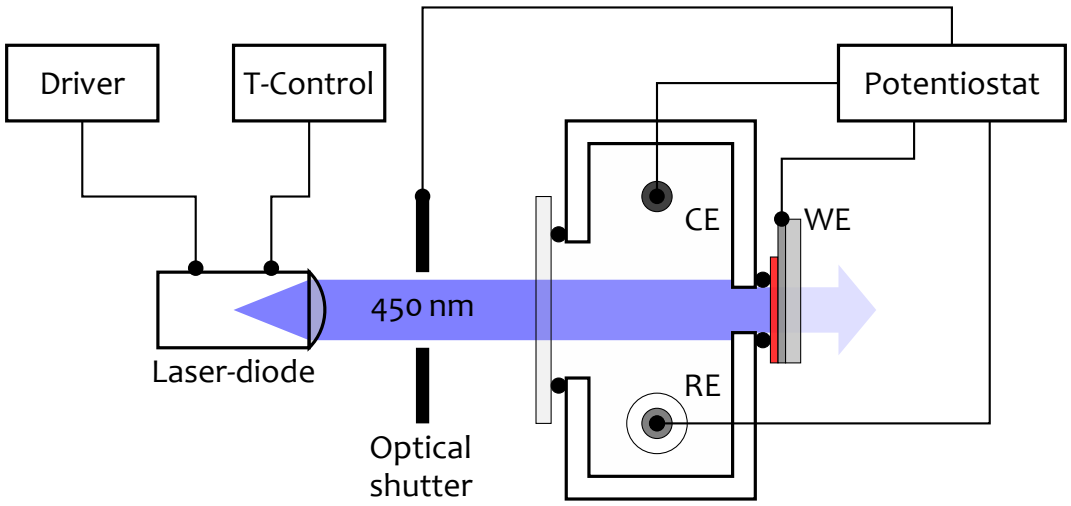

Figure 4.4: Experimental setup for photoelectrochemical (PEC) characterization of α-Fe_2O_3 thin films.

O-ring. The photoelectrode is connected to the potentiostat in a three-electrode setup with an Ag/AgCl reference electrode (RE) and a Pt-wire as counter electrode (CE). Additionally, an optical shutter can be triggered by the potentiostat in order to drive and record photocurrent and -voltage transients. The author wishes to particularly acknowledge Reinhard Franke for manufacturing the photoelectrochemical cell.
This setup has been used to record the photocurrent transients of α-Fe_2O_3 samples which served as experimental base for a published reaction rate-law analysis of the OER mechanism at α-Fe_2O_3 photoanodes, where a comparison between peak and steady state photocurrents has shown a third order rate law dependence of the OER reaction rate on the surface hole concentration.[44]

4.3 In situ SHG spectroscopy of photoanode interfaces

SHG spectroscopy requires illumination of the sample with a high power pulsed laser system. The SHG signal intensity has a quadratic dependence on intensity of the fundamental light (see Eq. 3.17).[119, 121, 176] Thus, small fluctuations of the NIR fundamental probe beam may have a large impact on the stability of the SHG signal. Therefore, an SHG setup was developed which provides simultaneous detection of a sample signal and a reference signal for each pulse on the same detector. This allows to eliminate fluctuations of the incident laser power.
Fig. 4.5 shows a scheme of the laser beam path setup which is used to conduct

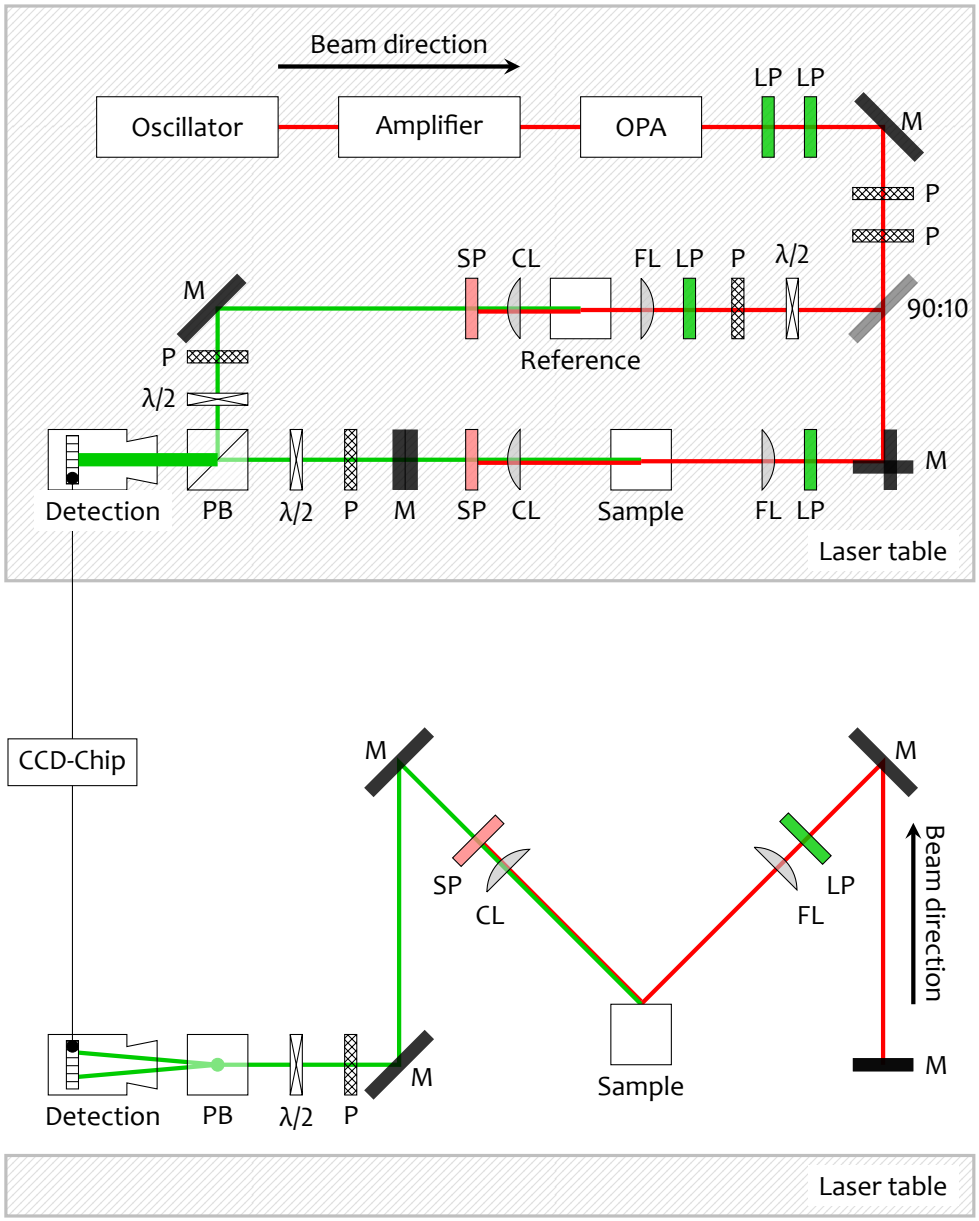

Figure 4.5: Laser setup for SHG measurements. Simultaneous detection of two signals at the same chip allows e.g. recording a reference signal to eliminate drifts and noise of the laser system. M: mirror, OPA: optical parametric amplifier, LP: long pass filter, P: polariser, 90:10: beamsplitter, $\lambda/2$: half waveplate, FL: focussing lens, CL: collimating lens, SP: short pass filter, PB: polarizing beamsplitter

in situ SHG experiments. An oscillator generates pulsed 800 nm light of 80 MHz repetition rate. This seed light is enhanced in a regenerative amplifier to generate 8 W of an 800 nm field with a repetition rate of 1 kHz and 120 fs pulse duration. The

amplified light is then converted by an optical parametric amplifier (OPA) to generate 1180 nm to 1400 nm NIR light which serves as fundamental probe beam for the SHG measurements.
A pair of polarisers (P) is used to both tune the incident laser power and to determine the polarization of the NIR probe beam. A 90:10 beamsplitter (90:10) separates the NIR fundamental into a reference and a sample arm. Long pass filters (LP) are used to remove residuals of Vis light from the NIR fundamental probe beam before it is focused onto the sample surface with a focusing lens (FL). The reflected beam which contains the SHG signal is then collimated with a collimating lens (CL) and a short pass filter (SP) is used to remove fundamental NIR light from the signal beam.
Both, sample and reference signal are then bundled and guided towards the detection system using a polarizing beamsplitter (PB). This requires selection of the SHG signal polarization of interest with another set of polarisers and $\lambda/2$ waveplates to optimize the propagation through the polarizing beamsplitter. A spectrometer with a set of gratings is used to disperse the signal into its spectral components and a CCD array chip to detect the intensity as function of photon energy. Tilting of the polarizing beamsplitter allows for a slight divergence between the merged sample and reference beams so that both signals can be selected and recorded separately on the CCD chip.

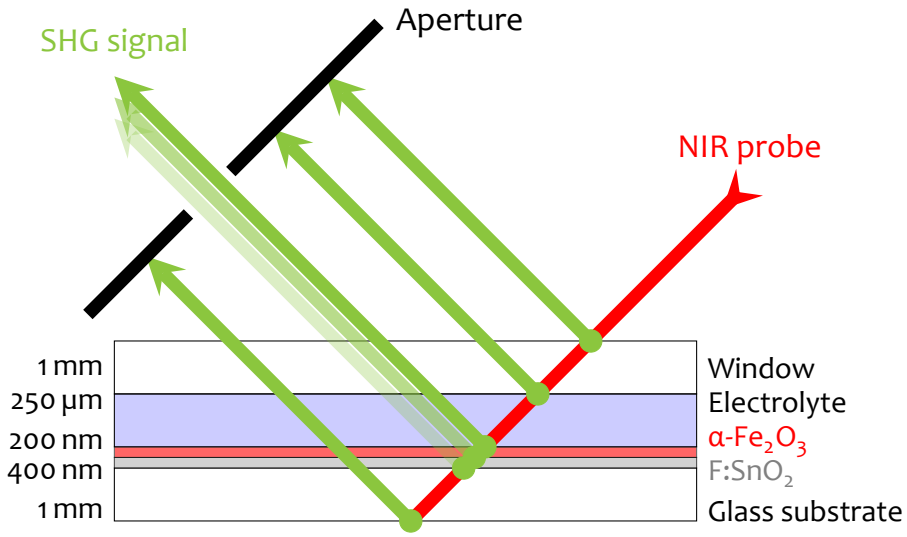

Figure 4.6: Simplified illustration of the layered reflective and transmissive contributions of an SHG probe through the sample system. Light reflected from the window and the liquid layer are sufficiently separated in space and can be removed by an aperture. Reflections from the F:SnO_2/Glass and the F:SnO_2/α-Fe_2O_3 interfaces might contaminate the SHG signal from the α-Fe_2O_3/electrolyte interface of interest.

In principle, the SHG signal can be generated at any interface of centro-symmmetric media.[121, 125, 176] Therefore one must be cautious when SHG measurements are taken on layered systems - such as the experiments aimed at here. Fig. 4.6 shows all relevant layers of the sample cell system and possibly reflective interfaces in a simplified fashion. In order to not overcomplicate this purely experimental aspect, beam refraction is neglected in this scheme. We see that SHG can in principle take place at multiple sites of the cell system. Thicker layers such as the cell window, the electrolyte and the glass substrate provide sufficient spatial separation of the SHG signal beams, and can be blocked with an aperture. On the other hand, all possible SHG signals from stacked the α-Fe_2O_3 and F:SnO_2 thin film interfaces would be merged in one beam. Therefore, one must find a way to evaluate signals arising from the electrolyte/α-Fe_2O_3, the α-Fe_2O_3/F:SnO_2 and the F:SnO_2/glass interfaces separately.
Therefore, a sample system has been developed which allows for separate SHG measurements on the α-Fe_2O_3 photoanode, the bare F:SnO_2 coated glass substrate and an Au reference in the same cell. Comparison between the signals from the bare F:SnO_2 coated glass substrate with and without a α-Fe_2O_3 thin film on top will then allow for an assignment of the measured signal to the respective layer, while the Au layer might serve as spectroscopic reference in some circumstances.

Fig. 4.7 illustrates the preparation route of such a multi material referencing sample system for in situ SHG spectroscopy. First, the different areas need to be electronically insulated to allow for individual contacting of each compartment. Therefore, the conductive F:SnO_2 film is partly removed to break the electric contact. This is done with an etching process, where those areas on the substrate which need to be preserved are masked with an adhesive PTFE tape. After etching with HCl and Zn, adhesive residuals are removed with a suitable solvent. Then, the Au film is deposited by electron beam evaporation. Finally, the α-Fe_2O_3 film is deposited according to the procedure shown in Fig. 4.1.

This sample is then mounted in a cell system for in situ SHG spectroscopy measurements. Fig. 4.8 shows a probing scheme and the sampling environment for the in situ SHG experiments. The sample, prepared as shown in Fig. 4.7, is mounted in a flow cell that is constantly purged with the electrolyte. An Ag/AgCl electrode serves as reference electrode, the Au-film serves as both spectral reference and counter electrode. SHG is measured in reflection mode at 45° angle of incidence, where both NIR fundamental and SHG probe beam are s-polarized. Sample illumination is

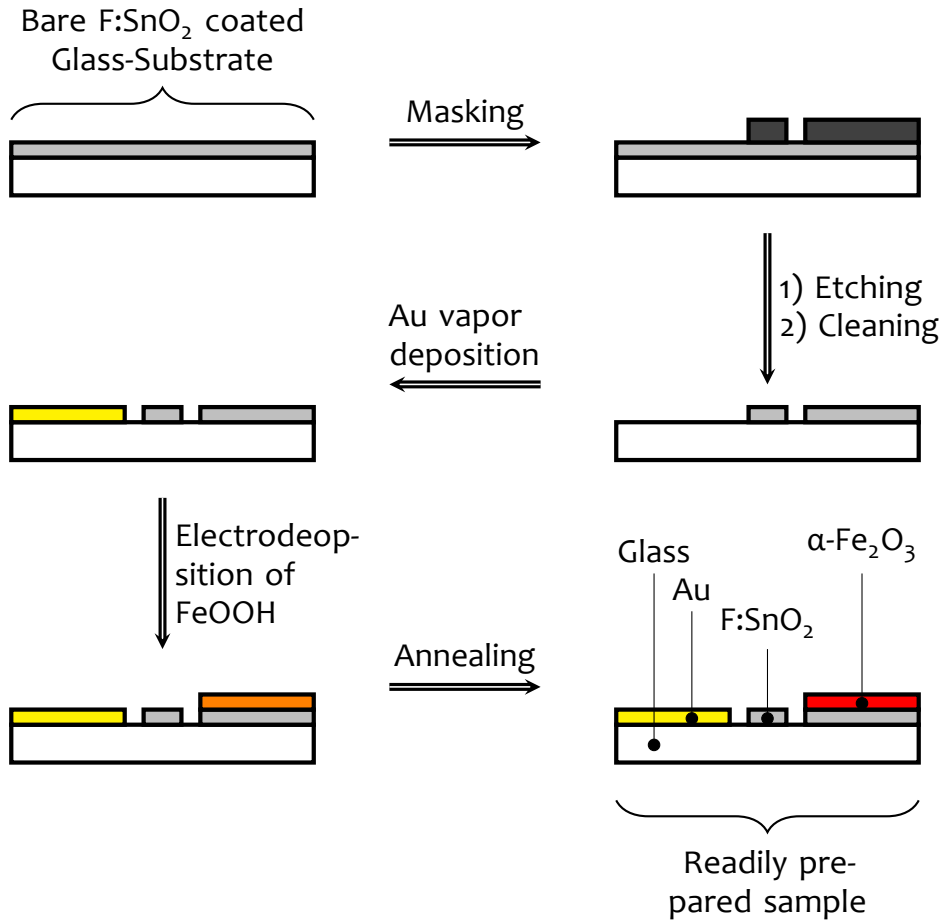

Figure 4.7: Multi-reference sample preparation for in situ SHG spectroscopy experiments. An α-Fe_2O_3 photoanode thin film system is prepared that enables for measurements on the photoanode and additional referencing to the bare F:SnO_2 coated glass substrate and an Au film in the same cell

provided by a 450 nm continuous wave (CW) laser-diode. Translation of the whole cell system parallel to the laser table provides selection of the sampling spot on the sample.

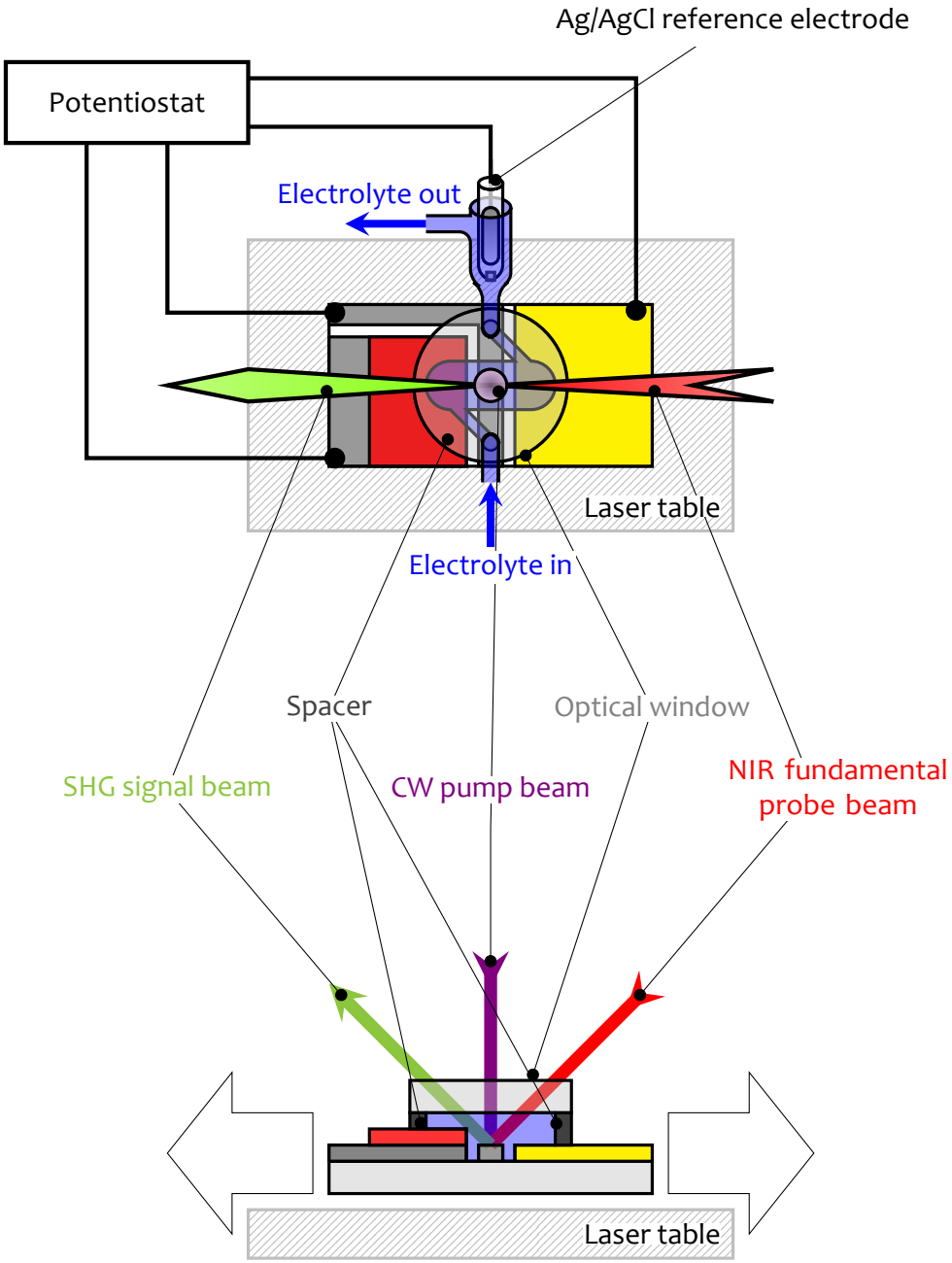

Figure 4.8: Sample environment and probing geometry for in situ SHG spectroscopy on an α-Fe_2O_3 photoanode, the underlying substrate and a Au spectral reference

5 α-Fe_2O_3 photoanode sample preparation and characterization

The preparation of an appropriate α-Fe_2O_3 photoanode sample system is an essential part of this work. While the goal of the thesis is the investigation of electronic structure and processes at the electrode/electrolyte interface using SHG spectroscopy, it is of crucial importance to provide a well-defined and representative sample system in order to make profound scientific statements and to be able to compare with published results. Therefore, particular care was taken in order to establish a stable and repeatable deposition process for the preparation of a photoactive and well-defined α-Fe_2O_3 thin film sample system. The electrode material as described from physico-chemical characterization methods in the following chapter served as base system for one published [44] and one submitted [170] scientific article.

5.1 Film growth repeatability and stability

Unless stated otherwise, in all following deposition processes and also for the SHG studies, α-Fe_2O_3 films were grown at a constant deposition potential of 0.54 V_{RHE} and annealed at 800 °C for 20 min in air. The same applies to further parameters such as precursor solution composition and pH which were globally kept constant as well (see also experimental details in Chapter 6).
First, we want to have a closer look at the stability and repeatability of the film growth. Depending on the property of interest, a thin film deposition process could in principle be evaluated by a range of characteristics, such as sheet resistance, film thickness, optical transmission, etc. Since the intention here is to prepare a photoanode for water splitting, the most important quantity would be the photocurrent under a given external potential and illumination intensity.[28] Therefore, we want to evaluate the growth of α-Fe_2O_3 thin films from various deposition processes with respect to their PEC performance.

Besides a range of parameters to define the physical and chemical boundaries (pH, concentration, buffer ions, potential, temperature, etc.), the most important parameter to control the film growth is the film thickness.[160] Due to the nanostructured texture of the α-Fe_2O_3 samples, a purely one dimensional growth direction normal to the substrate surface is not provided. Thus, we can not directly relate the deposited mass of FeO_xH_y to the film thickness. For that reason, we should strictly speaking use the term *film mass*, $m_{\alpha\text{-}Fe_2O_3}$, as measure for the deposited amount of α-Fe_2O_3 in analogy the thickness in a one dimensional growth regime.[116] The film mass is linearly related to the amount of charge exchanged during the film growth Q_{Dep} via Faraday's law Eq. 5.1, where $M_{\alpha\text{-}Fe_2O_3}$ is the molar mass of α-Fe_2O_3, F represents Faraday's constant $F = 96\,485\,\mathrm{C\,mol^{-1}}$ and $z = 2$ for the two charge carriers exchanged per unit α-Fe_2O_3 reaction product from two $Fe^{2\oplus}$ precursor ions (see Eq. 3.1 and Eq. 3.2).[27, 177]

$$Q_{\mathrm{Dep}} = \frac{m_{\alpha\text{-}Fe_2O_3}}{M_{\alpha\text{-}Fe_2O_3}} * z * F \quad , \tag{5.1}$$

Since the cell current during the deposition process is known to correspond to the oxidation of $Fe^{2\oplus}$ (see Section 3.1, Eq. 3.1)[109, 112, 116] it can be directly linked to the deposition rate of the growing FeO_xH_y films.[116] Although we can not certainly define a film thickness due to the nanoscopic roughness of the material, we can state that $m_{\alpha\text{-}Fe_2O_3}$ is directly proportional to the deposited amount of the charge exchanged during the film growth, Q_{Dep}.[116]
Thus, Q_{Dep} allows us to directly control $m_{\alpha\text{-}Fe_2O_3}$, so that we can use the exchanged charge to examine the repeatability and stability of the deposition process. A repeated deposition of a certain amount of Q_{Dep} should yield an α-Fe_2O_3 film with the same PEC properties if we leave the remaining process parameters constant. Therefore, we want to see how our films behave from a PEC point of view under variation of Q_{Dep}.

Fig. 5.1 shows two sets of deposition curves with varying film masses in the upper panel and the corresponding OER water splitting IV curves of the obtained samples in the lower panel – as given in Section 5.1 and Section 5.1, respectively. These two series were conducted at two different days from two independently prepared precursor solutions while all other chemical and physical process parameters were kept constant. The film mass was controlled by the deposition time and the IV-curves were recorded under standardized conditions using a continuous wave 450 nm laser-diode

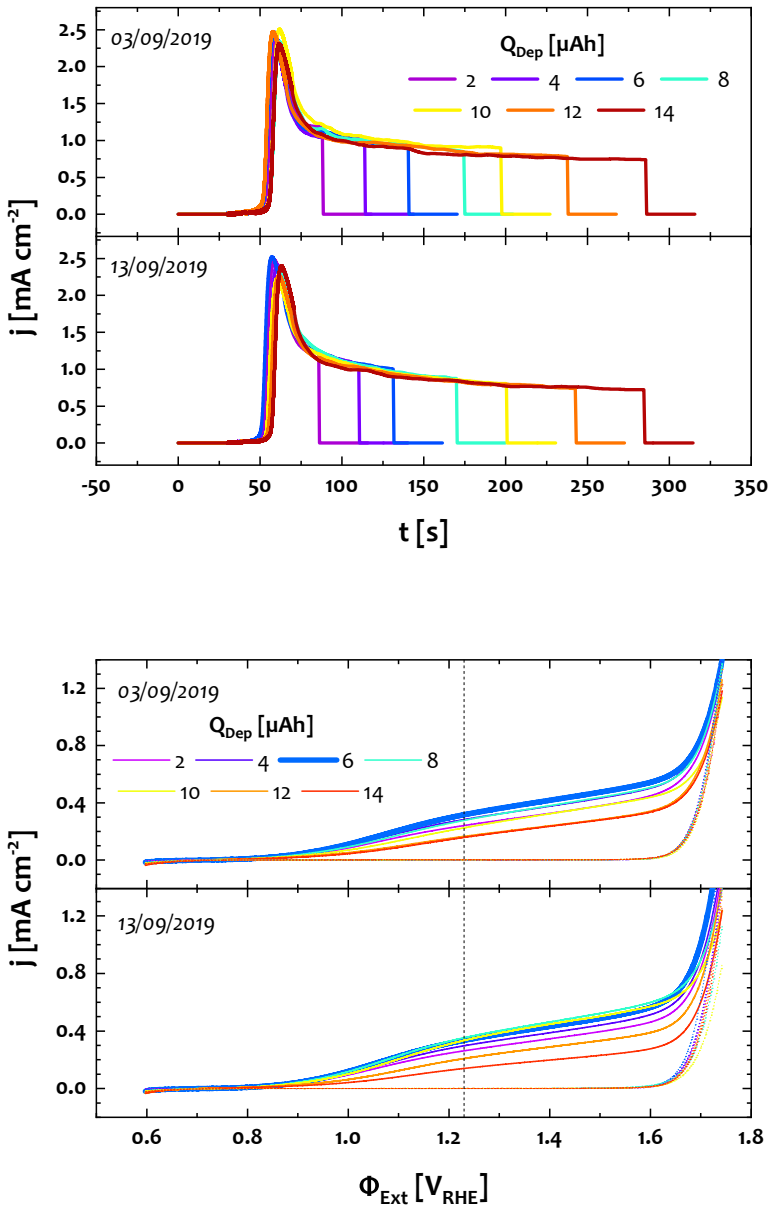

Figure 5.1: Repeatability of the preparation of α-Fe_2O_3 photoanodes from a PEC perspective. Section 5.1: Deposition current transients of two series of varying film masses from different precursor solutions at 0.54 V_{RHE} and Section 5.1: corresponding IV-curves for PEC water oxidation

and a 1 M KOH electrolyte.
We can see that both deposition series exhibit fairly the same deposition curves, which indicates a well controlled and repeatable growth process. The corresponding IV curves are also quite similar between both series, which indicates a stable and reproducible thin film deposition process to allow for repeatable growth of photoactive α-Fe_2O_3 thin film photoanodes with constant PEC properties.

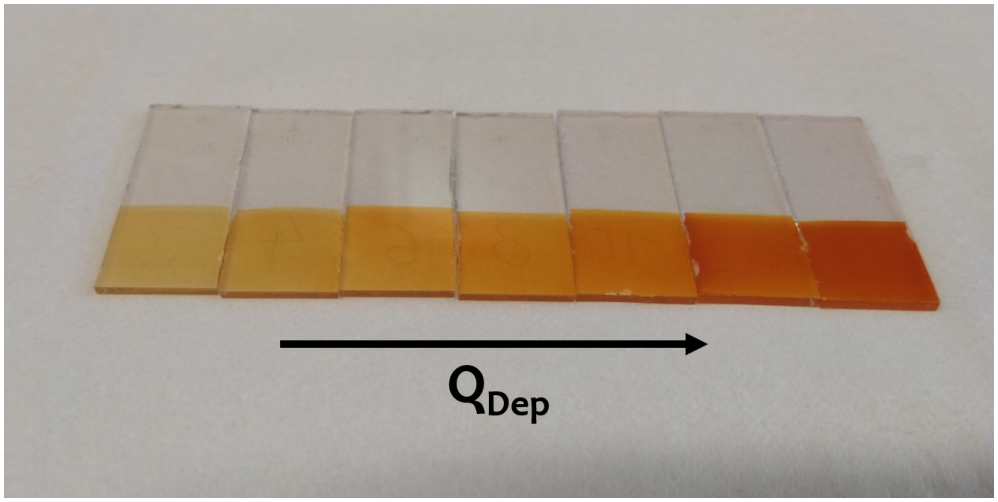

Figure 5.2: Photograph of a α-Fe_2O_3 photoanode sample series from Fig. 5.1 with varying film masses

The human eye often provides an already good metric to assess the film quality in terms of crystallographic and chemical homogeneity, transparency, exfoliation and uniformity, for instance. A set of α-Fe_2O_3 films from the deposition in Fig. 5.1 is shown in Fig. 5.2. The films were grown under constant conditions except for the α-Fe_2O_3 film mass. We can see that the deposition process delivers sets of uniform and transparent films of varying film masses.
The film thickness or film mass is of crucial importance for the performance of a photoelectrode. A film that is too thin would transmit most of the incident light and leave most of the illumination power unused. If the film becomes too thick, on the other hand, the electric resistance of the film would become too high, and the water splitting efficiency would suffer from bulk recombination losses.[160] Thus, the PEC performance as function of the film mass should exhibit a maximum.
An optimization of the film mass with respect to the PEC performance is shown in Fig. 5.3. Photocurrents at 1.23 V_{RHE} were extracted from standardized IV-curves, as shown in Section 5.1, and plotted over the deposited charge per electrode area. Samples from four different precursor solutions are included in order to further

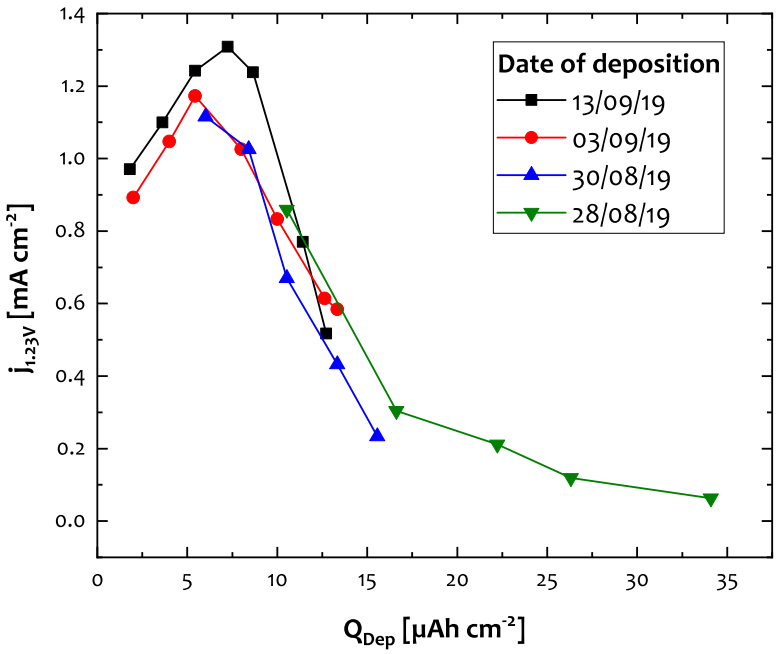

Figure 5.3: Photocurrent at 1.23 V_{RHE} under standardized illumination with varying film mass obtained from four different precursor solutions

assess the repeatability of the sample preparation. Again, all steps from film growth over thermal annealing to photoelectrochemical characterization were conducted under standardized conditions. The plot of the photocurrent at 1.23 V_{RHE} versus Q_{Dep} in Fig. 5.3 shows a pronounced optimum at approximately 7 µAh/cm^2 under the applied photoelectrochemical measurement protocol. Fig. 5.3 also shows a quite repeatable dependence of the photocurrent on the deposited charge over many deposition processes which further indicates a stable and reproducible sample preparation method.

5.2 Characterization of α-Fe_2O_3 thin films

Once a stable and repeatable process for the sample preparation is established, we can characterize the samples with respect to their intrinsic physical properties and PEC performance. The optical band-gap will be determined by means of UV-Vis absorption spectroscopy, the bulk crystallographic phase is investigated using Raman spectroscopy and XRD. Scanning electron microscopy (SEM) and transmission

electron microscopy (TEM) will visualize the nanoscopic structure of α-Fe_2O_3 thin films and the PEC performance is assessed by the IV characteristics in the dark and under chopped and steady illumination. The author wishes to acknowledge the support from the inorganic chemistry department of the Fritz-Haber-Institute of the Max-Planck-Society for the support in several of the following measurements.

5.2.1 Crystallographic characterization

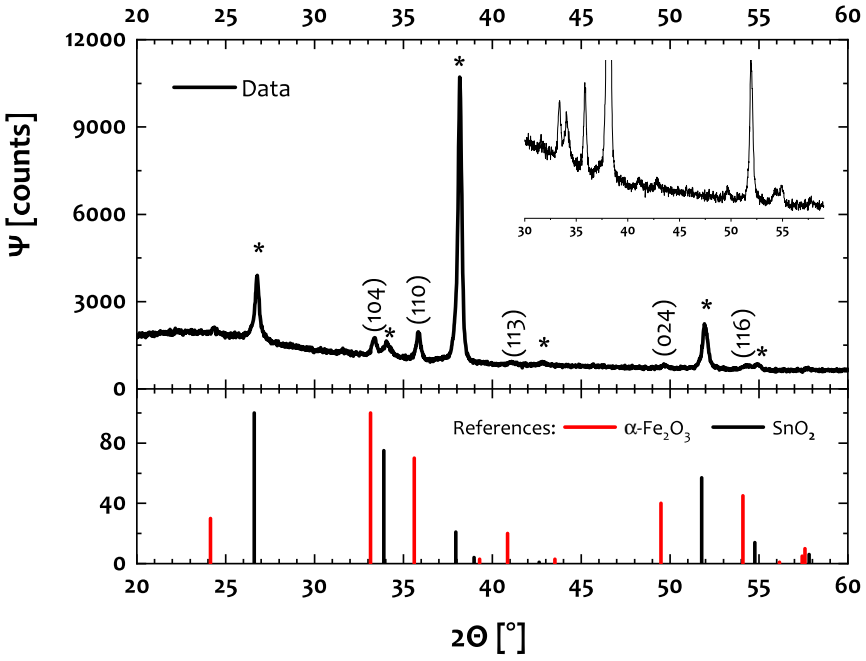

Figure 5.4: XRD analysis of a typical α-Fe_2O_3/F:SnO_2 photoanode thin film system. The measured diffractogram is given in the top panel, crystallographic references are shown at the bottom. Reflexes from the α-Fe_2O_3 phase are indicated by their (hkl)-indices based on the crystallographic reference, substrate F:SnO_2 reflexes are marked with an asterisk based on the Kassiterite reference structure. A Cu K-α line was used as X-ray source.

The method of choice to determine the lattice structure of a crystalline material is X-ray diffraction (XRD). An X-ray diffractogram of a representative sample is given in Fig. 5.4. Besides a strong contribution from the underlying substrate, we can clearly find all reflexes as expected for a α-Fe_2O_3 crystallographic phase.[178–180]
The XRD patterns also provide some further interesting features. For instance, the reflex from the (110) plane of α-Fe_2O_3 is larger compared to the reference, which

could indicate a preferred growth along this lattice direction. The same could be the case for the intense reflex from F:SnO_2 at 38°. Also, the (116) reflex of α-Fe_2O_3 at 54° seems to be split, which could provide some insight into lattice distortion, for instance from doping impurities.[61, 181, 182] However, this work aims for the investigation of the photoanode/electrolyte interface, so that we want to skip an in-depth crystallographic discussion at this point.

$$D = \frac{K * \lambda}{w_{1/2} * \cos\Theta_0} = \underline{33\,\text{nm}} \tag{5.2}$$

A defined reflex in the XRD pattern provides an option to estimate the average crystallite size D from the Scherrer equation Eq. 5.2.[183, 184] In this equation, the approximate crystallite size D can be obtained from the wavelength of the used X-ray line λ, a form factor K that accounts for the three dimensional shape of the crystallite, typically close to unity, the full width at half maximum $w_{1/2}$ (FWHM) $w_{1/2}$ and the central angle Θ_0 of the reflex. If we use the pronounced (110) line of α-Fe_2O_3 at 35.6° and insert $K = 1$, $\lambda = 1.5406$ Å and $w_{1/2} = 0.284°$ into Eq. 5.2, we obtain an average crystallite size of 33 nm. The same results are obtained from the (104) reflex at 33.3° and an FWHM of 0.280°. Two fits of the measured data to Lorentzian line shapes are appended in Fig. I.
It should be mentioned that the Scherrer equation delivers an average crystallite size which depends on the abundance distribution, not on the mass distribution. Therefore it is possible that the majority of the film mass is composed of larger particles, whereas an amount of small particles causes the line broadening so that a smaller particle size is obtained from the Scherrer equation. We want to keep this in mind and compare it with the microscopic investigation of the α-Fe_2O_3 films (see Section 5.2.3).

Fig. 5.5 shows a Raman spectrum of a typical α-Fe_2O_3 photoanode that was prepared under standardized conditions. The spectrum is in very good agreement with the works by Jubb et al.[185] A comparison between the measured Raman modes of the sample system with several literature values for α-Fe_2O_3 is shown in Tab. 5.1. As one can see, we have excellent agreement with literature data and can safely verify that the bulk phase of our photoanode material is hematite α-Fe_2O_3.[44]

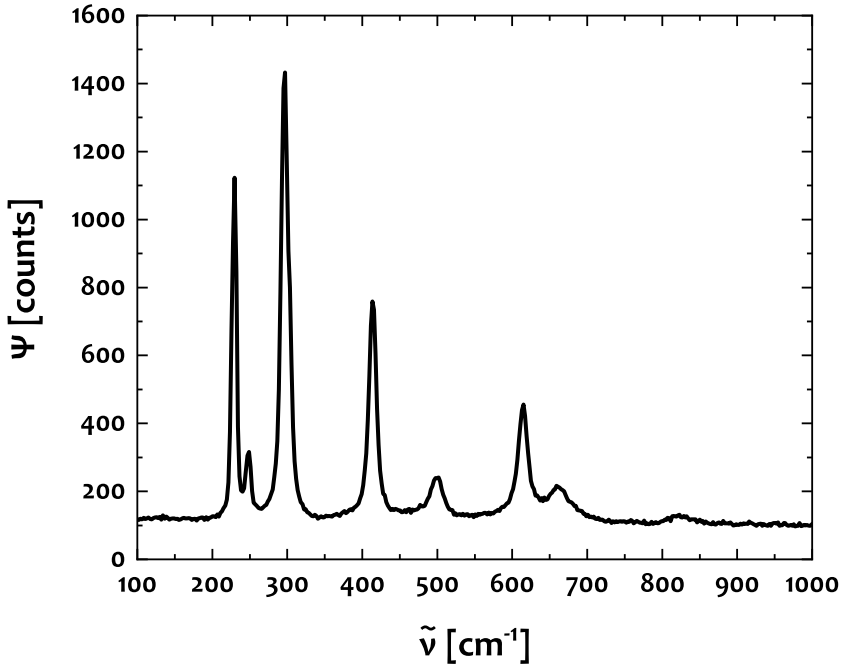

Figure 5.5: Raman spectrum of a typical α-Fe_2O_3 photoanode obtained at 633 nm fundamental wavelength

Normal mode	This work cm^{-1}	[185]	[186] cm^{-1}	[187]
A_{1g}	229	229	225	225
E_g	248	249	247	245
E_g	296	302	293	294
E_g	414	414	412	412
E_g	500	500	498	500
A_{1g}	614	615	613	612

Table 5.1: Comparison between central frequencies from Raman modes of α-Fe_2O_3 samples in Fig. 5.5 with literature values from: Jubb et al.[185], Chamritsky et al.[186] and Marshall et al.[187].

5.2.2 Opto-electronic properties

UV-Vis-NIR-spectroscopy allows us to get some insight into the electronic structure of the material. Fig. 5.6 shows the absorption coefficient α of a α-Fe_2O_3 thin film over a UV-Vis-NIR range of the electromagnetic spectrum. The absorption coefficient

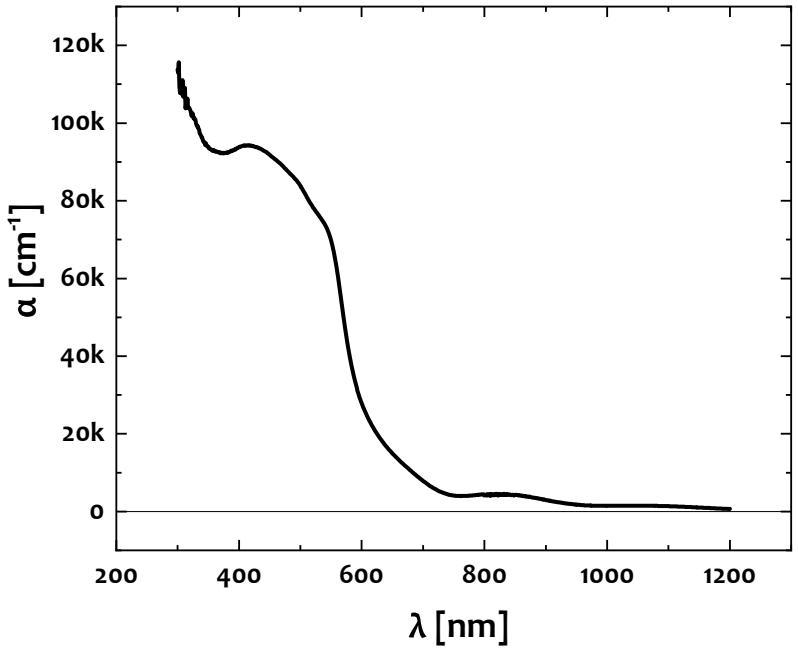

Figure 5.6: Transmission mode UV-Vis-NIR absorption spectrum of a the α-Fe_2O_3 photoanode sample

was estimated from the film thickness as derived from TEM measurements (see Section 5.2.3). At first glance, we can see a steep band-edge at wavelengths shorter than 600 nm and a long tail of the band-edge beyond wavelengths of 700 nm. Additionally, a small, broad absorption feature is located around 830 nm.

Such a pronounced tail of the band-edge is typically explained in two different ways. It may be assigned to indirect, phonon-mediated interband-transitions or to the presence of intra-gap states typically induced from shallow donors which are inherently present in any n-type semiconducting material.[26, 188, 189] The measured UV-Vis-NIR spectra and also the flim morphology (see Section 5.2.3) exhibit strong similarity the sample system that is discussed in Sivula et al.,[61] who conducted a rigorous analysis of changes in the optoelectronic properties depending on the annealing temperature. This work shows an effect of Sn-doping from the F:SnO_2 substrate that diffuses into the α-Fe_2O_3 film at 800 °C annealing temperature.[181, 182]

One way to estimate the direct and indirect band-gap is a linearization of the absorption coefficient α according to Eq. 5.3, where $\mathcal{E}$ denotes the photon energy and the

coefficient γ is set to $1/2$ and 2 for direct and indirect transitions, respectively.[61, 190, 191]

$$(\alpha * \mathcal{E})^{1/\gamma} = B(h\nu - \mathcal{E}_G) \tag{5.3}$$

We want to follow this approach and have a closer look at the UV-Vis absorption spectrum and conduct an optoelectronic analysis according to Tauc.[61, 190–192] The results are shown in Fig. 5.7. We see that the UV-Vis-NIR absorption properties of our sample system are well comparable with the α-Fe_2O_3 photoanodes investigated in reference [61]. As shown in Fig. 5.7, the Tauc analysis yields a direct band-gap of $\mathcal{E}_G^{\text{Tauc}} = 2.1$ eV. The indirect gap, depending on the exact fitting boundaries and parameters is essentially the same as in [61]. Since the Tauc analysis reveals a very similar band-gap for direct and indirect transitions, we can suppose that the origin of the pronounced tail of the UV-Vis absorption band-edge is rather related to shallow electronic states than to a phonon mediated transition. Such a pronounced set of electronic states a few tenths eV below the conduction band has been observed for α-Fe_2O_3 samples obtained from a sputtering process by means of X-ray photoemission spectroscopy (XPS), for instance,[188] and is also generally considered to be present in oxide semiconductor structures.[26, 61, 91, 189] Thus, the similarity between direct and indirect band-gap suggests that the tail of the band-gap in the absorption spectrum corresponds to a set of electronic states below the conduction band.
Doping of the material, however, might be caused by intrinsic or extrinsic defects which are commonly assumed to form electronic states below the conduction band. The former are typically ascribed to the presence of oxygen vacancies which are known to play an important role in the performance of water splitting α-Fe_2O_3 photoanodes.[91, 193, 194] Extrinsic doping was reported to stem from Sn-diffusion from the F:SnO_2 substrate into the α-Fe_2O_3 bulk during the thermal annealing at 800 °C for sample systems with very similar morphological and optoelectronic properties.[61, 181, 182]

At this point, we can not clarify, which type of defect is doping our α-Fe_2O_3 photoanode. However, due to the negligible difference between direct and indirect Tauc-gap and from comparison with literature, we can state that there is probably a set of point

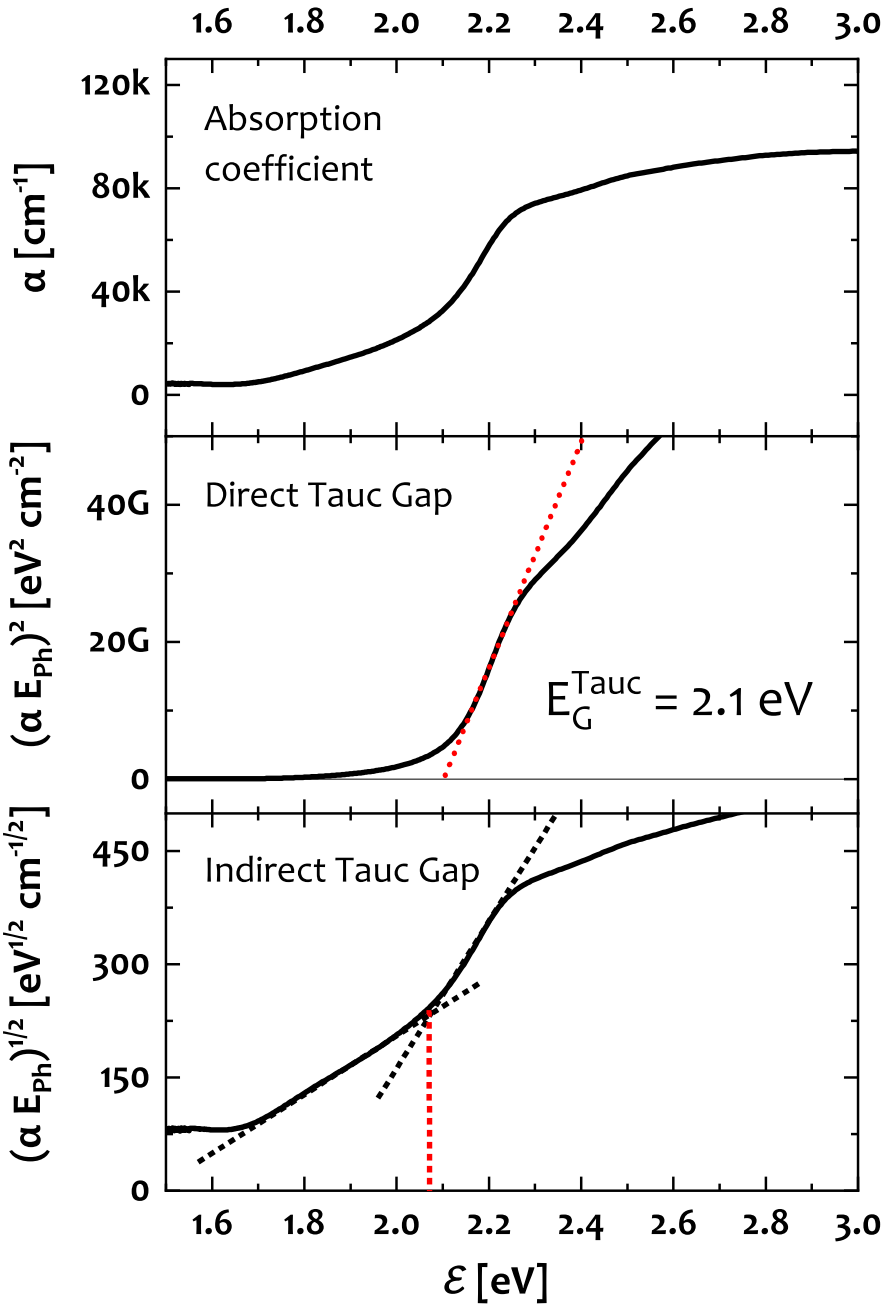

Figure 5.7: Tauc analysis of the absorption coefficient α as function of the photon energy E to determine the direct and indirect band-gap[61, 190–192]

defects ≈300 mV below the conduction band that causes a tailing of the band-gap towards the mid gap region.[26, 61, 91, 188, 193, 194]

5.2.3 Nanoscopic morphology

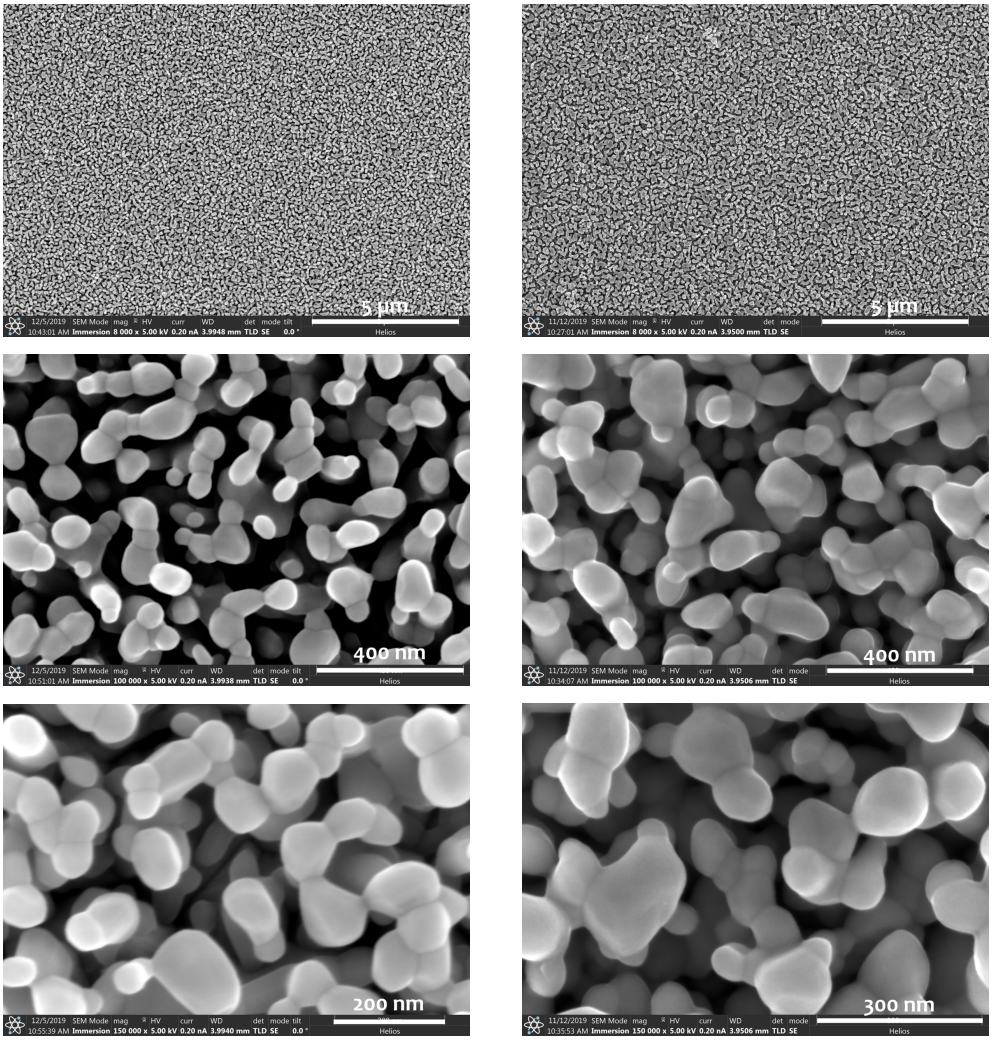

(a) Freshly prepared α-Fe_2O_3 photoanode

(b) After PEC exposure to OER conditions over several days

Figure 5.8: Top view SEM images of α-Fe_2O_3 photoanodes in various magnifications comparing a freshly prepared sample, 5.8(a), and an electrode that has been exposed to strong alkaline and oxidizing conditions for several days, 5.8(b). Scale bars were manually traced for better visibility.

An important aspect of a photoelectrode, such as for any other catalytic material is its nanoscopic morphology. In particular for α-Fe_2O_3 photoanode systems, a nanostructured morphology is necessary to overcome the poor carrier mobility of the material.[26, 61] A nanostructured texture provides a short carrier diffusion path length for photogenerated holes to the electrode surface while maintaining a

long light absorption path length.[26, 195] Therefore, we want to have a look at the α-Fe_2O_3 thin films if we zoom in to the nanoscale using electron microscopies SEM and TEM. The author wishes to explicitly acknowledge Franz Schmidt and Adnan Hammud for contributing the SEM and FIB-TEM measurements to this study.[44]

Fig. 5.8 shows top view SEM micrographs of a freshly prepared α-Fe_2O_3 thin film photoanode and one post operando sample after prolonged in situ SHG experiments. The post operando sample has been exposed to strongly oxidizing OER conditions for many hours and to 1 M KOH over several days.

On the top side of the figure, we can see that both samples, the fresh α-Fe_2O_3 film and the post operando electrode, exhibit a quite homogenous structure without the appearance of any cracks or pinholes. Also, no structural difference can be found between both samples so that we can further confirm a stable deposition process to reproducibly prepare samples of constant nanoscopic morphology. The images in the center and at the bottom of Fig. 5.8 show larger magnifications of both the fresh and the post operando samples. Both films exhibit very similar particle morphologies indicating that no corrosion or other sample degradation processes occur to the α-Fe_2O_3 thin films also over prolonged oxidizing and alkaline OER conditions.

The centre and bottom images of Fig. 5.8 also give us an idea of the nanoscopic morphology of the α-Fe_2O_3 photoanode thin films. We can see that the films are composed of a three dimensional network of fairly round crystallites of approximately 50 nm to 100 nm diameter. This morphology seems to be typical for α-Fe_2O_3 thin films from liquid based deposition routes after annealing at 800 °C.[61, 111, 196] Thus, we obtain further good agreement of our α-Fe_2O_3 sample system with literature.

From the SEM micrographs we can estimate that the particle size ranges between approximately 50 nm to 100 nm. This not in perfect agreement with the integral value of 33 nm obtained from the Scherrer-equation Eq. 5.2, but still comparable (see Section 5.2.1). In the larger magnified TEM images in Fig. 5.9 we will find that a fraction of smaller particles is present as well, which are not resolved by the SEM images. Thus, the Scherrer model might also reflect contributions from small particles to the film mass, that are not resolved by the SEM images.[183, 184]

The different layers of our thin film photoanode system were also investigated with FIB-TEM, which allows for microscopic imaging parallel to the electrode surface and permits a higher magnification than SEM. TEM-images of the layered structure normal to the surface are shown in Fig. 5.9. Again, we find a three-dimensional network of fairly spherical crystallites which are approximately 50 nm to 100 nm in

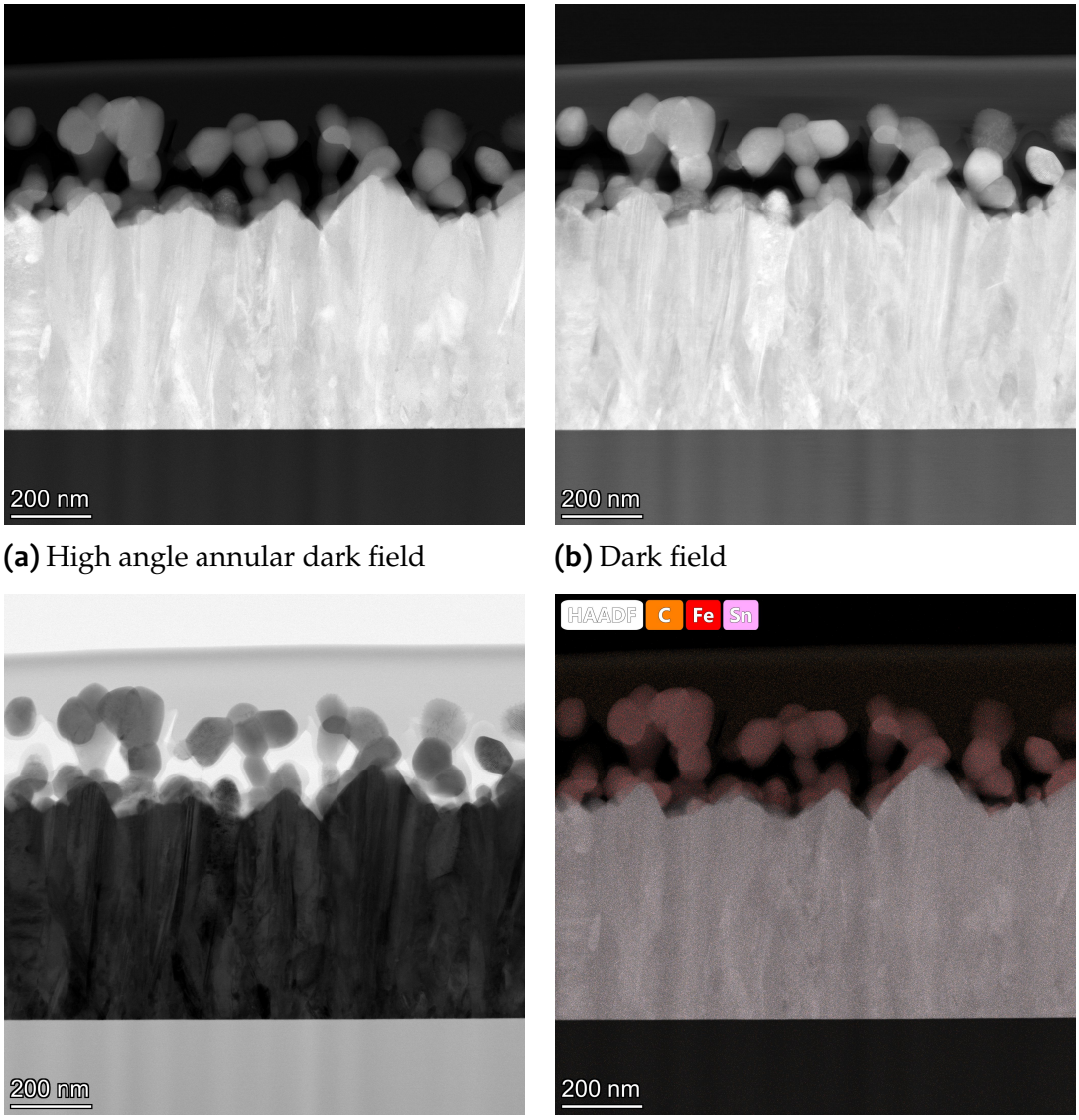

(a) High angle annular dark field

(b) Dark field

(c) Bright field

(d) Color coded energy dispersive X-ray analysis (EDX) analysis

Figure 5.9: Cross-sectional FIB-TEM image of a post-operando α-Fe_2O_3 sample with different imaging techniques [44]

diameter. An energy dispersive X-ray analysis (EDX) analysis of the cross-section clearly identifies the different layers of the photoanode system - the glass substrate at the bottom, the F:SnO_2 back-contact and the photoactive α-Fe_2O_3 film. We can also see that the surface of the F:SnO_2 layer is well-covered with smaller α-Fe_2O_3 particles, which are also contributing to the average particle size in the Scherrer equation. Additional branches of α-Fe_2O_3 crystallites are pointing out perpendicular to the F:SnO_2 layer. The nominal thickness of the α-Fe_2O_3 layer is 200 nm, the F:SnO_2

film is 400 nm thick. Thus, we have developed a closed α-Fe_2O_3 film of relatively low density and high nanoscopic roughness.
It should be noted that this FIB-TEM technique provides a view through the whole FIB-lamella, the imaging plane is not infinitely sharp so that one can not certainly decide whether the image shows a view through one single particle or a stack of particles.

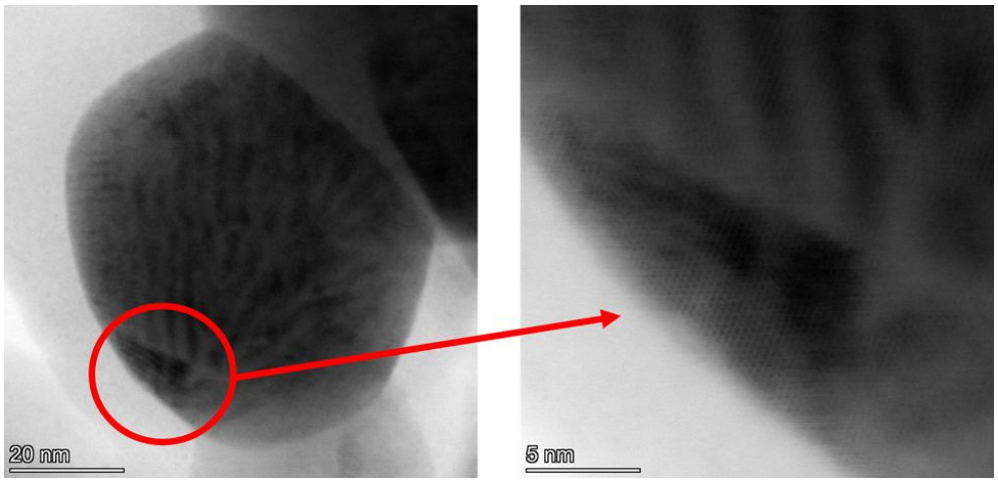

Figure 5.10: High resolution bright field TEM image of one crystallite from α-Fe_2O_3 sample with electron diffraction pattern [44]

An even closer look into the α-Fe_2O_3 thin film is given in Fig. 5.10. We can see high resolution images of one single crystallite of the α-Fe_2O_3 film which is of fairly spherical shape and ≈60 nm in diameter. Depending on the thickness and the angular orientation of the crystallite, it should even be possible to obtain electron diffraction patterns. And indeed, we find such an electron diffraction pattern in the high resolution image of Fig. 5.10. Thus, we can confirm that our particles of 50 nm to 100 nm in diameter are crystallites of extended lattice periodicity.

5.3 Photoelectrochemical performance

Typical current-voltage characteristics of our nanostructured α-Fe_2O_3 thin films in a 1 M KOH electrolyte are shown in Fig. 5.11. The sample exhibits common characteristics of an n-type semiconductor photoanode system. We see a photocurrent of 0.33 mA cm^{-2} at 1.23 V_{RHE} which is quite comparable with undoped α-Fe_2O_3 photoanode systems in literature. As for instance, Klahr et al. have published EIS studies on a system that delivered ≈0.2 mA cm^{-2} at one sun illumination[65]. Monllor-Satoca

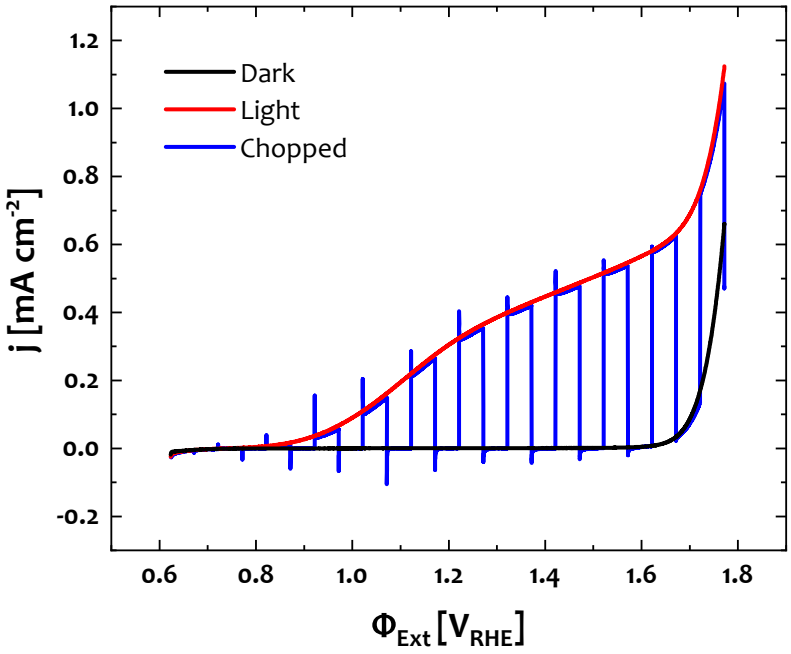

Figure 5.11: Current-voltage curves of a typical α-Fe_2O_3 photoanode in the dark and under static and chopped illumination with 24 mW cm^{-2} of a 450 nm CW laser-diode in a 1 M KOH electrolyte [44]

et al. have published EIS studies for different doping levels with a current density of ≈0.1 mA cm^{-2} for an undoped α-Fe_2O_3 sample.[63] Other reported pristine α-Fe_2O_3 photoanodes prepared via solution based approaches deliver photocurrents between 0.2 mA cm^{-2} and 1.2 mA cm^{-2} at 100 mW cm^{-2} of AM 1.5 simulated solar irradiation at 1.23 V_{RHE}.[61, 111, 160, 196]

It might also be worth noting that the light source employed here is not directly comparable with the PEC standard of 100 mW cm^{-2} of AM 1.5 simulated solar irradiation. The photometrically measured illumination intensity of 24 mW cm^{-2} with a 450 nm CW laser-diode is set slightly below the 1 sun excitonic equivalent of 32 mW cm^{-2} estimated from 100 mW cm^{-2} of AM 1.5 illumination (see Section 4.2). In addition, it is known that the excitation wavelength or phonon coupling play an important role in the charge transport.[173, 197] Therefore, we cannot directly compare the PEC performance with the research standard from simulated sunlight. However, we find an appropriately photoactive sample system for in situ SHG studies on the

α-Fe_2O_3 electrode/electrolyte interface was developed that compares very well with published sample systems in literature.

The blue graph in Fig. 5.11 shows current-voltage characteristics under chopped illumination. We find pronounced positive and negative current spikes when the light is turned on and off, respectively. These photocurrent transients are a known characteristic of several water splitting photoanodes and have been widely studied in literature. From a range of experiments such as PEC impedance and photocurrent spectroscopies,[59, 65] surface passivation[57, 59] and the application of hole scavengers[67], an accumulation of holes in surface states was shown to cause the photocurrent transients under dynamic illumination.[26, 44, 57, 59] These works have demonstrated that the large initial current upon sample illumination is governed by a transfer of positive charges into populated surface states causing a positive current transient, that diminishes with electronic saturation of surface states. When the sample illumination is turned off, the accumulated positive charge instantly flows into the opposite direction and a negative current transient is observed.[44, 57, 59] The presence and energetic distribution of surface charge will be further discussed in Chapter 12 and Chapter 11.[44]

A dedicated kinetic analysis of the photocurrent transients in Fig. 5.11 of this sample and cell system has been published in [44] as one main result of this thesis. In these works, a comparison between the initial and steady state photocurrents was analysed and interpreted by a third order reaction rate-law dependence on the surface hole concentration. A combined DFT and microkinetic (MK) model accordingly demonstrated a multi-hole water oxidation mechanism that demands the formation of three vicinal oxyl radical anions as rate limiting step to form molecular oxygen.[44]

One very important criterion for the performance of a photoanode but also for any physico-chemical experiment in general, is the stability of the sample system under operating conditions – in our case the PEC performance under prolonged exposure to an OER environment in a strongly alkaline electrolyte.[28, 45, 198] While stability is also important for an economically competitive hydrogen production process, particular attention must be taken to electrode corrosion and degradation as we aim to conduct a reliable in situ SHG spectroscopy experiment under highly abrasive conditions due to electrolyte pH values far from neutral, strongly oxidizing conditions and highly reactive intermediates.[46]

In order to assess the electrode stability under operating conditions, we want to see how the photocurrent changes over hours of PEC water oxidation. Fig. 5.12

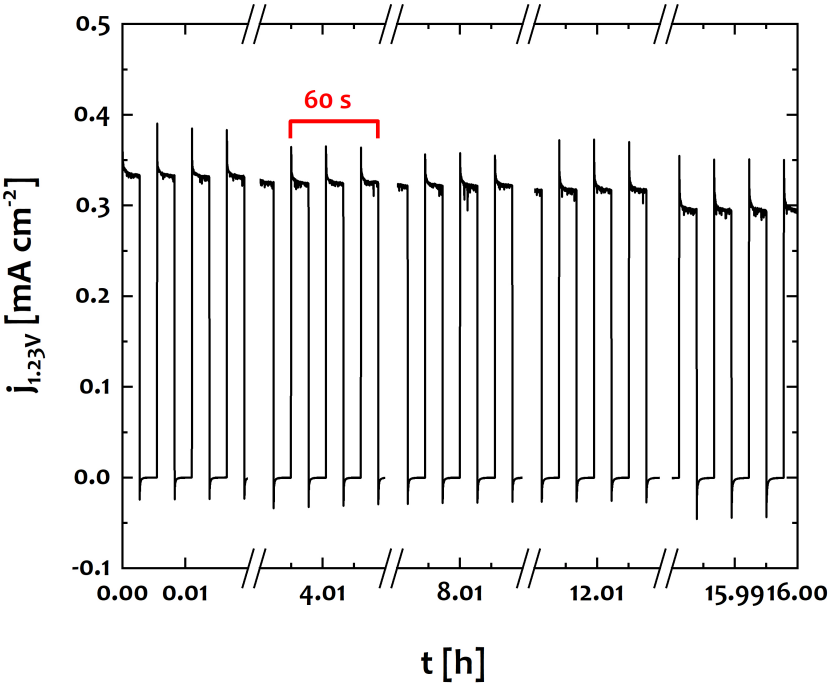

Figure 5.12: Long term chronoamperometry of a typical α-Fe_2O_3 photoanode at 1.23 V_{RHE} under chopped illumination with 24 mW cm^{-2} of a 450 nm CW laser-diode

shows a long term chronoamperometry experiment at 1.23 V_{RHE} under chopped illumination with 24 mW cm^{-2} of a 450 nm laser-diode over 16 h. We find that our α-Fe_2O_3 photoanode delivers a quite constant photocurrent of 0.33 mA cm^{-2} that decayed by less than 5 % after twelve hours of permanent OER exposure. After sixteen hours, the photocurrent has decayed about 10 %. However, this decay is not necessarily caused by electrode degradation, it might also be due to changes in the electrolyte such as oxygen accumulation in front of the electrode or pH-drifts. Anyhow, Fig. 5.12 shows that compared to other dark and photoelectrochemical OER catalysts, the α-Fe_2O_3 thin films provide comparably high stability under prolonged OER conditions.[45, 198]

Thus, we can conclude that a α-Fe_2O_3 thin film system has been developed which shows common PEC characteristics and allows for the investigation of typical intrinsic phenomena of water splitting photoanodes.

6 Experimental Details

6.1 Sample preparation

The preparation of α-Fe_2O_3 thin film photoanode samples was carried out according to a modified version of a well known wet-thermo chemical route.[109–111, 115] A solution of 16 mM $(NH_4)_2Fe(SO_4)_2 \cdot 6\,H_2O$ (Mohr's salt), 2.4 M $(NH_4)_2SO_4$ and 2 mM H_2SO_4 in Millipore© water was transferred into the deposition cell (see Section 4.1 and Fig. 4.2) and purged with purified ≥99.9999 % Ar for ≥30 min. After that, the pH of the plating solution was adjusted to 7.5 by injection of $w_{\mathrm{Mass}} = 50\,\%\,\mathrm{KOH}$ into the deposition cell. All chemicals for the synthesis were analytical grade compounds purchased from Carl Roth GmbH + Co. KG.
F:SnO_2 coated aluminobosilicate glass as purchased from Solaronix S.A. served as substrate for the α-Fe_2O_3 samples. Prior to each deposition, these substrates were subsequently cleaned in 2-propanol and two times in Millipore© water for ≥5 min in a supersonic bath and dried in a N_2 stream. After that, the substrates were contacted and mounted in the deposition cell. The ED setup was a conventional three electrode configuration where the F:SnO_2 substrate was connected as working electrode, an Ag/AgCl electrode purchased from SI Analytics GmbH served as reference electrode and a platinum wire was used as counter electrode. Unless stated otherwise, the film growth is induced by imposition of a bias potential of –0.1 V vs Ag/AgCl to the substrate. The film mass is controlled by the deposited amount of charge, where 10 µA h cm^{-2} are the standard value unless specified otherwise. The as-deposited FeO_xH_y coated F:SnO_2 substrates were thoroughly rinsed with Millipore© water, dried in a N_2 stream and annealed in a pre-heated furnace at 800 °C for 20 min in air.
Au films were deposited onto the glass surface of the etched and uncovered F:SnO_2 substrate by an electron beam evaporation process conducted by Sabine Wasle and Sven Kubala, where the deposition growth parameters were set to yield a Au film thickness of 500 nm which was monitored and confirmed by a quartz crystal micro-

balance device. A 5 nm Cr adhesion film was deposited onto the substrate prior to the deposition.

6.2 Photoelectrochemical measurements

Technical aspects on the setup for the PEC characterization are explained in more detail in Section 4.2 and Fig. 4.4. A home built PTFE cell was used for dedicated PEC experiments on α-Fe_2O_3 samples without sensible in situ SHG data acquisition demands.[44] The design was adapted from elsewhere.[26] For the measurement, the sample was mounted to the cell by pressing it against an Viton© O-ring of 5 mm inner diameter exposing an electrode area of 0.196 cm^2 to the electrolyte. On the other side of the cell, a quartz disc was pressed against the cell with a Viton© O-ring that served as window for the incident light source for photoexcitation. In all measurements through this study, the sample was irradiated through the electrolyte, so called front-side illumination.[26]
All samples were contacted using a conductive copper tape. An analytical grade 1 M KOH solution purchased from Carl Roth GmbH + Co. KG. was used as electrolyte through all PEC experiments in this thesis. A BioLogic© VSP or SP200 potentiostat in combination with the EC-Lab© software was used for all EC and PEC experiments in this study.
An Ag/AgCl reference electrode purchased from SI analytics GmbH in a 3 M KCl electrolyte served as reference electrode with a standard redox potential of $\varphi^\circ(\mathrm{Ag/AgCl}) = 0.196\,V_{SHE}$. Externally measured potentials were converted to the RHE scale using the Nernst-equation $\Phi_{Ext}(\mathrm{RHE}) = \Phi_{Ext}(\mathrm{Ag/AgCl}) + \varphi^\circ(\mathrm{Ag/AgCl}) + 0.059\,\mathrm{mV} * \mathrm{pH}$,[26, 117] where $\Phi_{Ext}(\mathrm{Ag/AgCl})$ is the measured working electrode potential versus the Ag/AgCl reference while a solution pH of 14 has been measured for the 1 M KOH electrolyte for all PEC experiments.
EIS data was obtained from a sinoidal potential perturbation onto varying static baseline potentials between 0.72 V_{RHE} and 1.72 V_{RHE} with an amplitude of 20 mV at frequencies between 100 mHz and 10 kHz.
A Thorlabs© LP450-SF15 450 nm monochromatic optical fibre laser-diode in combination with a Thorlabs© TTC001 temperature controller and a Thorlabs© LDM9LP diode mount served as light source for photoexcitation of the sample. A potentiostat channel in chronopotentiometry (CP) mode was used as power source to drive the diode. The illumination power density of the laser-diode was determined to

24.2 mW cm^{-2} as measured using a calibrated Thorlabs© PM100A optical power meter.

6.3 Electrode Characterization

A comprehensive characterization of the electrode could be gratefully done in the facilities of the Department of Inorganic Chemistry of the Fritz Haber Institute of the Max Planck Society. The author wishes therefore to particularly acknowledge Annette Trunschke, Yanquing Wang, Gregory Huff and Jutta Kröhnert for their support to measure Raman and UV-Vis spectra of the sample; Frank Girgsdies and Michael Scherzer for XRD charaterization and Franz Schmidt, Adnan Hammud and Thomas Lunkenbein for taking SEM and TEM images of the sample.

6.3.1 UV-Vis-NIR spectroscopy

Linear optical absorption spectra were measured using an Agilent© Cary 5000 UV--Vis-NIR spectrometer. The measurement was executed in transmission mode where the bare F:SnO_2 substrate served as baseline. No significant reflective losses were found between light incidence from the coated front side compared to beam incidence from the back side of the sample.

6.3.2 Raman spectroscopy

The Raman spectrum was recorded at a Raman microscope, assembled by S&I Spectroscopy & Imaging GmbH. A TriVista© TR557 spectrometer provided spectral dispersion and a Princeton Instruments© PyLoN:2kBUV UV enhanced CCD camera was used for signal detection. The fundamental wavelength was 633 nm at a CW incident power of 1.24 mW.

6.3.3 FIB preparation and scanning electron microscopy

The FIB-preparation of a lamella from the α-Fe_2O_3/F:SnO_2 sample system and SEM images were carried out in a Bruker© FEI FIB/SEM DualBeam Helios NanoLab G3 UC device. The FIB-lamella was prepared using a beam of Ga atoms, after a protecting Pt layer was evaporated onto the sample. The acceleration voltage was 5.00 kV at a probe current of 0.2 nA.

6.3.4 Transmission electron microscopy

The TEM images were measured with a Bruker© FEI Talos F200X using a XFEG field emission gun. A SuperX 4 SDD EDX detector and bright field, dark field and a high angular attenuated dark field imaging techniques were used. The acceleration voltage and spatial resolution were set by the operator depending on the imaging demands.

6.3.5 X-Ray Diffraction

The X-ray diffractogram was measured in Bragg-Brentano geometry at a Bruker© D8 Advance diffractometer. The Cu – Kα line ($E = 8.04\,\text{keV}$, $\lambda = 1.5406\,\text{Å}$) was used as light source. The step size is $2\Theta = 0.02°$ with an integration time of 0.185 s.

6.4 In situ SHG-spectroscopy

A detailed description of the flow cell system for in situ SHG studies of α-Fe_2O_3 photoanodes under PEC control is presented in Section 4.3. The cell was assembled of an F:SnO_2 coated glass that served as substrate for the deposition of α-Fe_2O_3 and Au as explained further in Section 4.3. A fused silica window of 1 mm thickness was ordered from Siegert Waver GmbH. The spacer material was made of a 500 µm Kalrez© sheet. A miniature Ag/AgCl reference electrode in a 3 M KCl electrolyte with a standard redox potential of $\Phi^0_{\text{Ag/AgCl}} = 0.196\,V_{\text{SHE}}$ was purchased from Sensolytics GmbH. The area of the α-Fe_2O_3 film in contact with the electrolyte was $0.27\,\text{cm}^2$, the total volume of the cell was 40 µL. The 1 M KOH electrolyte is purged through the cell using a Harvard Apparatus© PHD ULTRA syringe pump and a Becton Dickinson© 60ml Plastic Syringe at a constant flow rate of 200 µL/min.

The light source for the SHG measurements was an amplified Ti:Sapphire based laser system. A Coherent© Vitesse oscillator is amplified by a Coherent© Legend Elite regenerative multipass amplifier to deliver 8 W of ≈120 fs short pulses at a repetition rate of 1 kHz. The 800 nm output is converted into the NIR fundamental probe beam using a Light Conversion© TOPAS OPA while the signal output of the OPA is utilized as NIR fundamental probe beam. The incident beam at the sample surface had a power of ≤5 µJ per pulse at a 1 kHz repetition rate. In all measurements presented here, both incident fundamental and reflected SH are polarized perpendicular to the incident plane (s-polarization). A typical potential dependent SHG spectrum

was acquired over 30 s during a 1 mV s^{-1} scan rate thus reflecting the average SH response of a 30 mV potential window. The excitational 450 nm beam was focused onto the sample with a 200 mm focal length. The laser diode current was set to 30 mA where the calibrated illumination power of the collimated beam of circular shape and 5 mm in diameter was determined 24.2 mW cm^{-2}.
The optical elements as shown in the setup in Fig. 4.5 were selected by their physical properties and purchased from Thorlabs GmbH, Edmund Optics Corp. and Newport Corp. A focal length of 100 mm was used to focus and collimate the NIR fundamental and SH signal beam, respectively. The signal was spectrally resolved using a Princetion Instruments© TriVista spectrometer and detected using a triggered Princeton Instruments© PI-MAX ICCD Camera that was synchronized with the pulse repetition of the laser system. Spectral reliability and accuracy was ensured by a Ne lamp reference using the commercial IntelliCal© calibration system. Concerted time resolution and synchronization was enabled using a TTL trigger signal that is guided between potentiostat, laser amplifier, camera and an optical shutter in an appropriate fashion.

7 SHG signal exploration

In order to draw profound scientific conclusions from SHG and PEC measurements, it is essential to identify appropriate experimental boundaries and see how they are related to the sample system. Therefore, we first need to find a suitable SHG signal, confirm that it corresponds to the α-Fe_2O_3 photoanode/electrolyte interface and see how it responds to PEC stimuli such as sample bias potential and illumination. Additionally, we need to make some small calculations in order to estimate how the experimentally accessible length scales relate to the dimensions of our nanostructured sample system.

7.1 Optical SHG signal assignment

The aim of this thesis is to investigate the electronic properties and processes of the α-Fe_2O_3 photoanode interface using optical SHG spectroscopy as an inherently surface specific probe under ambient and in situ conditions with the prospect of ultrafast time resolution.[80, 125, 142, 176] SHG was shown to provide interface-specific information on semiconductor particles[125, 142] and in particular on semiconductor electrode interfaces such as n-Si[81] and TiO_2.[79, 80] Besides these dedicated approaches to semiconductor electrodes, some SHG studies on the α-Fe_2O_3/liquid junction have also focused on the electrolyte ionic distributions and adsorption processes[199, 200] and one work has elaborated some third order non-linear effects in different iron oxide lattice systems.[201]
In the works by Bian et al. and Lantz et al. on Si and TiO_2 semiconductor electrodes, respectively, the SH response of semiconductor electrode surfaces was measured as function of an externally applied bias potential Φ_{Ext}. Both studies showed a clear enhancement of the SHG signal intensity as function of the applied potential. These findings are typically explained in terms od a DC-electric field enhancement within the SCR at the electrode surface, called EFISH (see Section 3.2.2).[143] Thus, EFISH provides a tool to probe the band-bending beneath the semiconductor surface and a

method to determine the flat-band potential under operating conditions.
We want to follow these lines and investigate our α-Fe_2O_3 electrode under OER conditions in contact with 1 M KOH electrolyte using EFISH spectroscopy in order to investigate the field distribution across the electrode interface. In contrast to the works done by Bian et al. and Lantz et al., we are able to measure the SH response with spectral resolution. This might provide an option to obtain further information on the signal formation and electronic properties and processes of the sample system. To the author's knowledge such an attempt to investigate the operating α-Fe_2O_3 photoanode surface band-bending using EFISH under OER conditions with spectral resolution has not been carried out, so far.

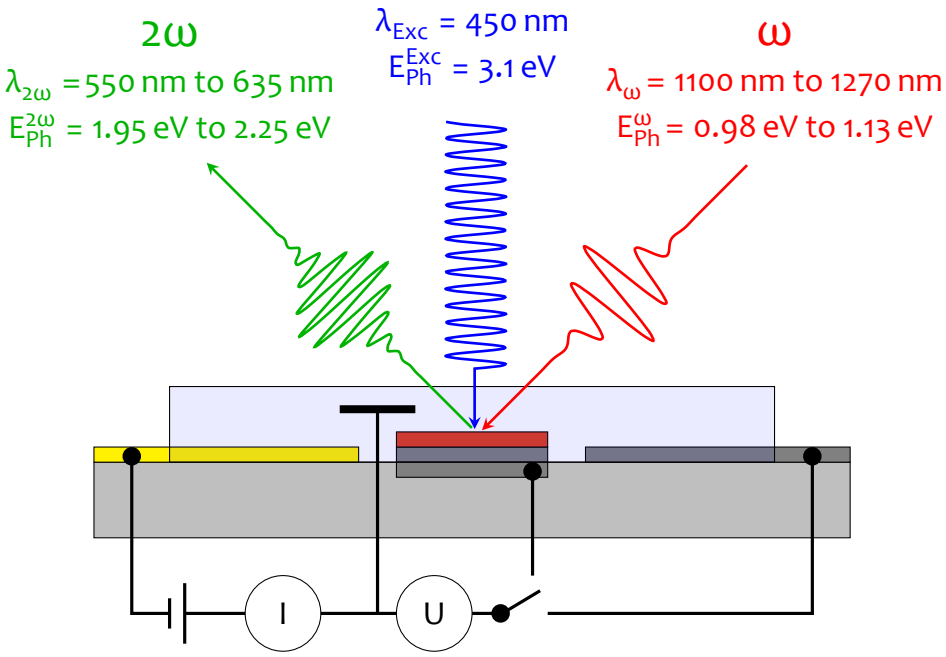

Figure 7.1: Sampling geometry for in situ SHG spectroscopy on the water splitting α-Fe_2O_3/electrolyte interface under PEC control. Probing and sampling pulses serve as guide to the eye, both are polarized parallel to the sample surface.

A scheme of the main subject SHG spectroscopy experiment of the thesis, is shown in Fig. 7.1. The quantity of interest is the SH response (2ω) from the electrode surface, generated from an ultrashort NIR-laserpulse (ω) in a 45 ° reflection geometry. Photoelectrochemical control is provided by an Ag/AgCl reference electrode and an Au film that serves as counter electrode. An area of bare and insulated FTO film can be connected on demand in order to compare the response of the α-Fe_2O_3 film with the underlying substrate. It is also possible to measure the SH response

from the Au film as spectral reference. A CW laser-diode of 450 nm wavelength is used as light source for carrier excitation. All relevant electronic control devices, i.e. the potentiostat for electrochemical control, the camera to record the SH response and an optical shutter to block and unblock electrode illumination are electronically synchronized in order to provide proper timing among the components through all measurements.

As we aim to perform SHG spectroscopy on the electrode/electrolyte interface, it is vital to find an SH signal that provides meaningful information on the α-Fe_2O_3 electrode surface. Therefore, the photon energy of the NIR fundamental wavelength is scanned around the band-gap of α-Fe_2O_3 ($\mathcal{E}_G = 2.1\,eV$). Such scans of the SH response are shown in Fig. 7.2. We see the SH response $I'_{2\omega}$ as function of the SH photon energy $\mathcal{E}$ from the three different materials in the dark and under illumination at open circuit voltage (OCV). The spectra from both, Au and F:SnO_2 are identical in the dark and under illumination, whereas the SH response of the α-Fe_2O_3 electrode is significantly lowered under illumination compared to the spectrum in the dark. The SH response from F:SnO_2 is much smaller than the signal from both, α-Fe_2O_3 and Au indicating that contributions from the underlying F:SnO_2 substrate to the SHG response from the α-Fe_2O_3 film are small. Also, the SH response from F:SnO_2 is only present at lower photon energies compared to the Au spectral reference while the SH response from α-Fe_2O_3 is stronger than the signal from Au and also more pronounced at lower photon energies.
The fact that illumination solely changes the SHG response from α-Fe_2O_3 without affecting the signal from Au and F:SnO_2 is already a strong indication that the SHG takes place in the α-Fe_2O_3 film and not in the underlying substrate. This lowering of the SH response under illumination is concomitant with a lowering of the OCV of the α-Fe_2O_3 electrode from $0.89\,V_{RHE}$ to $0.67\,V_{RHE}$ in contrast to a constant OCV at the F:SnO_2 electrode of $0.86\,V_{RHE}$. The formation of a photovoltage is a pre-requirement for a functional photoelectrode and the fact that this change is solely reflected by the SH response from the α-Fe_2O_3 film suggests that our SH signal is generated in the α-Fe_2O_3 film instead of the underlying photo-inactive substrate.

In order to evaluate possible contributions from the underlying F:SnO_2 substrate, the integral SHG response $I_{2\omega}$ as function of the applied potential Φ_{Ext}, is compared between the complete α-Fe_2O_3 photoanode system and the bare F:SnO_2 substrate. The corresponding dataset is presented in Fig. 7.3. $I_{2\omega}$ is shown for both the α-Fe_2O_3 sample electrode and the bare F:SnO_2 substrate, both in the same cell in contact with

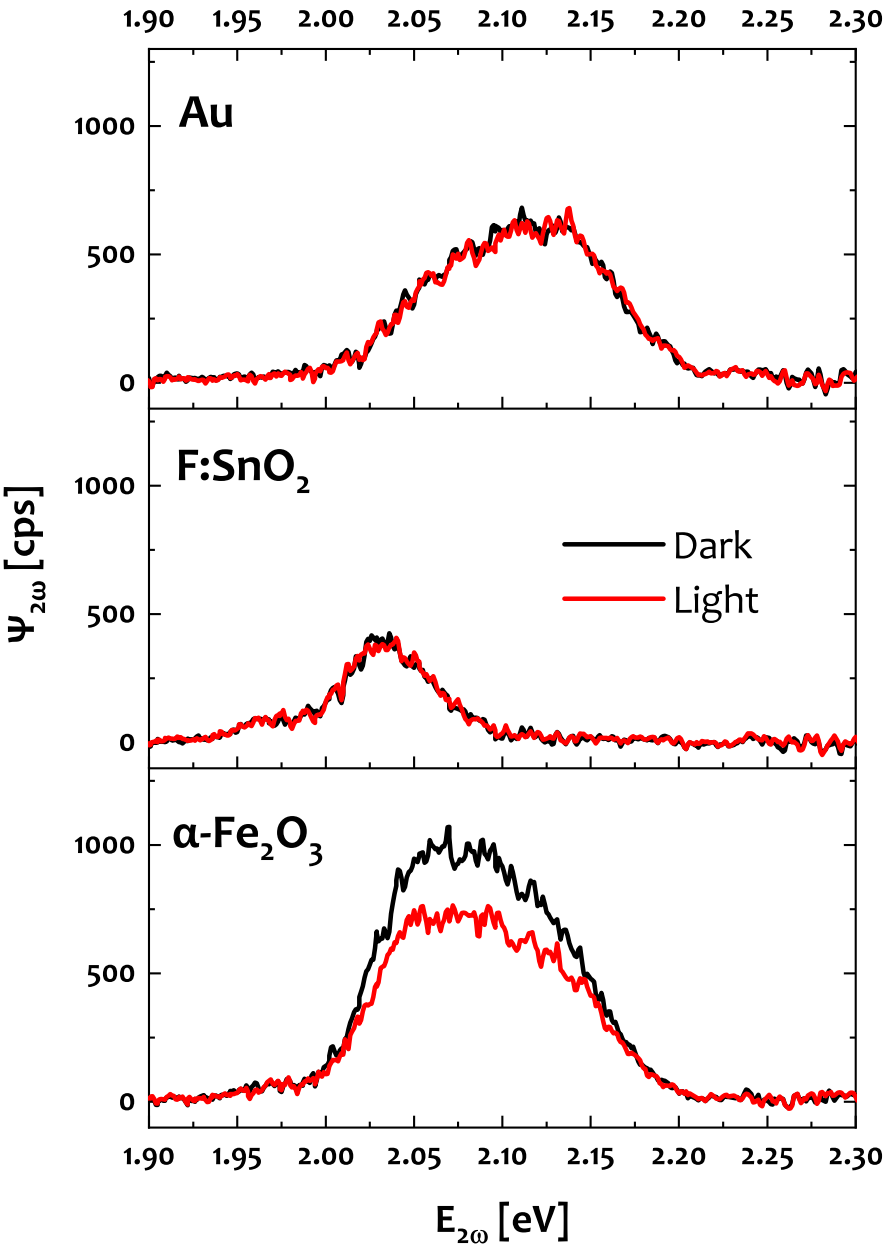

Figure 7.2: SHG Signal assignment. Scanned SHG spectra of Au, F:SnO_2 and α-Fe_2O_3 under open circuit voltage (OCV) conditions in the dark and under illumination in the same cell. The SH response from α-Fe_2O_3 exceeds the reference signals and can be modified by sample illumination. This allows for a certain ascription of the SH response to the α-Fe_2O_3 film.

the same electrolyte. We see that $I_{2\omega}$ from the α-Fe_2O_3 electrode is at least five times larger than $I_{2\omega}$ from the F:SnO_2 substrate. $I_{2\omega}$ from α-Fe_2O_3 is also strongly increas-

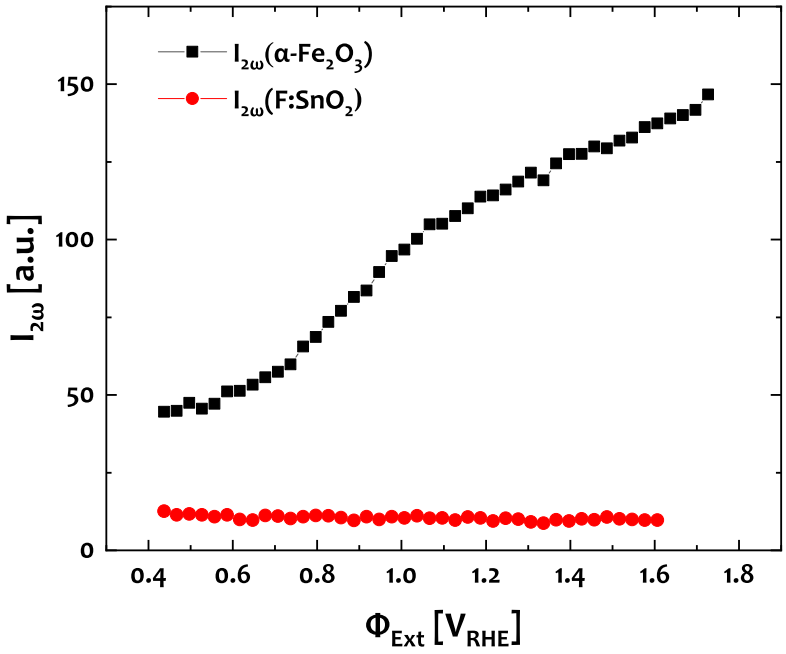

Figure 7.3: Potential dependent SHG spectrometry measurement of an operating α-Fe_2O_3 photoanode in the dark: Signal magnitude $I_{2\omega}$ from α-Fe_2O_3 and the F:SnO_2 substrate

ing with elevated electrode potentials, whereas it remains constant for the F:SnO_2 substrate. Besides observed SHG photo-response and increased signal intensity in Fig. 7.2, this is a further indication that the SH signal is generated in the α-Fe_2O_3 film and not in the underlying substrate nor in the electrolyte.
The author wishes to note that particular attention was paid towards repeatability and stability of the potential dependent SHG spectroscopy experiment. Plots from multiple repetitions of this measurement from two different samples are appended in Fig. II and also for the spectral shift that was observed in common with the intensity changes as shown in Fig. III (see Section 9.1 and Fig. 9.2). These graphs demonstrate that both quantities, $I_{2\omega}$ and $\langle \mathcal{E}_{2\omega} \rangle$, show a distinct potential dependence that can repeated over several measurements and also for different samples which verifies the reliability and significance of the experiment presented here.

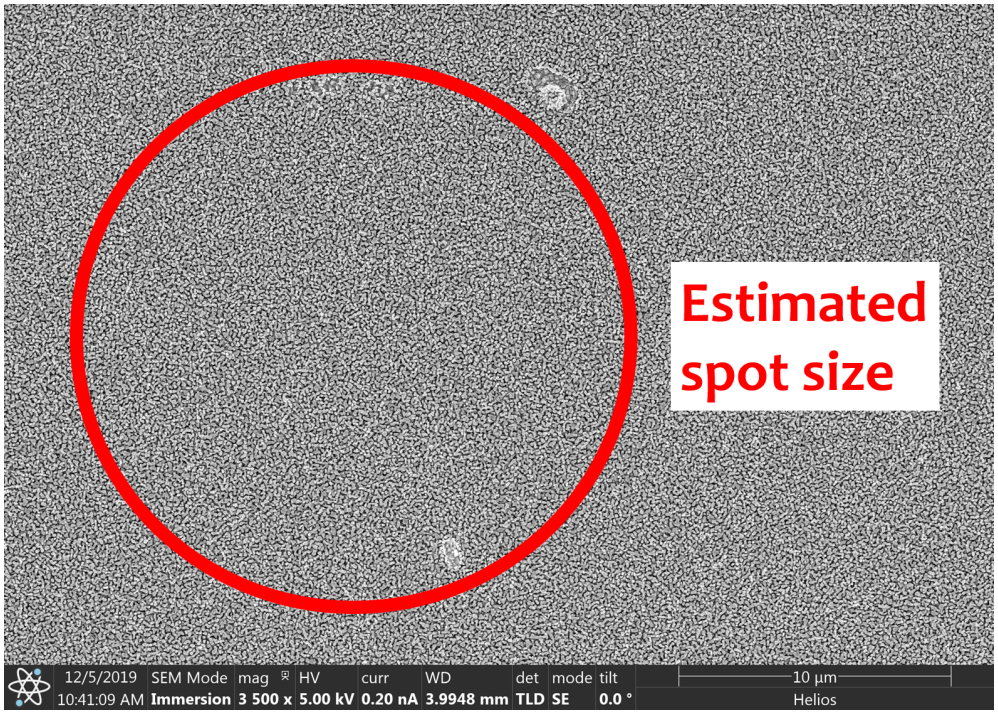

Figure 7.4: SEM image with estimated spot size of the NIR probe beam at the α-Fe_2O_3 sample

7.2 Sampling boundaries

Before we can analyse our SHG observables and fill these quantities with physical meaning, we need to get an idea of the spatial dimensions of the system that is sampled. Fig. 7.4 shows an SEM image of the α-Fe_2O_3 film with the estimated spot size of our probe beam. The spot size was estimated from a Gaußian beam waist given by the focal length, the NIR probe beam wavelength and the aperture of the beam and found to be 19 µm in diameter. We can see that this spot size is very large compared to the particle size of 50 nm to 100 nm. Since the particles in the α-Fe_2O_3 film are randomly oriented, we can conclude that the SHG signal is independent of crystallographic orientation of the material and that the SHG signal provides an isotropic, integral probe of the electrode surface.

From the UV-Vis-NIR absorption spectroscopy measurements (see Section 5.2.2) we can also calculate the NIR penetration and Vis escape depths of the NIR probe and SH signal beams, respectively, using the absorption coefficient α. The probing and escape depth L of light is typically defined as the length where the photon flux of a

given energy I' has decreased to a fraction of $1/e$ of the initial value I'_0 according to Eq. 7.1.[202, 203]

$$\frac{I'}{I'_0} = \frac{1}{e} = e^{-\alpha L} \tag{7.1}$$

From this, we obtain a maximum penetration or escape path length L according to Eq. 7.2.

$$L = \frac{1}{\alpha} \tag{7.2}$$

The absorption coefficients as determined by UV-Vis-NIR absorption spectroscopy with the film thickness from TEM are $\alpha_{1180\,\mathrm{nm}} = 1000\,\mathrm{cm}^{-1}$ and $\alpha_{590\,\mathrm{nm}} = 30\,000\,\mathrm{cm}^{-1}$ for the fundamental NIR and SH light, respectively (see Fig. 5.7). With this we obtain an NIR penetration depth $L_{1180\,\mathrm{nm}} = 10\,\mu\mathrm{m}$ and an SH escape depth of $L_{590\,\mathrm{nm}} = 330\,\mathrm{nm}$ probing through an approximate α-Fe_2O_3 film thickness of 200 nm. In order to obtain optical responses from SHG and electrode illumination, both fields, the incident 1180 nm NIR fundamental beam and the excitational 450 nm were focused onto the one spot at the α-Fe_2O_3 sample in order to provide sufficient field strength overlap. The respective spot sizes from Gaußian beam waists are 19 µm for the fundamental light and 23 µm for the UV/Vis sample excitation. Considering the pulse duration of 120 fs with an energy of 5 µJ per pulse of the NIR fundamental beam and a circular spot of 19 µm we obtain an NIR illumination power density of $1.5 \times 10^{17}\,\mathrm{W\,m^{-2}}$. For the exciting power density of $24.2\,\mathrm{mW\,cm^{-2}}$ we obtain a concentrated power density of $1.1 \times 10^{13}\,\mathrm{W\,m^{-2}}$. Both values indicate huge illumination power densities which would cause an almost unity transition population ratio and lead to a saturation of any absorptive processes,[119] which also indicates negligible effects from light absorption. Therefore, we can conclude that the sampling depth normal to the electrode surface is not limited by light absorption, that a complete field-overlap is provided across the entire α-Fe_2O_3 film and that an integral SH signal is homogeneously generated over the whole α-Fe_2O_3 film.
It might be worth noting here that light absorption is a prerequisite for PEC water splitting. Therefore, the 450 nm laser diode as chosen to drive the photo-oxidation needs to have a finite penetration depth. The corresponding absorption coefficient at $\alpha_{450\,\mathrm{nm}} = 9.2 \times 10^4\,\mathrm{cm}^{-1}$ would indicate an excitational penetration depth of 110 nm,

unless transition population ratios are saturated, just as required for a functional photoelectrode system.
From these considerations we find that the experimental requirements to probe PEC interface effects at a functional thin film semiconductor electrode are provided: An unhindered SHG probing mechanism normal to the electrode surface and a sample illumination channel that allows for photoelectric carrier excitation and generation of photocurrent or photovoltage, respectively. Note that a detailed description of possible distributions of the photo-excitation processes through the homogeneously doped, nano-porous sample system can not be subject to the SHG studies on integral electrostatic effects through the α-Fe_2O_3 thin film as presented here.

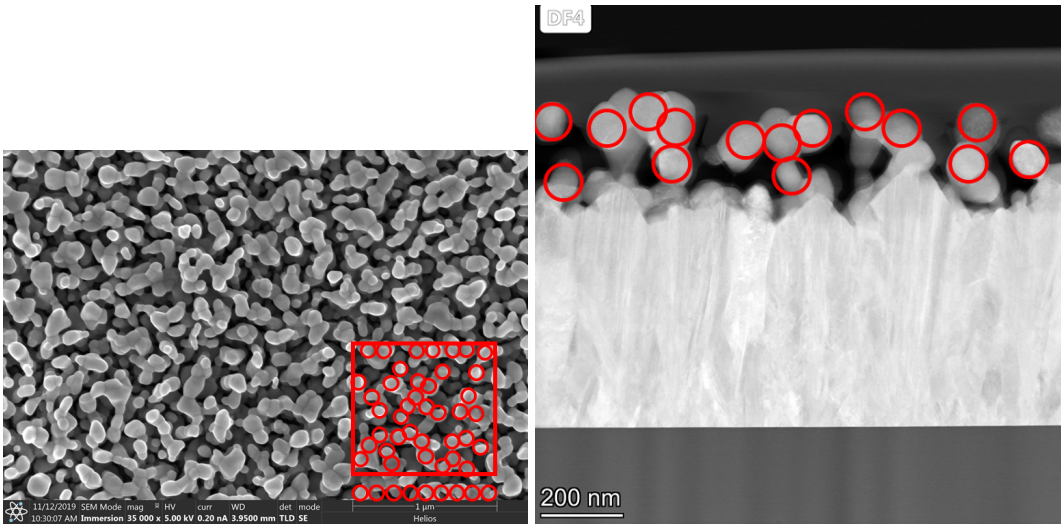

(a) SEM-image with estimated 40 spherical particles of 100 nm diameter within a square of $A_{\mathrm{Geo}} = 1\,\mu\mathrm{m} \times 1\,\mu\mathrm{m}$

(b) FIB-TEM-image showing approximately two layers of particles of 100 nm diameter

Figure 7.5: Estimation of the active electrode surface area approximating a two-layered film of spherical particles of 100 nm diameter

Another information we can infer from the EM images is the roughness of the electrode surface. In order to improve the accuracy of all spatial quantities in the following sections, we want to estimate a roughness factor f_{R} to relate the geometric electrode surface that is exposed to the electrolyte A_{Geom} with the electrochemically active surface of the nanostructured α-Fe_2O_3 film that forms the solid-liquid-contact S_{Act} according to Eq. 7.3.

$$S_{\mathrm{Act}} = f_{\mathrm{R}} * A_{\mathrm{Geom}} \tag{7.3}$$

As illustrated in Fig. 7.5, we want to approximate the α-Fe_2O_3 film by two layers of spherical particles of 100 nm diameter. Following this simple model we would find (2×40) particles per µm^2. From these numbers we obtain a surface roughness factor f_{R} of ten according to Eq. 7.4.

$$f_{\mathrm{R}} = \frac{S_{\mathrm{Act}}}{A_{\mathrm{Geom}}} = \frac{80 * 4 * \pi * (0.1\,\mu\mathrm{m})^2}{1\,\mu\mathrm{m}^2} = \underline{10} \tag{7.4}$$

Thus, we can approximate that the electrochemically active surface of the α-Fe_2O_3 film S_{Act} is approximately ten times larger than the geometric electrode area A_{Geo}. This value will be used in the following sections to calculate densities of donor atoms and charge carriers. Since these values range over several orders of magnitude for semiconducting materials ($N_{\mathrm{D}} \approx 10^{16}$ cm^{-3} to 10^{20} cm^{-3}),[26] the relative error of this estimation will be still small compared to the large range of absolute carrier and donor densities.

Part III

Results

8 Electrodeposition of FeO_xH_y films

While the main goal of this doctoral endeavour is an investigation of an α-Fe_2O_3 photoanodes' interfacial electronic structures and processes using SHG spectroscopy, the sample preparation is an essential part of the activities. And so, some insight could also be gained on the physico-chemical characteristics of the sample preparation process. Therefore, before we move on to the in situ characterisation of the electrode interface, we want to see how we can monitor and the FeO_xH_y film growth progress and which conclusions could be drawn for future activities towards iron oxide thin films of tailored optical, electronic, magnetic or catalytic properties.

8.1 Growth progress monitoring

The α-Fe_2O_3 photoanode samples used in these works were prepared by anodic electrodeposition and subsequent thermal annealing (see Fig. 4.1). While the anodic deposition of FeO_xH_y thin films was first described by Cohen and co-workers already in the late 1960s,[108, 109] its application to PEC has gained particular attention in the last decade.[110, 204] This route was shown to offer access to a broad range of film morphologies in common with a range of parameters to control the deposition process.[112] A number of works have investigated the influence of process parameters such as pH, temperature and precursor solution $Fe^{2\oplus}$ concentration,[110, 111, 113, 205] deposition potential[115] and annealing temperature[111, 206] on the morphology and PEC behaviour of α-Fe_2O_3 films, just to mention those investigations conducted on F:SnO_2 substrates as it is applied here.[112]

$$Fe^{2\oplus} \longrightarrow Fe^{3\oplus} + e^{\ominus} \tag{8.1}$$

$$Fe^{3\oplus} + 2\,H_2O \longrightarrow FeOOH\downarrow + 3\,H^{\oplus} \tag{8.2}$$

The film growth is typically described by a two step reaction where the deposition is initialized by oxidation of $Fe^{2\oplus}$ ions, Eq. 8.1, followed by precipitation of an FeO_xH_y film at the substrate due to the lowered solubility of $Fe^{3\oplus}$, Eq. 8.2.[109, 110, 112] However, the crystallographic phase and chemical composition of the as-deposited film is strongly varying depending on the process parameters.[112] For instance, Martinez et al. showed that, depending on the applied potential, the as deposited film on a Ti substrate can range from magnetite (Fe_3O_4) over goethite (α-FeOOH) to lepidocrocite (γ-FeOOH).[115]
While most work has focussed on the morphologies and PEC performance of electrodeposited α-Fe_2O_3 films, there is only scarce literature that investigated the nucleation and growth mechanism of this process.[112] On the other hand, in contrast to many other growth processes, electrodeposition inherently offers the chance to monitor the film growth progress based on the deposition current which is directly related to precursor adsorption and oxidation at the substrate electrode (see Section 3.1).[116, 177] Several studies on the cathodic deposition of metal films have shown that a range of mechanistic information can be gained from basic electrochemical observables of the substrate in contact with the electrolyte precursor.[207–209] Deposition current transients, for instance, allow us to distinguish between adsorption and diffusion limited growth and a normal sweep voltammogram provides insight on electrode adsorption and redox processes.[116]
Although the goal of the activities here is the preparation of a reliable, well-defined and representative sample system for in situ SHG spectroscopy on the α-Fe_2O_3 electrode/electrolyte interface, some insight could be obtained on the nucleation and film growth mechanism from basic electrochemical observables. The deposition process presented here is conducted from a $(NH_4)_2Fe(SO_4)_2$ (Mohr's salt) solution, the most durable $Fe^{2\oplus}$ salt which is less prone to hydrolysis and air oxidation compared to the two other most common $Fe^{2\oplus}$ precursor compounds for anodic electrodeposition $FeCl_2$ and $FeSO_4$.[112, 172] Commercial F:SnO_2 coated glass served as substrate, a standard TCO that provides the highest thermal and chemical stability of common TCOs.[26, 171] Therefore, together with the versatility of electrodeposition, this growth process provides a scalable and prospective method for the production of a tailored photoanode system.

Fig. 8.1 shows cyclic voltammetry (CV) curves of the bare F:SnO_2 substrate in contact with the $Fe^{2\oplus}$ precursor solution where the current density j is plotted over the externally applied potential Φ_{Ext} for three different scan rates. We can see two

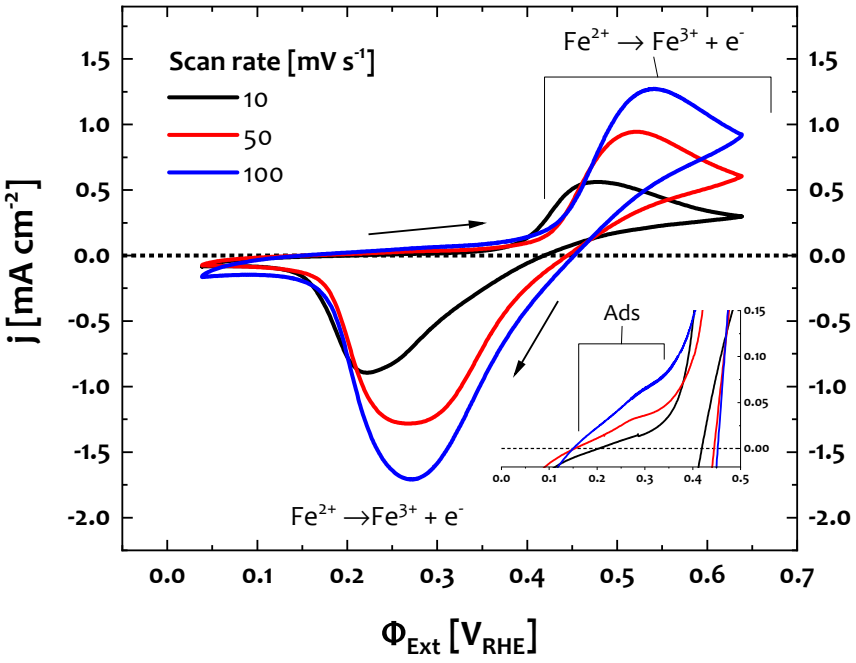

Figure 8.1: Precursor adsorption and oxidation. Cyclic voltammetry (CV) measurement of the bare F:SnO_2 substrate in contact with the plating solution at three different scan rates showing a small shoulder preceding the Faradaic oxidation current of $Fe^{2\oplus}$ ions

pronounced waves of Faradaic current – an anodic current at potentials above 0.5 V_{RHE} and a cathodic current at potentials lower than 0.3 V_{RHE}. Due to the absence of other redox active species in this system and from comparison with standard potentials we can clearly ascribe these two waves to the oxidation and reduction of bulk solution $Fe^{2\oplus}$ and $Fe^{3\oplus}$, respectively.[27, 172] We can further confirm this assignment as the current diminishes at more cathodic potentials: Since no reductant other than $Fe^{3\oplus}$ is available in the system, no significant reduction is taking place. Both waves are well separated along the potential axis, which indicates that the overpotential or activation barrier between oxidation and reduction wave is quite high.[27, 210] From that we can infer rather slow kinetics or an irreversible reaction along the Arrhenius equation,[211] which seems quite plausible for the precipitation deposition and dissolution of FeO_xH_y.[172] Since the electrochemically controllable and visible process is the anodic electrodeposition Eq. 8.1, we want to examine the anodic current wave in more detail.

A closer look at the oxidation current of our electrodeposition system is shown in the inset in Fig. 8.1. It reveals a small anodic current feature preceding the oxidation wave. This signal appears as shoulder slightly cathodic from the onset of reaction Eq. 8.1. Such a small feature preceding a large redox wave is a typical indication for an adsorption process of reactant species at the electrode surface prior to the bulk charge transfer reaction.[27, 163, 210] Thus, we want to hypothesise that the oxidation of $Fe^{2\oplus}$ from the precursor solution at potentials above $0.4\,V_{RHE}$ is preceded by an adsorption process at $0.3\,V_{RHE}$ and see how the applied potential will affect the film growth.

Technically spoken, the electrodeposition process employed here is a chronoamperometry measurement in a conventional three electrode configuration. A constant bias potential is imposed to the substrate and the current is recorded as function of elapsed time. Since we provide potentiostatic conditions, we want to neglect capacitive effects, suppose a 100 % Faradaic efficiency and directly relate the current during the electrodeposition to the amount of deposited $Fe^{3\oplus}$ (Eq. 8.1). Thus, the growth curves – the deposition current j_{Dep} as function of time t – allow us to directly monitor the deposition rate during the film growth (see also Section 3.1).[116]

A set of growth curves at different applied potentials Φ_{Ext} is shown in Fig. 8.2. The integral film mass was controlled by the deposition time and kept constant through the whole series. We find that the shape of the growth curves is essentially constant at $\Phi_{Ext} \geq 0.44\,V_{RHE}$, whereas more dramatic changes only occur at lower potentials. We also see that an increase of the potential above $0.44\,V_{RHE}$ does not increase the deposition rate. This behaviour is a clear indication for a diffusion limited growth process where the deposition rate is limited by the mass transport of the reactant to the electrode surface and the reaction driving force Φ_{Ext} does no longer affect the deposition rate.[116]

Fig. 8.3 shows a magnification of the deposition regime transition. We see the growth curves and the corresponding Φ_{Ext} for those three curves from Fig. 8.2 over which the strong change of the current transients is observed. After a period of open circuit conditions with zero current, the potential is ramped up to its final value and kept constant for the whole deposition process. When a fixed amount of charge has been deposited, another period of zero current is applied to finalize the film growth.

From Fig. 8.3 and Fig. 8.2 we see that at potentials above the $Fe^{2\oplus}$ oxidation onset at $0.4\,V_{RHE}$ (see also Fig. 8.1), j_{Dep} shows a peak when a bias potential Φ_{Ext} is imposed to the electrode. After Φ_{Ext} is kept constant, j_{Dep} is decreasing and flattening out

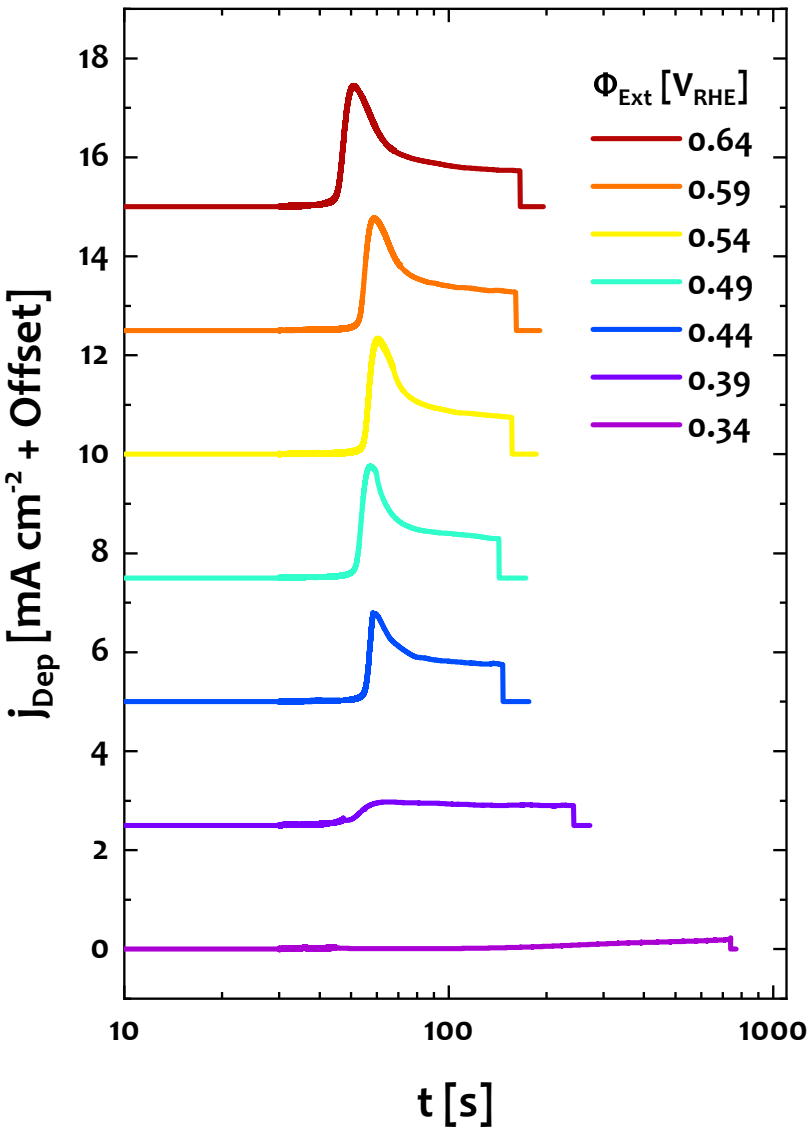

Figure 8.2: Growth progress monitoring. Anodic EC of FeO_xH_y under amperometric conditions with evolution of the deposition current density j_{Dep} during the growth of FeO_xH_y thin films at different potentials Φ_{Ext}

with prolonged deposition time. This time dependent evolution of the deposition current is a further typical feature of a diffusion limited growth mechanism as the diffusion layer in front of the electrode is depleted until a steady state between reac-

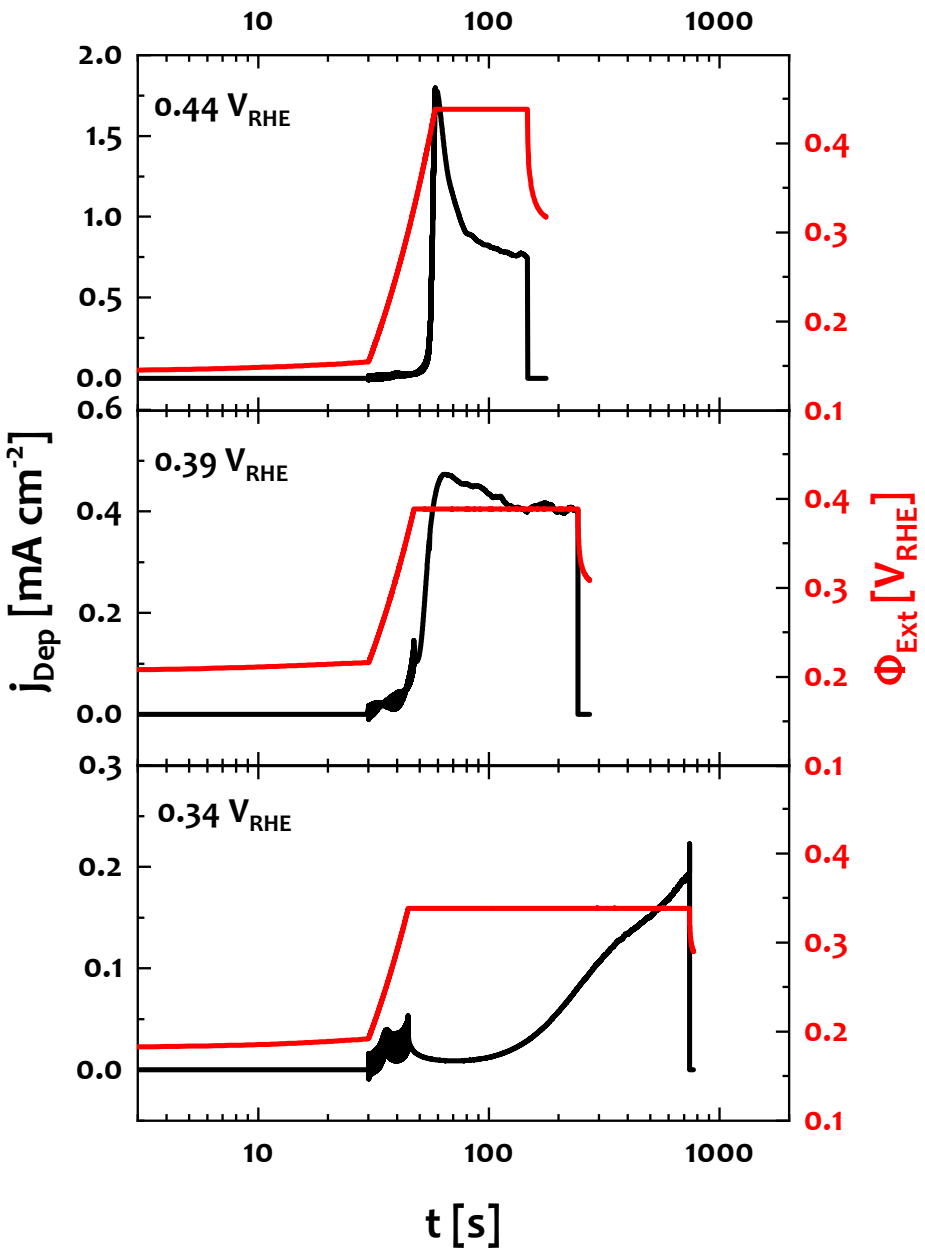

Figure 8.3: Transition of the ED regime from adsorption to diffusion controlled film growth. The deposition current transients are changing dramatically when the applied potential is varied between 0.34 V_{RHE} and 0.44 V_{RHE}

tant diffusion and its oxidation in front of the electrode is established.[116]
The shape of the growth curve at 0.34 V_{RHE} is strongly differing from those at higher potentials. While the deposition current is reaching a peak when the potential was

ramped up to its final value at potentials $\geq 0.4\,V_{RHE}$, the deposition rate at $0.34\,V_{RHE}$ is very small at the beginning and just slowly increasing over the whole deposition process without any peak in the deposition current transients. An intermediate process seems to be the case at $0.39\,V_{RHE}$, where the deposition current is approximately constant.

We can explain this transition of the deposition current transients considering the findings on the chemical characteristics of the system as inferred from the CV measurement in Fig. 8.1. From this data we found that the bulk $Fe^{2\oplus}$ oxidation with an onset of $\approx 0.4\,V_{RHE}$ is preceded by an adsorption process of reactant species. Therefore, the deposition at $0.34\,V_{RHE}$ is clearly below the thermodynamic onset of the $Fe^{2\oplus}$ oxidation reaction Eq. 8.1, i.e. this process occurs in an under potential deposition (UPD) regime at $\Phi_{Ext} < \varphi^{\circ}(Fe^{2\oplus}/Fe^{3\oplus})$ (see Section 3.1).[116, 117] Thus, as the increase of the deposition potential from $0.34\,V_{RHE}$ to $0.44\,V_{RHE}$ crosses the thermodynamic onset of the $Fe^{2\oplus}$ oxidation, the changing deposition current evolution corresponds to a transition from under potential deposition (UPD) to over potential deposition (OPD) conditions. Or, in other words, at deposition potentials of $0.34\,V_{RHE}$ we observe an adsorption limited growth whereas diffusion limited growth dominates at potentials of $0.44\,V_{RHE}$ and above.[116, 207, 209]
The shape of the UPD current transient at $0.34\,V_{RHE}$ also gives rise to another mechanistic speculation. In contrast to all potentials above, the deposition rate at $0.34\,V_{RHE}$ is very slow at the beginning and accelerating with prolonged deposition time. Since we apply constant system parameters (particularly potential, temperature, precursor concentration, pH and electrolyte convection), the only changing parameter with prolonged film growth is the coverage of the substrate electrode with the FeO_xH_y deposit. From Fig. 8.1 we also know that the film growth is preceded by the adsorption of the $Fe^{2\oplus}$ precursor ions at the substrate electrode. Thus, since the growth rate is increasing with ongoing deposition, the film growth might be accelerated by the presence of FeO_xH_y at the substrate surface. This indicates that the adsorption of $Fe^{2\oplus}$ precursor species is stronger at the growing FeO_xH_y film than the pristine $F{:}SnO_2$ substrate which is a typical indication for Volmer-Weber or island growth type.[116, 207, 212]

The fact that an UPD type growth occurs, also implies an incomplete oxidation of $Fe^{2\oplus}$ in the as-deposited film. The UPD type growth below $0.4\,V_{RHE}$ is further indicated by the photographs of the as-deposited films in Fig. 8.4, which shows all samples from the deposition curves in Fig. 8.2. Even though the film mass was kept

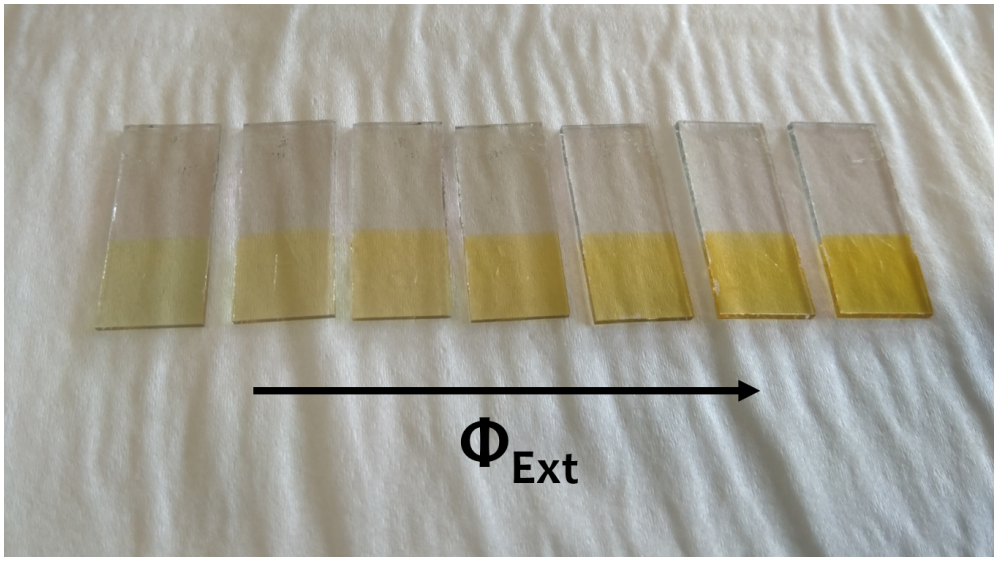

Figure 8.4: Photographs of as-deposited FeO_xH_y thin films from Fig. 8.2 grown at different potentials and constant film mass

constant through this series of deposition, a clear change of the deposits' colour and opacity is observed. In particular, the presumptive UPD grown sample on the left side has a green tinge. While a detailed UV-Vis spectroscopic study on as-deposited FeO_xH_y films, conceivably taking precautions to prevent air oxidation, is beyond the scope of this thesis, a green colour in FeO_xH_y phases is a typical indication of lattice $Fe^{2\oplus}$ as in green rusts, for instance.[172, 213] Additionally, the formation of Fe_3O_4 at low deposition potentials has been reported.[115] This is an incompletely oxidized FeO_xH_y phase, so that we can further confirm the possibility to deposit FeO_xH_y phases of mixed oxidation states of Fe and support our findings of an UPD type film growth.

8.2 Mechanistic control

Besides some profound hints on the growth mechanism of the bulk FeO_xH_y film, an even closer look at the growth curves provides additional information on the nucleation of the film growth. As mentioned above, the film growth is initialized after an OCV period when Φ_{Ext} at the F:SnO_2 substrate is ramped up to its final value (see Fig. 8.3). As one can already suspect from Fig. 8.3 and Fig. 8.2, an increase of Φ_{Ext} at the F:SnO_2 substrate working electrode instantly causes a small, distinct current signal for all processes. A magnified illustration of this early electrode current

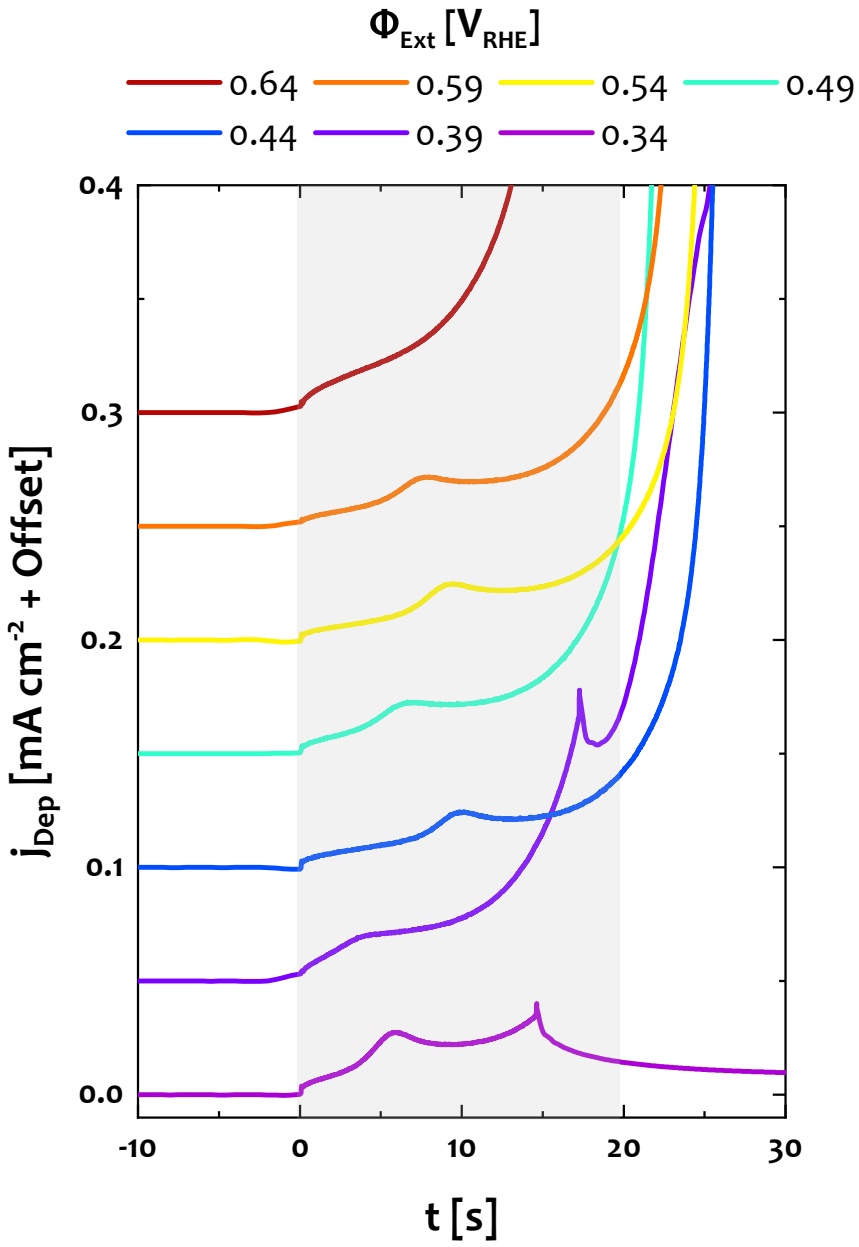

Figure 8.5: Initialization of $Fe^{3\oplus}$ deposition. Cell current during the early stages of the film growth as function of time after an OCV period showing a small nucleation current signal prior to each deposition

at the initialization of the film growth is shown in Fig. 8.5 where a fast Fourier transformation (FFT) filter has been applied to the dataset from Fig. 8.3 and Fig. 8.2 in order to remove electronic noise.

We see that as soon as a bias potential above OCV is applied from $t \geq 0$ on, a distinct anodic signal is formed in all processes that is well separated from the growth of the bulk film. According observations were made in Fig. 8.1 where a small adsorption feature was found to precede the bulk oxidation wave of $Fe^{2\oplus}$ from the solution. Thus, these small anodic waves preceding the main deposition current transients most probably act as prerequisite for the growth of the FeO_xH_y film, which implies that these small features correspond the nucleation of the first particles on the bare $F:SnO_2$ surface. The controllable formation of nuclei provides an option to separate the nucleation phase from the bulk film growth and to control and monitor the phase formation of FeO_xH_y films from bottom up. While these considerations on the nucleation would require additional gravimetric or microscopic confirmation, an adsorption or nucleation current is often observed for the cathodic electrodeposition of metals, prior to the bulk film growth.[116]

From these findings we can infer that the FeO_xH_y deposition mechanism involves an adsorption step preceding the full oxidation of the $Fe^{2\oplus}$ precursor ions. An incompletely oxidized FeO_xH_y phase was also observed here and elsewhere,[115] so that we can refine the conventional mechanism from Eq. 8.1 and Eq. 8.2[109, 110, 112] with the observations from our time and potential resolved deposition current measurements.

$$Fe^{2\oplus}_{Solv} \longrightarrow Fe^{(2+\delta)\oplus}_{Ads} + \delta e^{\ominus} \tag{8.3}$$

$$Fe^{(2+\delta)\oplus}_{Ads} + x\,H_2O \longrightarrow FeO_xH_{(2x-2-\delta)}\downarrow + (2+\delta)\,H^{\oplus} \tag{8.4}$$

One possible chemical formulation of these findings is shown in the equation system above. In Eq. 8.3, an oxidation grade δ was introduced to Eq. 8.1. This coefficient may vary from 0 to 1 for a hypothetical, fully adsorption controlled growth without charge transfer up to a complete oxidation to $Fe^{3\oplus}$ as shown in Eq. 8.1, respectively. Since an adsorption step was found to take place before or in parallel to the oxidation, we can state a first step that forms an adsorbed Fe-species of varying oxidation state $Fe^{(2+\delta)\oplus}_{Ads}$ from the solvated precursor ion $Fe^{2\oplus}_{Solv}$ as given in Eq. 8.3. In a subsequent step Eq. 8.4, the $Fe^{(2+\delta)\oplus}_{Ads}$-species would undergo a hydrolytic precipitation reaction analogously to Eq. 8.2 that forms the FeO_xH_y-deposit due to the lowered solubility product.[109, 112] In this case, the amount of water contributing to the reaction may vary, depending on the as-deposited FeO_xH_y-phase.[115].

It was found that the degree of oxidation can be controlled by the external potential. For potentials >0.4 V_{RHE}, the $Fe^{2\oplus}$ ions are completely oxidized to $Fe^{3\oplus}$, whereas smaller potentials were found to result in an UPD growth type and also to deliver FeO_xH_y phases with an average Fe oxidation state <3.

These investigations indicate a novel and convenient method to monitor and control progress of FeO_xH_y film anodic electrodeposition from plain electrochemical parameters. Such mechanistic studies from chronoamperometric measurements have been performed on a range of metal deposition processes.[116, 209, 214–217] However, to the author's knowledge, a mechanistic discussion of an anodic electrodeposition process has not been transferred from the mono-atomic growth of metals to the more complex deposition of oxides and oxy-hydroxides, so far. Even though further spectroscopic and gravimetric confirmation may be beneficial, these studies demonstrate the high potential to grow iron oxide and hydro-oxide films with a relatively simple method but still high degree of mechanistic control.
To the author's knowledge, this approach to characterize, tailor and monitor the anodic electrodeposition of metal oxides is barely described in literature.[112] Furthermore, the option to control the crystallographic structure of the as-deposited FeO_xH_y films with the applied potential, involving the co-deposition of $Fe^{2\oplus}$,[115] provides manifold options to conduct fundamental studies on the huge phase space of the Fe-O-H system and to tailor iron oxide thin films of desired catalytic, optical, electronic or magnetic properties.[114, 196, 213, 218–220]

In conclusion, these works point out that an examination of the deposition curves provides a convenient way to obtain mechanistic information on the anodic FeO_xH_y electrodeposition growth process from basic electrochemical observables. A plain CV measurement is shown to determine appropriate potentials to stir the process towards UPD or OPD regimes. The deposition current transients, which are inherently recorded during most electrodeposition processes, provide the option to not only monitor the growth rate but also to deliver information on the nucleation and growth mechanism online.
It should be mentioned that the conclusions on the deposition mechanism are in accordance with a range of studies on cathodic electrodepositions of metals on single crystal surfaces.[116, 207] However, the process investigated here may be more complex as the deposition of FeO_xH_y involves at least two reaction steps Eq. 8.1 and Eq. 8.2, which might be a sequence of further elementary reactions. Also, the process employed here is conducted on a polycrystalline substrate which may allow

several elementary steps to take place in parallel. Thus, a substantial study on the growth mechanism would require complementation with microscopic, spectroscopic or gravimetric measurements for confirmation.

9 SHG under photoelectrochemical control

9.1 Bias dependent SHG

As developed in Chapter 7, the experimental setup provides a substantial SHG response that corresponds to the α-Fe_2O_3 photoanode material and relates to PEC parameters. The most important quantity to control electrode interface processes is the potential with respect to an external reference Φ_{Ext}. Thus, we now want to inspect the SHG signal with spectral resolution as function of Φ_{Ext}. Fig. 9.1 shows a typical dataset that is obtained from this measurement for the α-Fe_2O_3 photoanode. The set of potential dependent SHG spectra are displayed from two different perspectives. We clearly see that the SHG intensity is increasing with more anodic potentials and that no dramatic spectral changes are sticking out over the spectral range. Thus, in order to analyse these datasets, we need to find suitable metrics to quantify the observed effects.

The analysis of the SHG spectra is illustrated in Fig. 9.2. The most important quantity to analyse the potential dependent SH response is magnitude of the SHG signal $I_{2\omega}$, which we obtain by integration of the SH response $I'_{2\omega}$ along the photon energy $\mathcal{E}$ over the entire spectral range $h\nu$ according to Eq. 9.1.

$$I_{2\omega} = \int_{\mathrm{h}\nu} I'_{2\omega}(\mathcal{E})\,\mathrm{d}\mathcal{E} \tag{9.1}$$

The measurement of potential dependent SHG intensity is a well-known probe for field-distributions across interfaces, that has been applied to solid-liquid[79, 81, 140, 142, 145] and also to solid-solid[221, 222] interfaces.

Another minor but detectable information apparent in the SHG spectra is a small but significant shift of the spectral centre of gravity. This quantity corresponds to the

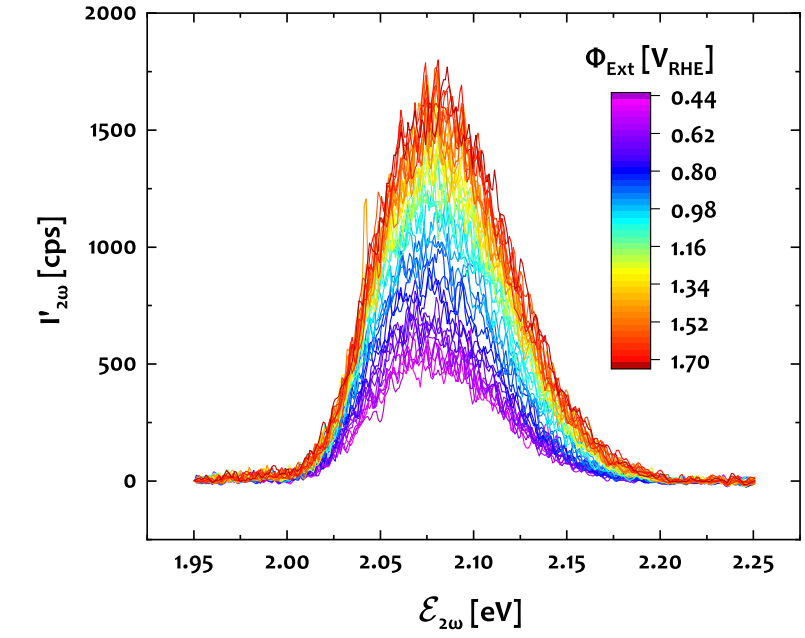

(a)

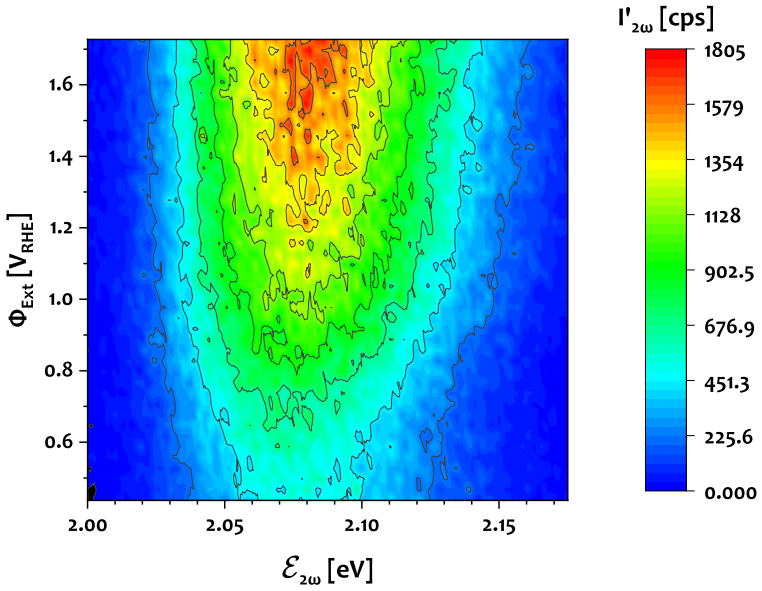

(b)

Figure 9.1: Potential-dependent SHG spectra. 9.1(a): SHG spectra with colour-coded electrode potential Φ_{Ext} and 9.1(b): heatmap of the photon energy - potential plane with colour coded SHG signal intensity

expectation value of the measured SHG photon energy $\langle \mathcal{E}_{2\omega} \rangle$ which can be obtained

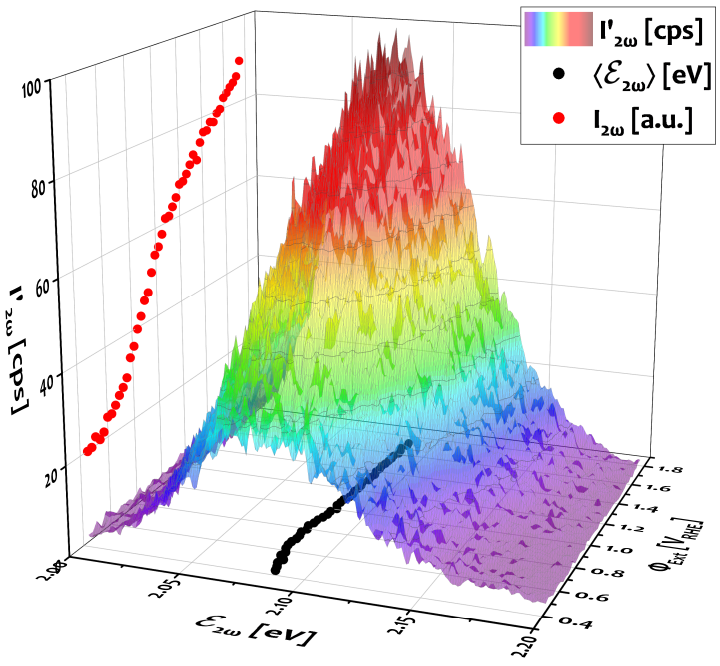

Figure 9.2: Analysis of potential dependent resolved SHG spectra. The Area under the SHG spectra $I_{2\omega}$ was used as measure of the signal intensity and a SH photon energy expectation value $\langle E_{2\omega} \rangle$ is used as measure of spectral changes

from the integral SHG intensity $I_{2\omega}$ and the energy dependent photon flux $I'_{2\omega}(\mathcal{E})$ according to Eq. 9.2.[136, 223]

$$\langle \mathcal{E}_{2\omega} \rangle = \frac{1}{I_{2\omega}} \int_{h\nu} \mathcal{E} * I'_{2\omega}(\mathcal{E}) \, d\mathcal{E} \tag{9.2}$$

Both quantities intensity $I_{2\omega}$ and spectral centre of gravity $\langle \mathcal{E}_{2\omega} \rangle$ from the SHG spectra show dependencies on the applied potential (see Fig. 9.2). To the author's knowledge, such a spectral shift has not yet been detected in a potential-resolved SHG measurement. However, the total observed shift of $\langle \mathcal{E}_{2\omega} \rangle$ is less than 0.01 eV with a very small effect compared to $I_{2\omega}$ so that a reliable interpretation within the limited SHG spectral range of 0.2 eV seems speculative at this point. Hence, a discussion of possible origins and effects to the potential dependent shift of $\langle \mathcal{E}_{2\omega} \rangle$ is presented in Chapter 14 and the following argumentations will focus on the α-Fe_2O_3 photoanode

SCR under OER conditions concerning the most obvious and established parameter of the SH response – the potential dependent SHG intensity $I_{2\omega}$.[79, 81, 120, 142]

9.2 Field enhancement

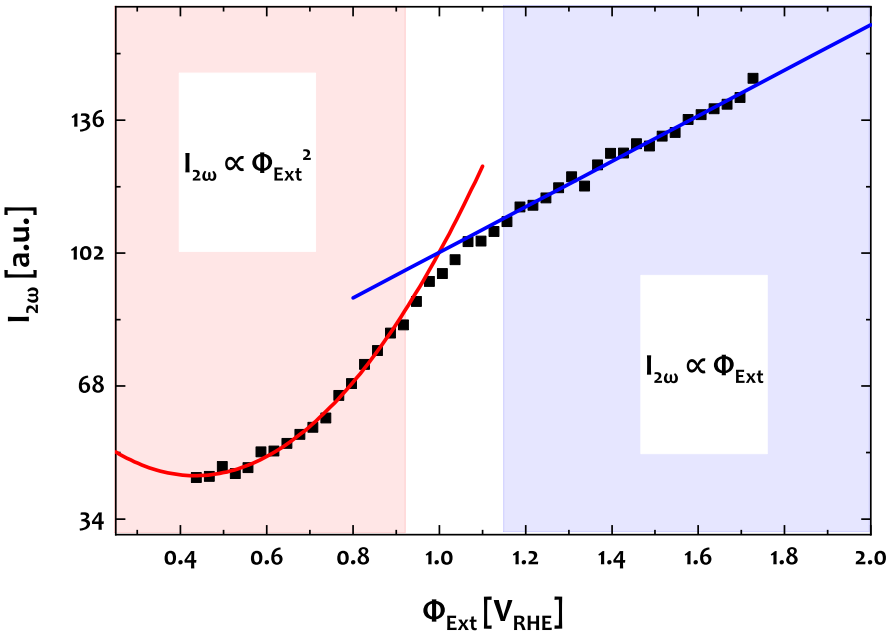

Figure 9.3: SHG intensity $I_{2\omega}$ as function of the applied potential Φ_{Ext} without electrode illumination. A parabolic potential dependence fits the intensity at lower potentials whereas more anodic conditions can be numerically represented by a linear slope [79, 81]

A first functional survey on the potential dependent SHG intensity $I_{2\omega}$ is shown in Fig. 9.3. We can see that $I_{2\omega}$ responds to an externally applied potential Φ_{Ext} in a quadratic dependence, with a parabolic minimum at 0.43 V_{RHE}. At higher potentials above 1.0 V_{RHE} the parabolic dependence changes towards a slope of lower order (see Section 3.2.2), which can be fit by linear model. The parabolic potential dependence of $I_{2\omega}$ suggests that the EFISH theory is fulfilled - at least in the lower potential range between 0.4 V_{RHE} to 0.9 V_{RHE} according to Eq. 13.2, so that $I_{2\omega}$ scales with the squared DC-Potential drop over the electrode (see Section 3.2.2).[149, 200, 224]

$$I_{2\omega} = \mathbf{E}_{2\omega}{}^2 \propto \mathbf{P}_{2\omega}^{(3)}{}^2 \propto \Phi_{\mathrm{DC}}{}^2 \tag{9.3}$$

A linear potential dependence as apparent at elevated electrode potentials in Fig. 9.3 has also been reported for comparable photoelectrode/electrolyte systems in particular for TiO_2[79, 80, 137] and n-Si [81] single crystals in contact with ionic electrolytes. In both studies, the transition from quadratic potential dependence is referred to a constraint probing depth as the measured SHG signal photon energies is situated way above the optical bandgaps of the materials.[79, 81] A quantitative description of the linear potential dependence is referred to the inverse quadratic relation between the static field $\mathbf{E}_{\mathrm{DC}}$ and the space charge Q_{SC} according to Eq. 13.7.[79, 81]

$$I_{2\omega} \propto |\mathbf{E}_{\mathrm{DC}}|^2 \propto Q_{\mathrm{SC}}{}^2 \propto \Phi_{\mathrm{SC}} \tag{9.4}$$

Thus, a quadratic potential dependence is usually associated with DC-contribution to the third order polarization forming the SH field $\mathbf{E}_{2\omega}$,[142, 144, 200] whereas a linear potential dependence is explained by a static electric field that directly contributes to the emitted SH signal. However, it should be noted that the Mott-Schottky approximation in Eq. 13.7 to describe the static potential is only fulfilled when the SHG probing depth samples the entire space charge width. If only a narrow top-layer is sampled in the SHG experiment, the relation $Q_{\mathrm{SC}}{}^2 \propto \Phi_{\mathrm{SC}}$ is not provided. Instead, all donor atoms in the top region are fully ionized so that $Q_{\mathrm{SC}} = const$ as the probed space charge region remains independent of any further electrode bias (see also Section 2.3).
Note that in both cases, linear and parabolic potential dependence of the SHG intensity, a minimum of the SHG intensity $I_{2\omega}$ indicates a minimum of the static field at the interface. Thus, for a third order a DC-contribution from the potential drop over the α-Fe_2O_3 electrode layer, the vertex of the parabola in Fig. 9.3 indicates the flat-band potential φ_{FB} according to Eq. 9.5 (see also Eq. 3.18).[79, 81]

$$\left.\frac{\mathrm{d}I_{2\omega}}{\mathrm{d}\Phi_{\mathrm{DC}}}\right|_{\Phi_{\mathrm{Ext}}=\varphi_{\mathrm{FB}}} = 0 \tag{9.5}$$

In order to evaluate a functional expression for the quadratic part of the potential dependent SHG response, we need to compare both terms in Eq. 3.18 with the measured data. The generic formulation of the electric field induced second harmonic (EFISH) effect in terms of second and third order non-linear susceptibilities is given in Eq. 9.6, where the DC potential drop Φ_{DC} in Eq. 3.18 is expressed by the difference between the external and the flat-band potential $\Phi_{\mathrm{Ext}} - \varphi_{\mathrm{FB}}$.[119, 144]

$$I_{2\omega} \propto \left| \left(\chi^{(2)}\right)^2 \pm 2 * \chi^{(2)}\chi^{(3)}(\Phi_{\mathrm{Ext}} - \varphi_{\mathrm{FB}}) + \left(\chi^{(3)} * (\Phi_{\mathrm{Ext}} - \varphi_{\mathrm{FB}})\right)^2 \right| * {I_\omega}^2 \qquad 9.6$$

From Eq. 9.6 we find that the potential dependence of the SH signal could in principle stem from the cross-term component between second and third order responses $2 * \chi^{(2)}\chi^{(3)} * (\Phi_{\mathrm{Ext}} - \varphi_{\mathrm{FB}})$, from a purely third order effect $\left(\chi^{(3)} * (\Phi_{\mathrm{Ext}} - \varphi_{\mathrm{FB}})\right)^2$ or a combination of both, while a solitary contribution from the cross-term seems quite unlikely as it would cause a purely linear potential dependent SHG response which is not reflected by the datasets.

A pragmatic approach to distinguish between both contributions is to numerically fit the dataset to the model in Eq. 9.6, where the cross-term is included and neglected. The results are presented in Fig. 9.4, where the dataset of the quadratic part between 0.4 V_{RHE} and 0.9 V_{RHE} is numerically analysed regarding the presence and absence of the cross-term contribution in Eq. 9.6. We see the potential dependent SHG intensity from the α-Fe_2O_3 photoanode without illumination as already shown in Fig. 9.3, Fig. 9.1 and Fig. 7.3, where Eq. 9.6 is fit to the dataset for two different cases – with and without a non-zero contribution from the cross-term. Fig. 9.4 shows that the potential dependence of the SHG response can be well represented by purely a third order contribution $I_{2\omega} \propto \chi^{(3)}(\Phi_{\mathrm{Ext}} - \varphi_{\mathrm{FB}})^2$, whereas an involvement of the second and third order cross-term $2 * \chi^{(2)}\chi^{(3)}(\Phi_{\mathrm{Ext}} - \varphi_{\mathrm{FB}})$ shows much less correlation with the measured data. Statistic reports of the numerical fits in Fig. 9.4 are appended in Fig. XIV(a) and Fig. XIV(b), respectively.

This analysis suggests that the cross-contribution from second and third order susceptibilities can be neglected in the measurements conducted here, i.e. $\chi^{(2)}\chi^{(3)} = 0$, a quite common statement in the analysis of third order effects to potential dependent SHG spectroscopy.[79, 81, 125, 142] With this, we can describe the potential dependent SHG response as a parabolic function with a vertex at flat-band conditions according to Eq. 9.7.

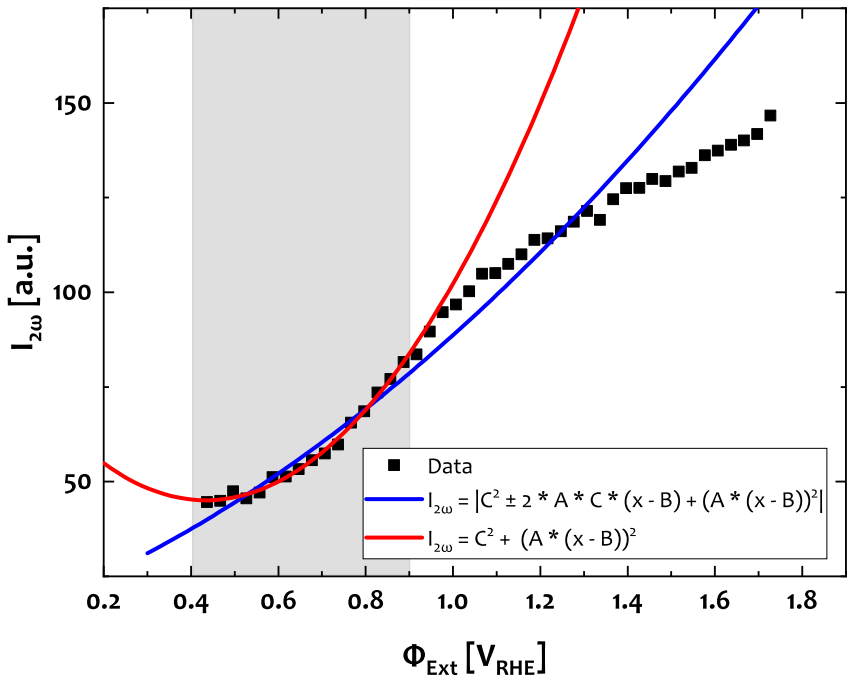

Figure 9.4: Numerical fits of SHG intensity $I_{2\omega}$ as function of the applied potential Φ_{Ext} to a purely quadratic and a polynomic model in order to identify contributions from second and third order susceptibilities

$$\boxed{I_{2\omega} = A * \left(\Phi_{\mathrm{Ext}} - \varphi_{\mathrm{FB}}\right)^2 + C} \qquad 9.7$$

This expression will be used to derive the space charge potential drop into the electrode as function of the external bias. Later on, we will compare various electrochemical, microscopic and diffractive methods and find that the space charge width as probed by SHG is in fact spatially constraint in cases of linear potential dependence. However, a quantitative explanation of this effect may rather not be provided by the Mott-Schottky approximation but more likely by a dielectric polarization of the entirely depleted semiconductor material. It will be argued that this effect experimentally resembles the conditions of a limited probing depth that only covers the completely depleted top layer of the semiconductor photoelectrode (see Chapter 10 and Section 13.1).

Eq. 9.7 provides a common model to describe the SHG response as function of the external bias potential that has been applied to a range of solid-solid and solid-liquid

interfaces. [125, 142, 144] Eq. 9.7 was also applied to the SH response from absorptive single crystal TiO_2 and n-Si semiconductor electrodes.[79, 81] In these studies, a linear potential dependence was observed and referred to limited SHG probing depths. In contrast, the experiments presented were conducted at a nano-porous α-Fe_2O_3 thin film of 200 nm thickness and evaluated regarding the absorption properties of the sample. As shown in Section 7.2, both, the NIR fundamental beam penetration and the SHG escape depths of 10 µm and 330 nm are significantly exceeding the film thickness of 200 nm, so that no limitation of the probing depth is expected for the electrode without illumination. A further argument for the unhindered SHG probing depth is presented in the following section, where the SHG response follows the electrode potential over the entire range, thus also indicating an unrestricted probing mechanism as opposed to [79] and [81], for instance.

9.3 Photovoltage and photocurrent

In order to further evaluate the capability of potential dependent SHG measurements for a description of space charge processes at the electrode interface, we want to see how the potential dependent SHG response is altered when the sample is illuminated with a monochromatic 450 nm CW light source.
Fig. 9.5 shows the SHG response for the α-Fe_2O_3 photoanode in the dark and under illumination and the corresponding cell currents, both as function of the externally applied potential Φ_{Ext}. The current-voltage (IV) characteristics are just as expected for a semiconductor photoanode – a significant OER current only flows in the dark at potentials beyond 1.6 V_{RHE}, when a sufficiently large overpotential of 0.4 V is imposed to the electrode. The IV curve under illumination shows a photocurrent with an onset at 0.6 V_{RHE} which is the common behaviour of a functional photoanode system as described in a previous chapter (see Section 5.3).[26, 42]
In the lower panel of Fig. 9.5, we see the corresponding SHG intensity from the electrode interface $I_{2\omega}$ as function of the applied potential Φ_{Ext}. In contrast to the IV characteristics, there is no significant difference between the electrode in the dark and under illumination. While the SHG response from the illuminated electrode might be slightly increased by a constant offset, the curvature and vertex of the parabolic part remain unchanged.
At first glance, these mostly unaltered characteristics might seem contradicting as a clear lowering of the SHG response was observed upon electrode illumination in

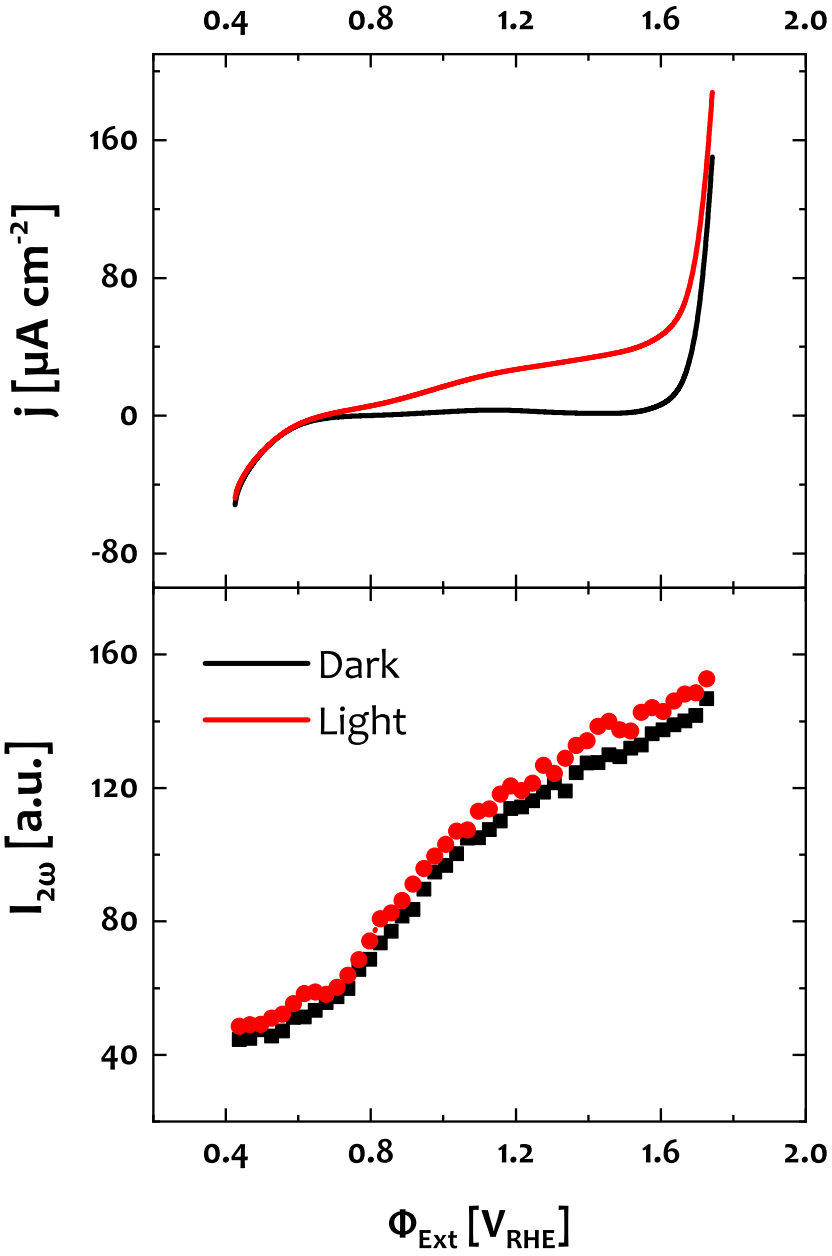

Figure 9.5: Photoresponse under amperometric conditions. SHG intensity $I_{2\omega}$ in the dark and under illumination with corresponding cell current j as function of the externally applied potential Φ_{Ext}

Fig. 7.2. However, there is one fundamental difference in the experimental framework of these two measurements in Fig. 7.2 and Fig. 9.5. The SHG spectra in Fig. 7.2 were

measured under OCV conditions, i.e. when a current of zero is applied to the electrode and the potential is left floating, which resulted in a change of the open circuit voltage (OCV) from $0.89\,V_{RHE}$ in the dark to $0.67\,V_{RHE}$ under illumination (see Section 7.1). In Fig. 9.5, on the other hand, an external potential is imposed to the electrode while the measured current is the dependent variable. Both experiments correspond to two different electrochemical setups: Fig. 9.5 shows an amperometric configuration, whereas Fig. 7.2 is measured in a potentiometric configuration, where a current is applied and the measured potential is left floating.

Consequently, in the next step we want to switch the dependency of the parameters from Fig. 9.5 and to conduct a potentiometric experiment, impose a current to the electrode and measure the corresponding SHG response and the floating potential. The results are shown in Fig. 9.6. In the upper panel, we see the measured electrode potential as function of the imposed current. This electrochemical data essentially reproduces the amperometric experiment in Fig. 9.5, just with exchanged axes. The lower panel shows the corresponding SHG response $I_{2\omega}$ also as function of the imposed current. In this potentiometric configuration, the SHG response agrees very well with the measured electrode potential for both cases, in the dark and under illumination. This shows a photo-induced band flattening, i.e. a decrease of Φ_{SC}, which is only enabled for a floating electrode potential.[137]
The most obvious conclusion of the experiment in Fig. 9.6 is that the SHG signal formation follows the electrode bias over the entire potential range from $0.4\,V_{RHE}$ to $1.7\,V_{RHE}$. This implies that the measured SHG intensity is not limited by light absorption as was shown to limit the SHG probing depth in other approaches [79, 81]. Therefore, the potential resolved SHG measurements provide a meaningful probe for the field distribution across the entire α-Fe_2O_3 electrode, instead of an absorption limited top layer (see also Section 13.1). A comparison between $I_{2\omega}$ and Φ_{Ext} for both EC configurations is appended in Fig. XI, where both potentiometric and amperometric SHG response are projected onto the potential axis in the dark and under illumination. It confirms the close relationship between $I_{2\omega}$ and Φ_{Ext}, as the shape of the $I_{2\omega}(\Phi_{\mathrm{Ext}})$ is preserved over both modes of the current-voltage measurement. This furthermore confirms the parabolic relationship between the SHG response and electrode surface band-bending as developed in Section 9.1 and Section 3.2.2.

We can qualitatively explain the observations from Fig. 9.6 and Fig. 9.5 with the concept of quasi-Fermi-levels (see also Section 2.5).[26] In order to account for changes of

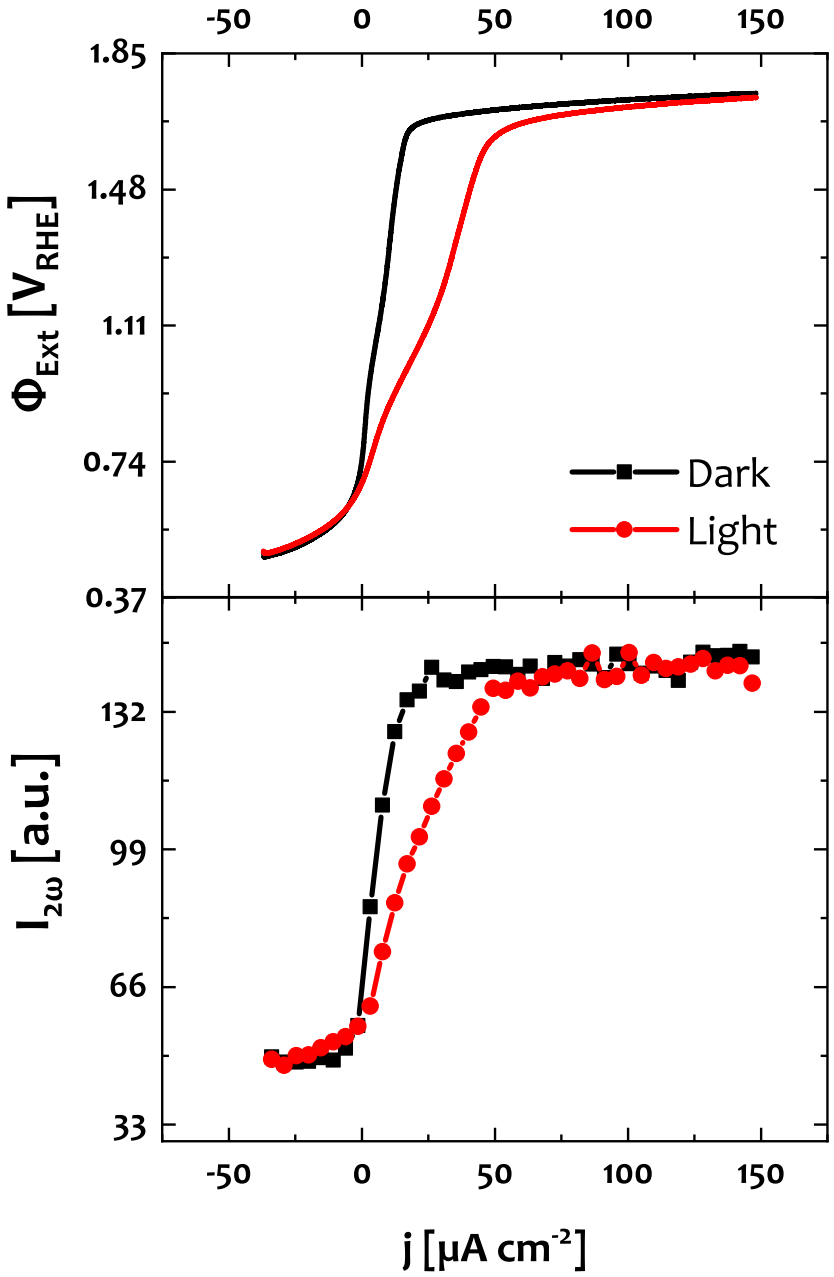

Figure 9.6: Photoresponse under potentiometric conditions. SHG intensity $I_{2\omega}$ in the dark and under illumination with corresponding potential Φ_{Ext} as function of the externally imposed current j

charge carrier energetic distributions from electrode illumination, one has conceived two different FERMI-levels, i.e. one for excited electrons $E^*_{\mathrm{F,n}}$ and one for holes $E^*_{\mathrm{F,h}}$.[26, 33] In this picture, the initial concentrations of electrons n_0 and holes p_0 in the dark would be offset under illumination by a term Δn and Δp, respectively. The carrier concentrations n and p under illumination are then given by Eq. 9.8 and Eq. 9.9, where N_C and N_V are the DOS in the conduction and valence band, respectively, k_B is the BOLTZMANN constant and T the absolute temperature.

$$n = n_0 + \Delta n = N_\mathrm{C} \exp\left\{\frac{-(E_\mathrm{C} - E^*_{\mathrm{F,n}})}{k_\mathrm{B}T}\right\} \tag{9.8}$$

$$p = p_0 + \Delta p = N_\mathrm{V} \exp\left\{\frac{-(E^*_{\mathrm{F,n}} - E_\mathrm{V})}{k_\mathrm{B}T}\right\} \tag{9.9}$$

For an n-type semiconductor there is an excess of electrons so that $n \approx n_0$ and $p \approx \Delta p$.[26, 33] At this point we can not gather quantitative information since n and N_C are unknown in Eq. 9.8, for instance. However, it is possible to qualitatively explain the SHG response under fixed and floating electrode potential with this model.

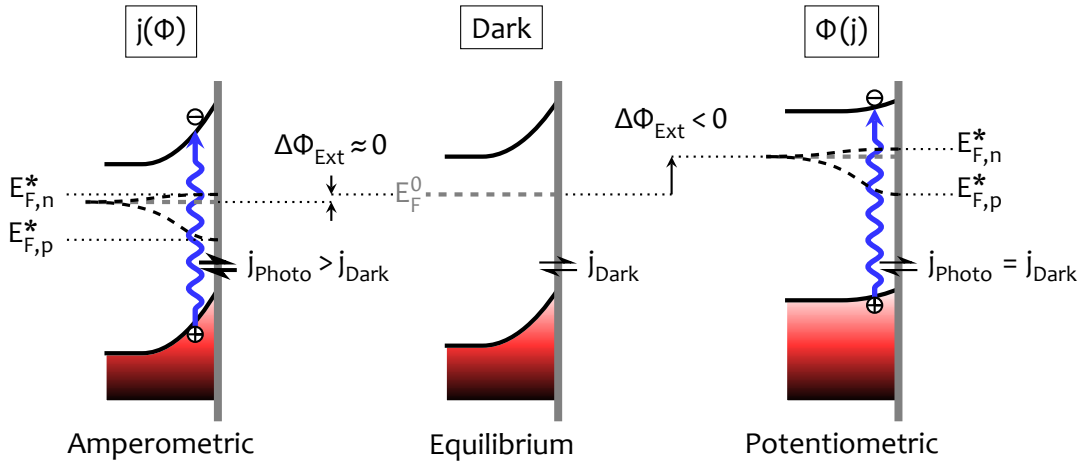

Figure 9.7: Photoresponse of an n-type semiconductor photoanode and formation of quasi-FERMI-levels within the SCR in different EC configurations. Photocurrent and -voltage under amperometric and potentiometric conditions, respectively [26]

The difference between sample illumination under both EC regimes is schematically illustrated in the energy diagrams in Fig. 9.7. In the centre of Fig. 9.7 we see the

semiconductor photoanode in the dark, i.e. in carrier distribution equilibrium and with a corresponding Fermi-Level E_{F}^{0}. In both the right and left-hand sides, the electrode is illuminated with photon energies above the band-gap of the material. This photonic carrier excitation generates electron-hole pairs which leads to the formation of quasi-Fermi-levels. The difference between illumination under amperometric and potentiometric conditions is illustrated in the left and right-hand sides of Fig. 9.7, respectively.

In an amperometric measurement, as presented in the left-hand side of Fig. 9.5, the external potential Φ_{Ext} is the independent variable and fixed with respect to a reference electrode. In this case the carrier excitation can not lead to a change of the electrode potential and the system can only compensate incident power by the formation of a photocurrent. Therefore, no changes from electrode illumination to the SHG response and thus to the SCR band bending are observed as apparent in Fig. 9.5. In this configuration, the excess excitational energy is solely compensated by the formation of a photocurrent j_{Photo}, while the electrode potential remains fixed.

It is worth mentioning that Fig. 9.5 might suggest that there is a slight increase of the SHG response under these conditions. This could be reflected by a small difference between E_{F}^{0} and $E_{\mathrm{F,n}}^{*}$ as illustrated in the left-hand panel of Fig. 9.7. A comparison between three different illumination intensities is appended in Fig. XII. However, aside from a further validation of the measurements, a significant difference between E_{F}^{0} and $E_{\mathrm{F,n}}^{*}$ can neither be confirmed nor eliminated at this point.

In the right-hand side of Fig. 9.7, we see the current-voltage behaviour under a potentiometric regime. In this configuration a current is externally imposed to the illuminated electrode and the floating electrode potential necessary to drive this current is independent. Since j is externally imposed, the electrode system can only respond to illumination with a significant flattening of the bands in order to maintain the same imposed current in the dark and under illumination. As the SHG senses the SCR potential drop, the flattening is also reflected by the SHG intensity.[26, 79]

This explanation demonstrates the interplay between photovoltage and photocurrent. An externally fixed electrode potential prevents significant changes of the band bending and forces the compensation of excited excess carriers by a photocurrent – which can not be tracked by EFISH spectroscopy. A floating electrode potential, on the other hand, allows for changes of Φ_{SC} that is visible in both the electrode potential Φ_{Ext} and the SHG response $I_{2\omega}$.

It might be worth noting that quasi-Fermi-levels are typically not constant along the

z-axis . Due to the systemically inherent absorption of the incident light, the amount of photo-excited carriers decreases with distance from the electrode surface into the bulk – as long as Lambert-Beer conditions are provided, which might not necessarily the case in presence the huge incident power densities from a focused light exposure as employed for the SHG experiments presented here (see also Section 7.2).[202, 203] Therefore, a serious discussion of the spatial distribution of quasi-Fermi-levels seems elusive at this point as the close correspondence between SHG measurement and electrode potential is experimentally obvious in Fig. 9.6.
It should also be noted that the works by Lantz et al. have also shown an investigation of the EFISH photoresponse of a TiO_2 electrode.[79, 80, 137] While these works showed a flattening of the bands under electrode illumination as well, the measurements were carried out under amperometric conditions – which did not show a significant effect on the SHG response in Fig. 9.5. However, the works at hand have paid particular attention to exclude possible contributions from the substrate or electrolyte so that one may tentatively put more credibility to the findings presented here.

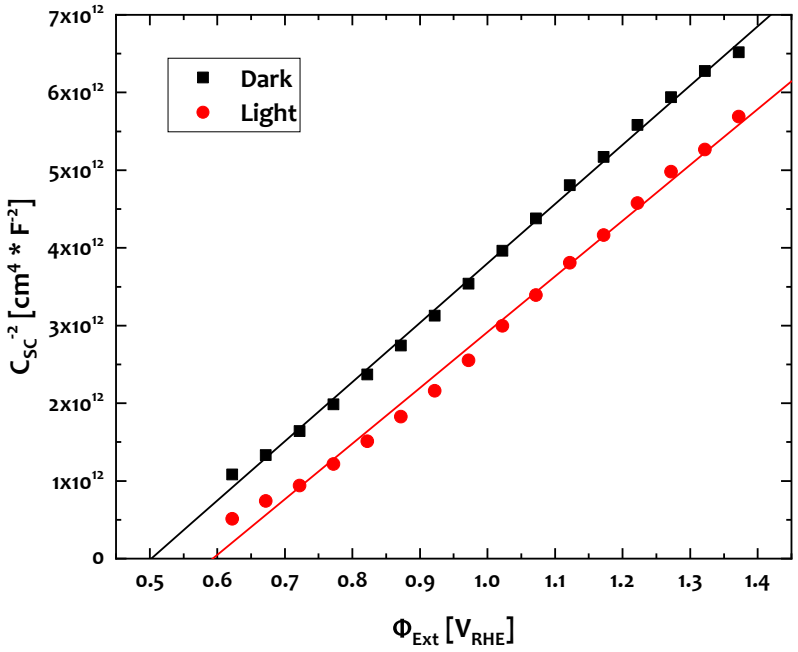

Figure 9.8: Mott-Schottky-plots of the α-Fe_2O_3 photoanode in the dark and under illumination

As we experimentally observed the dualism between photovoltage and photocurrent, we want to see how these are reflected by other techniques. Fig. 9.8 shows Mott-Schottky plots of the α-Fe_2O_3 electrode in the dark and under illumination, where the space charge capacitance was obtained from a plain RC-element as will be further explained in Section 10.1.2. The electrode illumination is the same as in the measurements shown in Fig. 9.5 and Fig. 9.6. Both Mott-Schottky curves show a quite similar linear slope, while the flat-band potential φ_{FB} is anodically shifted under illumination by an offset of 90 mV. Even though most EIS studies have particularly focused on the irradiated α-Fe_2O_3 photoanode,[63, 77, 91, 160] Klahr et al. have also observed an anodic shift of φ_{FB} upon electrode illumination.[65]

Method	φ_{FB}^{Dark}	φ_{FB}^{Light}
	[V_{RHE}]	
EIS	0.48	0.57
SHG	0.43	0.43

Table 9.1: Comparison between flat-band potentials φ_{FB} of the electrode in the dark and under illumination obtained from EIS and SHG measurements

An alternative way to determine φ_{FB} are EFISH measurements as introduced in Section 3.2 and Section 3.2.2 where the electrode potential at minimum SHG response is shown to directly reflect φ_{FB}.[79, 81] A comparison between measured values of φ_{FB} obtained from SHG and EIS is shown in Tab. 9.1, corresponding fits of the SHG curves are appended in Fig. XIII. We see that the anodic shift of φ_{FB} for the irradiated electrode is only observed in the impedance measurements, i.e. where the cell current is probed. EFISH spectroscopy as an external optical probe, instead, is fully independent of any charge transfer and accumulation processes and shows no significant difference between the dark and irradiated electrode. This observation indicates that the solitary examination of electrode current-voltage characteristics might yield somewhat ambiguous results as the cell current can be obscured by a range of effects, or, more generally spoken, because charge and voltage are recursively dependent. As for instance, the charge transfer and accumulation pathways can differ in the dark and under illumination. The SHG response, on the other hand, is completely decoupled from the cell current and therefore provides a highly specific probe for electrostatic characteristics and processes, as it solitarily reflects the integral electric field across the α-Fe_2O_3 electrode interface.

In this section, we have found a strong experimental indication for the agreement between the SHG response and the space charge potential drop as band flattening upon electrode illumination is only visible to the affecting SHG intensity when rearrangement of band bending is provided. This relation holds over the entire bias potential range so that the SHG probing mechanism appears unhindered by light absorption. The good agreement in between electrode potential and SHG response in Fig. 9.6 indicates a close correspondence between SH intensity and electrode band bending. Therefore, as the shape of the $I_{2\omega}(\Phi_{\mathrm{Ext}})$ curves is also resembled by the electrode potential, the transition from a quadratic to a linear potential dependence would rather correspond to an electronic material property instead of a limited SHG probing depth, so that we now want to investigate further charging effects in order to assess possible origins of the split potential dependence of the SHG response the following chapters.

10 Space charge evolution

So far, we found that the magnitude of the potential dependent SHG response $I_{2\omega}$ shows a parabolic dependence on the applied potential: $I_{2\omega} \propto {\Phi_{\mathrm{Ext}}}^2$, which is referred within the EFISH framework to a third order enhancement of the emitted SHG field doe from the static field across the electrode. Next, we want to see how this relation can be applied to electronic properties and processes at the operating α-Fe_2O_3 electrode system.

10.1 Band bending at the α-Fe_2O_3 photoanode surface

10.1.1 EFISH analysis

As discussed Section 9.1, we found that a minimum of the $I_{2\omega}$ response can be explained by zero DC filed contribution to the SH signal. In case of a semiconductor space charge potential drop, this minimum indicates zero band bending $\Phi_{\mathrm{SC}} = 0$, thus the flat-band potential φ_{FB}. This is a quite common conclusion from EFISH measurements on semiconductor interfaces.[79, 81] Consequently, we can infer φ_{FB} from the vertex of the parabolic part of the potential dependent SHG measurements. A quadratic fit of the SHG response $I_{2\omega}(\Phi_{\mathrm{ext}})$ will therefore deliver φ_{FB} according to Eq. 10.1, where the coefficients A and B correspond to the quadratic slope and an offset of the $I_{2\omega}(\Phi_{\mathrm{ext}})$ parabolic curves respectively. A numerical justification of this assumption was developed in Section 9.1.

$$I_{2\omega}(\Phi_{\mathrm{ext}}) = A * (\Phi_{\mathrm{ext}} - \varphi_{\mathrm{FB}})^2 + B \tag{10.1}$$

A fit of $I_{2\omega}$ as function of Φ_{Ext} is shown in Fig. 10.1. It reveals a flat-band potential of $\varphi_{\mathrm{FB}} = 0.43\,\mathrm{V_{RHE}}$, while the transition from quadratic to linear potential dependence at $1.0\,\mathrm{V_{RHE}}$h as not been explained, yet.
In Section 9.1 we found that the integrated SHG response is proportional to the

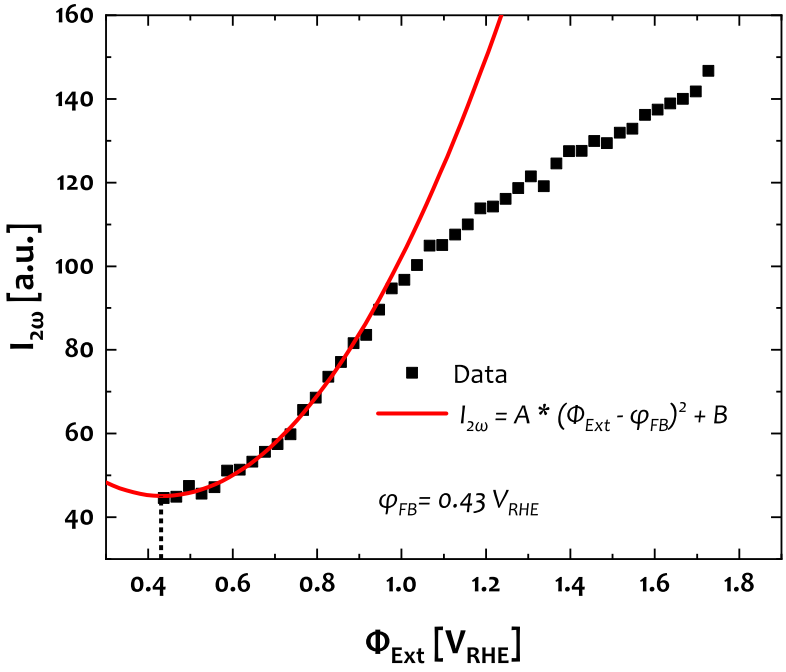

Figure 10.1: Parabolic fit of SHG intensity $I_{2\omega}$ as function of the externally applied potential Φ_{Ext} to extract the flat-band potential φ_{FB}

squared potential drop across the α-Fe_2O_3 electrode Φ_{DC}. This relationship was validated over the entire potential range in good agreement with the potovoltage measurements as shown in Section 9.3. Contributions from other effects in the sample system can be neglected as discussed in Chapter 7 so that we assume that interference effects and limitations of the optical penetration and escape depths are not significantly affecting the SHG response. Consequently, we can suppose that the linear part of the potential dependent SHG response does not arise from changes of the probing mechanism. This implies that the deflection of the $I_{2\omega}(\Phi_{\mathrm{Ext}})$ curves at 1.0 V_{RHE} rather indicates a physical change of the sample system than a changing probing mechanism. Therefore, we need to find an appropriate physical explanation for the loss of band-bending when the external bias exceeds 1.0 V_{RHE}.

As a starting point, we want to suppose that i) under slight depletion conditions, below 0.9 V_{RHE}, Φ_{Ext} falls entirely across the SCR of the electrode surface, whereas ii) at potentials beyond 1.2 V_{RHE}, Φ_{Ext} is distributed between Φ_{SC} and another compartment of the electrode system. We can support this assumption considering that the material is moderately doped (see Section 10.1.2) whereas the electrolyte is con-

centrated, so that the capacitance of the SCR is much smaller than the Helmholtz capacitance (see Section 3.3.1 and Fig. 3.5).[26] We also see a perfect quadratic dependence, which indicates that the EFISH theory is fulfilled in this lower potential range. Therefore, we can state that $\Delta\Phi_{\mathrm{SC}} = \Delta\Phi_{\mathrm{Ext}}$ under gentle depletion conditions. This one-to-one correspondence allows us to calibrate the SHG intensity with the band-bending and to determine the more general static field contribution across the electrode Φ_{DC} from the quadratic part of the $I_{2\omega}(\Phi_{\mathrm{Ext}})$ curves in Eq. 10.1 according to Eq. 10.2.

$$\Phi_{\mathrm{DC}}(\Phi_{\mathrm{Ext}}) = \sqrt{\frac{I_{2\omega}(\Phi_{\mathrm{Ext}}) - B}{A}} \tag{10.2}$$

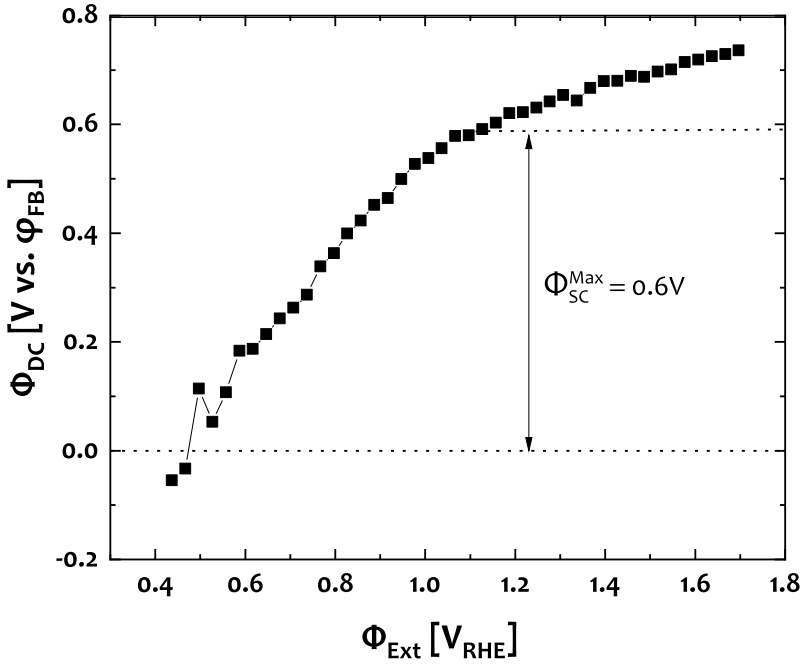

Figure 10.2: Band-bending at the α-Fe_2O_3 electrode surface as function of external bias, revealed by EFISH spectroscopy, and deflection point of the band-bending $\Phi_{\mathrm{SC}}^{\mathrm{Max}}$

Fig. 10.2 shows a plot of Φ_{DC} as function of Φ_{Ext} as derived from Eq. 10.2. Based on the previous assumptions, we now are able to monitor the band-bending at the electrode surface as function of the external bias. It is also shown that the direct

correspondence decays beyond a potential drop of $\Phi_{SC}^{Max} = 0.6\,V$.
To the author's knowledge, this is the first direct representation of the bias dependent electrode polarization of an operating water spitting α-Fe_2O_3 photoanode interface which was derived from first principles on an optical probe of the static electric field at the electrode surface. These findings might point a path to address some persisting ambiguities on the field distribution at the α-Fe_2O_3/electrolyte interface and further semiconductor electrode systems.[55, 76, 77] However, since most reports on the SCR are based on EIS measurements, we also want to consider this technique and see how it compares to our EFISH results.

10.1.2 MOTT-SCHOTTKY analysis

As an optical probe is established to follow the band-bending at the electrode surface, it would be beneficial to also conduct a MOTT-SCHOTTKY analysis of the sample system in order to compare the results between those two complementary approaches. Impedance spectra were taken in the same cell and under the same conditions as the SHG measurements which might lead to some experimental differences compared to conventional EIS studies reported so far.[63, 65, 225]
The most common way to determine the flat-band potential φ_{FB} of semiconductor electrodes is electrochemical impedance spectroscopy (EIS), a model-based method that is typically biased by a range of presumptions, often in terms of an electric equivalent circuit of the electrode system.[63, 65, 76] Results from EIS measurements vary a lot in literature, e.g. reported values of φ_{FB} for α-Fe_2O_3 photoanodes in alkaline media range from $0.12\,V_{RHE}$ to $0.96\,V_{RHE}$.[77] Besides a somewhat ambiguous extraction of φ_{FB} from impedance data,[76] the variation of φ_{FB} may also be due to differing parameters of the sample system such as doping and carrier concentration,[77] nanoscopic morphology [160] or electrolyte composition or any further deviations from the idealized MOTT-SCHOTTKY-like behaviour.[65, 160, 226–228]
Such effects are difficult to separate from the electrochemical response of the electrode system so that a determination of φ_{FB} from EIS remains ambiguous.[76] In contrast to the electrochemical approach, EFISH spectroscopy is based on a self-contained optical probe and directly related to the integral electric field at the electrode surface. The values we obtain for φ_{FB} are well within the range of reported values so that we can tentatively put more reliability on the SHG measurements shown here over those obtained from EIS studies.
Fig. VIII in the appendix shows NYQUIST plots of the α-Fe_2O_3 photoanode complex

impedance frequency response in the cell system that was also utilized during the in situ SHG measurements. These plots show a strongly capacitive behaviour under non-Faradaic conditions, so that we want to abstain from a fit of an equivalent circuit to this dataset and conduct an analysis based on different capacitive contributions across the electrode system (see Section 3.3.1).

$$C_{\mathrm{Eff}} = \frac{1}{-Z_{\mathrm{Im}}\, 2\pi\, f} \quad . \tag{10.3}$$

Following this approach, we want to directly calculate an effective capacitance C_{Eff} from the imaginary part of the complex impedance Z_{Im} and the perturbation frequency f according to Eq. 10.3 (see also Section 3.3).[75, 160, 225] Bode plots of the impedance spectra are appended in Fig. IX. These curves show a pronounced potential dependence of the phase shift at perturbation frequencies between 180 Hz and 1800 Hz and the typical shape of an RC-series circuit up to potentials of 1.4 V_{RHE}. Therefore, it is reasonable to directly utilize this phase shift for a Mott-Schottky analysis (see Section 3.3.3).

$$\frac{1}{{C_{\mathrm{SC}}}^2} = \frac{1}{\epsilon_0 \epsilon_{\mathrm{r}} e_0 {S_{\mathrm{Act}}}^2 N_{\mathrm{D}}} \left(\Phi_{\mathrm{Ext}} - \varphi_{\mathrm{FB}} - \frac{k_{\mathrm{B}} T}{e_0} \right) \tag{10.4}$$

The SCR analysis is based on the Mott-Schottky equation,Eq. 10.4 [85, 229] with the density of donor atoms per volume N_{D}, the absolute and relative permittivities ϵ_0 and ϵ_{r}, respectively, the elementary charge e_0, the electrochemically active electrode surface S_{Act}, the applied potential Φ_{Ext}, the flat-band potential φ_{FB}, the Boltzmann constant k_{B} and the absolute temperature T (see also Section 2.3). According to Eq. 10.4, a plot of ${C_{\mathrm{SC}}}^{-2}$ over Φ_{Ext} should produce a linear curve that intersects the potential axis at $\Phi_{\mathrm{Ext}} = \varphi_{\mathrm{FB}} - k_{\mathrm{B}} T / e_0$. The slope of the curve provides information on the type and concentration of dopants in the semiconductor material.[26, 33, 40] Mott-Schottky plots for C_{Eff} obtained via Eq. 10.3 from five different perturbation frequencies are shown in the appendix in Fig. X(a), a linear regression was performed over a potential range from 0.82 V_{RHE} to 1.43 V_{RHE}. We see that all graphs are shaped linearly, that the slope slightly increases with increasing perturbation frequencies f and that φ_{FB} is varying by less than 0.1 V_{RHE}. Even though the graphs exhibit some frequency dispersion,[164, 227] we find an excellent linear slope of the Mott-Schott-

KY-plots and suppose that $C_{\mathrm{Eff}} \approx C_{\mathrm{SC}}$. Therefore, this approach provides meaningful information on the donor density of the material N_{D} and the flat band potential φ_{FB}. The determination of the donor density and flat-band potential was taken from the average of the fit parameters appended in Fig. X(b).

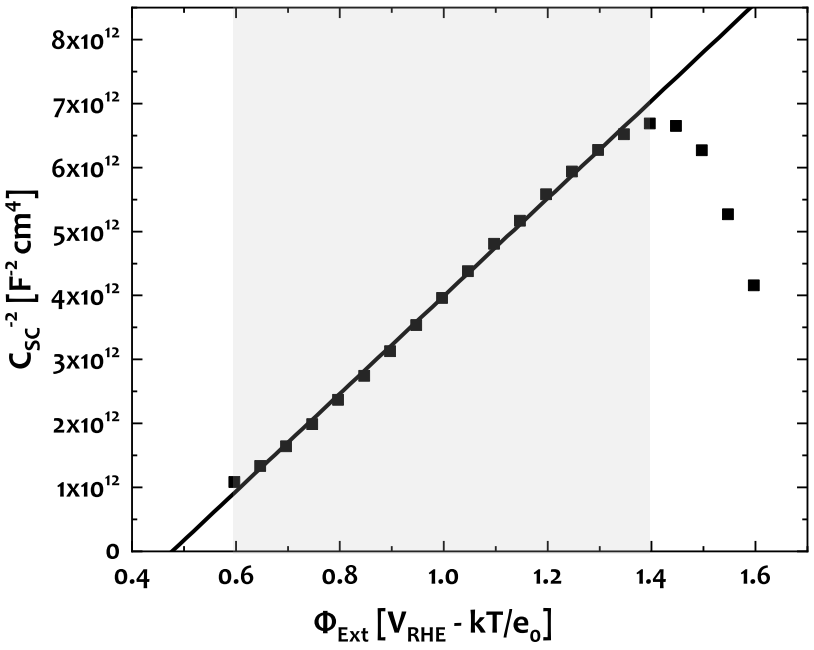

Figure 10.3: MOTT-SCHOTTKY-Plot of the operating α-Fe_2O_3 photoanode in 1 M KOH without sample illumination

The MOTT-SCHOTTKY plot is shown in Fig. 10.3. We see a linear shape over a large potential range between 0.6 V_{RHE} and 1.4 V_{RHE} suggesting that the MOTT-SCHOTTKY approximation is fulfilled over the potential range and that the applied bias can be well described by a carrier depletion of the n-type semiconductor electrode.
A survey of the two fit parameters in the MOTT-SCHOTTKY plots from Fig. 10.3 is shown in Tab. 10.1. The values for flat-band potentials φ_{FB} and donor densities N_{D} were obtained from Eq. 10.4 using a relative permittivity e_{r} = 25.[26, 230, 231] The corresponding MOTT-SCHOTTKY-Curve is shown in Fig. 10.3. The density of ionized donor atoms, N_{D}, obtained by MOTT-SCHOTTKY analysis, is (7.7 ± 1.8) × 10^{17} cm^{-3}.
A comparison between the values of N_{D} and φ_{FB} with literature is shown in Tab. 10.1. We see that the values for N_{D} of several undoped α-Fe_2O_3 photoanode systems are comparable with the presented data which verifies the experimental results.[63, 65,

Study	Method	N_D [10^{17} cm^{-3}]	φ_{FB} [V_{RHE}]
This work	SHG	–	0.43
	EIS	7.7	0.47
Klahr et al.[65]	EIS	49	0.8
Monllor-Satoca et al.[63]		4.3	0.71
Cesar et al.[160]		0.1 to 1	–

Table 10.1: Comparison of SCR characteristics donor density N_D and flat-band potential φ_{FB} between different measurements and with literature values

160] The donor density from Klahr et at.[65] is about one order of magnitude larger, which is likely due to the omission of an electrochemically active electrode surface correction which was taken into account here (see Section 7.2) and also in [63] and [160].

There is a range of further methods available to determine flat-band potentials, in particular the optical reflectance phase inversion, so called electrolyte electroreflectance (EER),[161, 232, 233] EIS and photocurrent onset or OCV measurements, for instance.[26, 77, 234] Each of these probes has their own peculiarities so that a confirmation between two different methods is always recommended for an accurate determination of the flat-band potential.[234] A measurement of φ_{FB} probing the cell current is often obscured by a range of charge transfer and accumulation phenomena, non-ideal Mott-Schottky-like behaviour, diffusion processes, frequency dispersion or particle size distribution.[75, 98, 160, 227, 228] In contrast to other optical methods to determine φ_{FB}, in particular EER,[161, 232, 233] the EFISH approach directly senses the potential-dependent bend bending and therefore also delivers additional information on the electrode potential distribution, as shown in Fig. 10.2, which is not accessible from the solitary determination of a phase inversion.[161, 232, 233]

The flat-band potential as derived from a parabolic fit of the quadratic part of the SHG intensity in Fig. 10.1 is in very good agreement with the Mott-Schottky-analysis thus verifying the EFISH model Eq. 9.7. Literature values of φ_{FB} for α-Fe_2O_3 photoanodes are varying a lot,[77] however, due to the good agreement between the values for φ_{FB} obtained by two fundamentally different techniques, we can assume a valid determination of φ_{FB}.

Even though the value of φ_{FB} from the Mott-Schottky analysis, (0.47 ± 0.02) V_{RHE}, is quite close to the 0.43 V_{RHE} as obtained from EFISH spectrometry, both curves are different in shape. While the Mott-Schottky-plot is quite linear through a potential range between 0.6 V_{RHE} to 1.4 V_{RHE}, the space charge potential drop Φ_{SC} as derived from the SH intensity shows a distinct deflection point at 1.0 V_{RHE}. We will further inspect the functional relation between potential and SHG response in the following paragraph.
The difference between the band bending derived from Mott-Schottky and EFISH is most likely caused by the EIS probing mechanism, i.e. a net current passing through the whole electrode system, which is composed of a nanostructured n-type semiconducting α-Fe_2O_3 film in on top of another nanoscopic n-type semiconductor F:SnO_2 back contact. Both films are not sharply separated as Sn diffusion from the substrate into the α-Fe_2O_3 film is reported for this sample system.[61, 181] Later on, we will also discuss space charge effects in the back contact at elevated potentials (see Section 13.3) so that the Mott-Schottky plots from EIS measurements would rather indicate a convoluted response from a compound of porous α-Fe_2O_3 and F:SnO_2 thin films. However, the Mott-Schottky analysis is still governed by the α-Fe_2O_3 impedance response as the quite metallic back contact in series with the α-Fe_2O_3 film should have a minor effect on the integral capacitance of the solid, while a transition from a depletion of the α-Fe_2O_3 film to a depletion of the F:SnO_2 back contact is not resolved by an integral capacitance measurement in such a porous and defective sample system.

10.2 Bulk depletion

A look at the Mott-Schottky plots in Fig. 10.3 reveals a well pronounced linear behaviour over a broad range of external potentials from 0.6 V_{RHE} to 1.4 V_{RHE}. We have also found that the space charge capacitance dominates the potential distribution across the electrode system. This suggests that Φ_{SC} is not affected by the presence of surface states as the occurrence of Fermi-level-pinning is typically indicated by the presence of a plateau in the Mott-Schottky plots (see also Chapter 12).[33, 40, 65] The absence of a plateau in the Mott-Schottky plots is supported by the references [65] and [63], which also reported straight linear Mott-Schottky plots for α-Fe_2O_3 photoanode in alkaline media – also in presence of surface states. While reference [65] reports a plateau in the Mott-Schottky plots only in a neutral electrolyte, both works,

[65] and [63], observed a strictly linear behaviour of the Mott-Schottky plots in an alkaline electrolyte. Also, the decay of band-bending at potentials above 1.0 V_{RHE}, as observed in Fig. 10.2, for instance, extends much more towards anodic potentials than what one would expect for a charging process across a defined set of surface states.[33, 65]
We can also support this statement considering the capacitive contributions from both space and surface charge. As we will find in a following Section 12.1, that the electrode is covered by a large set of surface states forming a surface state capacitance C_{SS} of $1.3 \times 10^{-4}\,F\,cm^{-2}$ at 1.0 V_{RHE} while the space charge capacitance C_{SC} at this potential as determined by the Mott-Schottky-Analysis is $2.5 \times 10^{-6}\,F\,cm^{-2}$. Since the shape of surface states is neither reflected by the EFISH spectroscopy nor the EIS measurement, we can state that the surface state capacitance is arranged in series with the space charge layer.[26] Therefore, the much larger surface state capacitance will have minor effect on the total capacitance of the electrode system (see also Section 3.3.1), so that the applied potential entirely falls across the α-Fe_2O_3 film and effects from Fermi-level-pinning are negligible under the experimental conditions employed here.

An alternative explanation for the decreased band banding in Fig. 10.2 is a complete depletion of the bulk α-Fe_2O_3 film free charge carriers. This seems reasonable as the Mott-Schottky analysis showed a relatively low donor density of $7.7 \times 10^{17}\,cm^{-1}$, so that the space charge width would extend far into the bulk material. This phenomenon has been reported for both, undoped α-Fe_2O_3 and also for TiO_2 thin film photoanodes.[88, 160]
From Fig. 10.2 we see that the maximum attainable band-bending that directly follows the external bias is $\Phi_{SC}^{Max} = 0.6\,V$. For a completely depleted, spherical and homogeneously doped particle, die particle diameter D can be derived from Φ_{SC}^{Max} via Eq. 10.5.[235]

$$D = \sqrt{\frac{6\epsilon_0\epsilon_r}{e_0 N_D} * \Phi_{SC}^{Max}} \quad . \tag{10.5}$$

Similarly, we can define a maximum space charge width W_{SC}^{Max} in the conventional and idealized one dimensional picture of semiconductor electrodes as shown in Fig. 2.1, for instance. This value can be derived from the Mott-Schottky approximation according to:[26, 33]

Method	D[nm]	$W_{\mathrm{SC}}^{\mathrm{Max}}$ [nm]
XRD	33	–
TEM	50 to 100	–
EIS + EFISH	79	46

Table 10.2: Comparison between particle size diameters D obtained from three different techniques and maximum space charge width $W_{\mathrm{SC}}^{\mathrm{Max}}$

$$W_{\mathrm{SC}}^{\mathrm{Max}} = \sqrt{\frac{2\epsilon_0\epsilon_{\mathrm{r}}}{e_0 N_{\mathrm{D}}} * \Phi_{\mathrm{SC}}^{\mathrm{Max}}} \quad . \tag{10.6}$$

Note that D and $W_{\mathrm{SC}}^{\mathrm{Max}}$ are only differing by a factor of $\sqrt{3}$ that is due to the three dimensional model in Eq. 10.5 and the one dimensional picture in Eq. 10.6. If we insert the values obtained from the Mott-Schottky analysis into Eq. 10.5 and Eq. 10.6 (i.e. $N_{\mathrm{D}} = 7.7 \times 10^{17}\,\mathrm{cm}^{-3}$, $\Phi_{\mathrm{SC}}^{\mathrm{Max}} = 0.6\,\mathrm{V}$ and $\epsilon_{\mathrm{r}} = 25$), we obtain a particle diameter D of 79 nm and a maximum space charge width of 46 nm, which matches quite well with the particle sizes as determined from XRD (33 nm) and TEM (50 nm to 100 nm) which is summarized in Tab. 10.2.
These values are capable to explain that the deflection of the potential dependent SHG response is not caused by a limited probing depth since the maximum space charge potential drop $\Phi_{\mathrm{DC}}^{\mathrm{Max}}$ corresponds to a one dimensional width of 46 nm or a crystallite size of 79 nm, respectively, thus being significantly lower than the SHG probing depth of 330 nm (see Section 7.2).

It might be worth mentioning that the spatial extents in Tab. 10.2 stem from different metrics. While the D and $W_{\mathrm{SC}}^{\mathrm{Max}}$ from the inflection of the $\Phi_{\mathrm{SC}}(\Phi_{\mathrm{Ext}})$ curves are based on the assumptions of the electrode surface roughness in Section 7.2, the values of D from XRD and TEM are based on direct analyses of the particle sizes. Thus, the derivation of D and $W_{\mathrm{SC}}^{\mathrm{Max}}$ is non-recursive with respect to the other methods of confirmation.
Even though the actual particle size distribution function and the influence of particle shape and grain boundaries on the SCR remain unknown, this correspondence shows that the flattening of the $\Phi_{\mathrm{SC}}(\Phi_{\mathrm{Ext}})$ curves at $\Phi_{\mathrm{Ext}} \geq 1.0\,\mathrm{V_{RHE}}$ is most probably due to a space charge region that exceeds the whole layer of the undoped α-Fe_2O_3

semiconductor photoanode. It also shows that a constraint depletion width might also play a role in the limitation of band-bending of undoped α-Fe_2O_3 photoanodes.

11 Surface chemistry

One important outcome of this thesis is reference [44]. In this publication, photocurrent transient measurements were analysed regarding the reaction kinetics of the OER mechanism. It was found that the OER rate can be represented by a third order dependence to the surface hole concentration. By means of DFT calculations, key chemical surface structures were identified and analysed by their activation energies and driving forces. Based on these findings, a three-hole chemical reaction mechanism for the OER is proposed in good accordance with literature, experimental and theoretical findings.
The photocurrent transient measurements were contributed within the framework of the thesis presented here. Key part of these chronoamperometry experiments is the PEC measurement setup which was constructed as shown in Fig. 4.4 and further explained in Section 4.1. The sample preparation route for this work is introduced in Chapter 5, a range physico-chemical characterizations of the sample system is presented in Section 5.2. DFT simulations and kinetic analyses were performed in collaboration with colleagues from the Inorganic Chemistry Department of the Fritz-Haber-Institute Berlin and from the Consiglio Nazionale delle Ricerche, Institute of Materials, Trieste, Italy. The author wishes to explicitly acknowledge Detre Teschner and Simone Piccinin for their guidance, contributions and advances to this publication.
The following chapter presents the experimental contributions from the author. Mechanistic insights from the findings in [44] will be further discussed in context of experimentally observed surface charge transfer processes as investigated in Chapter 12.

11.1 Kinetic analysis

The experimental basis of the surface chemical analysis in [44] is a chronoamperometry measurement of photocurrent transients as shown in Fig. 11.1. In this plot, we

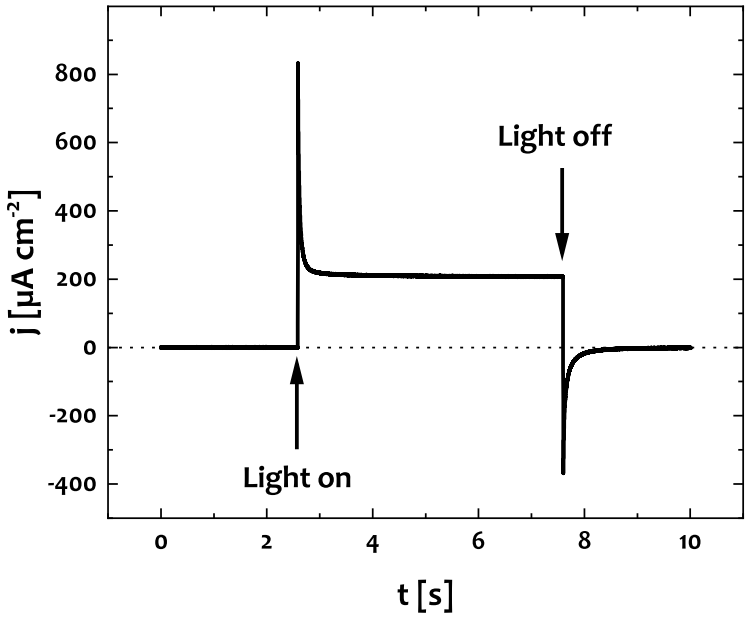

Figure 11.1: Chronoamperometry measurement of a α-Fe_2O_3 photoanode in 1 M KOH at 1.0 V_{RHE}. Photocurrent transients are recorded while the sample illumination is switched on and off, respectively.

see the time dependent cell current when the sample illumination is switched on and off, respectively. For both cases, the instant exposure and extinction of carrier excitation causes a distinct current transient which is measured under imposition of a constant bias potential.

These photocurrent transients have been observed frequently and are typically assigned to the accumulation of photo-generated holes at the electrode surface [26, 57, 74, 89] In this picture, the overall charge transfer kinetics is governed by a fast electronic charge transfer within the electrode material and a slow surface chemical charge transfer along the OER mechanism.[60, 67] Therefore, a high anodic current is typically observed initially upon instant light exposure: photo-generated holes migrate rapidly to the electrode surface while the subsequent OER process is just slowly consuming the electrode surface holes so that the cell current decreases until it converges to a steady state level under the given electrochemical boundaries. Analogously, when the light is instantly turned off from equilibrium OER photo-oxidation conditions, the surface accumulated holes recombine rapidly with bulk electrons to form a high initial cathodic dark current that diminishes as surface accumulated

holes are increasingly depleted and a net dark current of zero is measured at the applied potential of 1.0 V_{RHE} due to revocation of thermodynamic propulsion.[26, 57, 74]

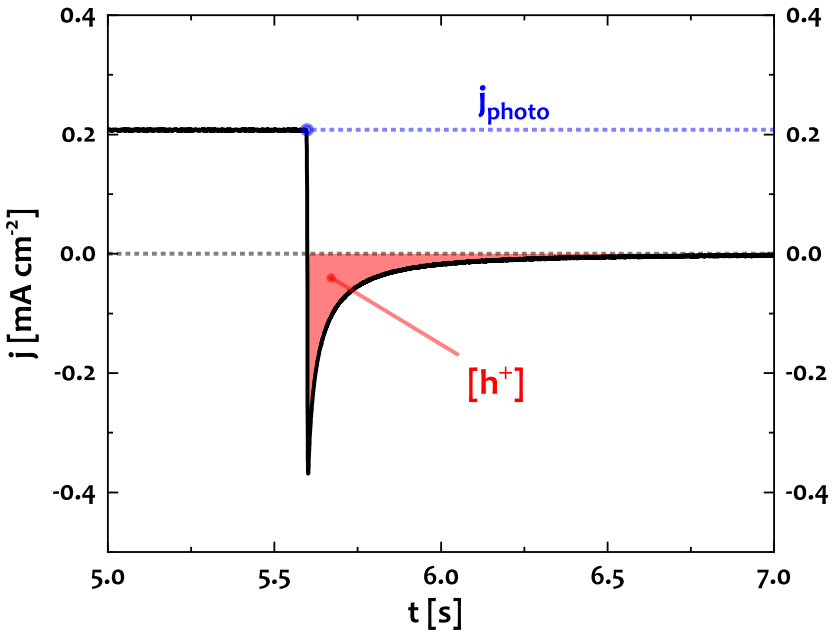

Figure 11.2: Analysis scheme to extract reaction kinetic information from a chronoamperometry measurement as shown in Fig. 11.1. The cathodic current transient is referred to the recombination of surface accumulated holes. Coulometric counting of the integral electrode surface charge up to the zero steady state charge flow allows for a determination of the photo-oxidation current j_{photo} as function of the accumulated of surface holes h^+ [44]

A scheme of the photocurrent transient coulometric analysis is presented in Fig. 11.2. Based on the previous considerations, we can extract two quantities from the photocurrent transients: the amount of surface accumulated holes and the steady state OER current. The OER photocurrent j_{OER} is obtained immediately before the blocking of the incident light, where steady state water oxidation conditions are provided. Since the cell current converges to zero in absence of light and since the bias potential is set well below the thermodynamic onset of the dark OER reaction at 1.23 V_{RHE}, the cell current j_{photo} immediately before the instant blocking of the incident light can be attributed to the photo-driven water oxidation reaction rate.[44] The amount surface holes h^+ is determined from the total cathodic discharging transient upon light ex-

tinction, i.e. the surface charge remaining when the driving force has been removed. In a subsequent chapter we will find that the surface charge density is 64 times larger than in bulk, so that we can approximate that the cathodic current transients is in fact governed by surface hole recombination processes (see Section 12.1).[44] The actual numerical values for $[h^+]$ and j_{photo} were calculated from a bi-exponential fit of the cathodic current transients.[44, 236]

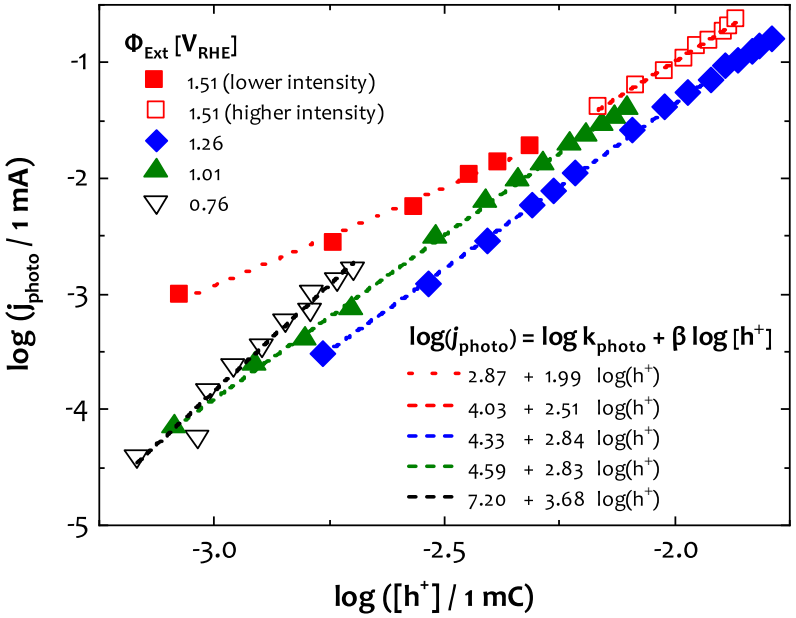

Figure 11.3: Kinetic analysis of the OER current j_{photo} as function of surface charge h^+ at different electrode potentials obtained as shown in Fig. 11.2. The amount of photo-generated surface holes was varied by the incident electrode illumination power density, the dataset at 1.51 V_{RHE} was arbitrarily split into two parts of higher and lower illumination intensity. The OER current is close to a third order dependency at electrode potentials between 1.01 V_{RHE}, 1.26 V_{RHE} and also at 1.51 V_{RHE} for higher illumination intensities [44]

The dependency of the steady state OER photocurrent j_{photo} on the amount of surface holes h^+ was measured at four different electrode potentials between 0.76 V_{RHE} and 1.51 V_{RHE} while the amount of surface holes was varied using the incident electrode illumination power density evoking different amounts of excited carriers. The results are plotted in Fig. 11.3 on a double logarithmic scale. This analysis can be employed to determine the OER photocurrent reaction order β with respect to the surface hole

concentration $[h^+]$ according to Eq. 11.1, where k_{photo} denotes the photo-oxidation reaction constant.[44, 237, 238]

$$\frac{d[O_2]}{dt} \propto j_{photo} = k_{photo}\,[h^+]^{\beta} \qquad \log j_{photo} = \log k_{photo} + \beta * \log [h^+] \tag{11.1}$$

All datasets can be fit well with a linear regression model.[44] The observed OER photo-oxidation rates approximately follow a third order dependency for electrode potentials between 1.01 V_{RHE} and 1.26 V_{RHE} over several orders of magnitude of OER current with experimentally determined values of $\beta = 2.83$ and $\beta = 2.84$, respectively. This dependency also holds for electrode potentials of 1.51 V_{RHE} for higher illumination intensities, with a reaction order $\beta = 2.51$, i.e. above a certain threshold surface hole concentration.[44, 237, 238] These findings correspond well with other published results, where a third order rate law was found when a certain threshold of surface hole concentrations is exceeded.[237, 239] Further studies have also observed a multi-hole OER mechanism with reaction orders larger than two and so showing that a set of single charge transfer steps is rather unfavoured under the given conditions.[238, 240]

11.2 OER reaction mechanism

The previous kinetic analysis suggests that the OER photo-oxidation mechanism of water at an α-Fe_2O_3 photoanode in 1 M KOH electrolyte follows a surface accumulation of positive charge. In order to identify corresponding chemical structures, DFT simulations were conducted at the Consiglio Nazionale delle Ricerche, Institute of Materials, Trieste, Italy.[44] For this, a positive charge was introduced into a 2×2 unit cell of a hydroxylated α-Fe_2O (0001) surface. It was found that the surface positive charge under alkaline conditions is stored in an anti-bonding orbital between Fe- and O-atoms labelled as oxyl-species $Fe(III)-O^-$ rather than a $Fe(IV)=O^{2-}$ oxo-species. This structure was compared with literature using a simulation of its spectroscopic fingerprint where the simulated NIR-spectrum was found to show good agreement with measured literature data from TAS experiments to ascribe a hole-accommodation within an oxyl-structure denoted as $^*O^-$.[60] This chemical structure was found to serve as host for surface hole-accumulation and also to provide attractive interaction between two $Fe-O^-$ sites stabilising the three-hole-intermediate.[44]

Based on this key hole-hosting structure in the OER mechanism, a set of possible elementary reactions was simulated and evaluated regarding the kinetic facilitation and thermodynamic cost with respect to the observed three-hole proximity transition state. All elementary reaction networks were compared within other possible OER catalytic cycles and one OER mechanism is proposed to fit the observed third order reaction kinetics involving a three-hole intermediate as suggested by the previous rate law analysis.[44]

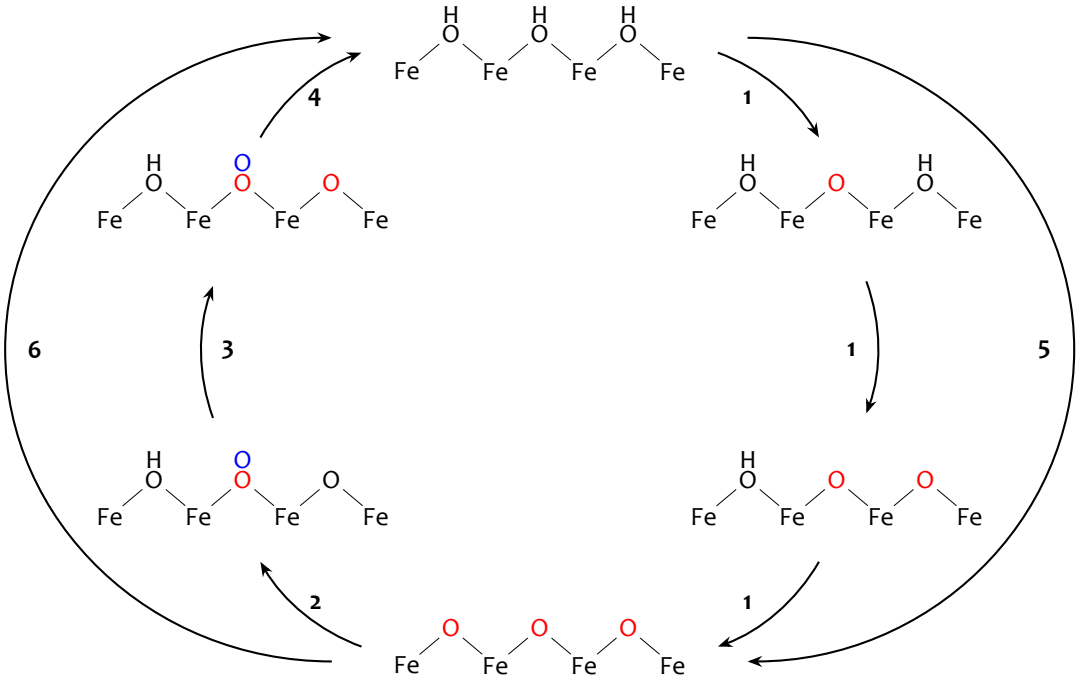

1	$*OH^- + h^+ + OH^- \longrightarrow *O^- + H_2O$	5	$3\,*OH^- + 3\,h^+ + 3\,OH^- \longrightarrow 3\,*O^- + 3\,H_2O$
2	$3\,*O^- + OH^- \longrightarrow *OO^- + *OH^- + *O^{2-}$	6	$3\,*O^- + OH^- + h^+ + H_2O \longrightarrow O_2 + 3\,*OH^-$
3	$*O^{2-} + h^+ \longrightarrow *O^-$		
4	$*OO^- + *O^- + H_2O \longrightarrow O_2 + 2\,*OH^-$	7	$4\,OH^- + 4\,h^+ \longrightarrow O_2 + 2\,H_2O$

Figure 11.4: OER photo-oxidation mechanism at a α-Fe_2O_3 photoanode derived from a third order reaction rate law analysis, DFT simulations and MK modelling as proposed in [44]. Surface bound species are marked by an asterisk.

Based on kinetic findings and DFT simulations, a catalytic reaction pathway for the photo-oxidation of water at an α-Fe_2O_3 photoanode under high surface hole concentration in alkaline media is proposed in [44]. This mechanism is shown in

Fig. 11.4. If we start our inspection of the catalytic cycle with a fully hydroxylated α-Fe_2O_3 electrode surface at the top of Fig. 11.4, we see that the photo-oxidation of water is initiated by an accumulation of holes at the electrode surface. This charge-accumulation occurs via a deprotonation of surface hydroxo species $^*OH^-$ to form a surface oxyl-species $^*O^-$ according to reaction **1**. A threefold repetition of reaction step **1** yields a key intermediate as sketched at the bottom of Fig. 11.4 that hosts three proximate positive charges as suggested by the previous rate law analysis determining the third-order reaction rate law. The subsequent step is the formation of a surface super-oxo species $^*OO^-$ according to reaction **2**. After a fourth hole is accomodated at the electrode surface according to reaction **3**, oxygen is released from the surface super-oxo species as shown in reaction **4** to recover the initial and fully hydroxylated α-Fe_2O_3 surface at the top of Fig. 11.4.[44]
Fig. 11.4 also shows a summation of the elementary reactions between the initial pristine, hydroxylated and uncharged α-Fe_2O_3 surface and the three-hole intermediate according to the reactions **5** and **6**. We see that the reaction cycle can be also split well into a charge accumulation process **5** to form the three-hole intermediate and a second surface-chemical half-cycle **6** where the accumulated surface holes convert liquid water and hydroxide ions into molecular oxygen. The sum of the partial reactions **5** and **6** delivers the generic OER half cell reaction **7** in alkaline media as already given in Eq. 1.3.[26, 44]

	Reaction	Rate $[s^{-1}]$	Reversibility $[k_{back}/k_{for}]$	DRC
1	$^*OH^- + h^+ + OH^- \longrightarrow {}^*O^- + H_2O$	1.56×10^{-2}	9.81×10^{-1}	0.05
2	$3\,{}^*O^- + OH^- \longrightarrow {}^*OO^-\,{}^*OH^- + {}^*O^{2-}$	5.19×10^{-3}	3.34×10^{-21}	0.94
3	$^*O^{2-} + h^+ \longrightarrow {}^*O^-$	5.20×10^{-3}	4.12×10^{-1}	0.00
4	$^*OO^- + {}^*O^- + H_2O \longrightarrow O_2 + 2\,{}^*OH^-$	5.20×10^{-3}	5.66×10^{-13}	0.00

Table 11.1: Microkinetic analysis of OER elementary reactions at 0.01 monolayer (ML) surface hole coverage according to [44]. Reaction rate, equilibrium constant and degree of rate control (DRC)[241] are presented for the elementary reactions relevant to the reaction pathway shown in Fig. 11.4. Minor reactions from the analysis are not listed, so that the cumulated value for degree of rate control (DRC) does not reach unity

A MK analysis of the elementary reaction steps **1** to **4** is shown in Tab. 11.1.[44, 242] We see the calculated reaction rates and equilibrium constants of the respective elementary reactions from Fig. 11.4, where the reversibility of each reaction is evaluated

by the ratio of backward to forward kinetic constant $k_{\mathrm{back}}/k_{\mathrm{for}}$. The values correspond to a moderate surface hole coverage of 0.01 monolayer (ML) which showed the best accordance between the measured charge dependent photocurrent and calculated reaction rate laws.
The surface hole accumulation reaction **1** has a calculated rate of $1.56 \times 10^{-2}\,\mathrm{s}^{-1}$ and is approximately three times faster than the subsequent surface chemical reaction **2** to **4** with reaction rates of $5.2 \times 10^{-3}\,\mathrm{s}^{-1}$ each. The equilibrium constant is larger for the surface hole accumulation reaction **1** with a value of 9.81×10^{-1} compared to the reactions **2** to **4** with $k_{\mathrm{back}}/k_{\mathrm{for}}$-values 3.34×10^{-21}, 4.12×10^{-1} and 5.66×10^{-13}, respectively.[44] The degree of rate control (DRC) is strongly concentrated at reaction **2** with a value of 0.94 – as quantitative pendant to the slow consumption of surface rapidly accumulated holes as qualitatively sketched in Section 11.1.
From these values we can infer that the O–O bond formation via dissociative adsorption of a hydroxide-ion at the 3 $^{*}\mathrm{O}^{-}$ intermediate **2** to form a surface superoxo-species is the rate determining step to the overall OER reaction **7**. It should also be noted that at larger surface hole coverages, the charge accumulation reaction **1** exhibits the highest DRC [241]. This is referred to slow hole diffusion in the oxide SCR, which becomes less effective as the surface hole concentration decreases and the consumption rate of positive surface charge gains more influence to the overall reaction rate.[44]

12 Surface charge

12.1 Surface states

Once a chemical understanding of the OER mechanism at the α-Fe_2O_3 photoanode and of the space charge propagation is established, we now want to investigate the charge accumulation processes at the electrode surface. The decreasing fraction of band-bending at $\Phi_{Ext} \geq 1.0\,V_{RHE}$ could be in principle explained by an unpinning of the band-edges at the electrode surface, so called Fermi-level-pinning (see Section 2.4). This phenomenon is referred to the presence of electronic states at the electrode surface which causes an unpinning of the bands at the electrode surface resulting in a distribution of the external bias potential over both, SCR and Helmholtz layer.[33, 36, 98, 99] Therefore, we want to see if it is possible to gather experimental information on electronic surface states at the operating α-Fe_2O_3 photoanode.
Fig. 12.1 shows the curves of the potential drop over the α-Fe_2O_3 electrode Φ_{DC} as function of the applied bias Φ_{Ext} and the corresponding electrode current in the dark. We see that Φ_{DC} follows a one to one correspondence to Φ_{Ext} up to a bias of $1.0\,V_{RHE}$ until the slope decreases. The corresponding electrode current density j_{Dark}, which was recorded simultaneously with the SHG response, is also shown in Fig. 12.1. In the total view, j_{Dark} exhibits the typical diode like shape of a photoanode in the dark, with significant extent only under strongly anodic conditions due to the formation of OER current.[61, 65]
A closer look of j_{Dark} is shown in the inset of Fig. 12.1. Here, we can find a small current signal which is centred around $1.1\,V_{RHE}$ with a half width of 0.3 V and a height of $3\,\mu A\ /cm^2$. Since the PEC measurements through all the studies in this thesis were conducted in an inert 1 M KOH electrolyte that is not redox active in this potential range, we can assign this signal to a chemical electrode process. In order to trace the origin of this oxidation wave, we first want to exclude a range of possible side effects.
A set of control experiments to this small feature shown in the supplementary infor-

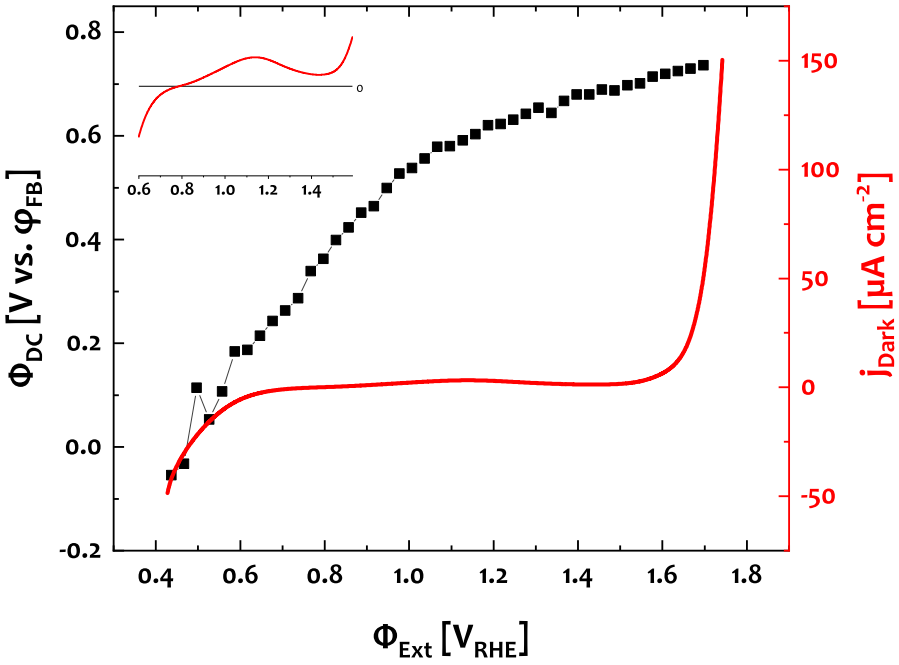

Figure 12.1: Bias dependent DC potential drop over the α-Fe_2O_3 photoanode layer with the corresponding cell current in the dark

mation Chapter D. First, the stability of the electrode is evaluated by repeated CV measurements of the sample and cell system. Fig. V shows multiple CV-curves of the in situ α-Fe_2O_3 photoanode sample which were repeated at a daily base in order to assess the stability of the system. No significant changes can be found neither within the three cycles which are shown in each plot, nor between the measurements on different days. Therefore, we can confirm a stable electrode system that does not suffer from corrosion or degradation processes.

Second, we need to check if some of the current may emerge from the underlying F:SnO_2 substrate. Fig. VI shows CV-curves from the sample, the α-Fe_2O_3 coated F:SnO_2 substrate, and the bare, uncoated F:SnO_2 substrate. Since there is a strong pattern in the CV-curves from the substrate which has completely declined upon coating with the α-Fe_2O_3 thin film, we can infer that the α-Fe_2O_3 film covers the substrate completely and that any electrochemical response arises from the α-Fe_2O_3 film and not from the underlying substrate.

Finally, we need to confirm the repeatability of this oxidation wave. Fig. VII shows repeated IV measurements of this signal on two different days. The signal shape

remains essentially the same within this period, so we can also state that this small oxidation wave centred at 1.1 V_{RHE} persists over multiple measurements and can be considered a repeatable, steady electrode process that i) is not due to electrode degradation or corrosion, ii) does not arise from the underlying electrode substrate and iii) persists over multiple experiments. Thus, we can suppose that this oxidation wave corresponds to a charging process at the α-Fe_2O_3 electrode surface.

There is a large amount of literature on α-Fe_2O_3 photoanode surface states including EIS,[65] intensity mpdulated photocurrent spectroscopy (IMPS)[59] and photocurrent transient experiments [101], however, such an oxidation current feature in an IV measurement has not explicitly been reported so far to the author's knowledge. One similar small feature can be found in Fig. 5 (b) in reference [243], which is centred a bit more cathodic at 0.9 V_{RHE} compared to the feature we observe here at 1.1 V_{RHE}. The absence of this current signal in a quite common IV experiment might be due to two peculiarities of the experimental conditions which were applied in these works for the simultaneous measurement of SHG and PEC quantities within one experiment in situ (see Section 4.3). First, the data shown in Fig. 12.1 was measured in a flow cell, that provides strong agitation of the electrolyte. This might consequently create a more compact diffusion layer, which would raise the double layer capacitance ($C_H \propto 1/d$) and decrease the contribution from the Helmholtz layer to the total capacitance of the electrode system (see Section 3.3.1 and Eq. 15.2).[27, 84, 163, 244–246] Accordingly, this feature may be overlaid by electrode/electrolyte interactions in other IV-measurements that often avoid electrolyte agitation in order to eliminate a source of electronic and chemical fluctuations. Second, the scan rate r of 1 mV/s is quite low compared to other IV measurements. A higher scan rate, however, would also lead to increased capacitive currents from the concentrated electrolyte according to $C_H = I_C/r$,[27, 163, 247] which may as well overlay surface process as observed under the conditions employed for this experiment presented here.

Once we have assigned this small IV response around 1.1 V_{RHE} to an electrochemical electrode surface process, we now want to hypothesize that this signal is due to the oxidation of surface states at the α-Fe_2O_3 electrode interface and see if we can confirm this assumption by a quantitative analysis of the feature and a comparison with literature values.[63, 65]

The method of quantification of this IV signal is illustrated in Fig. 12.2. It shows a fit of the measured cell current J from Fig. 12.1 over a potential range from 0.8 V_{RHE} to 1.45 V_{RHE}. We see that J can be fit very well by a linear background BG and a

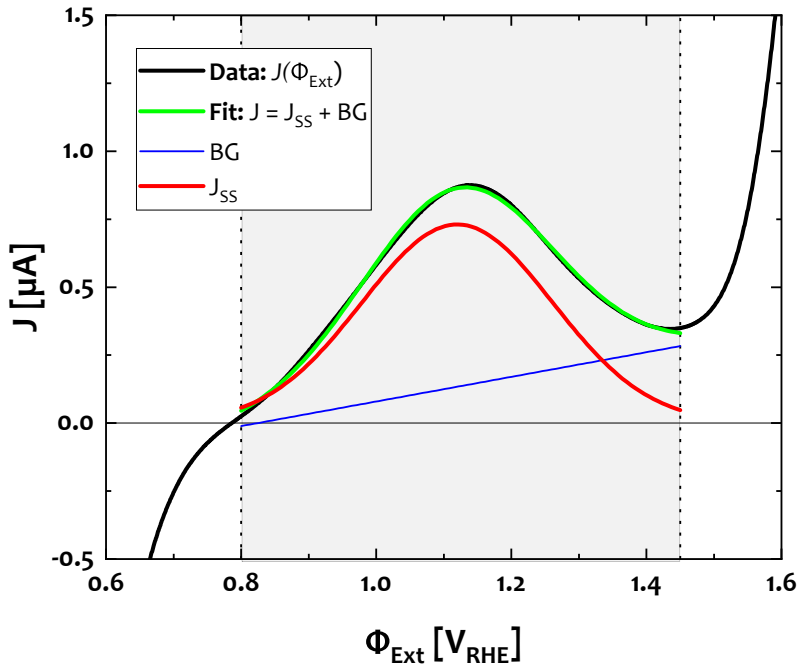

Figure 12.2: Modelling of the IV signal (J) from Fig. 12.1 by a linear background (BG) and a Gaußian surface state oxidation signal (J_{SS})

Gaußian line shape J_{SS}. Consequently, we can suppose that the IV current signal $J_{SS}(\Phi_{Ext})$ can be represented by a Gaußian peak with an integral Area J_T, a centre potential φ°_{SS} and a standard deviation w_{SS} according to Eq. 12.1.[248]

$$J_{SS}(\Phi_{Ext}) = \frac{J_T}{w_{SS}\sqrt{2\pi}} * \exp\left\{\frac{-(\Phi_{Ext} - \varphi^{\circ}_{SS})^2}{2\,{w_{SS}}^2}\right\} \qquad 12.1$$

Since our model describes the measured current very well, it is now possible to fill this quantitative relation with physical meaning. First, we can suppose that, due to the purely Gaußian line shape and the control measurements mentioned above, $J_{SS}(\Phi_{Ext})$ is not contaminated by any other contributions and corresponds to the oxidation of surface states.[63, 65] Second, as the measured signal has the dimension of a current J we want to suppose that it reflects a capacitive load of surface charge Q_{SS} being exchanged within a given time t according to Eq. 12.2 where e_0 is the elementary charge.

$$J_{SS} = e_0 * \frac{dQ_{SS}}{dt} \tag{12.2}$$

The time t can be obtained from the constant scan rate r of the potential sweep by Eq. 12.3.

$$r = \frac{d\Phi_{Ext}}{dt} = 1\,mV/s \tag{12.3}$$

Considering the current signal as charging of a surface state capacitance we can calculate the surface state density N_{SS} from the charging capacitive current given in Eq. 12.2 according to Eq. 12.4.[63, 65]

$$N_{SS} = \frac{C_{SS}}{e_0} = \frac{1}{e_0}\frac{dQ_{SS}}{d\Phi_{Ext}} \tag{12.4}$$

Combination of Eq. 12.2, Eq. 12.3 and Eq. 12.4 yields the following expression Eq. 12.5 to calculate the density of surface states as function of the external bias from the capacitive current J_{SS} and the scan rate r, where the cell current is normalized to the electrochemically active surface area according to $j_{SS} = J_{SS}/(A_{Geo} * f_R)$ (see Eq. 7.3). We obtain Eq. 12.5 to relate the amount of surface states N_{SS} with the measured surface state oxidation current J_{SS} at a given potential.

$$N_{SS}(\Phi_{Ext}) = \frac{J_{SS}(\Phi_{Ext})}{S_{Act} * e_0 * r} \tag{12.5}$$

Fig. 12.3 shows fits of the current signal J_{SS} from Fig. 12.2 to the Gaußian lineshape in Eq. 12.1, where the current was normalized to the amount of electronic surface states according to Eq. 12.5. We find that a set of surface states that is distributed over a Gaußian line shape with a centre at 1.1 V_{RHE} and a half width of 0.3 V.
Similar measurements on N_{SS} have been done by Klahr et al.[65, 101] and Monllor-Satoca et al.[63]. The difference between those works and these presented here is that both, [65] and [63], have employed EIS measurements and fit an equivalent circuit model to the impedance spectra. Another approach was also published by Klahr et al. in a chronoamperometry (CA) setup, where a fast cathodic potential sweep

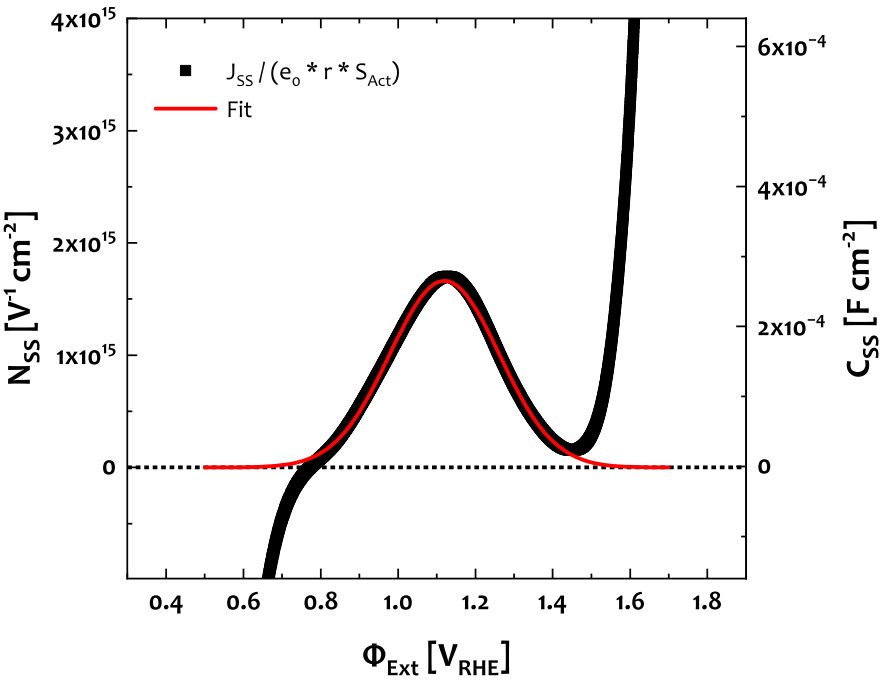

Figure 12.3: Determination of the density of surface states N_{SS} as function of electrode potential Φ_{Ext} by fitting the capacitive surface state oxidation current J_{SS} from Fig. 12.2 to Eq. 12.5 and corresponding surface state capacitance C_{SS} according to Eq. 12.4

was applied upon strong anodic bias and electrode irradiation. Those works showed two surface charging processes with varying capacitances centred at 1.2 V_{RHE} and 0.8 V_{RHE} strongly depending on the sweep potential scan rate and sample illumination. The fit in Fig. 12.3 resulted in a trap state capacitance which is well comparable to the findings presented here in height, centre and width but with an important difference: The experiments in Fig. 12.3 and Fig. 12.1 were performed without electrode illumination. Thus, we find that the effect of surface charge is intrinsic to the electrode material and not solitarily caused by photonic excitation of the electrode.

A comparison between the surface states characteristics of α-Fe_2O_3 photoanodes from different studies is given in Tab. 12.1. It shows the height $N_{\mathrm{SS}}^{\mathrm{Max}}$, half width $w_{1/2}^{\mathrm{SS}}$ and expectation value $\varphi_{\mathrm{SS}}^{\circ}$ of the surface state distribution. We see that all values measured here are well comparable to those from [65], [63] and [101]. Both, the width $w_{1/2}^{\mathrm{SS}}$ and expectation value $\varphi_{\mathrm{SS}}^{\circ}$ are quite similar through all works. The total surface DOS is increased here compared to [65], [101] and [63]. This might be due to deviations in the multi-dimensional fits of the impedance spectra in [65] and

Source	Method [eV^{-1} cm^{-2} 10^{14}]	N_{SS}^{Max} [V]	$w_{1/2}^{SS}$ [V_{RHE}]	φ_{SS}°
This work	IV	17	0.3	1.1
Klahr et al. [65]	EIS	≈7	≈0.2	≈1.3
Monllor-Satoca et al.[63]	EIS	2	≈0.3	≈1.0
Klahr et al. [101]	CA	1 to 7	≈0.2	≈0.8, 1.2 to 1.4

Table 12.1: Comparison between mid gap surface state DOS characteristics from this work and literature values.

[63]. Tentatively, our IV measurement provides a direct probe of the charge passing along surface states, so that we have found a promising approach to probe the DOS of surface states at the semiconductor electrode interface with a quite direct and convenient experimental method.
Interestingly, the amount of surface states seems to increase with time as appended in Fig. VII, where the signal was recorded over multiple days of the measurement campaign. Supposing that published results were measured on freshly prepared sample systems, the increased surface state density in the data presented in Tab. 12.1 might be a result of prolonged electrolyte contact and OER activity of the sample system which might be worth considering in future investigations.
Due to the good comparability between the energetic distribution of surface states in our IV measurement and published EIS results, we can suppose that the potential dependent measurement of J_{SS} provides an appropriate probe to investigate the population and density of electronic states at the electrode surface.
Even though a large amount of surface states is observed, no capacitive effects of C_{SS} appear in the Mott-Schottky plots in Fig. 10.3. The potential dependent SHG response also does not follow the disappearing of surface state density as shown in Fig. 12.1 at potentials beyond 1.4 V_{RHE} and instead shows good agreement with other methods to explain a complete depletion of the space charge layer.[88] Other works also observed large surface state densities without a distinct effect on Mott-Schottky analyses in alkaline media.[63, 65] In Chapter 10 and Section 12.2 we find that the SHG intensity is in close correspondence with the space charge band bending and not affected by surface charge accumulation processes and cell current characteristics. Therefore, it seems more likely that the surface states do not affect the potential drop

over the SCR in terms of Fermi-level-pinning. A more detailed discussion on possible explanations is presented in Section 15.2.

12.2 Charging dynamics

12.2.1 Photovoltage transients

In this section want to have a look at the potential evolution dynamics when the electrode irradiation is instantly switched on and off. This measurement configuration is rather unusual, since typically current transients are recorded over time, i.e. by a chronoamperometric experiment.[57] However, as the SHG intensity responds to the static field in the SCR, instead of the charge flow, we need to keep the current and potential axes inverted and record the electrode potential Φ_{Ext} and SHG response $I_{2\omega}$ as function of time in terms of a chronopotentiometry (CP) experiment.
A scheme of the CP measurement on the α-Fe_2O_3 photoanode sample system is appended in Fig. XV. A constant current of 11.1 µA cm^{-2} is imposed to the electrode while the potential is left floating and recorded over time upon instant exposure and removal of electrode illumination. The IV characteristics show that the electrode potential would ba altered by illumination between 0.93 V_{RHE} and 1.65 V_{RHE}.
Fig. 12.4 shows both Φ_{Ext} and $I_{2\omega}$ transients after an instant change of the electrode illumination. In the top panel we see how Φ_{Ext} evolves upon irradiation of the electrode, the lower panel shows the recovery of Φ_{Ext} to its initial value in the dark after the illumination is turned off.
In the upper panel we see that $I_{2\omega}$ follows Φ_{Ext} very well, which further confirms the close correlation between SHG response and the DC potential drop over the α-Fe_2O_3 film Φ_{DC} as developed in Section 9.1 and Fig. XI. This congruence between $I_{2\omega}$ and Φ_{Ext} also holds for the relaxation process in the lower panel. However, the noise of the SHG data is quite large. Therefore, we want to further analyse the evolution of the floating electrode potential.

12.2.2 Charge accumulation

The measurement of dark- and photovoltage transients inherently also provides data on the time dependent evolution of cell current j and the total amount of exchanged charge Q_{T}. The corresponding full dataset is appended in Fig. XVI. Note that both time and charge are referred to the initiation of the experiment where $t = t_0$ and

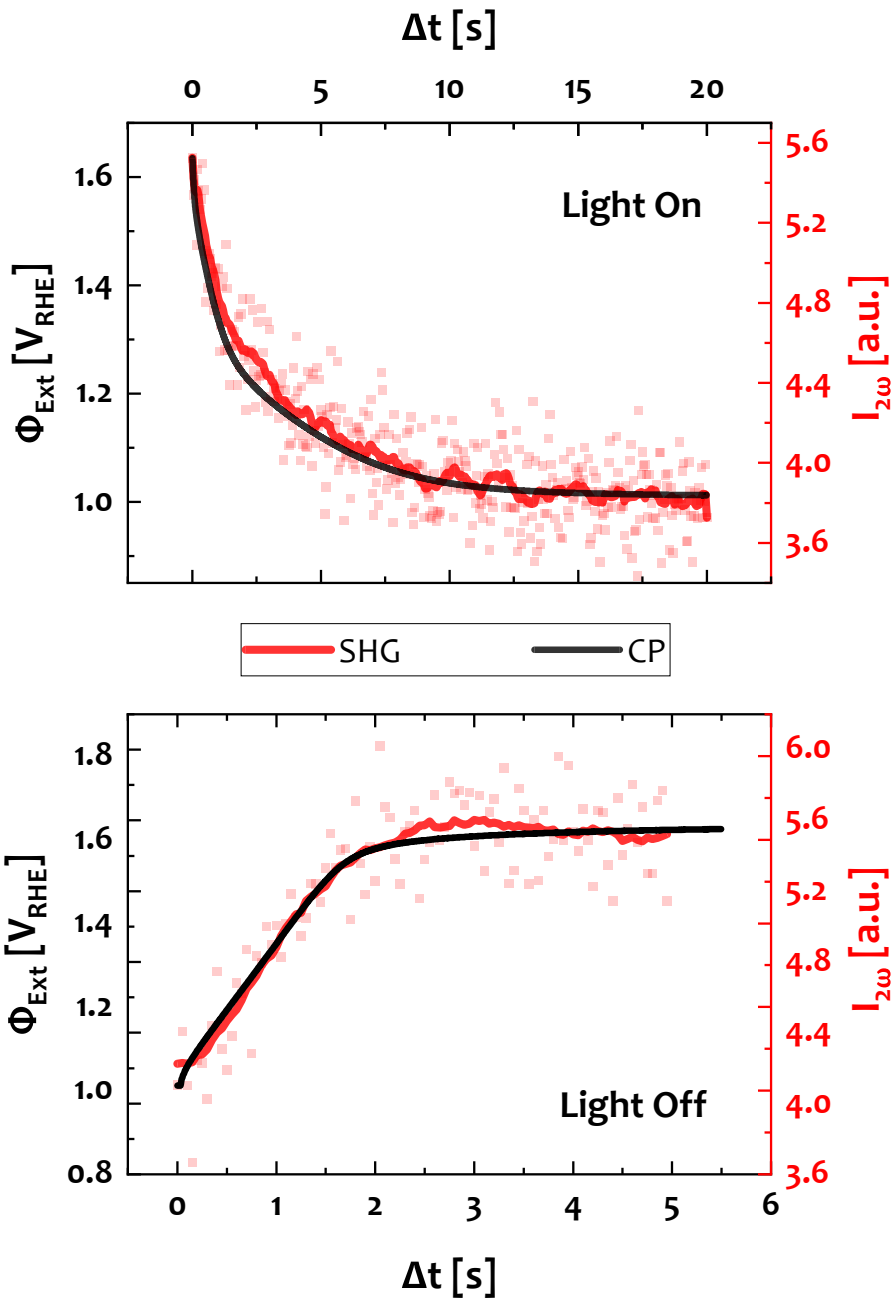

Figure 12.4: Photovoltage transients. Time dependent evolution of SHG response $I_{2\omega}$ and electrode potential Φ_{Ext} under imposition of a constant current of 11.1 µA cm^{-2} when electrode illumination is instantly switched on (top panel) and off (bottom panel). An adjacent average over 20 data points was applied to SHG data to remove statistical noise.

$Q = Q_0$ so that $\Delta t = t - t_0$ and $Q_{\mathrm{T}} = Q - Q_0$. Knowing Q_{T} and the corresponding

potential Φ_{Ext} we can calculate a total capacity of the sample system C_{T} according to Eq. 12.6.

$$C_{\mathrm{T}} = \frac{\mathrm{d}Q_{\mathrm{T}}}{\mathrm{d}\Phi_{\mathrm{Ext}}} \quad . \tag{12.6}$$

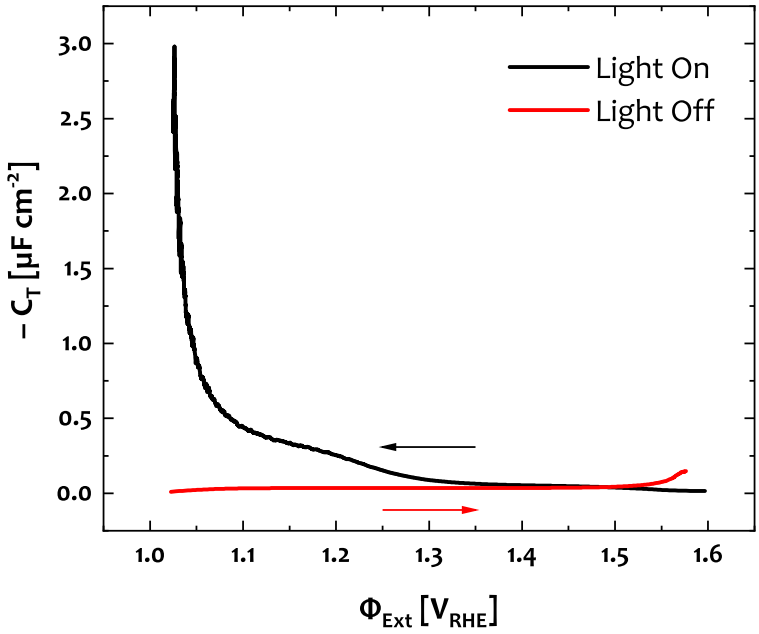

Figure 12.5: Charge accumulation transients. Total capacitance of the α-Fe_2O_3 electrode system C_{T} as function of the external potential Φ_{Ext} upon instant exposure (black) and blocking (red) of electrode illumination. Voltage traces were smoothed by a 20 point sliding average.

A plot of C_{T} as function of Φ_{Ext} for both instant exposure and blocking of electrode illumination is shown in Fig. 12.5. The black curve reflects the evolution of the photovoltage upon electrode illumination, the red curve corresponds to the evolution of the electrode potential in the dark back to equilibrium after the electrode illumination was turned off. Interestingly, both curves are clearly differing in shape. While the red curve seems to be fairly constant over the whole potential range, we find a pronounced shaping of the photovoltage evolution from the black curve.
The observations in Fig. 12.5 are quite similar to the measurements by Klahr et al., where the electrode was equilibrated under highly anodic bias before the cell

current is measured during a fast cathodic potential sweep.[101] These works also showed a characteristic capacitive shaping under cathodic potential evolution with two distinct features at 1.2 V_{RHE} and 0.8 V_{RHE}, while an anodic scan or a fast cathodic sweep showed no pronounced capacitive features over the potential range. This shaping was discussed in terms of a surface charge accumulation by the formation of an iron-oxo-species, where a high amount of accumulated charge is required to enable Faradayic photo-oxidation of water.[44, 101]

A similar behaviour is observed for the cell current. Fig. 12.6 shows the SHG response and the simultaneously recorded cell current as function of the externally applied potential in different scan directions. In the red curves, Φ_{Ext} was swept in anodic direction, the black curves show scans towards cathodic potentials. In the top panel we see the corresponding SHG intensity, which remains unaffected by the scan direction. The cell current, on the other hand, only shows the distinct oxidation wave that was analysed in Section 12.1 when the potential is swept in anodic direction which is consistent with behaviour of the total capacitance in Fig. 12.5, where the potential evolution upon light exposure can be considered an anodic propagation of the quasi-Fermi-level of photogenerated holes (see also Section 9.1). Besides that, the absence of the surface charging effects to the SHG response indicates that the space charge evolution is not influenced by the presence, occupation or depopulation of surface states and thus no Fermi-level-pinning to occur.

A comparison between the photovoltage evolution capacitance and the surface state oxidation current is shown in Fig. 12.7. We see that both metrics exhibit a distinct feature around 1.1 V_{RHE}, while the total capacitance is overlaid by a steep increase towards lower potentials. It should be noted that the chronopotentiometry experiment was dedicated to measure the SHG response so that the sample was illuminated with a focused 450 nm CW laser diode beam. Therefore, the photoresopnse is not directly comparable to the homogeneous illumination with simulated solar irradiation as applied in [101] and also in Chapter 11, for instance. However, both, the surface state oxidation current and photovoltage capacitance qualitatively exhibit a clear charge accumulation process comparable to the results in [101].
Following the discussion from [101], the capacitive effects indicate an irreversible surface charge accumulation process which was assigned to an oxidation of hydroxylated surface iron(III) species according to Eq. 12.7. This reaction was proposed as rate limiting step, where an accumulation of positive surface charge along the oxidation of Fe−OH species is required as initiation for the OER mechanism.[101] For

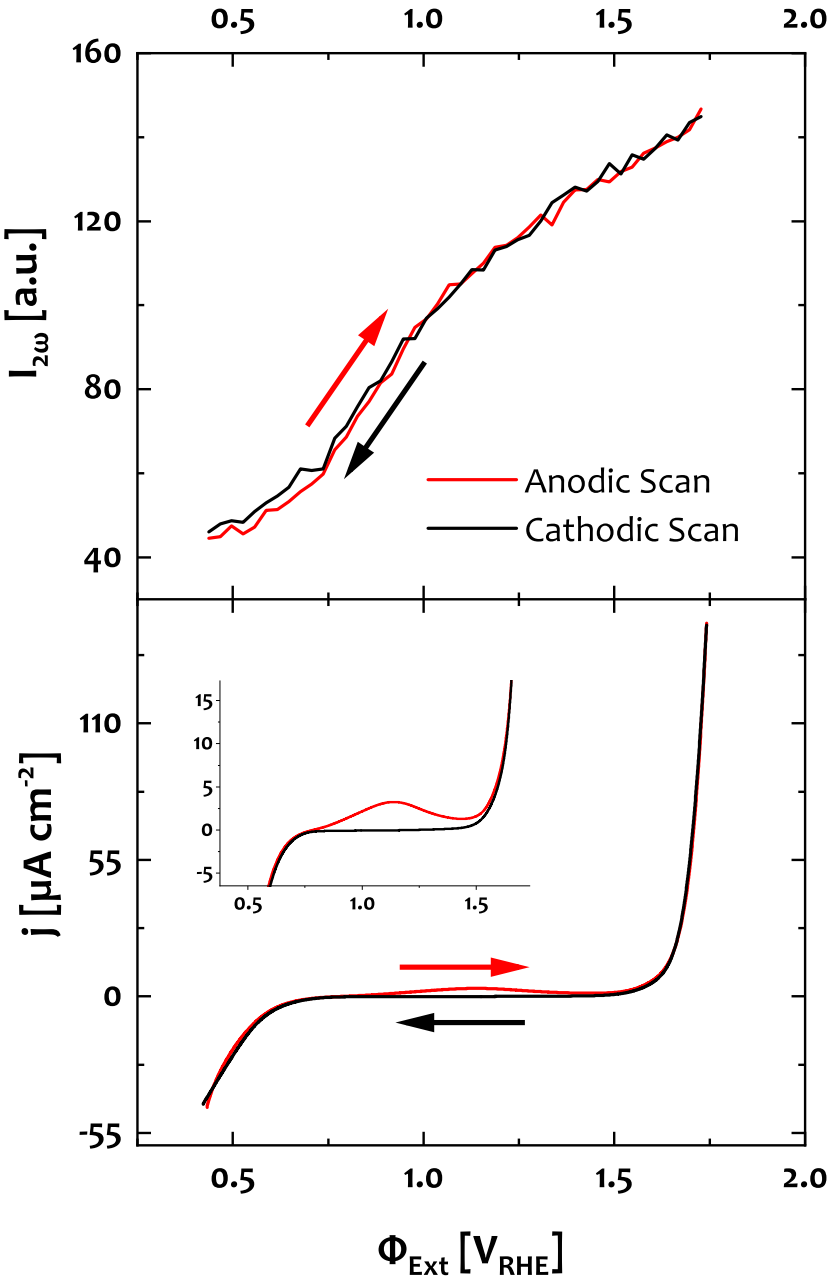

Figure 12.6: Potential dependent SHG intensity $I_{2\omega}$ and corresponding cell current density j for anodic and cathodic scan directions

comparison, the rate limiting steps as derived from the kinetic analysis in Chapter 11 (see Fig. 11.4 and Tab. 11.1) are given in Eq. 12.8 and Eq. 12.9.[44]

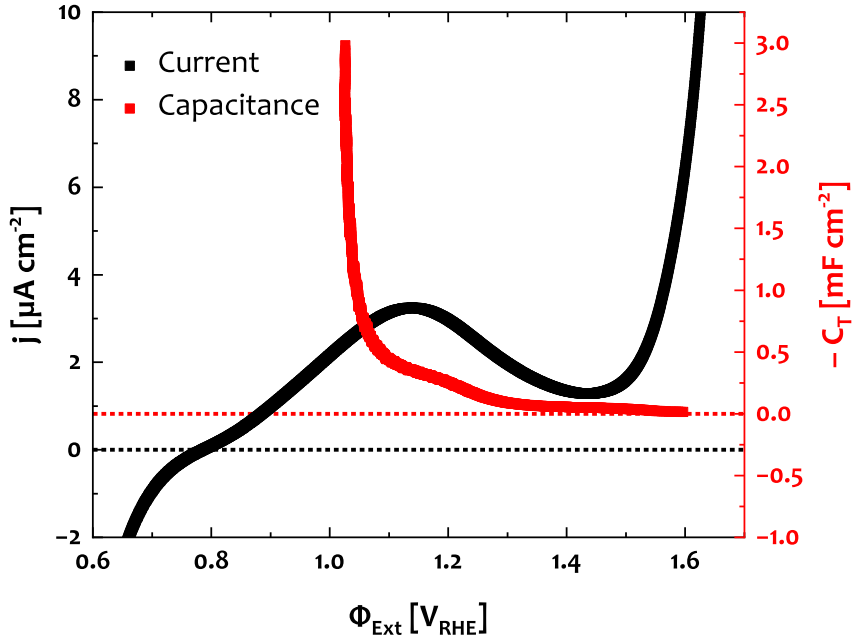

Figure 12.7: Comparison between surface state oxidation current and photovoltage evolution capacitance from the datasets presented in Fig. 12.1 and Fig. 12.5, respectively

$$Fe^{III}-OH + h^+ \rightleftharpoons Fe^{IV}=O + H^+ \tag{12.7}$$

$$Fe-OH^- + h^+ + OH^- \rightleftharpoons Fe-O^- + H_2O \tag{12.8}$$

$$3\,Fe-O^- + OH^- \rightleftharpoons Fe-OO^- + Fe-OH^- + Fe-O^{2-} \tag{12.9}$$

The expression Eq. 12.7 from [101] is quite similar to the rate limiting step Eq. 12.8 from [44], where the surface charge accumulation also occurs via an Fe–OH oxidation step to drive a three hole OER mechanism. The difference between both equations is that in [44] the positive charge was found to be shared between Fe and O atoms, which was therefore labelled as oxyl-species $*O^{1-}$ rather than an iron centred charge Fe^{IV} and that Eq. 12.8 states a release of water instead of a deprotonation step in Eq. 12.7.[44, 101]

In any case, the unidirectional pronunciation of the surface state oxidation current as measured in Fig. 12.2 and Fig. 12.5 only appears at very slow scan rates in anodic voltage evolution. This unidirectional behaviour corresponds with the results in [101]

and indicates a slow but irreversible surface charging step to constitute the charge accumulation process as rate limiting step of the OER photo-oxidation mechanism at the α-Fe_2O_3 photoanode. In contrast, step **1** in Tab. 11.1 was found to be the most reversible reaction in the whole catalytic cycle, whereas the unidirectional pronunciation of the surface state oxidation indicates a highly irreversible reaction. Following this argumentation, the surface state oxidation current could rather reflect reaction Eq. 12.9 corresponding to step **2** in Tab. 11.1 where the accumulated surface charge oxyl-species are consumed, which is essentially only occurring in forward direction.[44] Also, electrochemical indications of surface state charge accumulation processes were observed for both the illuminated and the dark electrode. This would rather indicate that photo-excited charge transfer to the electrode surface plays a minor role in the slow OER kinetics at α-Fe_2O_3 electrodes but rather a chemical process as indicated by Eq. 12.9. In any case, the determination of the energetic localization of surface states and charge accumulation processes might provide options for future activities on the identification of the corresponding chemical processes.

Part IV

Discussion

13 Field confinement

13.1 Static field width

In Chapter 10 we have observed a transition from a parabolic to a linear SHG potential dependence when the space charge layer has expanded to the back contact of the α-Fe_2O_3 film. Now we want to analyse the underlying mechanism of the lower order SHG potential dependence at potentials above 1.0 V_{RHE} which appears to be similar to the linear behaviour reported by Lantz et al.[79, 137] and Bian et al.[81]
These studies point out that the limited SHG probing depth essentially constrains the measured SHG signal to a certain width. This behaviour is explained by the Mott-Schottky-approximation where $Q_{SC} \propto |\mathbf{E}_{DC}| \propto \sqrt{\Phi_{SC}}$ so that $I_{2\omega} \propto |\mathbf{E}_{DC}|^2 \propto \Phi_{SC}$. However, it should be noted that, if just a narrow top layer is probed by the SHG fields, this layer is completely depleted of free charge carriers, so that the space charge $Q_{SC} = const$ and would not further affect the static field (see Fig. 13.1(a)). While this width is constraint by the material absorption coefficients in those works, the maximum attainable third order field overlap is given by W_{SC}^{Max} i.e. the α-Fe_2O_3 film thickness or particle size in the works presented here. Therefore, the transition from quadratic to a lower order potential dependence in EFISH measurements would rather correspond to a constraint Gaußian surface as no expansion of the depletion width into the material is provided from further electrode bias in both cases. An illustration of both effects is shown in Fig. 13.1.

A mathematical formulation of this observation would be the definition of a maximum DC field width z_{Max}, which is given by the light absorption pathlength for the single crystals and by the film thickness in case of a completely depleted electrode material as shown Fig. 13.1(a). The phenomenological effect for both cases is a transition from a quadratic to a linear potential dependence of the SH response as given in Fig. 13.1(b).

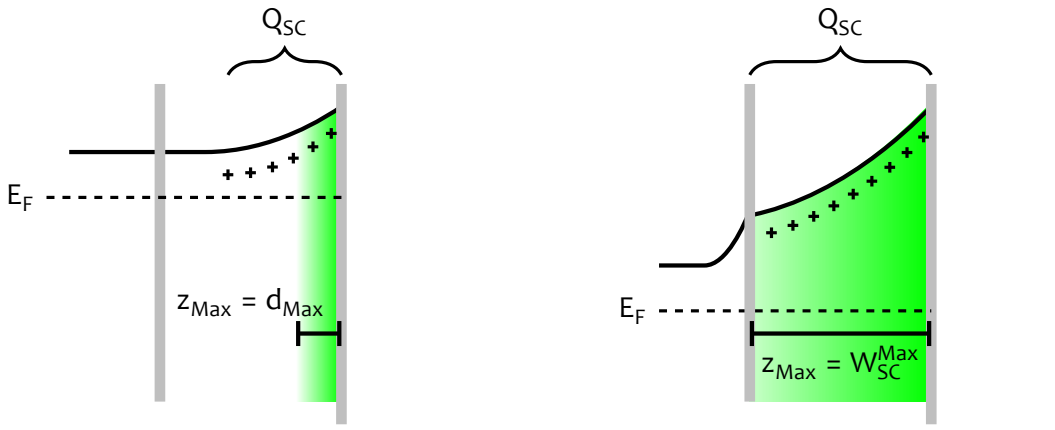

Absorption limited field enhancement | Thickness limited field expansion

(a) SHG under constraint expansion of the static field due to absorption limited probing depth and thickness limited field expansion (see Section 10.2).[81, 88, 137]

$$I_{2\omega}\Big|_{\mathrm{I}_\omega,\,\chi^{(2)}=\mathrm{const}} \propto \begin{cases} {\Phi_{\mathrm{DC}}}^2 & \text{for} \quad x < x_{\mathrm{Max}} \\ \Phi_{\mathrm{DC}} & \text{for} \quad x > x_{\mathrm{Max}} \end{cases} \tag{13.1}$$

(b) Empirical description for the SHG potential dependence under optically constraint DC-field probing depth and film thickness limited space charge expansion width

Figure 13.1: Empirical description of the linear potential dependence of the SHG response due to constraint static field expansion

13.2 Field enhancement

The empirical findings in Chapter 10 suggest that the SHG response is proportional to the squared intensity of the space charge potential drop.

$$I_{2\omega} \propto (\Phi_{\mathrm{DC}})^2 \tag{13.2}$$

This assumption is justified by i) the very good agreement between the flat-band potentials as derived from SHG and complementary EIS in Section 10.1.2, ii) the explanation of the linear part of the $I_{2\omega}(\Phi_{\mathrm{Ext}})$ curves by a material electronic effect instead of an optical probing restriction in Section 10.2, iii) the clear correspondence between the $I_{2\omega}$ and Φ_{Ext} as function of the cell current up to very anodic bias potentials in Section 9.3, iv) the absence of significant absorptive limitations to the

SHG response as derived from the absorption coefficient in Section 7.2 and v) the numerically excluded cross-term contribution to the field enhancement in Section 9.2.

$$I_{2\omega}\big|_{\mathrm{I}_\omega=\mathrm{const}} \propto \left|\chi^{(2)} + \chi^{(3)} * \Phi_{\mathrm{DC}}\right| \tag{13.3}$$

Based on the postulated and justified equation Eq. 13.2, we want to follow the most common formulation of the EFISH effect and define the potential dependence of the SHG intensity for constant incident field according to Eq. 13.3.[79, 81, 125, 142, 144] A parametric description of Eq. 13.3 in terms of $I_{2\omega} = A * (\Phi_{\mathrm{Ext}} - \varphi_{\mathrm{FB}})^2 + C$ reproduces the fit equation of the $I_{2\omega}(\Phi_{\mathrm{Ext}})$ curves that was quite successfully applied to derive EC effects in Chapter 10.

13.3 Dielectric polarization

So far we have elaborated a quadratic relationship between the SHG intensity and the potential drop across the α-Fe_2O_3 film Φ_{DC}. From experimental comparison between the particle size with the donor density in Section 10.2 it was also found that this parabolic behaviour is not provided at potentials above 1.0 V_{RHE}. In this case, the polarization of the sparsely doped α-Fe_2O_3 film can be no longer compensated by a depletion of free carriers, as the space charge width in an idealized one-dimensional α-Fe_2O_3 film has reached the back contact so that the n-type semiconducting material is exhausted of free charge carriers. Therefore, the α-Fe_2O_3 film would not behave as semiconductor at elevated anodic potentials but rather as a dielectric material.
Under such dielectric conditions, the external bias would be distributed over another layer of the sample system, which could in principle be the F:SnO_2 back contact or the Helmholtz layer. A similar behaviour was observed in Mott-Schottky experiments by van de Krol et al., where the potential drop was found to be distributed over an entirely depleted TiO_2 electrode and an indium tin oxide (ITO) back contact.[88, 249] We want to follow this assignment, which also seems a plausible scenario because i) the α-Fe_2O_3 and F:SnO_2 space charge capacitances seem to be quite close as apparent from the Mott-Schottky analysis in Section 10.1.2 and ii) the double layer capacitance, instead, exceeds the space charge by more than two magnitudes as shown in Section 12.1. Assuming a serial arrangement of back-contact, α-Fe_2O_3 film and surface

layers, we can neglect contributions from the electrolyte or the electrode surface to the overall capacitive response.[26]

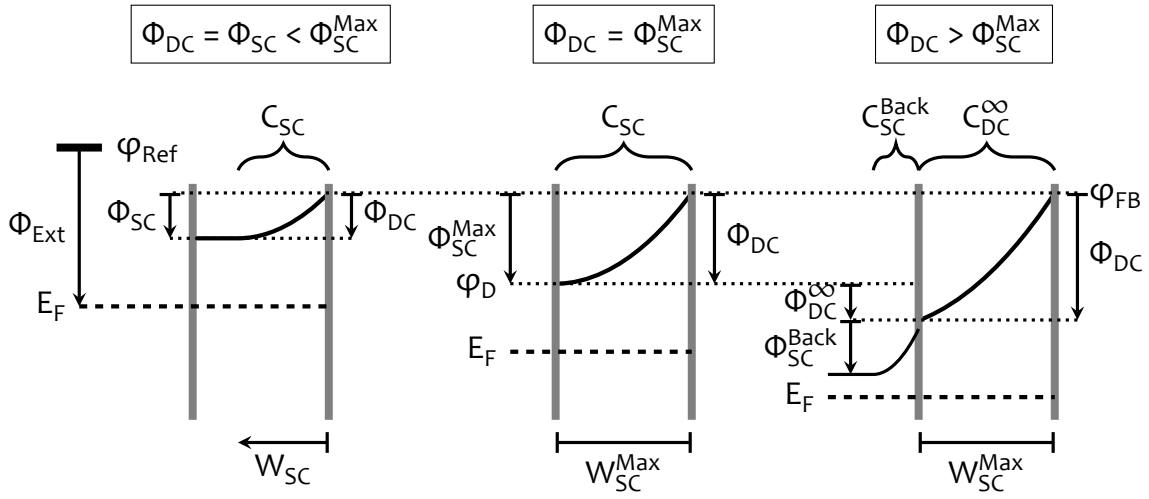

Figure 13.2: Electric field distribution over the α-Fe_2O_3 electrode with an n-type semiconductor back contact under finite carrier depletion and dielectric polarization conditions [88]

A model of the DC-field distribution over the electrode system at different bias potentials is illustrated in Fig. 13.2. We see an energy diagram of the α-Fe_2O_3 electrode and an n-type semiconducting back contact at increasing bias potentials from the left to the right. At moderate bias, i.e. for $(\Phi_{\mathrm{Ext}} - \varphi_{\mathrm{FB}}) < \Phi_{\mathrm{SC}}^{\mathrm{Max}}$, the external bias entirely falls across the α-Fe_2O_3 SCR so that $\Delta\Phi_{\mathrm{Ext}} = \Delta\Phi_{\mathrm{SC}}$. If the bias is further increased, the space charge width W_{SC} approaches the back contact and no further carrier depletion is possible. Under these conditions the Mott-Schottky relation is no longer fulfilled as $\mathrm{d}Q_{\mathrm{SC}} = 0$ for $\mathrm{d}\Phi_{\mathrm{Ext}} > 0$. The material is exhausted of free carriers and the space charge potential drop has reached a maximum where $\Phi_{\mathrm{Ext}} = \varphi_{\mathrm{D}}$, $\varphi_{\mathrm{D}} - \varphi_{\mathrm{FB}} = \Phi_{\mathrm{SC}}^{\mathrm{Max}}$ and $W_{\mathrm{SC}} = W_{\mathrm{SC}}^{\mathrm{Max}}$. The deflection potential value, here denoted as φ_{D}, would correspond to the deflection point of the $I_{2\omega}(\Phi_{\mathrm{Ext}})$ curve, where the parabolic relation changes to a linear potential dependence at 1.0 V_{RHE}. Any further bias is no longer be compensated by a depletion of free carriers from the semiconductor material.

Following the conclusions in reference [88] and considering a large surface charge density in series with the space charge potential drop, the α-Fe_2O_3 electrode would then behave as a conventional dielectric and form a plate capacitance in series with the semiconducting F:SnO_2 back contact when the potential is further increased beyond $\Phi_{\mathrm{Ext}} \geq \varphi_{\mathrm{D}}$.[87, 88]

Along this plain model, we want to consider the two layers from α-Fe_2O_3 and F:SnO_2 as two capacitors in series where the SHG response shows a linear potential dependence, so that the fully depleted α-Fe_2O_3 film serves as plate capacitor C_{DC}^{∞} and the F:SnO_2 back contact would form a supplementary n-type space charge capacitance C_{SC}^{Back}. As two similar serial capacitances have the same charge associated with them, they serve as voltage divider and the potential distribution is given by Eq. 13.4.[26, 166] In this equation Φ_{DC}^{∞} denotes the potential drop over the α-Fe_2O_3 film under henceforth complete carrier depletion, i.e. linear potential dependence of the SHG response at $\Phi_{Ext} \geq 1.0\,V_{RHE}$.

$$\Delta\Phi_{DC}^{\infty} = \Delta\Phi_{SC}^{Back} * \frac{C_{SC}^{Back}}{C_{DC}^{\infty}} \tag{13.4}$$

As the fully depleted α-Fe_2O_3 film serves as plate capacitance which is independent of the applied bias according to $C_{DC}^{\infty} = const$, the potential drop over the dielectric α-Fe_2O_3 film is proportional to the potential drop and the capacitance of the back contact according to Eq. 13.5.

$$\Delta\Phi_{DC}^{\infty} \propto \Delta\Phi_{SC}^{Back} * C_{SC}^{Back} \tag{13.5}$$

Considering an n-type semiconducting behaviour of the substrate [87] we can suppose Mott-Schottky properties of the back contact $C_{SC}^{Back} \propto {\Phi_{SC}^{Back}}^{-1/2}$. The potential change over the depleted α-Fe_2O_3 film would be therefore proportional to the square root of the potential drop over the back contact according to Eq. 13.6, where the back contact potential drop is given by the difference between external bias change and the respective back contact flat-band conditions φ_0^{Back}.

$$\Delta\Phi_{DC}^{\infty} \propto \sqrt{\Delta\Phi_{SC}^{Back}} \propto \sqrt{\Delta\Phi_{Ext} - \varphi_0^{Back}} \tag{13.6}$$

As the SHG intensity is solitarily generated in the α-Fe_2O_3 film and only responds to the potential drop over the α-Fe_2O_3 film according to Eq. 13.3 (see also Section 9.2), we can now express the linear relationship between $I_{2\omega}$ and Φ_{Ext} according to Eq. 13.7 and introduce an analytical expression for the linear potential dependence of the SHG response at semiconductor electrodes.[79, 81]

$$\boxed{I_{2\omega}\Big|_{\Phi_{\mathrm{DC}}>\Phi_{\mathrm{SC}}^{\mathrm{Max}}} \propto \left(\Phi_{\mathrm{DC}}^{\infty}\right)^2 \propto \sqrt{\left(\Phi_{\mathrm{SC}}^{\mathrm{Back}}\right)^2} \propto \left(\Phi_{\mathrm{Ext}} - \varphi_0^{\mathrm{Back}}\right)} \tag{13.7}$$

The preceding considerations allow for a quantitative description of the potential dependent SHG response $I_{2\omega}(\Phi_{\mathrm{Ext}})$. In any case, the SHG response scales with the squared DC electric field over the α-Fe_2O_3 film according to Eq. 3.16 and Eq. 10.1. For an unconstrained space charge expansion into the bulk α-Fe_2O_3 electrode material, the SH scales with the space charge evolution, i.e. $I_{2\omega} \propto {\Phi_{\mathrm{SC}}}^2$. If the expansion of the probed electric field is spatially constraint, which might be the case for both, a limited probing depth or a completely depleted semiconductor thin film as sketched in Fig. 13.1(a), the SHG would effectively probe a dielectric material in series with a semiconducting back contact. Under these conditions, the dielectric polarization follows a field distribution over a potential independent plate capacitance with an unrecorded space charge capacitance in series. The fraction of dielectric polarization would depend on the space charge potential drop beneath the probed electrode layer and therefore follow a Mott-Schottky behaviour of the semiconducting back contact according to Eq. 13.7. Note that this model would also apply to the studies on other n-type semiconductor electrode systems in [79, 81]. In these experiments, due to the dielectric polarization as function of the serial back contact space charge layer, the determination of flat-band potentials corresponding to $\varphi_0^{\mathrm{Back}}$ is still valid in these studies, as the bulk α-Fe_2O_3 material serves as back layer to the probed top layer which is sensed in case of an absorption limited SHG probing process.

13.4 Third order SHG field confinement

From the preceding considerations we can develop a quantitative model to describe the potential dependent SHG response over the entire potential range which is illustrated in Fig. 13.3. In Eq. 9.7 we have already developed a model to describe the quadratic part of the SH response in terms of a parabola with a vertex at φ_{FB}, a scaling coefficient A and an offset $C = I_{2\omega}^0$. The quadratic curve deflects to a linear shape due to a dielectric polarization above a dividing dependence deflection potential φ_{D}. From the quadratic fit parameters we can construct an analytic expression of the linear part of the SHG response, where $I_{2\omega} \propto \Phi_{\mathrm{SC}}^{\mathrm{Back}}$. From Eq. 13.7, we can infer

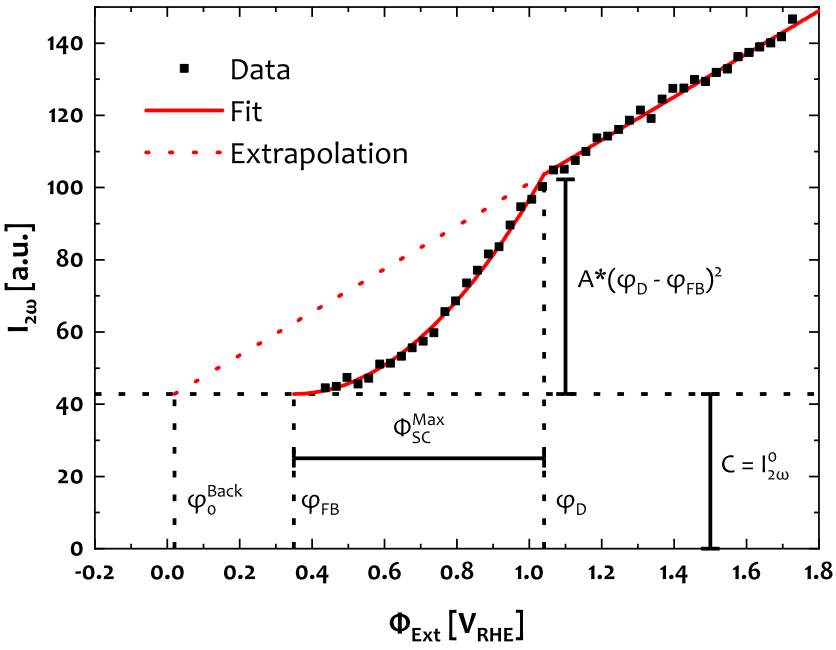

(a) Global fit of the potential dependent SHG response at changing boundaries from constrained and unimpeded space charge evolution with the corresponding parameters

$$I_{2\omega}(\Phi_{\mathrm{Ext}}) = \begin{cases} A * (\Phi_{\mathrm{Ext}} - \varphi_{\mathrm{FB}})^2 + I^0_{2\omega} & \text{for} \quad \Phi_{\mathrm{Ext}} < \varphi_{\mathrm{D}} \\ \dfrac{A * (\varphi_{\mathrm{D}} - \varphi_{\mathrm{FB}})^2}{\varphi_{\mathrm{D}} - \varphi_0^{\mathrm{Back}}} * (\Phi_{\mathrm{Ext}} - \varphi_0^{\mathrm{Back}}) + I^0_{2\omega} & \text{for} \quad \Phi_{\mathrm{Ext}} \geq \varphi_{\mathrm{D}} \end{cases} \tag{13.8}$$

(b) Numerical model of the SHG potential dependence at changing boundary conditions due to a transition from carrier depletion to dielectric polarization

Figure 13.3: Bimodal fit of the potential dependent SHG intensity for unimpeded and constrained space charge following the energetic considerations from Fig. 13.2

that the extrapolated linear curve leads to the potential of zero back contact band bending $\varphi_0^{\mathrm{Back}}$ according to $I_{2\omega}(\Phi_{\mathrm{SC}}^{\mathrm{Back}} = 0) = 0 + I^0_{2\omega}$, while the offset of the parabola vertex $C = I^0_{2\omega} = const$ is not affected by the static field. The slope of this linear plot would correspond to the fraction of the potential differences $A * (\varphi_{\mathrm{D}} - \varphi_{\mathrm{FB}})^2$ divided by $\varphi_{\mathrm{D}} - \varphi_0^{\mathrm{Back}}$ as shown in Eq. 13.8. A five parameter case dependent fit of this expression is shown in Fig. 13.3(a), a summary of the parameters and statistical quantities of this fit are appended in Fig. XX(a).

Model	Parameter	Value	Unit
Two case global fit	φ_{FB}	0.38 ± 0.03	V_{RHE}
	$\varphi_0^{\mathrm{Back}}$	0.07 ± 0.03	V_{RHE}
	φ_{D}	1.02 ± 0.01	V_{RHE}
	$I_{2\omega}^0$	43.8 ± 1.2	a.u.
	A	141 ± 11	a.u.
Separate parabolic fit	φ_{FB}	0.43 ± 0.02	V_{RHE}
	$I_{2\omega}^0$	45.1 ± 0.7	a.u.
	A	178 ± 14	a.u.

Table 13.1: Space charge evolution parameters obtained from the case-sensitive global parabolic and linear fits of the potential dependent SHG response

The numerical fit parameters of the potential dependent SHG response are presented in Tab. 13.1, where a comparison is drawn between the case dependent global fit as shown in Fig. 13.3 and the separate parabolic fit that was applied to determine the flat-band potential in Section 10.1. We see that the extrapolation of the linear part of the SHG response indicates virtual flat-band potential of the F:SnO_2 substrate $\varphi_0^{\mathrm{Back}}$ at 0.02 V_{RHE}, i.e. the back contact is set to more than 0.3 V band bending when the α-Fe_2O_3 electrode material is biased to flat-band conditions. The case dependent fit of the parabolic part shows both a smaller scaling coefficient and a decreased flat-band potential, most probably due to the infinitely sharp transition at φ_{D} in this model, whereas a more gradual transition between both boundary conditions is physically reasonable due to size and dopant distributions, for instance, and also numerically visible in the dataset. Therefore, the transition range between both cases causes a transitional flattening of the quadratic scaling coefficient which is not reflected in Eq. 13.8 resulting in a slight overestimation of the quadratic slope and a reduced parabolic vertex potential.

While a proof of this two case model would require further experimental confirmation in terms of a series of varying thickness or dopant concentration, for instance, Fig. 13.3 in principle provides experimental access not only to directly measure the α-Fe_2O_3 photoanode space charge evolution under operating conditions but also to draw conclusions on the field distribution between an SHG active top layer and a semiconducting back contact. This model is in principle also applicable to experiments where the probing depth is limited by light absorption in the sample while the passive polarization of a depleted and dielectric top layer at a semiconducting

bulk material still allows for determination of bulk film flat-band potentials (see also Fig. 13.1(a) and Fig. 13.2).[79, 81] In this case, the flat-band potential of the bulk electrode, which is not sampled by the sensed fields, would correspond to $\varphi_0^{\mathrm{Back}}$ in Eq. 13.8 which can be simply extracted from the intersection of the potential dependent SHG response with minimum SHG intensity.[79, 81]

14 Spectral analysis

14.1 Optical transitions

Now, as we gathered some ideas of the electrostatic field distribution across the α-Fe_2O_3 photoanode system, we want to see if we can infer information on the electronic structure from spectroscopic observations. In general, the SH is generated in a potentially absorptive medium so that electronically resonant contributions to the signal should be considered here. Also, the potential dependent SHG response shows a relatively large intensity under flat-band conditions, which would rather indicate a resonant SHG than a non-resonant process so that the SH emission seems to be rather *enhanced* than induced by the static field at the electrode interface.[128]
An overview of possible electronic transitions contributing to the SHG signal formation is shown in Fig. 14.1. In the upper panel of Fig. 14.1(a), we see the line shapes of the NIR fundamental probe beam at 1180 nm and the corresponding SHG signal from α-Fe_2O_3 as set through all the previous potential dependent SHG measurements, in combination with the linear absorption spectrum of the sample. Considering the spectral overlap between the laser lines from the SHG experiment with the absorption spectrum of the sample, we can hypothesise three possible optical transitions contributing to the SHG response, which are shown in Fig. 14.1(b).
The first possible transition, shown in red in Fig. 14.1(b), could stem from a quite small overlap of the fundamental NIR with a small absorption feature at 1.5 eV. As this absorption feature appears 0.6 eV below the conduction band-edge energy of the sample, it would correspond to a set of mid-gap electronic states.[65, 226, 228] Thus, with $\mathcal{E}_{2\omega} = 2 * (\mathcal{E}_{\mathrm{SS}} - \mathcal{E}_{\mathrm{VB}})$, an initial state transition between the valence band and this mid-gap feature, would cause an SHG signal at photon energies above the band gap.
A second possible transition is sketched in green in Fig. 14.1. This transition would correspond to a final state resonance between the valence band of the material and shallow donor states just below the conduction band.[26, 188, 189] The spectral over-

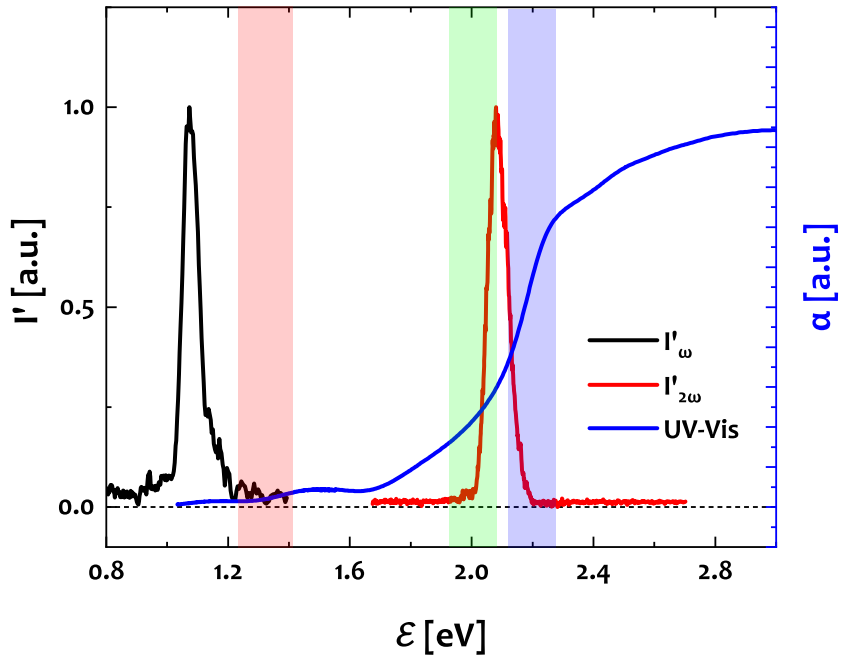

(a) Energetic overlap between fundamental and SHG signal lines with UV-Vis-NIR optical absorption spectrum

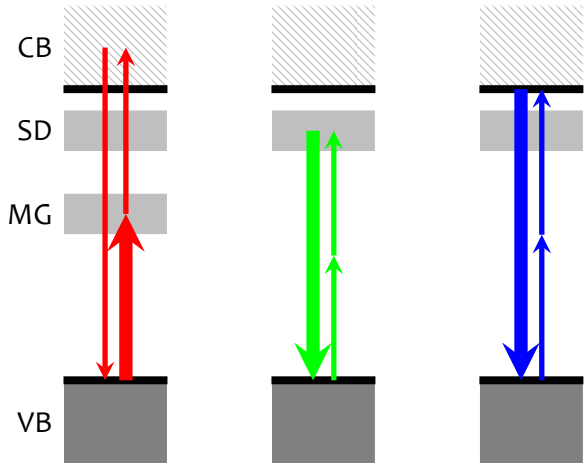

(b) Possible optical transitions involved in the formation of the SHG response considering valence band (VB), conduction band (CB), shallow donor (SD) and mid gap (MG) electronic states

Figure 14.1: Analysis of the SHG signal formation considering the spectral overlap between the incident NIR and emitted SH fields with the opto-electronic properties of the α-Fe_2O_3 sample and possible corresponding electronic transitions

lap between the SHG signal and the tail of the band-gap is relatively large so that the probability of this transition between the tail of the band-gap is quite high (see also Section 5.2.2). The green transition in Fig. 14.1 is also likely to take place as shallow donor states act as point defects in the lattice and hence as sites of broken symmetry which are in principle SHG active.[131, 250] In this context, an XPS study on sputtered α-Fe_2O_3 films has shown that a broad polaronic band approximately 0.45 eV below the conduction band is lowering the effective band-gap and constraining the Fermi-level of the material.[188] Such point defects are homogeneously distributed over the whole lattice of the material and therefore could generate a bulk active resonance and a quite large SH response from the α-Fe_2O_3 film (see Fig. 7.2).
A third possible resonance is sketched in blue in Fig. 14.1(a) and Fig. 14.1(b). It would correspond to an inter-band transition between the valence band and the conduction band of the material. Similar to the red transition, an SHG signal from the blue transition would be expected at the blue end of the spectral scale as the probing SHG photon energy is set slightly below the conduction band.
Besides these single domain lattice effects, there are further options to explain the SHG signal formation. It is also likely that the SH signal is generated in an interfacial top layer [251, 252] or in the liquid side of the interface, i.e. in the Helmholtz or double layer.[150, 152, 199] However, in a previous chapter Chapter 10 we found good agreement between flat-band potentials as determined from both EIS and SHG measurements and also between the photovoltage formation observed in quast-static and dynamic potentiometric SHG experiments (Fig. 9.6 and Fig. 12.4). Based on these experimental indications, we want to assume the SH signal formation to occur within the α-Fe_2O_3 film of the sample and see how we can assign it to one of the optical transitions as hypothesised in Fig. 14.1.

One way to distinguish between these three transitions is to compare the SHG response from the α-Fe_2O_3 photoanode with appropriate spectral references. The spectral shape of the SHG signal is strongly dependent on the incident field, according to Eq. 3.17, and a range of additional parameters.[121, 125] Therefore, it is common practise to track spectral changes in non-linear spectroscopies relative to a spectral reference in order to eliminate the fundamental beam shape from the spectra.[156, 253, 254] Thus, we want to normalize the energy dependent SH response from our α-Fe_2O_3 film $I'_{2\omega}$ to the response from a spectral reference I'_{Ref} in order to calculate a normalized SH response $\overline{I'}$ according to Eq. 14.1.

$$\overline{I'} = \frac{I'_{2\omega}}{I'_{\mathrm{Ref}}} * 100\,\% \tag{14.1}$$

A common SHG reference medium is the non-linear response from Au, as it often provides a good reference due to very broad and intense plasmonic resonances, which might reflect the spectral shape of the fundamental field quite well. Therefore, the α-Fe_2O_3 SHG response divided by the Au SHG response according to Eq. 14.1 can provide information on resonant contributions from the α-Fe_2O_3 film (see also Section 3.2.3).[156, 254] However, a normalization to the SHG response from Au can also be problematic as studies have shown resonant effects which might perturb a spectrally flat SHG response.[255]
The ideal spectral reference is the fundamental NIR probe beam, as it is completely unaffected by any sample-specific contributions, so that a spectrum normalized to the incident field would solitarily reflect possible resonant contributions from the sample system according to Eq. 3.17. However, a normalization to the fundamental probe beam is also somewhat delicate as the signal formation is correctly described by a convolution of the NIR line with itself. A numerical convolution of the fundamental field with itself is influenced by a range of non-linear effects such as signal noise, SH formation threshold field strength, integration boundaries and the optical resolution of the measured spectrum. Therefore, the NIR spectra were compared to the SHG response from the α-Fe_2O_3 film by the squared NIR amplitude and the doubled NIR photon energy according to $\mathbf{E}_{2\omega} \propto {\mathbf{E}_{\omega}}^2$ (see Section 3.2, Eq. 3.17). A detailed description of this analysis is appended in Chapter D. The measurement is based on a summation of four different spectra at fundamental wavelengths of 1140, 1160, 1180 and 1200 nm and the corresponding SHG response from the α-Fe_2O_3 film, where the NIR photon energy was converted to frequency doubling according to $\mathcal{E}_{2\omega} = 2\mathcal{E}_{\omega}$ (see Fig. XVII). The NIR spectral scale was referenced to the calibrated SHG spectrometer scale using two common characteristic features of the sum spectra as shown in Fig. XVIII. An overview of the calibrated linear and squared NIR fields and the corresponding SHG responses from α-Fe_2O_3 and Au is shown in Fig. XIX, where good spectral alignment is found between the square of the NIR fundamental at the two-photon energy of the α-Fe_2O_3 SHG spectral response. In Fig. 7.2 we can already see that the SHG response from α-Fe_2O_3 is enhanced at lower two-photon energies

compared to the squared NIR fundamental beam shape while the Au film shows increasing SHG response with increasing two-photon energies.
The normalized SHG spectra from the α-Fe_2O_3 film relative to the squared fundamental spectra at two-photon energy scale is shown in Fig. 14.2. We see that the α-Fe_2O_3 SH response is increased at lower two-photon energies, just as also observed in comparison with the SHG spectral response from Au in Fig. 7.2.
Fig. 14.3(a) shows the normalized α-Fe_2O_3 SHG spectra from Fig. 7.2 as references to the response from Au and the fundamental NIR beam shape according to Eq. 14.1 together with the linear UV-Vis-absorption spectrum of the sample. We can see that the SHG response is increasing with lowering two-photon energies away from the band-gap of the material (see Section 5.2.2). While the SH response from α-Fe_2O_3 is lower than that from Au above the band-gap ($E_G = 2.1\,\mathrm{eV}$), i.e. $\overline{\Psi}_{Au} < 100\,\%$, it increases towards the red side of the spectrum. The same is observed for the normalization to the squared fundamental NIR beam shape. This analysis suggests that the main SH signal from the α-Fe_2O_3 film is most likely generated at the two-photon energy range within the tail of the band-gap, which was hypothesized as green transition in Fig. 14.1(a) and Fig. 14.1(b). This assignment would also explain the high SHG intensity from the α-Fe_2O_3 electrode even compared to the very SHG active Au surface: A transition into a set of electronic defect states would be allowed through the whole bulk crystallites since such point defects are constituting sites of broken lattice symmetry.[131, 222, 250] This assignment is also supported by the large offset of the SHG response under flat-band conditions in Fig. 10.1, for instance. As there is also a quite large SHG signal, i.e. where no static field is present at the electrode surface, an optical transition through the bulk electrode material seems favourable over a non-resonant or a surface limited SHG process.
Thus, due to the large enhancement of the SHG response in overlap with the tail of the conduction band-edge, it seems very likely that the main SHG signal intensity stems from a bulk active final state resonance between the valence band and a set of defect states below the conduction band of the material.[61, 188, 189, 222]

14.2 Potential dependent spectral shift

As already shown in Fig. 9.2, the potential dependent SHG spectra exhibit a small but significant shift of the spectral centre of gravity, i.e. the expectation value of the SH photon energy $\langle \mathcal{E}_{2\omega} \rangle$ which is emitted from the α-Fe_2O_3 photoanode. For a given

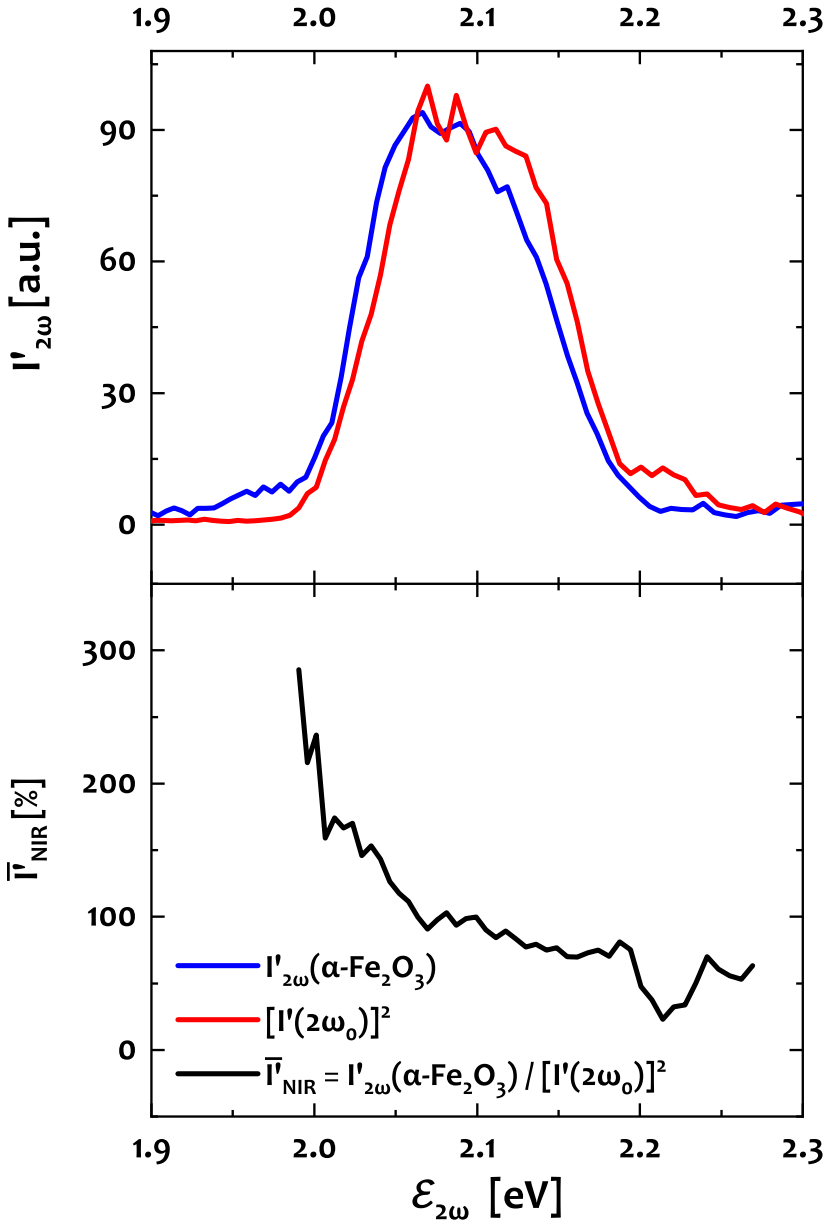

Figure 14.2: Normalization of the α-Fe_2O_3 SHG response to the squared intensity of the fundamental beam shape at the two-photon energy scale. More details of the data analysis are appended in Fig. XVII, Fig. XVIII and Fig. XIX.

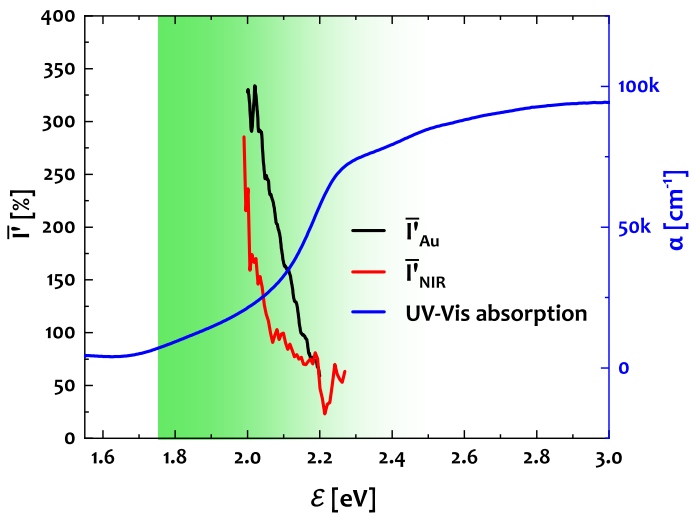

(a) Relative α-Fe_2O_3 SHG spectra as derived from normalization to an Au and a NIR reference in comparison with the UV-Vis-NIR absorption spectrum. The primary data for $\overline{I'}_{\mathrm{Au}}$ and $\overline{I'}_{\mathrm{NIR}}$ is shown in Fig. 7.2 such as Fig. 14.2, Fig. XVII, Fig. XVIII and Fig. XIX, respectively.

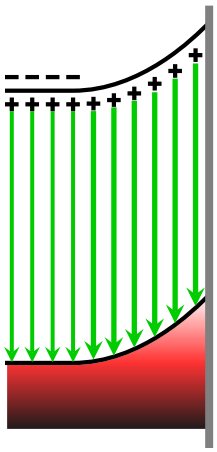

(b) Supposed formation of the main SHG response due to electronic transition into shallow electronic states

Figure 14.3: SHG signal analysis by normalization to Au and NIR line shapes. Due to the increasing relative intensity with decreasing two-photon energy, an optical transition into electronic defect states below the conduction band and appears as most likely optical transition to form the SH response [61, 131, 188, 189, 222, 250]

discrete amount of photons k, $\langle \mathcal{E}_{2\omega} \rangle$ corresponds to the sum of all photon energies $\mathcal{E}_{\mathrm{k}}$, weighted by their normalized probability $p(k)$ to appear in the SH spectra according to Eq. 14.2. An alternative expression for continuous distributions is the integral form with a probability density function $p(\mathcal{E})$ according to Eq. 14.2.[136, 223]

$$\langle \mathcal{E}_{2\omega} \rangle = \sum^{k} \mathcal{E}_{\mathrm{k}} * p_{\mathrm{k}} = \int_{\mathrm{h}\nu} E * p(\mathcal{E}) \mathrm{d}\mathcal{E} \qquad 14.2$$

The normalized probability density function $p(\mathcal{E})$ to find an SH photon at a given energy $\mathcal{E}$ within the spectral range $\mathcal{E}_{\mathrm{Min}} = 1.95\,\mathrm{eV} \leq \mathcal{E}_{2\omega} \leq 2.25\,\mathrm{eV} = \mathcal{E}_{\mathrm{Max}}$ is given

by the detected counts at this energy $I'_{2\omega}$ relative to the integral sum of all counted photons $I_{2\omega}$ according to Eq. 14.3.[136, 223]

$$p(\mathcal{E}) = I'_{2\omega}(\mathcal{E}) * \left(\int_{\mathcal{E}_{\mathrm{Min}}}^{\mathcal{E}_{\mathrm{Max}}} I'_{2\omega}(\mathcal{E})\,\mathrm{d}\mathcal{E} \right)^{-1} = \frac{I'_{2\omega}(\mathcal{E})}{I_{2\omega}} \tag{14.3}$$

Inserting Eq. 14.2 in Eq. 14.3 delivers an expression for the SH signal photon energy expectation value $\langle E_{2\omega} \rangle$ under the given experimental boundaries according to Eq. 14.4.[136, 223]

$$\boxed{\langle \mathcal{E}_{2\omega} \rangle = \frac{1}{I_{2\omega}} \int_{\mathcal{E}_{\mathrm{Min}}}^{\mathcal{E}_{\mathrm{Max}}} \mathcal{E} * I'_{2\omega}(\mathcal{E})\,\mathrm{d}\mathcal{E}} \tag{14.4}$$

A plot of the SHG spectra expectation values trace as function of the applied potential is shown in Fig. 14.4. The values of $\langle \mathcal{E}_{2\omega} \rangle$ span over a range of 0.08 eV and thus indicate a spectral shift of less than 3 % of the line width that was used to examine the α-Fe_2O_3 photoanode interface. We can already see that the data trace might also follow the two-modal parabolic and linear potential dependence that we have examined in Section 13.1. In this regard, as described in the previous chapter Section 13.1 and as further discussed in Section 14.4, the potential dependent expectation value has a minimum 0.72 V_{RHE}.

14.3 Spectral deconvolution approaches

As the spectral shape of the SHG response is quite indifferent, we need to find suitable methods to deconvolve the SH spectral response in order to provide the observed shift with physical meaning. One approach could be a normalization procedure as already applied in Section 14.1 (see Eq. 14.1). However, in this case we want to investigate spectral changes *within* the $I_{2\omega}(\Phi_{\mathrm{Ext}})$ datasets so that an *internal reference* seems preferable instead of the external Au and NIR references as applied in Section 14.1. An intuitive signal to refer spectral changes could be a normalization to the SHG spectra at characteristic internal potentials, i.e. the flat-band conditions obtained

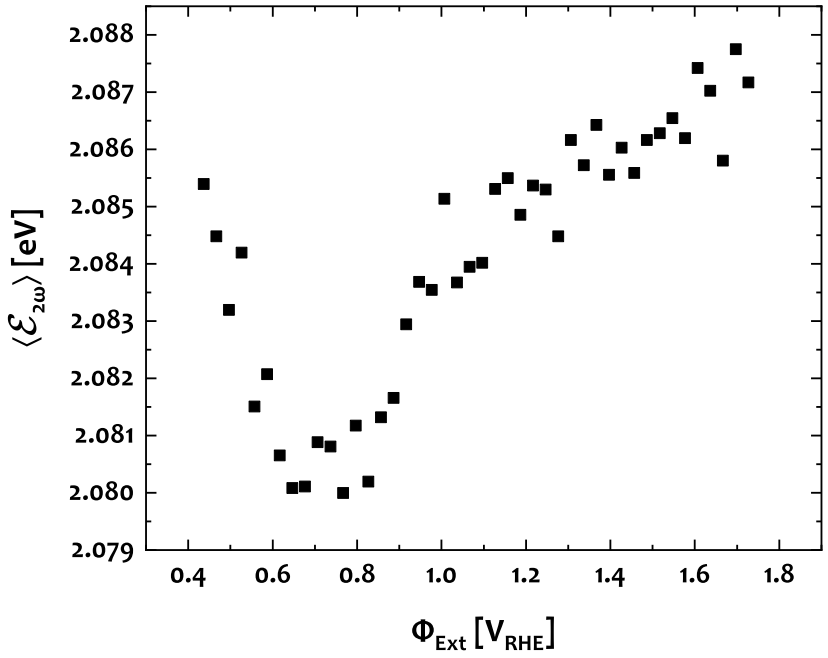

Figure 14.4: Centre of gravity of the potential dependent SHG spectra from an operating α-Fe_2O_3 photoanode in the dark corresponding to the extensively inspected dataset as already presented in Fig. 9.1, Fig. 9.2, Fig. 9.3 and Fig. 13.3, for instance

from the minima of $I_{2\omega}(\Phi_{\mathrm{Ext}})$ and $\langle\mathcal{E}_{2\omega}\rangle\,(\Phi_{\mathrm{Ext}})$ data plots according to Eq. 14.5. This approach should in principle provide information on the spectral changes relative to minimum extent of the SHG intensity and spectral shift, respectively.

$$\overline{I'}_{\mathrm{FB}}(\mathcal{E}_{2\omega},\Phi_{\mathrm{Ext}}) = \frac{I'_{2\omega}(\mathcal{E}_{2\omega})}{I'_{2\omega}(\mathcal{E}_{2\omega},\Phi_{\mathrm{Ext}})\Big|_{\Phi_{\mathrm{Ext}}=\varphi_{\mathrm{FB}}}} \tag{14.5}$$

Fig. 14.5 shows the normalized SHG spectra $\overline{I'}_{\mathrm{FB}}$ with respect to the SHG spectra at minimum $I_{2\omega}$ and $\langle\mathcal{E}_{2\omega}\rangle$, respectively, as function of the applied potential Φ_{Ext} in a colour coded intensity map. In the left-hand side of Fig. 14.5 we see spectral changes relative to the SHG response at minimum SHG intensity at $\Phi_{\mathrm{Ext}} = \varphi^{I}_{\mathrm{FB}} = 0.43\,\mathrm{V_{RHE}}$, the right-hand side shows the corresponding results with respect to the shift for $\Phi_{\mathrm{Ext}} = \varphi^{\mathcal{E}}_{\mathrm{FB}} = 0.72\,\mathrm{V_{RHE}}$. The horizontal white lines indicate $\varphi^{I}_{\mathrm{FB}}$ and $\varphi^{\mathcal{E}}_{\mathrm{FB}}$, respectively, which correspond to a normalized SHG intensity of $\overline{I'}_{\mathrm{FB}} = 100\,\%$

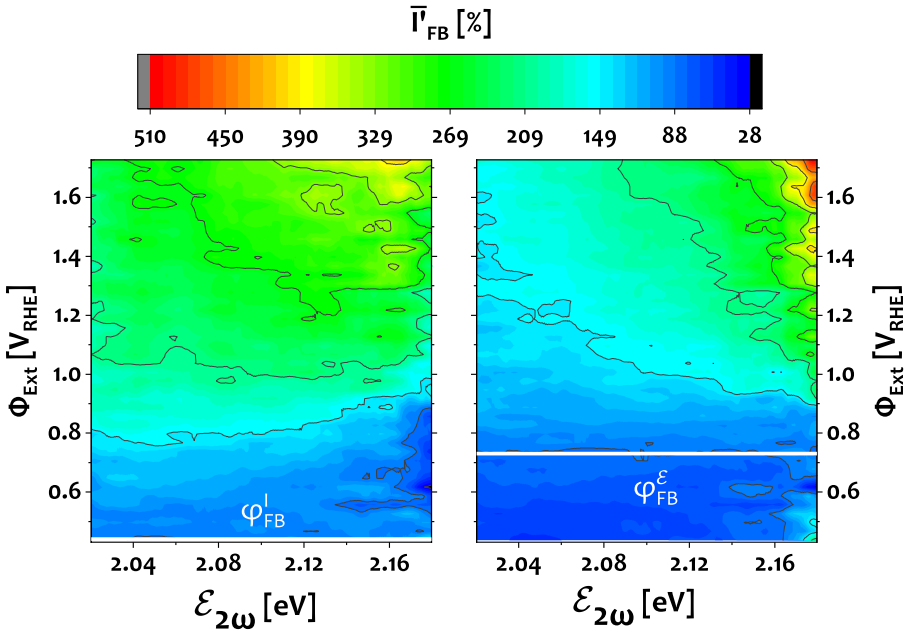

Figure 14.5: Spectral changes of the SHG response with respect to the two flat-band conditions according to the intensity $I_{2\omega}$ and spectral shift $\langle E_{2\omega} \rangle$ minima. The normalization to minimum spectral shift reveals larger SHG response at the blue side of the spectrum whereas the spectral changes relative to minimum SH intensity are more distributed over the spectral range

according to Eq. 14.1.
The left-hand side of Fig. 14.5 shows spectral changes relative to the minimum of the $I_{2\omega}(\Phi_{\mathrm{Ext}})$ curves. We see that the increase of the SHG intensity with increasing electrode potential Φ_{Ext} mainly takes place over the whole spectral range. On the right-hand side, instead, we find that $\overline{I'}_{\mathrm{FB}}$ is increasing significantly stronger at higher two-photon energies when it is referred to the spectra at the minimum of the $\langle \mathcal{E}_{2\omega} \rangle (\Phi_{\mathrm{Ext}})$ curves. Therefore, we find that the spectral shift of the SHG response probably stems from contributions at higher photon energies.

Another option to decompose the SHG spectral response is a singular value decomposition (SVD). In this analysis, the $\{I'_{2\omega}, \mathcal{E}_{2\omega}, \Phi_{\mathrm{Ext}}\}$ data triplet is represented in a rectangular matrix $\mathbf{M}$. This matrix can be factorized by a set of elemental components $\mathbf{\Sigma}$ with singular values $\{\sigma_1, \sigma_2, ..., \sigma_n\}$ according to Eq. 14.6, where $\mathbf{U}$ is a unitary matrix $\mathbf{V}$ and the adjunct matrix.[256]

$$\mathbf{M} = \mathbf{U}\mathbf{\Sigma}\mathbf{V}^{*} \tag{14.6}$$

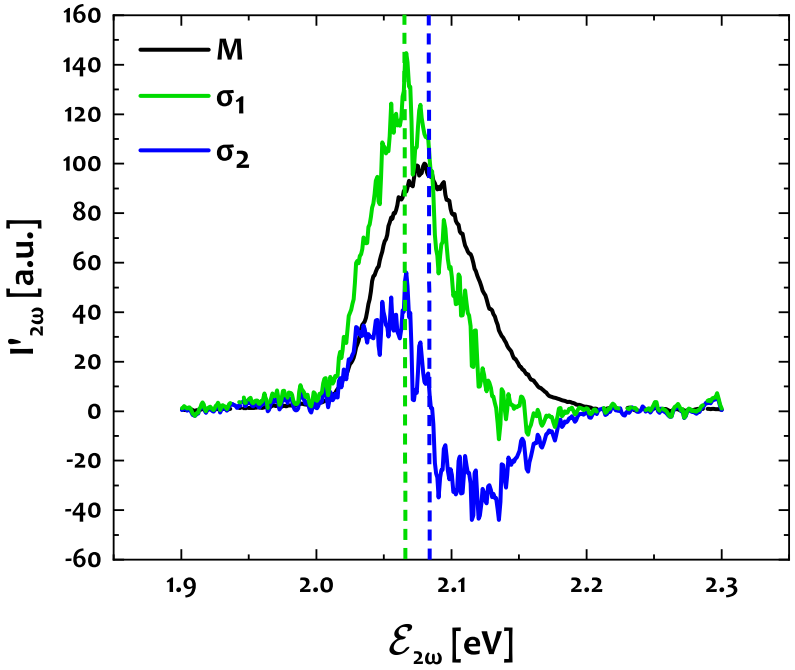

Figure 14.6: SVD of the potential dependent SHG spectra matrix **M**. Two components in the **Σ**-matrix were obtained above noise level, where a main component of fairly Gaußian shape and a blue shifted minor component are obtained

The corresponding SVD analysis is presented in Fig. 14.6. The graph shows an SVD of the potential dependent SHG spectra, where the **M**-matrix of the SHG signal is represented by a linear combination of its principal components σ_i. Two singular values were obtained with significance. While the first component σ_1 is of fairly Gaußian shape, the second singular value σ_2 is rather forming of a peak derivative curve. While this shape is suitable for a numerical representation of spectral shifts,[257, 258] a physical interpretation is rather delicate. Nevertheless the centre of σ_2 is blue shifted compared to σ_1, similar to the right hand side in Fig. 14.5, where the spectral changes relative to the minimum of $\langle \mathcal{E}_{2\omega} \rangle$ were also found to occur at the blue side of the spectrum.
Therefore, both analyses indicate an SHG signal composition of one main compo-

nent and one additional contribution that is blue-shifted with respect to the main component.

14.4 SHG Signal composition

So far we found indication that the SHG response is composed of two spectral components causing a shift of the two-photon emission spectra, with one main constituent and a minor component that appears at photon higher energies in the spectrum. Following this assumption, we can suppose that the measured SHG response reflects a bimodal spectral composition according to Eq. 14.7.

$$\begin{aligned} I'_{2\omega} &= I'_1 + I'_2 \\ I_{2\omega} &= I_1 + I_2 \end{aligned} \tag{14.7}$$

Both components are centred at their respective constant line positions at $\langle \mathcal{E}_1 \rangle$ and $\langle \mathcal{E}_2 \rangle$ and weighted by their partial contributions to the overall SH response according to Eq. 14.8.

$$\langle \mathcal{E}_{2\omega} \rangle = \frac{I_1}{I_{2\omega}} * \langle \mathcal{E}_1 \rangle + \frac{I_2}{I_{2\omega}} * \langle \mathcal{E}_2 \rangle \tag{14.8}$$

Considering the very small ratio of the spectral shift of less than 3 % compared to the probing line width and the assignment to a dominant final state resonance along a defect band in Section 14.1, we can suppose that $I_1 >> I_2$ so that $I_1/I_{2\omega} \approx 1$. With this, we can assume a constant contribution from the dominant signal component $I_1/I_{2\omega} * \langle \mathcal{E}_1 \rangle \approx \text{const} = \left\langle \mathcal{E}^0_{2\omega} \right\rangle$. If we implement this assumption in Eq. 14.8 we find the following expression Eq. 14.9.

$$\boxed{\langle \mathcal{E}_{2\omega} \rangle = \left\langle \mathcal{E}^0_{2\omega} \right\rangle + I_2 * \langle \mathcal{E}_1 \rangle \propto I_2} \tag{14.9}$$

Thus, for constant centre frequencies of the two signal components Eq. 14.9 and a dominating signal constituent I_1, we would find a direct proportionality relation between the observed spectral shift and the intensity of a small additional signal component contributing to the SHG response. This explanation is also supported

as each of both metrics, $I_{2\omega}$ and $\langle \mathcal{E}_{2\omega} \rangle$, shows a quite distinct parabolic and linear potential dependence as elaborated in Section 13.1.

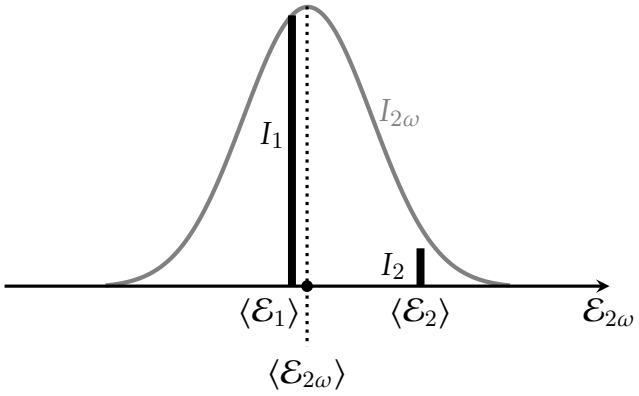

Figure 14.7: Plain two line model the describe the two photon energy expectation value $\langle \mathcal{E}_{2\omega} \rangle$ as spectral centre of gravity balanced between two independent signal components I_1 and I_2 of constant spectral position

An illustration for this model is presented in Fig. 14.7, where the SHG response $I_{2\omega}$ is interpreted as the sum of two separate signal components I_1 and I_2. The spectral centre of gravity $\langle \mathcal{E}_{2\omega} \rangle$ is very close to a dominating component I_1 so that the potential dependence of $\langle \mathcal{E}_{2\omega} \rangle$ is governed by a levering from a contribution of a minor spectral component I_2 according to Eq. 14.9. Following this model, we can interpret the spectral shift as a metric for the contribution from a minor signal component which allows for further speculations on the physical nature of the signal component I_2.

14.5 Multi-band structures

At this point, we have elaborated a global model for the potential dependent SHG response as presented in Section 13.3, while two metrics were found to show a distinct potential dependence, i.e. the integral SHG intensity $I_{2\omega}$ and a shift of the SHG spectra expectation value $\langle \mathcal{E}_{2\omega} \rangle$. The spectral shift was attributed a minor second component of the SHG response according to Eq. 14.9. Thus, both metrics would reflect an enhancement of the emitted SH field according to Eq. 3.16. Therefore, we now want to see how these two observables can be related to electronic properties of the sample system.

Fig. 14.8 shows fits of the two SHG metrics $I_{2\omega}$ and $\langle \mathcal{E}_{2\omega} \rangle$ to the case dependent model as developed in Section 13.1, the values of the respective fit parameters are

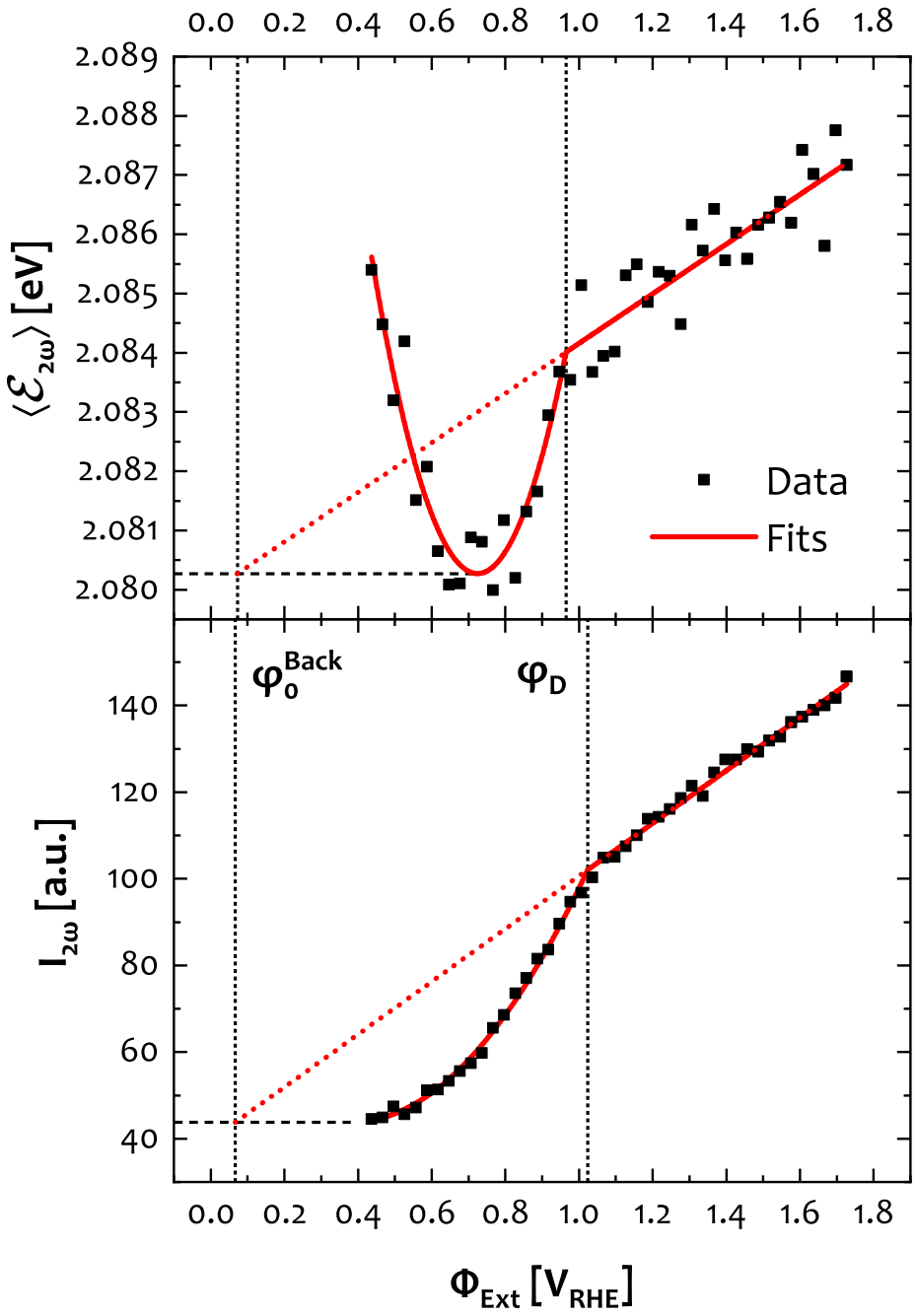

Figure 14.8: Numerical fits of the two SHG spectroscopy metrics $I_{2\omega}$ and $\langle \mathcal{E}_{\omega} \rangle$ as function of the applied potential according to the two case model as developed in Section 13.3

given in Tab. 14.1 and fit reports with the regression quantities are appended in Fig. 13.3. We see a quite similar behaviour for both observables: A parabolic shape

Parameter	Metric	
	$I_{2\omega}$	$\langle \mathcal{E}_{2\omega} \rangle$
φ_{FB} [$\mathrm{V_{RHE}}$]	0.38 ± 0.03	0.72 ± 0.01
$\varphi_0^{\mathrm{Back}}$ [$\mathrm{V_{RHE}}$]	0.07 ± 0.03	0.07 ± 0.14
φ_{D} [$\mathrm{V_{RHE}}$]	1.02 ± 0.01	0.96 ± 0.02
A	(140.7 ± 1.1) cpseVV^{-1}	(0.065 ± 0.001) eV V^{-1}
C	(43.8 ± 0.1) cpseV	(2.080 ± 0.002) eV

Table 14.1: Comparison between fit parameters for the two SHG metrics $I_{2\omega}$ and $\langle \mathcal{E}_{2\omega} \rangle$ as function of the applied potential to the case dependent split potential dependency model as presented in Fig. 13.3

for potentials less that 1.0 $\mathrm{V_{RHE}}$ and a linear shape beyond. The extrapolation of the linear part leads to very similar potentials $\varphi_0^{\mathrm{Back}} = 0.1\,\mathrm{V_{RHE}}$, both curves show a deflection from quadratic to linear potential dependence at 1.0 $\mathrm{V_{RHE}}$ and only the parabolic vertices are differing with values of $\varphi_{\mathrm{FB}}^{I} = 0.38\,\mathrm{V_{RHE}}$ and $\varphi_{\mathrm{FB}}^{\mathcal{E}} = 0.72\,\mathrm{V_{RHE}}$, respectively.

First, the agreement for both the back contact flat-band conditions $\varphi_0^{\mathrm{Back}}$ and also the deflection points φ_{D} between the two SHG metrics indicate that the model Eq. 13.8 is applicable to both of them. If we follow the physical interpretation presented in Section 13.1 and the assignment in Eq. 14.9, we would infer that both metrics $I_{2\omega}$ and $\langle \mathcal{E}_{2\omega} \rangle$ reflect band bending and dielectric polarization processes of two different electronic compartments of the sample system. While the physical boundaries of a complete depletion of these two compartments and the passive polarization due to a semi-conductive back layer are the same, $I_{2\omega}(\Phi_{\mathrm{Ext}})$ and $\langle \mathcal{E}_{2\omega} \rangle (\Phi_{\mathrm{Ext}})$ exhibit different parabolic minima thus indicating different flat-band positions at $\varphi_{\mathrm{FB}}^{I} = 0.38\,\mathrm{V_{RHE}}$ and $\varphi_{\mathrm{FB}}^{\mathcal{E}} = 0.72\,\mathrm{V_{RHE}}$, respectively.

The electronic conclusion from this observation would be that both SHG signal compartments correspond to different space charge capacitances that are simultaneously depleted and thus polarized *in parallel*. A serial depletion as for a top layer and a bulk material, for instance, would cause a potential distribution over both layers whereas the observations from $I_{2\omega}$ and $\langle \mathcal{E}_{2\omega} \rangle$ indicate a concurrent depletion of two different band structures. The findings that both flat-band potentials differ significantly by ≈0.3 V, on the other hand, suggests differing band positions for two different space charge layers.

We can use the fit parameters in Tab. 14.1 to model the band bending as function of

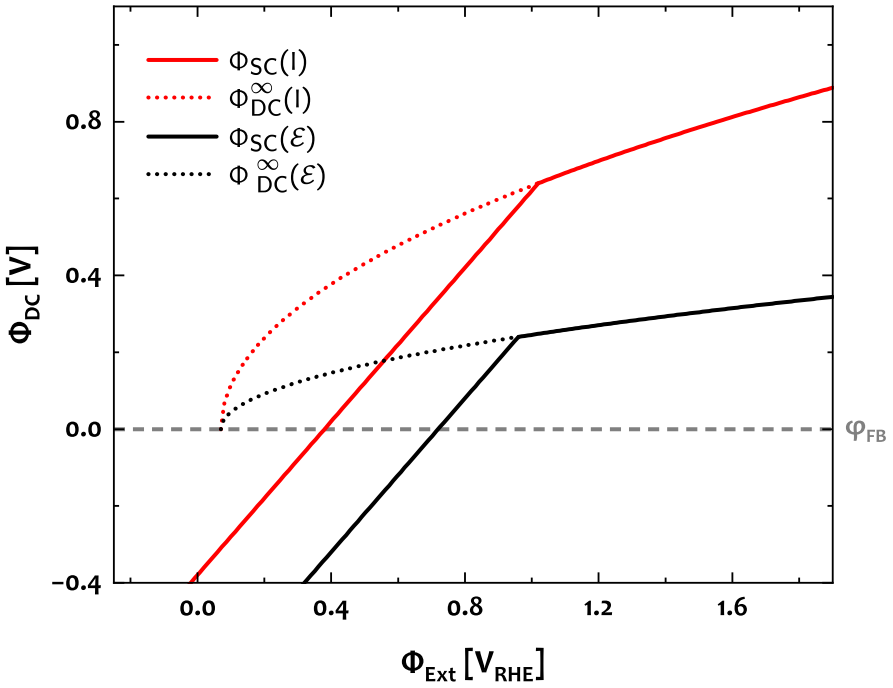

(a) Modelled band bending for two different band structures in parallel obtained from numerical fits of potential dependent SHG intensity and spectral shift according to Fig. 13.3

$$\Phi_{DC} = \Phi_{SC} = \Phi_{Ext} - \varphi_{FB} \quad \text{for} \quad \Phi_{Ext} < \varphi_D$$

$$\Phi_{DC} = \Phi^{\infty}_{DC} = \sqrt{\frac{(\varphi_D - \varphi_{FB})^2}{\varphi_D - \varphi_0^{Back}} * \left(\Phi_{Ext} - \varphi_0^{Back}\right)} \quad \text{for} \quad \Phi_{Ext} \geq \varphi_D$$

(b) Quantitative model of the bias dependent potential drop over the α-Fe_2O_3 electrode film as function of SHG intensity and spectral shift fitting parameters

Figure 14.9: Functional modelling of the potential distribution over the α-Fe_2O_3 electrode film overt two different band structures and an n-type semiconductive back contact as determined from SHG intensity and spectral shift fitting parameters

the applied potential for two different band structures corresponding to the intensity and spectral shift of the SHG response, which is shown in Fig. 14.9. Following the arguments in Section 13.1, the static field over the electrode Φ_{DC} is directly biased by the external potential Φ_{Ext} so that $I/A = (\Phi^{I}_{DC})^2$ and $\langle\mathcal{E}\rangle/A = (\Phi^{\mathcal{E}}_{DC})^2$ for lower potentials $\Phi_{Ext} < \varphi_D$, as long as the space charge potential drop is equal to the static field $\Phi_{DC} = \Phi_{SC}$. If the bias exceeds φ_D, the static field is distributed over a semi-

conducting back contact and a dielectric α-Fe_2O_3 film, so that $\Phi_{\mathrm{Ext}} \propto \Phi_{\mathrm{DC}}^{\infty} \propto \sqrt{\Phi_{\mathrm{SC}}^{\mathrm{Back}}}$. We can insert these expressions in Eq. 13.8 and obtain two equations Fig. 14.9(b) to model the potential drop over the α-Fe_2O_3 electrode material as function of the external bias.

The modelled potential drop over the α-Fe_2O_3 electrode film as function of the external bias are shown in Fig. 14.9(a). We see a functional reproduction of the considerations as developed before. The space charge potential drop increases linearly with the applied bias until a common threshold potential φ_{D} for both SHG metrics is exceeded. Beyond this bias threshold potential, the external bias is distributed over the dielectric α-Fe_2O_3 film and an n-type semiconductor back contact leading to an inverse quadratic increase of the potential drop over the electrode with respect to the external bias.

The findings in this chapter suggest that the α-Fe_2O_3 photoanode material is composed of a more complex band structure than just a conventional valence and a conduction band. Both bands are polarized in parallel since both respond to the external bias in the same fashion instead of sharing the applied potential as it would be the case for two layers in series, for instance. Both band positions are separated by 0.3 V which is in good agreement with the findings from Lohaus et al. In these works, an additional polaron band was observed 0.45 volt below the conduction band in XPS measurements for a magnetron sputtered α-Fe_2O_3 sample.[188] Even though there are differences between both sample preparation and probing environment between those works and the results presented here, the presence of an additional band structure seems plausible with regard to the observed parallel bending process of two different electronic compartments.

15 Electronic structures

In the previous chapters we gathered a range of spectroscopic and electrochemical findings to describe structures and processes at a water splitting α-Fe_2O_3 photoanode. This chapter presents some comprehensive thoughts over several experimental findings from different methods. The following executions will not suffice the demands for experimentally proven results but rather provide a speculative outlook for future research hypotheses.

15.1 Multi-band components

A summary of three different metrics for electronic structures through the thesis is presented in Fig. 15.1, where results from linear optical absorption spectroscopy, amperometry and potentiometry are summarized and merged at one energy axis as presented in the previous chapters Chapter 10, Chapter 12 and Section 14.1. As for that, the absorption spectroscopy energy scale from Fig. 14.1(a) was converted to the potential scale according to $\mathcal{E} = -e_0 * \Phi$. As arbitrary referencing, the small absorption feature from Fig. 14.1(a) at 1.5 eV was equated with the small surface state oxidation current at 1.1 V_{RHE} in Fig. 12.2 which yielded the best agreement between all three measurements. Additional to the optical transmission T from Fig. 14.1(a), both the cell current j from Fig. 12.1 is plotted in the centre of Fig. 15.1 and the total capacitance from upon sample illumination C_T from Fig. 12.5 in the right-hand side. Based on this supplement, we can identify three different aligning features structures along the RHE potential scale. The first is the set of surface states at 1.1 V_{RHE} as identified in Chapter 12, which is apparent through all three plots. The linear absorption spectroscopy energy scale in the left-and side was arbitrarily shifted to match the small NIR absorption feature with the Gaußian surface state oxidation current in the centre. A shoulder of the total electrode capacitance derived from photovoltage transients aligns as well as already inspected in Section 12.2.
A second common characteristic is the overlap between the increasing cell reduction

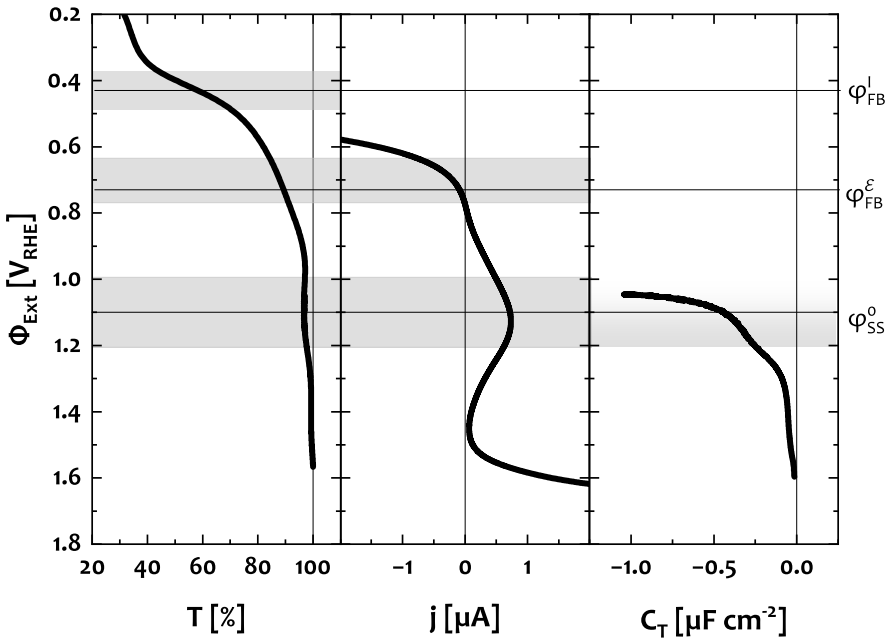

Figure 15.1: Comparison between optical transmission, cell current, and cell capacitance from linear absorption spectroscopy, voltammetry and chronopotentiometry along the RHE scale. The optical energy scale was arbitrarily referenced to match the small absorption feature at 800 nm with the surface state oxidation current at 1.1 V_{RHE}. Flat-band potentials as derived from minimum SHG intensity and spectral shift, at φ^{I}_{FB} = 0.43 V_{RHE} and $\varphi^{\varepsilon}_{FB}$ = 0.72 V_{RHE}, respectively, and the energetic centre of surface states φ^{0}_{SS} = 1.1 V_{RHE} are represented as horizontal lines.

current and a tail of the UV-Vis absorption around 0.7 V_{RHE}. The emerging cell current appears just as one would expect from a population of ionized lattice donor states. This cathodic current at potentials lower than 0.7 V_{RHE} emerges well below the thermodynamic HER onset at 0 V_{RHE} and also significantly below the conduction band-edge of the α-Fe_2O_3 electrode material, typically assumed between 0.3 to 0.4 V_{RHE}.[188]
Third, the conduction band-edge appears around 0.4 V_{RHE} when the energy scale is referenced to the surface state oxidation current feature thereby also showing good agreement with literature values.[188]

From this comparison we can identify three electronic compartments along the RHE energy scale. First, the conduction band-edge would be located at 0.4 V_{RHE} as found from linear optical absorption which also matches well with the flat-band potential

as derived from the SHG intensity at $\varphi^{I}_{\mathrm{FB}} = 0.43\,\mathrm{V_{RHE}}$. Second, a defect band at $0.7\,\mathrm{V_{RHE}}$ is indicated by a large cathodic cell current and in good correspondence with a tail of the absorption band-edge and flat-band conditions as obtained from the minimum spectral shift at $\varphi^{\mathcal{E}}_{\mathrm{FB}} = 0.72\,\mathrm{V_{RHE}}$. And third, a set of surface states at $1.1\,\mathrm{V_{RHE}}$ is manifested by a small oxidation current, a shoulder of the total capacitance and a small optical absorption feature. Interestingly, the band-edge absorption and the shallow defect band are separated by $\approx 0.3\,\mathrm{V_{RHE}}$, just as the two flat-band potentials as obtained from intensity and spectral shift of the potential dependent SHG measurements.

Following this observation, we want to ascribe the origin of the spectral shift to the blue inter-band transition in Fig. 14.1 and the main SHG intensity to the defect-band mediated final state resonance indicated as green transition in Fig. 14.1. As both, the SHG intensity and spectral shift were found to reflect electronic capacitances in parallel, we can hypothesize that both compartments behave under external bias as differently but simultaneously polarized bands.

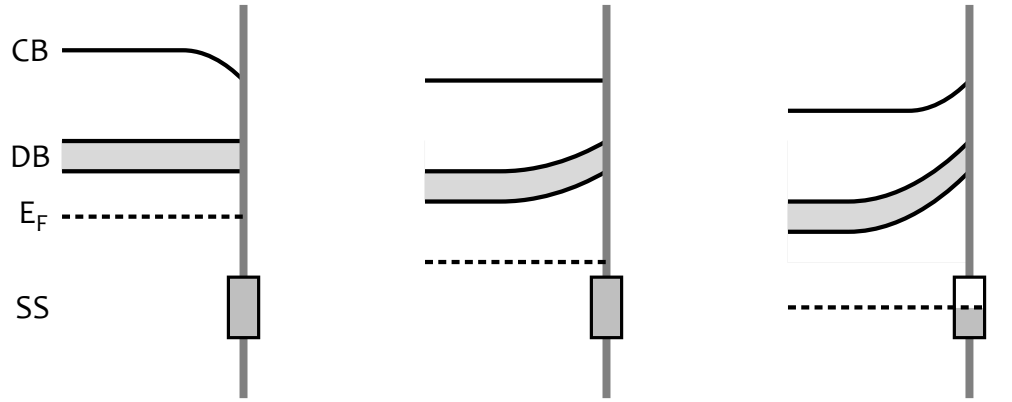

(a) $\Phi_{\mathrm{Ext}} = 0.4\,\mathrm{V_{RHE}}$ **(b)** $\Phi_{\mathrm{Ext}} = 0.7\,\mathrm{V_{RHE}}$ **(c)** $\Phi_{\mathrm{Ext}} = 1.0\,\mathrm{V_{RHE}}$

Figure 15.2: Electronic structures the α-Fe_2O_3 electrode at different bias potentials as derived from Fig. 15.1 The space charge layer is formed by a conduction band (CB) and a defect band (DB) in parallel with a set of large surface states (SS) density in series.

An interpretation of these findings is illustrated in Fig. 15.2. We see electronic structures as identified in Fig. 15.1 under three different externally applied potentials. At $0.43\,\mathrm{V_{RHE}}$, the defect band would be biased to flat-band conditions, whereas the conduction band is in accumulation mode, which is indicated by the cathodic cur-

rent at these potentials – just as one would expect for a population of anti-bonding states. Following the assignment of the spectral shift to an inter-band transition, the conduction band is set to flat-band conditions at 0.72 V_{RHE}, where the defect band is already significantly depleted. Further increase of the external potential would cause a depopulation of surface states as apparent from the oxidation feature in the amperometric IV-curves in Fig. 15.1, for instance.
This interpretation suggests a more complex band structure than commonly applied models to describe α-Fe_2O_3 photoanode electronic processes. The findings are supported by the observation of a polaron band in photoemission experiments in [188], where, however, the experimental conditions are somewhat differing in terms of pressure gap, electrolyte contact and sample preparation. Other studies have also suggested the presence of deep-level or mid-gap bands to influence the space charging effects of semiconductor electrode structures.[226, 228] One mechanism to consider in the opposite polarization of defect and conduction band could be an accumulation of donor state charge in the conduction band as already shown in Fig. 2.2.[26] This would increase the concentration of electrons in the conduction band and thus the electron energy. This mechanism could be favoured by the presence of a strongly negative surface charge to repulse electron transfer to the lattice surface as might be the case for the strongly alkaline electrolyte providing strong surface hydroxylation.[26] However, future activities might be necessary in order to refine the instructional and quite speculative considerations offered here.

15.2 Charge distribution

The vast majority findings of the electronic structures and processes through this thesis are approximated to a system of capacitances formed by a back contact, two different space charge compartments and a sheet of high density surface charge. This approximation of a currentless potential distribution is insofar valid as the SHG response is blind to any current passing the α-Fe_2O_3 electrode so that any potential induced changes of the SHG response would solitarily reflect capacitive effects instead of resistive charge transfer contributions to the impedance. This approximation is also supported as most of the SHG experiments to deliver the band bending characteristics were carried out in the dark at moderate electrode potentials, where net static charge flow can be neglected, as is also manifested by the vertical shapes of the Nyquist plots in Fig. VIII and the IV-characteristics in Fig. 12.1,

for instance. Therefore, the essential findings presented here would reflect charge distribution effects under open circuit conditions for different source voltages.

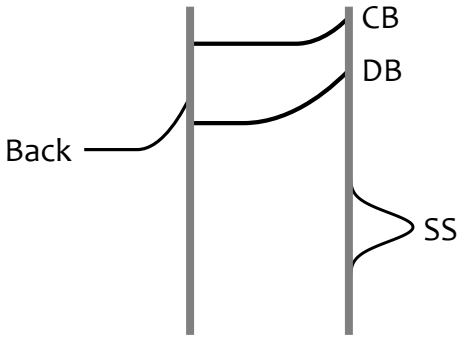

(a) Charge accumulation centres as derived from optical SHG spectroscopy and voltammetry measurements

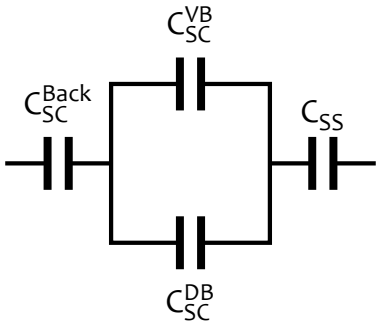

(b) Open equivalence circuit to describe charge accumulation centres approximated for amperostatic conditions at zero net charge flow

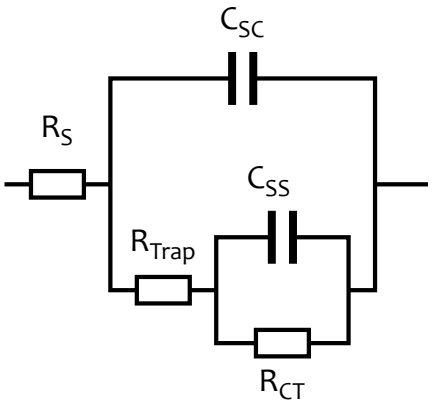

(c) Closed equivalence circuit model applied by Klahr et al. [65, 101]

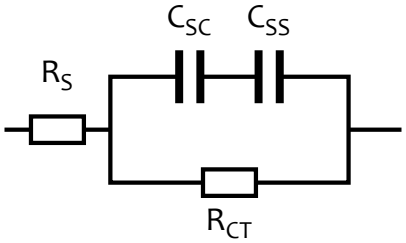

(d) Closed equivalence circuit model applied by Cesar et al. [160]

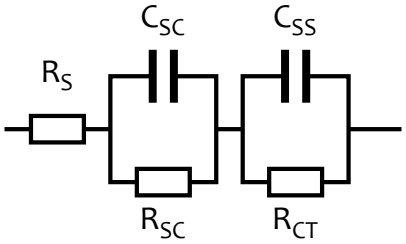

(e) Closed equivalence circuit model applied by Lopes et al. [167]

Figure 15.3: Open circuit capacitance approximation to describe the space and surface charging effects over the α-Fe_2O_3 electrode system in comparison with published closed circuit models

As supplementary illustration of the electronic charge accumulation network in the sample system is schematically illustrated in Fig. 15.3(a). Following the argumentation in Chapter 10, Section 13.1 and Section 14.5, the space charge layer contains two different electronic band structures, a conventional conduction band (CB) and a defect band (DB), which is located approximately 300 mV below the conduction band edge. Both of these bands are polarized differently by external bias, as one might, however, also expect from a polaronic perturbation of the lattice structure observed elsewhere.[188] As sketched in Fig. 15.3(b), these band structures would behave as parallel capacitances as the outer boundaries from complete carrier distribution and the extrapolation to zero back contact band bending were found to be identical for both the conduction band and the defect band in Section 14.5.
A set of high density surface states (SS) was identified by amperometric and potentiometric measurements in Chapter 12. These surface states appeared as distribution over a Gaußian line shape with a centre at 1.1 V_{RHE} in good agreement with literature.[63, 65, 101] No effects from the surface states on the space charge evolution was observed in Mott-Schottky analysis and SHG potential dependence so that the surface charge is attributed to a large capacitance in series with the space charge layer, as sketched in Fig. 15.3(b), so that effects from Fermi-level-pinning are negligible under these conditions.[26]
A polarization of the back contact is observed when the free carriers in the n-type semiconductor α-Fe_2O_3 photoanode material were completely depleted at external potentials beyond 1.0 V_{RHE}.[88] Under these conditions, the applied bias distributes over a henceforth dielectric α-Fe_2O_3 electrode in series with an n-type semiconducting F:SnO_2 back contact which was able to explain the potential dependent SHG response in Section 13.1 which would manifest as an additional serial capacitance in Fig. 15.3(b).

As the results presented here solitarily reflect conditions of zero static charge flow, it should be noted that additional resistive elements bridging the capacitances are necessary to more accurately describe the water splitting electrode under operation instead of the idealized open circuit conditions as discussed here. However, as equivalent circuits provide a frequently applied technique to assign charge transfer and accumulation processes across electrode systems, it might be worth to compare these results with other models from literature.
An overview of equivalent circuit models to interpret complex impedance of the α-Fe_2O_3 electrode and identify electronic structures and processes in literature is pre-

sented in the right panel of Fig. 15.3. Fig. 15.3(c) shows a quite successful model, that has been applied to impedance and other amperometric measurements of α-Fe_2O_3 electrodes in various works.[63, 65, 101] In this model, the space charge capacitance was merged as a bulk capacitance herein denoted as C_{SC}. The flat-band potential obtained in these studies is quite close to the minimum SHG spectral shift at 0.72 V_{RHE}, so that it might be possible that the parallel space charge capacitances are dominated by the conduction band capacitance for $C_{CB} > C_{DB}$ in this model. The surface states follow a path parallel to the space charge layer, which is different to the findings presented here. This might be one reason that an effect for Fermi-level-pinning on the Mott-Schottky plots is visible in [65] in contact with a neutral electrolyte whereas no perturbation of the space charge evolution from surface states is observed in alkaline media and also not in the results presented here.
In the equivalent circuits shown in Fig. 15.3(d) and Fig. 15.3(e), as published by Cesar et al.[160] and Lopes et al.[167], respectively, the surface states are arranged in a serial pathway to the α-Fe_2O_3 space charge layer. In both works, the surface charge is represented by a Helmholtz layer as no pronounced set of surface states was observed in the Mott-Schottky analyses, which is in agreement with the observations presented in Chapter 12.

The measurements presented in Section 10.1 and Section 12.1 determined the surface and space charge capacitances around the deflection of the potential dependent SHG intensity at 1.0 V_{RHE} of 1.6×10^{-4} F cm^{-2} and 2.5×10^{-6} F cm^{-2}, respectively (see Section 10.1.2 and Section 12.1). The linear Mott-Schottky plot at 1.0 V_{RHE}, instead, shows a constant increase of the SCR barrier height over a potential range from 0.4 V_{RHE} to 1.4 V_{RHE}, thus no indication of Fermi-level-pinning over the potential range.

A common picture to describe the charge distribution by capacitive layers is shown in Fig. 15.4, where the Helmholtz layer is arranged in series with the space and surface charge layers.[36] This description follows an interpretation of three layers of charge forming a set of three quasi-capacitances C_{SC}, C_{SS}, C_H corresponding to the space charge, surface state and double layer, respectively.[26, 33, 36] Space and surface charge are assumed as parallel capacitances in series with the Helmholtz layer yielding a model for the total capacitance as given in Eq. 15.1.[36] The serial arrangement of the Helmholtz layer with space and surface capacitances also implies that $Q_H = Q_{SC} + Q_{SS}$, which can be approximated to $Q_H \approx Q_{SS}$ for $Q_{SS} \gg Q_{SC}$.

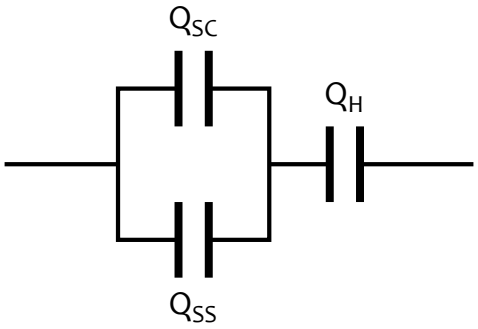

Figure 15.4: Common description of the total capacitance of the semiconductor/electrolyte interface using space and surface charge and HELMHOLTZ or double layer capacitances C_{SC}, C_{SS}, and C_H, respectively[26, 65, 160, 167]

$$C_T{}^{-1} = (C_{SC} + C_{SS})^{-1} + C_H{}^{-1} \tag{15.1}$$

Since the SCR capacitance at 1.0 V_{RHE} is as small as $2.5 \times 10^{-6}\,F\,cm^{-2}$, while the HELMHOLTZ layer capacitance C_H would need to compensate for the whole amount of surface charge with $C_{SS} \approx C_H = 1.6 \times 10^{-4}\,F\,cm^{-2}$, C_H should be much larger than the space charge capacitance, as well. If we insert this approximation $C_H \approx C_{SS}$ into Eq. 15.1 and rearrange the expression, we find an equation Eq. 15.2 to relate the total capacitance C_T as function of space ad surface charge.

$$\boxed{C_T = C_{SC} + \frac{C_{SC}}{C_{SS}}} \tag{15.2}$$

Eq. 15.2 suggests that the ratio between space and surface state capacitance is determining whether the bias entirely falls across space charge layer or also along a charging of surface states. As the experiments presented here indicated a surface state capacitance that is 64 times larger that the surface state capacitance, C_T approaches C_{SC}. With that, the assumptions that the external bias entirely falls across the α-Fe_2O_3 film independently of surface charging processes, can be justified by Eq. 15.2. A replacement of C_{SS} by C_H in Eq. 15.2 delivers similar results to explain in particular the imprint of surface state capacitance in the MOTT-SCHOTTKY plots in a pH 6.9 neutral electrolyte in [65, 101], where the HELMHOLTZ capacitance might

be lowered due to less dramatic surface deprotonation to cause a stronger coupling between space and double layer charge.

16 Conclusions

16.1 Summary

The thesis at hand presents a comprehensive pioneering work on the direct mapping of semiconductor electrode band-bending and electronic surface states. For this, a α-Fe_2O_3 photoanode system was developed characterized in 1 M KOH electrolyte by means of second harmonic generation (SHG) spectroscopy in combination with a range of PEC methods.
An electrochemical deposition process is described that provides opportunities to monitor and modify properties of the as-deposited films using the deposition current and potential, respectively. A threshold potential is found where the growth type changes from adsorption to diffusion controlled deposition. A mechanistic analysis demonstrated the option to conduct an UPD growth regime and to separate early nucleation stages from bulk film deposition. A self-accelerating growth rate under UPD conditions is interpreted as Volmer-Weber or island growth type. These finding might help to grow FeOx and FeO_xH_y films of tailored catalytic, optical, electronic or magnetic properties.[114, 196, 213, 218–220]
The materials properties of the α-Fe_2O_3 sample system are well documented by means of SEM, TEM, Raman-spectroscopy, UV-Vis spectroscopy and XRD. All of these techniques confirmed a representative sample system that agrees well with α-Fe_2O_3 photoanodes in literature.[61, 111, 168] The sample is further characterized by common PEC techniques which confirm a representative photoanode system that provides a proper reference and that allows for discussion with literature studies.[61, 63, 111]
Technical obstacles and their respective solutions are presented in order to demonstrate how a profound operando SHG characterization of a semiconductor electrode system may be realised. A cell design is presented that provides simultaneous control over all vital PEC parameters such as electrode potential, cell current, electrolyte

composition, electrode illumination and temporal resolution at the ms scale while the SHG signal can be recorded simultaneously with spectral resolution in real time.

Based on a chronoamperometric measurement of photocurrent transients in the developed setup, a kinetic analysis was performed to infer the reaction order of the OER mechanism at the α-Fe_2O_3 photoanode. The findings indicated a third order reaction-rate law in good agreement with other studies.[237–240] A DFT simulation was carried out in order to identify mechanistic pathways where the consumption of a three-hole intermediate is identified as rate limiting step in the catalytic cycle. The results were published in the nature catalysis journal.[44]
A current signal in the amperometric current-voltage (IV) curves of the sample system was found, that follows a Gaußian distribution and matches very well with literature values on surface states. Both, the energetic position and the width of this current signal are in good agreement with reported surface state capacitances obtained from modelled EIS spectra.[63, 65, 101] However, Mott-Schottky plots for the sample system do not show the typical plateau of Fermi-level-pinning, even though a clear indication of surface states is observed. This is also the case for other EIS measurements in alkaline electrolytes,[63, 65] so that the occasion of Fermi-level-pinning may be not necessarily caused by the sheer presence of a large density of surface states. This observation is explained by much larger capacitances of the Helmholtz and surface state layers in series with the SCR, so that any externally applied potential will fall across the SCR.[26] The surface state oxidation current is discussed with respect with the surface chemical findings in [44].
The time dependent evolution of the depletion layer is measured in a chronopotentiometry (CP) experiment. For this, a constant current is imposed onto the electrode and the electrode illumination is instantly switched on and off during a continuous measurement of the time dependent evolution of electrode potential and SHG response, where a close relation between SHG response and electrode potential is confirmed. The resulting photo- and dark-voltage transients show a quite different behaviour. While a band flattening upon electrode illumination seems to occur via charging of surface states, the carrier recombination after blocking of electrode illumination rather resembles a linear capacitor. This suggests a directional and irreversible pathway of the surface charge accumulation in accordance with [101]. The observation of irreversible charge transfer pathways is also supported by the surface state oxidation current feature which is only observed in anodic scan direction, but not for the cathodic scan. A comparison with a DFT and MK study indicates

an irreversible reaction step under release of water as one bottleneck of the charge transfer reaction.[44]

An SHG signal is detected around 2.1 eV that can be altered by both external bias potential and sample illumination. Control measurements on the bare F:SnO_2 substrate and an Au film in the same cell showed that neither the underlying sample substrate nor the electrolyte contribute to the SHG response and that the signal can be safely ascribed to a spectrally broad optical resonance process in the α-Fe_2O_3 film. A range of further control experiments demonstrated stability and repeatability of the SHG measurements. Comparison with optical absorption coefficients and with the electrode potential under potentiometric conditions indicate that the probing depth is not limited by light absorption.
Additionally, illumination of the electrode and excitation of charge carriers is found to only affect the SHG response under a potentiometric setup. A conventional amperometric measurement, where a fixed electrode potential is imposed and the current is measured, showed no significant change of the corresponding SHG response in the dark and under illumination. If a current is imposed to the electrode and the potential remains unbiased, on the other hand, the SHG response follows the measured potential very well. This observation can be explained by the concept of quasi-Fermi-levels, where the electrode potential is governed by the majority carriers, whereas minority carriers mainly contribute to the cell current.[26] This finding confirms the close relationship between SHG response and α-Fe_2O_3 photoanode band bending which is preserved under both potentiometric and amperometric conditions and along the entire potential range.
Changes of the SHG response with the externally applied potential are manifested by two different metrics. First, the integral intensity is increasing with more anodic potentials. And second, a small but significant shift of the SHG photon energy expectation value is also taking place when the potential is changed. Both observables, the SHG intensity and spectral shift show a parabolic potential dependence at lower potentials which changes to a linear dependence when the potential is increased to more anodic conditions. Due to the much better signal quality and the comparability with literature references, the potential dependence of the SHG intensity is analysed in more detail, while the spectral shift is discussed in analogy to the findings from the SHG light intensity.
The quadratic potential dependence of the SHG response is interpreted in terms of the electric field induced second harmonic (EFISH) theory, where the magnitude of

the SHG response is enhanced by the built-in electric field of the electrode surface depletion layer.[79, 81] Consequently, the potential at the minimum SHG response indicates flat-band conditions. An additional electrochemical impedance spectroscopy (EIS) experiment was carried out in the same cell system in order to conduct a Mott-Schottky analysis as complementary and most common method to determine the flat-band potential. The obtained flat-band potentials at 0.43 V_{RHE} and 0.48 V_{RHE} for SHG and Mott-Schottky analysis, respectively, showed that both methods are in good agreement and confirm that the electric field induced second harmonic (EFISH) theory applies well to the SHG signal formation.

Both SHG observables exhibit a split dependence on the external bias potential. While the intensity and spectral shift respond quadratically to the external bias under moderate depletion conditions at $\Phi_{Ext} < 1.0\,V_{RHE}$, both observables are increasing linearly with the external potential at more anodic potentials $\Phi_{Ext} > 1.0\,V_{RHE}$. This behaviour is attributed to a complete majority carrier depletion of the bulk semiconductor material. The corresponding particle size obtained from the deflection point of the potential dependent SHG, visual inspection of EM images and Scherrer analysis of an XRD reflex are in good agreement and point out that no conventional Fermi-level-pinning takes place. In accordance with reported SHG studies on other semiconductor electrodes, it is found that a linear potential dependence might correspond to a constrained evolution of the Gaußian surface into the bulk. While in [79] and [81], the Gaußian surface is restricted due to a limited probing depth beneath the electrode surface, it is in our case constrained by the film thickness due to limited propagation of the space charge with into the bulk electrode due to a complete majority charge carrier depletion of the semiconductor material.[88, 235] Under conditions of a complete depletion, the semiconductor material is described as conventional dielectric in contact with a series with a semiconducting back-contact. Based on these considerations, a two case global model is developed to fit the entire SHG response as function of the applied potential. This model also provides information on the back-contact and can be still applied to determine flat-band conditions of the layer beneath the sheet that is sampled by SHG.
The small but significant SHG spectral shift also shows a parabolic potential dependence as the SHG intensity but with a more anodic vertex at 0.72 V_{RHE}. Based on a supplementary inspection of spectroscopic and electrochemical findings, both metrics, SHG intensity and spectral shift, discussed in terms of an electronic substructure additional to the main valence and conduction bands in agreement with

literature reports.[188, 226, 228] The finding, that the SHG intensity and spectral shift deflect at the same potential, indicates that both metrics correspond to two distinct band-structures in parallel within the α-Fe_2O_3 photoanode lattice. Along these lines, the occurrence of two parabolic vertices is referred to two different flat-band condition which might also help to explain persisting obscurities of α-Fe_2O_3 photoanode flat-band potentials in literature and reveal one possible way to explain charge carrier recombination and loss processes.[26, 77]

16.2 Outlook

The presented works show a fundamental, comprehensive and prospective pioneering for the investigation of semiconductor electrode surface band-bending using EFISH spectroscopy in close correspondence with established EC techniques. A novel probe for the population and distribution of surface states is presented and also some suggestions for a more versatile deposition process for the preparation of FeO_xH_y thin films.
After the first submission of the thesis in January 24th 2023, a similar study was published in March 22nd 2023, which describes quite similar experiments.[259] Even though these works do not include a detailed discussion of the linear potential dependence, dielectric polarization, spectral shift, surface chemistry and charge accumulation, electronic structures, capacitive coupling and photovoltage as presented here, for instance, the publication [259] already shows the significance and relevance of the works presented in the thesis at hand.
The findings on the film growth offer a range of options to tune the materials properties of FeO_xH_y thin films. For instance, it could facilitate the growth of FeO_xH_y films of certain optical, magnetic or catalytic properties.[114, 196, 213, 218–220] Also, further advances might be possible for the design of a catalytically active FeOOH top layer on the photoactive α-Fe_2O_3 film.[196, 219] In order to make use of these new findings on the growth mechanism, it would be necessary to conduct a systematic study of the as-deposited materials properties as function of the applied potential, e.g. using UV-Vis- or Raman spectroscopies, gravitational or EM imaging techniques. This would provide a chance to produce FeO_xH_y films of tailored and controlled optical, magnetic and catalytic properties.
While the observation of a completely depleted bulk material was already found to be in good agreement with other techniques, a systematic EFISH study on films of

varying masses, donor concentrations or even different deposition process, might provide fundamental insight on the formation and propagation of the depletion layer as function of the film thickness, defect concentration or crystallite size and shape.

Although a current signal was identified that corresponds to the oxidation of surface states, no indication for FERMI-level-pinning was found. Neither in an MOTT-SCHOTTKY analysis nor in EFISH spectroscopy – the space charge evolution is not affected by surface charging processes. Therefore, further investigations would be necessary in order to clarify the role of surface states. As for this, a systematic study on the effect of dopant concentrations, electrolyte pH and ionic strength and passivation layers on the SHG response might help to elucidate the interplay between the SCR, the HELMHOLTZ layer and surface states, respectively, with the space charge band bending.

Besides the clear correspondence between the SHG signal intensity and surface band bending, a small spectral shift of the signal is observed as well. While this shift is shown to be repeatable and significant, it is discussed in terms of an additional band component, which, however, is far from being proven at this point. Therefore, further experiments such as UV-Vis-NIR spectroscopies or XPS and ultra violet photoemission spectroscopy (UPS) in combination with an extended bandwidth of the SHG experiments would be helpful in order to clarify and validate corresponding electronic structure models. More dedicated impedance measurements under variation of excitation power and wavelength or electrolyte composition, for instance, might be useful to further clarify relevant charge transfer pathways across the α-Fe_2O_3 electrode.

The observation of light induced band flattening under potentiometric conditions provides some direct access to track band reorganisation under electrode illumination and to further elucidate the concepts of photovoltage and quasi-FERMI-levels. Additional studies, in particular systematic variations of the illumination power density and possibly also of the illumination wavelength might provide valuable information on the actual photo-electric energy conversion process within this particular photoanode system and also on other semiconductor systems in general.

Finally, several indications were found that the solitary investigation of cell current, electrode potential and illumination may be not sufficient to fully clarify all electronic structures and processes across the electrode system. Besides the asymmetry of the charging and discharging transients, the flat-band potentials determined by SHG and MOTT-SCHOTTKY analysis are only in good agreement for the electrode in the dark.

Under illumination, a Mott-Schottky analysis shows an increase of the flat-band potential of 90 mV, whereas SHG measurements reveal constant values for the electrode for both the irradiated sample and in the dark. All of these findings point out, that the cell current might be influenced by a number of unknown parameters such as different electron and hole current pathways, scan direction or spin orientation effects.
Therefore, a systematic variation of electrolyte pH, illumination power and colour, surface state passivation, surface hole charge transfer kinetics and SHG wavelength might provide additional information on the semiconductor electrode interface charge transfer reactions in order to address persisting challenges of PEC energy conversion.

Appendix

A Glossary

1 Acronyms

a.u.	Arbitrary units
AC	Alternate current
CA	Chronoamperometry
CB	Conduction band
CP	Chronopotentiometry
cps	Counts per second
CV	Cyclic voltammetry
CW	Continuous wave
DB	Defect band
DC	Direct current
DFT	Density functional theory
DOS	Density of states
DRC	Degree of rate control
EC	Electrochemistry
ED	Electrodeposition
EDX	Energy dispersive X-ray analysis
EER	Electrolyte electroreflectance
EFISH	Electric field induced second harmonic
EIS	Electrochemical impedance spectroscopy
EM	Electron microscopy

FFT	Fast Fourier transformation
FIB	Focused ion beam
FTO	F:SnO_2, fluourine doped tin oxide
FWHM	Full width at half maximum $w_{1/2}$
HER	Hydrogen evolution reaction
IHP	Inner Helmholtz-plane
IMPS	Intensity mpdulated photocurrent spectroscopy
IR	Infrared
ITO	Indium tin oxide
IV	Current-voltage
MK	Microkinetic
ML	Monolayer
NIR	Near infrared
OCV	Open circuit voltage
OER	Oxygen evolution reaction
OHP	Outer Helmholtz-plane
OPA	Optical parametric amplifier
OPD	Over potential deposition
PEC	Photoelectrochemistry
PTFE	Polytetrafluoroethylene
pzc	Point of zero charge
RHE	Reversible hydrogen electrode
SCR	Space charge region
SEM	Scanning electron microscopy
SFG	Sum frequency generation
SH	Second harmonic
SHG	Second harmonic generation
SS	Surface states
STH	Solar to hydrogen

SVD	Singular value decomposition
TAS	Transient absorption spectroscopy
TCO	Transparent conductive oxide
TEM	Transmission electron microscopy
UHV	Ultra high vacuum
UPD	Under potential deposition
UPS	Ultra violet photoemission spectroscopy
UV	Ultra violet
VB	Valence band
Vis	Visible
XPS	X-ray photoemission spectroscopy
XRD	X-ray diffraction

2 Symbols

α	Absorption coefficient in cm^{-1}
A_{Geom}	Geometric electrode area exposed to the electrolyte in cm^{-1}
C	Electric capacitance referred to the geometric electrode surface in F or $F\,cm^{-2}$, $1F = 1A\,s\,V^{-1}$
D	Particle diameter in nm
e_0	Elementary charge $e_0 = 1.602 \times 10^{-19}\,C$
$\mathcal{E}$	Energy in eV
$\langle \mathcal{E}_{2\omega} \rangle$	SH Photon energy expectation value or spectral centre of gravity of the SHG response signal in eV
$\mathcal{E}_{\mathrm{C}}$	Conduction band energy in eV
$\mathcal{E}_{\mathrm{G}}$	Electronic band-gap in eV
$\mathcal{E}_{\mathrm{V}}$	Valence band energy in eV

$\mathbf{E}$	Electric field in $\mathrm{V\,m^{-1}}$
$\widetilde{\mathbf{E}}$	Oscillating electric field in $\mathrm{V\,m^{-1}}$
ϵ_0	Vacuum permittivity $\epsilon = 8.854 \times 10^{-12}\,\mathrm{C\,V^{-1}\,m^{-1}}$
ϵ_r	Relative permittivity for α-Fe_2O_3 estimated as $\epsilon_\mathrm{r} = 25$ [26]
f	Ordinary frequency in Hz
Φ	Electric potential difference with respect to a reference value φ in V
φ	Reference potential in V
$\hbar$	Reduced Planck-constant $\hbar = h/2\pi = 6.582 \times 10^{-16}\,\mathrm{eV\,s}$
$I_{2\omega}$	Integral SH intensity in cps * nm or a u
I'	Energy dependent photon flux in a.u. or cps
$I'_{2\omega}$	Energy dependent SHG photon flux in a.u. or cps
J	Cell current in A
j	Cell current density, referred to the electrode area in contact with the electrolyte in $\mathrm{mA\,cm^{-2}}$ or $\mathrm{\mu A\,cm^{-2}}$
k_B	Boltzmann-constant $k_\mathrm{B} = 1.380\,649 \times 10^{-23}\,\mathrm{J\,K^{-1}}$
λ	Wavelength in nm or Å
$\widetilde{\nu}$	Wavenumber in $\mathrm{cm^{-1}}$
η	Overpotential in V
N	Density of states per area or volume in $\mathrm{cm^{-2}}$ or $\mathrm{cm^{-3}}$, respectively
ω	Angular frequency in $\mathrm{s^{-1}}$
$\mathbf{P}$	Polarisation amplitude in $\mathrm{C\,m^{-2}}$
$\widetilde{\mathbf{P}}$	Periodic polarisation in $\mathrm{C\,m^{-2}}$
Q	Electric charge in C or µA h
R	Electric resistance in Ω
ρ	Volume charge density in $\mathrm{cm^{-3}}$
S_Act	Electrochemically active electrode surface obtained from the geometric electrode area A_Geo multiplied by a roughness factor f_R
σ	Surface charge density in $\mathrm{cm^{-2}}$
T	Absolute temperature $T = 296.15\,\mathrm{K}$

t	Time in s, min or h
$w_{1/2}$	Full width at half maximum, FWHM
W_{SC}	Space charge width in nm,
$\chi^{(n)}$	n^{th} Order electric susceptibility in $(\mathrm{m\,V^{-1}})^{n-1}$
$\mathbf{Z}$	Complex electric impedance in 1Ω = V / A

B Indices

1 List of publications

[44] G. Righi, J. Plescher, F.-P. Schmidt, R. K. Campen, S. Fabris, A. Knop-Gericke, R. Schlögl, T. E. Jones, D. Teschner, S. Piccinin, "On the origin of multihole oxygen evolution in haematite photoanodes", *Nature Catalysis* **2022**, *5*, 888

[170] D. Teschner, J. Plescher, S. Piccinin, T. E. Jones, A. Hammud, F. Schmidt, A. Knop-Gericke, H. Bluhm, A. Shavorskiy, "Understanding Anomalous Gas-Phase Peak Shifts in Dip-and-Pull Ambient Pressure XPS Experiments", *The Journal of Physical Chemistry C*, *128*, 7096

2 List of figures

3 List of tables

C References

[1] United Nations, *Paris Agreement – United Nations Treaty Collection, Chapter XXVII 7. d*, **2015**.

[2] Climate Change 2021: The Physical Science Basis. Contribution of Working Group I to the Sixth Assessment Report of the Intergovernmental Panel on Climate Change, Cambridge University Press, **2021**.

[3] S. Solomon, G.-K. Plattner, R. Knutti, P. Friedlingstein, "Irreversible climate change due to carbon dioxide emissions", *Proceedings of the National Academy of Sciences* **2009**, *106*, 1704.

[4] R. Revelle, H. E. Suess, "Carbon Dioxide Exchange Between Atmosphere and Ocean and the Question of an Increase of Atmospheric CO_2 during the Past Decades", *Tellus* **1957**, *9*, 18.

[5] A. Stips, D. Macias, C. Coughlan, E. Garcia-Gorriz, X. S. Liang, "On the causal structure between CO_2 and global temperature", *Scientific Reports* **2016**, *6*, 21691.

[6] T. P. Barnett, D. W. Pierce, R. Schnur, "Detection of Anthropogenic Climate Change in the World's Oceans", *Science* **2001**, *292*, 270.

[7] G. Hansen, D. Stone, "Assessing the observed impact of anthropogenic climate change", *Nature Climate Change* **2016**, *6*, 532.

[8] M. Höök, X. Tang, "Depletion of fossil fuels and anthropogenic climate change – A review", *Energy Policy*, Special Section: Transition Pathways to a Low Carbon Economy **2013**, *52*, 797.

[9] R. K. Kaufmann, H. Kauppi, M. L. Mann, J. H. Stock, "Reconciling anthropogenic climate change with observed temperature 1998–2008", *Proceedings of the National Academy of Sciences* **2011**, *108*, 11790.

[10] National Aeronautics and Space Administration (NASA), Goddard Institute for Space Studies (GISS), `https://data.giss.nasa.gov/gistemp/` (visited on December 8, 2021).

[11] N. J. L. Lenssen, G. A. Schmidt, J. E. Hansen, M. J. Menne, A. Persin, R. Ruedy, D. Zyss, "Improvements in the GISTEMP Uncertainty Model", *Journal of Geophysical Research: Atmospheres* **2019**, *124*, 6307.

[12] J. Hansen, R. Ruedy, M. Sato, K. Lo, "GLOBAL SURFACE TEMPERATURE CHANGE", *Reviews of Geophysics* **2010**, *48*, RG4004.

[13] J. A. Church, N. J. White, "Sea-Level Rise from the Late 19th to the Early 21st Century", *Surveys in Geophysics* **2011**, *32*, 585.

[14] R. Domingues, G. Goni, M. Baringer, D. Volkov, "What Caused the Accelerated Sea Level Changes Along the U.S. East Coast During 2010–2015?", *Geophysical Research Letters* **2018**, *45*, 13367.

[15] Hawaii Ocean Time-series (HOT), `https://hahana.soest.hawaii.edu/hot/products/products.html` (visited on December 8, 2021).

[16] OAR US EPA, Climate Change Indicators: Ice Sheets, **2021**, `https://www.epa.gov/climate-indicators/climate-change-indicators-ice-sheets` (visited on December 8, 2021).

[17] Our World in Data, Our World in Data, `https://ourworldindata.org` (visited on December 8, 2021).

References

[18] N. US Department of Commerce, Global Monitoring Laboratory - Carbon Cycle Greenhouse Gases, https://gml.noaa.gov/ccgg/trends/gl_data.html (visited on December 6, 2021).

[19] Which sources does our global energy come from? How much is low-carbon?, Our World in Data, https://ourworldindata.org/sources-global-energy (visited on January 19, 2022).

[20] H. Ritchie, M. Roser, CO_2 and Greenhouse Gas Emissions, **2020**, https://ourworldindata.org/co2-emissions (visited on January 19, 2022).

[21] *Energie in Zahlen: Arbeit und Leistungen der AG Energiebilanzen*, 2. Auflage, (Ed.: A. Energiebilanzen), Arbeitsgemeinschaft Energiebilanzen e. V, Berlin, **2019**, 44 pp.

[22] A. Liebich, T. Fröhlich, D. Münter, H. Fehrenbach, S. Simon, S. Maier, F. Albrecht, T. Pregger, C. Schillings, M. Moser, R. Reißner, S. Hosseiny, G. Jungmeier, M. Beermann, D. Frieden, N. Bird, "System comparison of storable energy carriers from renewable energies", *Umweltbundesamt*, 49.

[23] M. Yue, H. Lambert, E. Pahon, R. Roche, S. Jemei, D. Hissel, "Hydrogen energy systems: A critical review of technologies, applications, trends and challenges", *Renewable and Sustainable Energy Reviews* **2021**, *146*, 111180.

[24] Bundesministerium für Wirtschaft und Energie (BMWi), *Die Nationale Wasserstoffstrategie*, **2020**.

[25] B. Zhang, S.-X. Zhang, R. Yao, Y.-H. Wu, J.-S. Qiu, "Progress and prospects of hydrogen production: Opportunities and challenges", *Journal of Electronic Science and Technology* **2021**, *19*, 100080.

[26] *Photoelectrochemical Hydrogen Production*, (Eds.: R. van de Krol, M. Grätzel), Springer US, Boston, MA, **2012**.

[27] C. H. Hamann, W. Vielstich, *Elektrochemie*, 4th ed., Wiley-VCH, **2005**.

[28] C. C. L. McCrory, S. Jung, J. C. Peters, T. F. Jaramillo, "Benchmarking Heterogeneous Electrocatalysts for the Oxygen Evolution Reaction", *Journal of the American Chemical Society* **2013**, *135*, 16977.

[29] M. Schmidt, "Grüner Wasserstoff als Schlüsseltechnologie für die europäische Energiewende", **2020**, 5.

[30] R. Diermann, "Energiewende: Wasserstoff aus dem Meer", *Süddeutsche.de*.

[31] Deutsches Zentrum für Luft- und Raumfahrt e. V. (DLR), *Wasserstoff als ein Fundament der Energiewende Teil 1: Technologien und Perspektiven für eine nachhaltige und ökonomische Wasserstoffversorgung*, **2020**.

[32] BDEW, Windkraft: https://www.bdew.de/online-magazin-zweitausend50/schwerpunkt-europa/windkraft-umgeben-von-wasser/ (visited on January 20, 2022).

[33] S. R. Morrison, *Electrochemistry at Semiconductor and Oxidized Metal Electrodes*, Plenum Press, **1980**.

[34] R. van de Krol, B. A. Parkinson, "Perspectives on the photoelectrochemical storage of solar energy", *MRS Energy & Sustainability* **2017**, *4*.

[35] S. Tembhurne, S. Haussener, "Integrated Photo-Electrochemical Solar Fuel Generators under Concentrated Irradiation", *Journal of The Electrochemical Society* **2016**, *163*, H988.

[36] In *Electrochemistry of Silicon and Its Oxide*, (Ed.: X. G. Zhang), Springer US, Boston, MA, **2001**, pp. 1–43.

[37] A. Fujishima, K. Honda, "Electrochemical Evidence for the Mechanism of the Primary Stage of Photosynthesis", *Bulletin of the Chemical Society of Japan* **1971**, *44*, 1148.

[38] A. Fujishima, K. Honda, "Electrochemical Photolysis of Water at a Semiconductor Electrode", *Nature* **1972**, *238*, 37.

[39] M. K. Van Aalst, "The impacts of climate change on the risk of natural disasters", *Disasters* **2006**, *30*, 5.

[40] S. R. Morrison, *The Chemical Physics of Surfaces*, 2nd ed., Plenum Press, New York, London, **1990**.

[41] S. Chen, S. S. Thind, A. Chen, "Nanostructured materials for water splitting - state of the art and future needs: A mini-review", *Electrochemistry Communications* **2016**, *63*, 10.

[42] K. Sivula, F. Le Formal, M. Grätzel, "Solar Water Splitting: Progress Using Hematite (α-Fe_2O_3) Photoelectrodes", *ChemSusChem* **2011**, *4*, 432.

[43] W. Shockley, H. J. Queisser, "Detailed Balance Limit of Efficiency of p-n Junction Solar Cells", *Journal of Applied Physics* **1961**, *32*, 510.

[44] G. Righi, J. Plescher, F.-P. Schmidt, R. K. Campen, S. Fabris, A. Knop-Gericke, R. Schlögl, T. E. Jones, D. Teschner, S. Piccinin, "On the origin of multihole oxygen evolution in haematite photoanodes", *Nature Catalysis* **2022**, *5*, 888.

[45] A. Moysiadou, X. Hu, "Stability profiles of transition metal oxides in the oxygen evolution reaction in alkaline medium", *Journal of Materials Chemistry A* **2019**, *7*, 25865.

[46] H. Dau, C. Limberg, T. Reier, M. Risch, S. Roggan, P. Strasser, "The Mechanism of Water Oxidation: From Electrolysis via Homogeneous to Biological Catalysis", *ChemCatChem* **2010**, *2*, 724.

[47] J. Jia, L. C. Seitz, J. D. Benck, Y. Huo, Y. Chen, J. W. D. Ng, T. Bilir, J. S. Harris, T. F. Jaramillo, "Solar water splitting by photovoltaic-electrolysis with a solar-to-hydrogen efficiency over 30%", *Nature Communications* **2016**, *7*, 13237.

[48] S. U. M. Khan, M. Al-Shahry, W. B. Ingler, "Efficient Photochemical Water Splitting by a Chemically Modified n-TiO_2", *Science* **2002**, *297*, 2243.

[49] F. F. Abdi, L. Han, A. H. M. Smets, M. Zeman, B. Dam, R. van de Krol, "Efficient solar water splitting by enhanced charge separation in a bismuth vanadate-silicon tandem photoelectrode", *Nature Communications* **2013**, *4*, 2195.

[50] V. Cristino, S. Caramori, R. Argazzi, L. Meda, G. L. Marra, C. A. Bignozzi, "Efficient Photoelectrochemical Water Splitting by Anodically Grown WO_3 Electrodes", *Langmuir* **2011**, *27*, 7276.

[51] S. Hu, M. R. Shaner, J. A. Beardslee, M. Lichterman, B. S. Brunschwig, N. S. Lewis, "Amorphous TiO_2 coatings stabilize Si, GaAs, and GaP photoanodes for efficient water oxidation", *Science* **2014**, *344*, 1005.

[52] J.-W. Jang, C. Du, Y. Ye, Y. Lin, X. Yao, J. Thorne, E. Liu, G. McMahon, J. Zhu, A. Javey, J. Guo, D. Wang, "Enabling unassisted solar water splitting by iron oxide and silicon", *Nature Communications* **2015**, *6*, 7447.

[53] W.-H. Cheng, M. H. Richter, M. M. May, J. Ohlmann, D. Lackner, F. Dimroth, T. Hannappel, H. A. Atwater, H.-J. Lewerenz, "Monolithic Photoelectrochemical Device for Direct Water Splitting with 19% Efficiency", *ACS Energy Letters* **2018**, *3*, 1795.

[54] K. L. Hardee, A. J. Bard, "Semiconductor Electrodes: V . The Application of Chemically Vapor Deposited Iron Oxide Films to Photosensitized Electrolysis", *Journal of The Electrochemical Society* **1976**, *123*, 1024.

[55] D. A. Grave, N. Yatom, D. S. Ellis, M. C. Toroker, A. Rothschild, "The "Rust" Challenge: On the Correlations between Electronic Structure, Excited State Dynamics, and Photoelectrochemical Performance of Hematite Photoanodes for Solar Water Splitting", *Advanced Materials* **2018**, *0*, 1706577.

References

[56] A. G. Tamirat, J. Rick, A. A. Dubale, W.-N. Su, B.-J. Hwang, "Using hematite for photoelectrochemical water splitting: a review of current progress and challenges", *Nanoscale Horizons* **2016**, *1*, 243.

[57] F. Le Formal, K. Sivula, M. Grätzel, "The Transient Photocurrent and Photovoltage Behavior of a Hematite Photoanode under Working Conditions and the Influence of Surface Treatments", *The Journal of Physical Chemistry C* **2012**, *116*, 26707.

[58] M. Barroso, C. A. Mesa, S. R. Pendlebury, A. J. Cowan, T. Hisatomi, K. Sivula, M. Grätzel, D. R. Klug, J. R. Durrant, "Dynamics of photogenerated holes in surface modified α-Fe_2O_3 photoanodes for solar water splitting", *Proceedings of the National Academy of Sciences* **2012**, *109*, 15640.

[59] L. M. Peter, K. G. U. Wijayantha, A. A. Tahir, "Kinetics of light-driven oxygen evolution at α-Fe_2O_3 electrodes", *Faraday Discussions* **2012**, *155*, 309.

[60] M. Barroso, S. R. Pendlebury, A. J. Cowan, J. R. Durrant, "Charge carrier trapping, recombination and transfer in hematite (α-Fe_2O_3) water splitting photoanodes", *Chemical Science* **2013**, *4*, 2724.

[61] K. Sivula, R. Zboril, F. Le Formal, R. Robert, A. Weidenkaff, J. Tucek, J. Frydrych, M. Grätzel, "Photoelectrochemical Water Splitting with Mesoporous Hematite Prepared by a Solution-Based Colloidal Approach", *Journal of the American Chemical Society* **2010**, *132*, 7436.

[62] R. van de Krol, Y. Liang, J. Schoonman, "Solar hydrogen production with nanostructured metal oxides", *Journal of Materials Chemistry* **2008**, *18*, 2311.

[63] D. Monllor-Satoca, M. Bärtsch, C. Fàbrega, A. Genç, S. Reinhard, T. Andreu, J. Arbiol, M. Niederberger, J. R. Morante, "What do you do, titanium? Insight into the role of titanium oxide as a water oxidation promoter in hematite-based photoanodes", *Energy & Environmental Science* **2015**, *8*, 3242.

[64] J. Su, J. Wang, C. Liu, B. Feng, Y. Chen, L. Guo, "On the role of metal atom doping in hematite for improved photoelectrochemical properties: a comparison study", *RSC Advances* **2016**, *6*, 101745.

[65] B. Klahr, S. Gimenez, F. Fabregat-Santiago, T. Hamann, J. Bisquert, "Water Oxidation at Hematite Photoelectrodes: The Role of Surface States", *Journal of the American Chemical Society* **2012**, *134*, 4294.

[66] C. A. Mesa, A. Kafizas, L. Francàs, S. R. Pendlebury, E. Pastor, Y. Ma, F. Le Formal, M. T. Mayer, M. Grätzel, J. R. Durrant, "Kinetics of Photoelectrochemical Oxidation of Methanol on Hematite Photoanodes", *Journal of the American Chemical Society* **2017**, *139*, 11537.

[67] H. Dotan, K. Sivula, M. Grätzel, A. Rothschild, S. C. Warren, "Probing the photoelectrochemical properties of hematite (α-Fe_2O_3) electrodes using hydrogen peroxide as a hole scavenger", *Energy & Environmental Science* **2011**, *4*, 958.

[68] L. Badia-Bou, E. Mas-Marza, P. Rodenas, E. M. Barea, F. Fabregat-Santiago, S. Gimenez, E. Peris, J. Bisquert, "Water Oxidation at Hematite Photoelectrodes with an Iridium-Based Catalyst", *The Journal of Physical Chemistry C* **2013**, *117*, 3826.

[69] S. D. Tilley, M. Cornuz, K. Sivula, M. Grätzel, "Light-Induced Water Splitting with Hematite: Improved Nanostructure and Iridium Oxide Catalysis", *Angewandte Chemie International Edition* **2010**, *49*, 6405.

[70] H. Hajibabaei, A. R. Schon, T. W. Hamann, "Interface Control of Photoelectrochemical Water Oxidation Performance with $Ni_{1-x}Fe_xO_y$ Modified Hematite Photoanodes", *Chemistry of Materials* **2017**, *29*, 6674.

[71] C. Du, X. Yang, M. T. Mayer, H. Hoyt, J. Xie, G. McMahon, G. Bischoping, D. Wang, "Hematite-Based Water Splitting with Low Turn-On Voltages", *Angewandte Chemie International Edition* **2013**, *52*, 12692.

[72] T. Hisatomi, F. L. Formal, M. Cornuz, J. Brillet, N. Tétreault, K. Sivula, M. Grätzel, "Cathodic shift in onset potential of solar oxygen evolution on hematite by 13-group oxide overlayers", *Energy & Environmental Science* **2011**, *4*, 2512.

[73] L. Fu, H. Yu, C. Zhang, Z. Shao, B. Yi, "Cobalt Phosphate Group Modified Hematite Nanorod Array as Photoanode for Efficient Solar Water Splitting", *Electrochimica Acta* **2014**, *136*, 363.

[74] C. Zachäus, F. F. Abdi, L. M. Peter, R. v. d. Krol, "Photocurrent of $BiVO_4$ is limited by surface recombination, not surface catalysis", *Chemical Science* **2017**, *8*, 3712.

[75] A. Lasia, *Electrochemical Impedance Spectroscopy and its Applications*, Springer, New York, **2014**.

[76] D. Klotz, D. S. Ellis, H. Dotan, A. Rothschild, "Empirical *in operando* analysis of the charge carrier dynamics in hematite photoanodes by PEIS, IMPS and IMVS", *Physical Chemistry Chemical Physics* **2016**, *18*, 23438.

[77] A. Hankin, J. C. Alexander, G. H. Kelsall, "Constraints to the flat band potential of hematite photo-electrodes", *Physical Chemistry Chemical Physics* **2014**, *16*, 16176.

[78] S. R. Pendlebury, M. Barroso, A. J. Cowan, K. Sivula, J. Tang, M. Grätzel, D. Klug, J. R. Durrant, "Dynamics of photogenerated holes in nanocrystalline α-Fe_2O_3 electrodes for water oxidation probed by transient absorption spectroscopy", *Chemical Communications* **2010**, *47*, 716.

[79] J. M. Lantz, R. Baba, R. M. Corn, "Optical second harmonic generation as a probe of electrostatic fields and flatband potential at single-crystal titania electrodes", *The Journal of Physical Chemistry* **1993**, *97*, 7392.

[80] J. M. Lantz, R. M. Corn, "Time-resolved optical second harmonic generation measurements of picosecond band flattening processes at single crystal TiO_2 electrodes", *The Journal of Physical Chemistry* **1994**, *98*, 9387.

[81] H.-t. Bian, Y. Guo, H.-f. Wang, "Non-parabolic potential dependence of optical second harmonic generation from the Si(111) electrode/electrolyte interface", *Physical Chemistry Chemical Physics* **2018**, *20*, 29539.

[82] S. B. King, K. Broch, A. Demling, J. Stähler, "Multistep and multiscale electron transfer and localization dynamics at a model electrolyte/metal interface", *The Journal of Chemical Physics* **2018**, *150*, 041702.

[83] H. Helmholtz, "Ueber einige Gesetze der Vertheilung elektrischer Ströme in körperlichen Leitern mit Anwendung auf die thierisch-elektrischen Versuche", *Annalen der Physik* **1853**, *165*, 211.

[84] H. Helmholtz, "Studien über electrische Grenzschichten", *Annalen der Physik* **1879**, *243*, 337.

[85] W. Schottky, "Halbleitertheorie der Sperrschicht", *Naturwissenschaften* **1938**, *26*, 843.

[86] M. Grundmann, *The physics of semiconductors: an introduction including devices and nanophysics*, Springer, Berlin ; New York, **2006**, 689 pp.

[87] F. Fabregat-Santiago, G. Garcia-Belmonte, J. Bisquert, P. Bogdanoff, A. Zaban, "Mott-Schottky Analysis of Nanoporous Semiconductor Electrodes in Dielectric State Deposited on SnO2 (F) Conducting Substrates", *Journal of The Electrochemical Society* **2003**, *150*, E293.

[88] R. van de Krol, A. Goossens, J. Schoonman, "Mott-Schottky Analysis of Nanometer-Scale Thin-Film Anatase TiO_2", *Journal of The Electrochemical Society* **1997**, *144*, 1723.

References

[89] T. H. Wang, Y.-J. Cheng, Y.-Y. Wu, C.-A. Lin, C.-C. Chiang, Y.-K. Hsieh, C.-F. Wang, C. P. Huang, "Enhanced photoelectrochemical water splitting efficiency of hematite electrodes with aqueous metal ions as in situ homogenous surface passivation agents", *Physical Chemistry Chemical Physics* **2016**, *18*, 29300.

[90] P. Saurabh Bassi, L. Xianglin, Y. Fang, J. S. Chye Loo, J. Barber, L. Helena Wong, "Understanding charge transport in non-doped pristine and surface passivated hematite (α-Fe_2O_3) nanorods under front and backside illumination in the context of light induced water splitting", *Physical Chemistry Chemical Physics* **2016**, *18*, 30370.

[91] Y. Hu, F. Boudoire, I. Hermann-Geppert, P. Bogdanoff, G. Tsekouras, B. S. Mun, G. Fortunato, M. Graetzel, A. Braun, "Molecular Origin and Electrochemical Influence of Capacitive Surface States on Iron Oxide Photoanodes", *The Journal of Physical Chemistry C* **2016**, *120*, 3250.

[92] W. Mönch, *Semiconductor Surfaces and Interfaces*, Springer, Berlin, Heidelberg, **2001**.

[93] J. Bardeen, "Surface States and Rectification at a Metal Semi-Conductor Contact", *Physical Review* **1947**, *71*, 717.

[94] J. Bardeen, S. R. Morrison, "Surface barriers and surface conductance", *Physica* **1954**, *20*, 873.

[95] F. G. Allen, G. W. Gobeli, "Work Function, Photoelectric Threshold, and Surface States of Atomically Clean Silicon", *Physical Review* **1962**, *127*, 150.

[96] P. Handler, "NEW METHOD FOR THE MEASUREMENT OF SURFACE ELECTRICAL CONDUCTIVITY OF Si AND Ge BY CLEAVAGE", *Applied Physics Letters* **1963**, *3*, 96.

[97] M. Green, "Electrochemistry of the Semiconductor-Electrolyte Electrode. I. The Electrical Double Layer", *The Journal of Chemical Physics* **1959**, *31*, 200.

[98] A. J. Bard, A. B. Bocarsly, F. R. F. Fan, E. G. Walton, M. S. Wrighton, "The concept of Fermi level pinning at semiconductor/liquid junctions. Consequences for energy conversion efficiency and selection of useful solution redox couples in solar devices", *Journal of the American Chemical Society* **1980**, *102*, 3671.

[99] A. J. Bard, F.-R. F. Fan, A. S. Gioda, G. Nagasubramanian, H. S. White, "On the role of surface states in semiconductor electrode photoelectrochemical cells", *Faraday Discussions of the Chemical Society* **1980**, *70*, 19.

[100] K. Uosaki, H. Kita, "Effects of the Helmholtz Layer Capacitance on the Potential Distribution at Semiconductor/Electrolyte Interface and the Linearity of the Mott-Schottky Plot", *Journal of The Electrochemical Society* **1983**, *130*, Publisher: IOP Publishing, 895.

[101] B. Klahr, S. Gimenez, F. Fabregat-Santiago, J. Bisquert, T. W. Hamann, "Electrochemical and photoelectrochemical investigation of water oxidation with hematite electrodes", *Energy & Environmental Science* **2012**, *5*, 7626.

[102] D. Wegkamp, M. Herzog, L. Xian, M. Gatti, P. Cudazzo, C. L. McGahan, R. E. Marvel, R. F. Haglund, A. Rubio, M. Wolf, J. Stähler, "Instantaneous Band Gap Collapse in Photoexcited Monoclinic ${\mathrm{VO}}_{2}$ due to Photocarrier Doping", *Physical Review Letters* **2014**, *113*, 216401.

[103] L. Perfetti, P. A. Loukakos, M. Lisowski, U. Bovensiepen, H. Berger, S. Biermann, P. S. Cornaglia, A. Georges, M. Wolf, "Time Evolution of the Electronic Structure of 1 T – TaS_2 through the Insulator-Metal Transition", *Physical Review Letters* **2006**, *97*, 067402.

[104] L. Waldecker, A. Raja, M. Rösner, C. Steinke, A. Bostwick, R. J. Koch, C. Jozwiak, T. Taniguchi, K. Watanabe, E. Rotenberg, T. O. Wehling, T. F. Heinz, "Rigid Band Shifts in Two-Dimensional Semiconductors through External Dielectric Screening", *Physical Review Letters* **2019**, *123*, DOI 10.1103/PhysRevLett.123.206403.

[105] J. Warby, S. Shah, J. Thiesbrummel, E. Gutierrez-Partida, H. Lai, B. Alebachew, M. Grischek, F. Yang, F. Lang, S. Albrecht, F. Fu, D. Neher, M. Stolterfoht, "Mismatch of Quasi–Fermi Level Splitting and Voc in Perovskite Solar Cells", *Advanced Energy Materials* **2023**, *13*, 2303135.

[106] J. Lee, H. Yeo, Y.-H. Kim, "Quasi-Fermi level splitting in nanoscale junctions from ab initio", *Proceedings of the National Academy of Sciences* **2020**, *117*, 10142.

[107] W. E. Pinson, "Measuring the quasi-fermi levels and flat band potential of an illuminated Au/n GaAs0.6P0.4 anode", *Surface Science* **1980**, *101*, DOI 10.1016/0039-6028(80)90618-4.

[108] V. Markovac, M. Cohen, "The Anodic Deposition of Iron Oxide Films on Platinum", *Journal of The Electrochemical Society* **1967**, *114*, 678.

[109] J.-L. Leibenguth, M. Cohen, "The Anodic Deposition of Oxide Films on Platinum from Ferrous Sulfate Solutions", *Journal of The Electrochemical Society* **1972**, *119*, 987.

[110] R. L. Spray, K.-S. Choi, "Photoactivity of Transparent Nanocrystalline α-Fe_2O_3 Electrodes Prepared via Anodic Electrodeposition", *Chemistry of Materials* **2009**, *21*, 3701.

[111] O. Zandi, A. R. Schon, H. Hajibabaei, T. W. Hamann, "Enhanced Charge Separation and Collection in High-Performance Electrodeposited Hematite Films", *Chemistry of Materials* **2016**, *28*, 765.

[112] Y. W. Phuan, W.-J. Ong, M. N. Chong, J. D. Ocon, "Prospects of electrochemically synthesized hematite photoanodes for photoelectrochemical water splitting: A review", *Journal of Photochemistry and Photobiology C: Photochemistry Reviews* **2017**, *33*, 54.

[113] C. Yilmaz, U. Unal, "Morphology and crystal structure control of α-Fe_2O_3 films by hydrothermal-electrochemical deposition in the presence of Ce^{3+} and/or acetate, F^- ions", *RSC Advances* **2016**, *6*, 8517.

[114] S. S. Kulkarni, C. D. Lokhande, "Structural, optical, electrical and dielectrical properties of electrosynthesized nanocrystalline iron oxide thin films", *Materials Chemistry and Physics* **2003**, *82*, 151.

[115] L. Martinez, D. Leinen, F. Martín, M. Gabas, J. R. Ramos-Barrado, E. Quagliata, E. A. Dalchiele, "Electrochemical Growth of Diverse Iron Oxide (Fe_3O_4, α-FeOOH, and γ-FeOOH) Thin Films by Electrodeposition Potential Tuning", *Journal of The Electrochemical Society* **2007**, *154*, D126.

[116] F. Nasirpouri, *Electrodeposition of Nanostructured Materials*, Springer International Publishing, **2017**.

[117] W. Nernst, *Zeitschrift für Physikalische Chemie* **1889**, *4U*, 129.

[118] P. A. Franken, A. E. Hill, C. W. Peters, G. Weinreich, "Generation of Optical Harmonics", *Physical Review Letters* **1961**, *7*, 118.

[119] R. W. Boyd, *Nonlinear optics*, Academic press, **2003**.

[120] I. Yagi in *Compendium of Surface and Interface Analysis*, (Ed.: The Surface Science Society of Japan), Springer, Singapore, **2018**, pp. 91–95.

[121] A. G. Lambert, P. B. Davies, D. J. Neivandt, "Implementing the Theory of Sum Frequency Generation Vibrational Spectroscopy: A Tutorial Review", *Applied Spectroscopy Reviews* **2005**, *40*, 103.

[122] R. M. Corn, D. A. Higgins, "Optical second harmonic generation as a probe of surface chemistry", *Chemical Reviews* **1994**, *94*, 107.

[123] E. J. Sie, C. M. Nyby, C. D. Pemmaraju, S. J. Park, X. Shen, J. Yang, M. C. Hoffmann, B. K. Ofori-Okai, R. Li, A. H. Reid, S. Weathersby, E. Mannebach, N. Finney, D. Rhodes, D. Chenet, A. Antony, L. Balicas, J. Hone, T. P. Devereaux, T. F. Heinz, X. Wang, A. M. Lindenberg, "An ultrafast symmetry switch in a Weyl semimetal", *Nature* **2019**, *565*, 61.

[124] H. Jang, K. P. Dhakal, K.-I. Joo, W. S. Yun, S. M. Shinde, X. Chen, S. M. Jeong, S. W. Lee, Z. Lee, J. Lee, J.-H. Ahn, H. Kim, "Transient SHG Imaging on Ultrafast Carrier Dynamics of MoS_2 Nanosheets", *Advanced Materials* **2018**, *30*, 1705190.

[125] L. Schneider, W. Peukert, "Second Harmonic Generation Spectroscopy as a Method for In Situ and Online Characterization of Particle Surface Properties", *Particle & Particle Systems Characterization* **2006**, *23*, 351.

[126] K. B. Eisenthal, "Liquid Interfaces Probed by Second-Harmonic and Sum-Frequency Spectroscopy", *Chemical Reviews* **1996**, *96*, 1343.

[127] G. Almogy, A. Yariv, "Second-harmonic generation in absorptive media", *Optics Letters* **1994**, *19*, 1828.

[128] S. Shree, D. Lagarde, L. Lombez, C. Robert, A. Balocchi, K. Watanabe, T. Taniguchi, X. Marie, I. C. Gerber, M. M. Glazov, L. E. Golub, B. Urbaszek, I. Paradisanos, "Interlayer exciton mediated second harmonic generation in bilayer MoS2", *Nature Communications* **2021**, *12*, 6894.

[129] B. Lu, D. H. Torchinsky, "Fourier domain rotational anisotropy-second harmonic generation", *Optics Express* **2018**, *26*, 33192.

[130] M. Thämer, T. Garling, R. K. Campen, M. Wolf, "Quantitative determination of the nonlinear bulk and surface response from alpha-quartz using phase sensitive SFG spectroscopy", *The Journal of Chemical Physics* **2019**, *151*, 064707.

[131] T. E. Tsai, M. A. Saifi, E. J. Friebele, U. Österberg, D. L. Griscom, "Correlation of defect centers with second-harmonic generation in Ge-doped and Ge–P-doped silica-core single-mode fibers", *Optics Letters* **1989**, *14*, 1023.

[132] A. Farenbruch, D. Fröhlich, D. R. Yakovlev, M. Bayer, "Two-photon absorption and second harmonic generation of 1*S* para- and orthoexcitons in Cu_2O coupled by a magnetic field", *Physical Review B* **2020**, *102*, Publisher: American Physical Society, 115203.

[133] G. Wang, X. Marie, I. Gerber, T. Amand, D. Lagarde, L. Bouet, M. Vidal, A. Balocchi, B. Urbaszek, "Giant Enhancement of the Optical Second-Harmonic Emission of WSe_2 Monolayers by Laser Excitation at Exciton Resonances", *Physical Review Letters* **2015**, *114*, DOI `10.1103/PhysRevLett.114.097403`.

[134] H. A. Lorentz, *The theory of electrons and its applications to the phenomena of light and radiant heat*, Dover ed, OCLC: 535812, Dover Publications, New York, **1952**, 343 pp.

[135] J. Liu, M. Brio, Y. Zeng, A. R. Zakharian, W. Hoyer, S. W. Koch, J. V. Moloney, "Generalization of the FDTD algorithm for simulations of hydrodynamic nonlinear Drude model", *Journal of Computational Physics* **2010**, *229*, 5921.

[136] P. Atkins, J. de Paula, *Physical Chemistry*, W. H. Freeman and Company, New York, **2006**.

[137] J. M. Lantz, R. M. Corn, "Electrostatic field measurements and band flattening during electron-transfer processes at single-crystal TiO_2 electrodes by electric field-induced optical second harmonic generation", *The Journal of Physical Chemistry* **1994**, *98*, 4899.

[138] A. J. Fresnel, *Mémoire sur la diffraction de la lumière*, **1926**.

[139] Y. Tong, Y. Zhao, N. Li, M. Osawa, P. B. Davies, S. Ye, "Interference effects in the sum frequency generation spectra of thin organic films. I. Theoretical modeling and simulation", *The Journal of Chemical Physics* **2010**, *133*, 034704.

[140] P. E. Ohno, H. Chang, A. P. Spencer, Y. Liu, M. D. Boamah, H.-f. Wang, F. M. Geiger, "Beyond the Gouy–Chapman Model with Heterodyne-Detected Second Harmonic Generation", *The Journal of Physical Chemistry Letters* **2019**, *10*, 2328.

[141] C. H. Lee, R. K. Chang, N. Bloembergen, "Nonlinear Electroreflectance in Silicon and Silver", *Physical Review Letters* **1967**, *18*, 167.

[142] K. B. Eisenthal, "Second Harmonic Spectroscopy of Aqueous Nano- and Microparticle Interfaces", *Chemical Reviews* **2006**, *106*, 1462.

[143] O. Aktsipetrov, A. Fedyanin, A. Melnikov, E. Mishina, A. Rubtsov, M. Anderson, P. Wilson, M. Beek, X. Hu, J. Dadap, M. Downer, "DC-electric-field-induced and low-frequency electromodulation second-harmonic generation spectroscopy of Si(001)-SiO_2 interfaces", *Physical Review B* **1998**, *60*, 8924.

[144] G. Gonella, C. Lütgebaucks, A. G. F. de Beer, S. Roke, "Second Harmonic and Sum-Frequency Generation from Aqueous Interfaces Is Modulated by Interference", *The Journal of Physical Chemistry C* **2016**, *120*, 9165.

[145] H.-t. Bian, R.-r. Feng, Y.-y. Xu, Y. Guo, H.-f. Wang, "Increased interfacial thickness of the NaF, NaCl and NaBr salt aqueous solutions probed with non-resonant surface second harmonic generation (SHG)", *Physical Chemistry Chemical Physics* **2008**, *10*, 4920.

[146] Y. R. Shen, V. Ostroverkhov, "Sum-Frequency Vibrational Spectroscopy on Water Interfaces: Polar Orientation of Water Molecules at Interfaces", *Chemical Reviews* **2006**, *106*, 1140.

[147] S. Pezzotti, D. Ruth Galimberti, Y. Ron Shen, M.-P. Gaigeot, "Structural definition of the BIL and DL: a new universal methodology to rationalize non-linear $\chi^{(2)}(\omega)$ SFG signals at charged interfaces, including $\chi^{(3)}(\omega)$ contributions", *Physical Chemistry Chemical Physics* **2018**, *20*, 5190.

[148] Y. Nagata, S. Mukamel, "Electrical Double Layer Probed by Surface-Specific Vibrational Technique", *Chem* **2018**, *4*, 1484.

[149] S. Ong, X. Zhao, K. B. Eisenthal, "Polarization of water molecules at a charged interface: second harmonic studies of the silica/water interface", *Chemical Physics Letters* **1992**, *191*, 327.

[150] Y. Chen, H. I. Okur, C. Liang, S. Roke, "Orientational ordering of water in extended hydration shells of cations is ion-specific and is correlated directly with viscosity and hydration free energy", *Physical Chemistry Chemical Physics* **2017**, *19*, 24678.

[151] H. I. Okur, Y. Chen, D. M. Wilkins, S. Roke, "The Jones-Ray effect reinterpreted: Surface tension minima of low ionic strength electrolyte solutions are caused by electric field induced water-water correlations", *Chemical Physics Letters* **2017**, *684*, 433.

[152] Y. Chen, H. I. Okur, N. Gomopoulos, C. Macias-Romero, P. S. Cremer, P. B. Petersen, G. Tocci, D. M. Wilkins, C. Liang, M. Ceriotti, S. Roke, "Electrolytes induce long-range orientational order and free energy changes in the H-bond network of bulk water", *Science Advances* **2016**, *2*, e1501891.

[153] M. Planck, "Über irreversible Strahlungsvorgänge.", *Sitzungsberichte der Königlich Preußischen Akademie der Wissenschaften zu Berlin.* **1899**, 479.

[154] M. Planck, "Zur Geschichte der Auffindung des physikalischen Wirkungsquantums", *Die Naturwissenschaften* **1943**, *31*, 153.

[155] M. Thämer, R. K. Campen, M. Wolf, "Detecting weak signals from interfaces by high accuracy phase-resolved SFG spectroscopy", *Physical Chemistry Chemical Physics* **2018**, *20*, 25875.

[156] T. Garling, Y. Tong, T. A. Darwish, M. Wolf, R. K. Campen, "The influence of surface potential on the optical switching of spiropyran self assembled monolayers", *Journal of Physics: Condensed Matter* **2017**, *29*, 414002.

[157] J. Wang, M. Clementi, M. Minkov, A. Barone, J.-F. Carlin, N. Grandjean, D. Gerace, S. Fan, M. Galli, R. Houdré, "Doubly resonant second-harmonic generation of a vortex beam from a bound state in the continuum", *Optica* **2020**, *7*, 1126.

[158] P. S. Kuo, G. S. Solomon, "On- and off-resonance second-harmonic generation in GaAs microdisks", *Optics Express* **2011**, *19*, 16898.

References

[159] B. Klahr, S. Gimenez, F. Fabregat-Santiago, J. Bisquert, T. W. Hamann, "Photoelectrochemical and Impedance Spectroscopic Investigation of Water Oxidation with "Co–Pi"-Coated Hematite Electrodes", *Journal of the American Chemical Society* **2012**, *134*, 16693.

[160] I. Cesar, K. Sivula, A. Kay, R. Zboril, M. Grätzel, "Influence of Feature Size, Film Thickness, and Silicon Doping on the Performance of Nanostructured Hematite Photoanodes for Solar Water Splitting", *The Journal of Physical Chemistry C* **2009**, *113*, 772.

[161] R. López, R. Gómez, "Band-gap energy estimation from diffuse reflectance measurements on sol–gel and commercial TiO2: a comparative study", *Journal of Sol-Gel Science and Technology* **2012**, *61*, 1.

[162] A. R. C. Bredar, A. L. Chown, A. R. Burton, B. H. Farnum, "Electrochemical Impedance Spectroscopy of Metal Oxide Electrodes for Energy Applications", *ACS Applied Energy Materials* **2020**, *3*, 66.

[163] A. J. Bard, L. R. Faulkner, *Electrochemical methods: fundamentals and applications*, 2nd ed, Wiley, New York, **2001**, 833 pp.

[164] D. S. Frolov, V. I. Zubkov, "Frequency dispersion of capacitance–voltage characteristics in wide bandgap semiconductor-electrolyte junctions", *Semiconductor Science and Technology* **2016**, *31*, 125013.

[165] V. F. Lvovich, *Impedance spectroscopy: applications to electrochemical and dielectric phenomena*, Wiley, Hoboken, N.J, **2012**.

[166] D. Halliday, R. Resnick, J. Walker, *Physik*, 2nd ed., Wiley-VCH, **2009**.

[167] T. Lopes, L. Andrade, F. Le Formal, M. Gratzel, K. Sivula, A. Mendes, "Hematite photoelectrodes for water splitting: evaluation of the role of film thickness by impedance spectroscopy", *Physical Chemistry Chemical Physics* **2014**, *16*, 16515.

[168] J. Y. Kim, G. Magesh, D. H. Youn, J.-W. Jang, J. Kubota, K. Domen, J. S. Lee, "Single-crystalline, wormlike hematite photoanodes for efficient solar water splitting", *Scientific Reports* **2013**, *3*, srep02681.

[169] O. Zandi, T. W. Hamann, "Determination of photoelectrochemical water oxidation intermediates on haematite electrode surfaces using operando infrared spectroscopy", *Nature Chemistry* **2016**, *8*, 778.

[170] D. Teschner, J. Plescher, S. Piccinin, T. E. Jones, A. Hammud, F. Schmidt, A. Knop-Gericke, H. Bluhm, A. Shavorskiy, "Understanding Anomalous Gas-Phase Peak Shifts in Dip-and-Pull Ambient Pressure XPS Experiments", *The Journal of Physical Chemistry C*, *128*, 7096.

[171] J. D. Benck, B. A. Pinaud, Y. Gorlin, T. F. Jaramillo, "Substrate Selection for Fundamental Studies of Electrocatalysts and Photoelectrodes: Inert Potential Windows in Acidic, Neutral, and Basic Electrolyte", *PLOS ONE* **2014**, *9*, e107942.

[172] N. Wiberg, A. N. Hollemann, *Lehrbuch der Anorganischen Chemie*, De Gruyter, **2008**.

[173] A. Kay, M. Fiegenbaum-Raz, S. Müller, R. Eichberger, H. Dotan, R. v. d. Krol, F. F. Abdi, A. Rothschild, D. Friedrich, D. A. Grave, "Effect of Doping and Excitation Wavelength on Charge Carrier Dynamics in Hematite by Time-Resolved Microwave and Terahertz Photoconductivity", *Advanced Functional Materials* **2020**, *30*, 1901590.

[174] S. Sorenson, E. Driscoll, S. Haghighat, J. M. Dawlaty, "Ultrafast Carrier Dynamics in Hematite Films: The Role of Photoexcited Electrons in the Transient Optical Response", *The Journal of Physical Chemistry C* **2014**, *118*, 23621.

[175] Z. Huang, Y. Lin, X. Xiang, W. Rodríguez-Córdoba, K. J. McDonald, K. S. Hagen, K.-S. Choi, B. S. Brunschwig, D. G. Musaev, C. L. Hill, D. Wang, T. Lian, "In situ probe of photocarrier dynamics in water -splitting hematite (α-Fe_2O_3) electrodes", *Energy & Environmental Science* **2012**, *5*, 8923.

[176] Y. R. Shen, "Optical Second Harmonic Generation at Interfaces", *Annual Review of Physical Chemistry* **1989**, *40*, 327.

[177] M. Faraday, "VI. Experimental researches in electricity.-Seventh Series", *Philosophical Transactions of the Royal Society of London* **1834**, *124*, 77.

[178] X. Zong, S. Thaweesak, H. Xu, Z. Xing, J. Zou, G. Lu, L. Wang, "A scalable colloidal approach to prepare hematite films for efficient solar water splitting", *Physical Chemistry Chemical Physics* **2013**, *15*, 12314.

[179] I. V. Chernyshova, M. F. H. Jr, A. S. Madden, "Size-dependent structural transformations of hematite nanoparticles . 1. Phase transition", *Physical Chemistry Chemical Physics* **2007**, *9*, 1736.

[180] D. E. Fouad, C. Zhang, H. El-Didamony, L. Yingnan, T. D. Mekuria, A. H. Shah, "Improved size, morphology and crystallinity of hematite (α-Fe_2O_3) nanoparticles synthesized via the precipitation route using ferric sulfate precursor", *Results in Physics* **2019**, *12*, 1253.

[181] A. Annamalai, A. Subramanian, U. Kang, H. Park, S. H. Choi, J. S. Jang, "Activation of Hematite Photoanodes for Solar Water Splitting: Effect of FTO Deformation", *The Journal of Physical Chemistry C* **2015**, *119*, 3810.

[182] P. S. Shinde, S. H. Choi, Y. Kim, J. Ryu, J. S. Jang, "Onset potential behavior in α-Fe_2O_3 photoanodes: the influence of surface and diffusion Sn doping on the surface states", *Physical Chemistry Chemical Physics* **2016**, *18*, 2495.

[183] P. Scherrer, "Bestimmung der Größe und der inneren Struktur von Kolloidteilchen mittels Röntgenstrahlen", *Nachrichten von der Gesellschaft der Wissenschaften zu Göttingen Mathematisch-Physikalische Klasse* **1918**, *1918*, 98.

[184] R. J. Matyi, L. H. Schwartz, J. B. Butt, "Particle Size, Particle Size Distribution, and Related Measurements of Supported Metal Catalysts", *Catalysis Reviews* **1987**, *29*, 41.

[185] A. M. Jubb, H. C. Allen, "Vibrational Spectroscopic Characterization of Hematite, Maghemite, and Magnetite Thin Films Produced by Vapor Deposition", *ACS Applied Materials & Interfaces* **2010**, *2*, 2804.

[186] I. Chamritski, G. Burns, "Infrared- and Raman-Active Phonons of Magnetite, Maghemite, and Hematite: A Computer Simulation and Spectroscopic Study", *The Journal of Physical Chemistry B* **2005**, *109*, 4965.

[187] C. P. Marshall, W. J. B. Dufresne, C. J. Rufledt, "Polarized Raman spectra of hematite and assignment of external modes", *Journal of Raman Spectroscopy* **2019**, 1522.

[188] C. Lohaus, A. Klein, W. Jaegermann, "Limitation of Fermi level shifts by polaron defect states in hematite photoelectrodes", *Nature Communications* **2018**, *9*, 4309.

[189] C. Xia, Y. Jia, M. Tao, Q. Zhang, "Tuning the band gap of hematite α-Fe_2O_3 by sulfur doping", *Physics Letters A* **2013**, *377*, 1943.

[190] J. Tauc, "Optical properties and electronic structure of amorphous Ge and Si", *Materials Research Bulletin* **1968**, *3*, 37.

[191] P. Makuła, M. Pacia, W. Macyk, "How To Correctly Determine the Band Gap Energy of Modified Semiconductor Photocatalysts Based on UV–Vis Spectra", *The Journal of Physical Chemistry Letters* **2018**, *9*, 6814.

[192] E. Nurlaela, A. Ziani, K. Takanabe, "Tantalum nitride for photocatalytic water splitting: concept and applications", *Materials for Renewable and Sustainable Energy* **2016**, *5*, 18.

[193] Z. Zhang, I. Karimata, H. Nagashima, S. Muto, K. Ohara, K. Sugimoto, T. Tachikawa, "Interfacial oxygen vacancies yielding long-lived holes in hematite mesocrystal-based photoanodes", *Nature Communications* **2019**, *10*, 4832.

References

[194] Z. Wang, X. Mao, P. Chen, M. Xiao, S. A. Monny, S. Wang, M. Konarova, A. Du, L. Wang, "Understanding the Roles of Oxygen Vacancies in Hematite-Based Photoelectrochemical Processes", *Angewandte Chemie International Edition* **2019**, *58*, 1030.

[195] G. K. Mor, H. E. Prakasam, O. K. Varghese, K. Shankar, C. A. Grimes, "Vertically Oriented Ti-Fe-O Nanotube Array Films: Toward a Useful Material Architecture for Solar Spectrum Water Photoelectrolysis", *Nano Letters* **2007**, *7*, 2356.

[196] J. Y. Kim, D. H. Youn, K. Kang, J. S. Lee, "Highly Conformal Deposition of an Ultrathin FeOOH Layer on a Hematite Nanostructure for Efficient Solar Water Splitting", *Angewandte Chemie* **2016**, *128*, 11012.

[197] D. W. Davies, C. N. Savory, J. M. Frost, D. O. Scanlon, B. J. Morgan, A. Walsh, "Descriptors for Electron and Hole Charge Carriers in Metal Oxides", *The Journal of Physical Chemistry Letters* **2020**, *11*, 438.

[198] S. Geiger, O. Kasian, A. M. Mingers, S. S. Nicley, K. Haenen, K. J. J. Mayrhofer, S. Cherevko, "Catalyst Stability Benchmarking for the Oxygen Evolution Reaction: The Importance of Backing Electrode Material and Dissolution in Accelerated Aging Studies", *ChemSusChem* **2017**, *10*, 4140.

[199] D. S. Jordan, C. J. Hull, J. M. Troiano, S. C. Riha, A. B. F. Martinson, K. M. Rosso, F. M. Geiger, "Second Harmonic Generation Studies of Fe(II) Interactions with Hematite (α-Fe_2O_3)", *The Journal of Physical Chemistry C* **2013**, *117*, 4040.

[200] J. M. Troiano, D. S. Jordan, C. J. Hull, F. M. Geiger, "Interaction of Cr(III) and Cr(VI) with Hematite Studied by Second Harmonic Generation", *The Journal of Physical Chemistry C* **2013**, *117*, 5164.

[201] T. Hashimoto, T. Yamada, T. Yoko, "Third-order nonlinear optical properties of sol–gel derived α-Fe_2O_3, γ-Fe_2O_3, and Fe_3O_4 thin films", *Journal of Applied Physics* **1996**, *80*, 3184.

[202] J. H. Lambert, *Photometria sive de mensura et gradibus luminis, colorum et umbrae*, Medium: 547 S., 6 Bl. ; 19 cm : 8 gef. Tafeln, AUGUSTAE VINDELICORUM, Sumptibus VIDVAE EBERHARDI KLETT Typis CHRISTOPHORI PETRI DETLEFFSEN. MDCCLX, **1760**.

[203] Beer, "Bestimmung der Absorption des rothen Lichts in farbigen Flüssigkeiten", *Annalen der Physik* **1852**, *162*, 78.

[204] A. Kleiman-Shwarsctein, Y.-S. Hu, A. J. Forman, G. D. Stucky, E. W. McFarland, "Electrodeposition of α-Fe_2O_3 Doped with Mo or Cr as Photoanodes for Photocatalytic Water Splitting", *The Journal of Physical Chemistry C* **2008**, *112*, 15900.

[205] C. Yilmaz, U. Unal, "Single step synthesis of (α-Fe_2O_3) hematite films by hydrothermal electrochemical deposition", *RSC Advances* **2015**, *5*, 16082.

[206] S. H. Tamboli, G. Rahman, O.-S. Joo, "Influence of potential, deposition time and annealing temperature on photoelectrochemical properties of electrodeposited iron oxide thin films", *Journal of Alloys and Compounds* **2012**, *520*, 232.

[207] L. Guo, P. C. Searson, "On the influence of the nucleation overpotential on island growth in electrodeposition", *Electrochimica Acta* **2010**, *55*, 4086.

[208] G. Y. Wu, S. Bae, A. A. Gewirth, J. Gray, X. D. Zhu, T. P. Moffat, W. Schwarzacher, "Pb electrodeposition on polycrystalline Cu in the presence and absence of Cl^-: A combined oblique incidence reflectivity difference and in situ AFM study", *Surface Science* **2007**, *601*, 1886.

[209] F. Nasirpouri, "On the electrodeposition mechanism of Pb on copper substrate from a perchlorate solution studied by electrochemical quartz crystal microbalance", *Ionics* **2011**, *17*, 331.

[210] J. Heinze, "Cyclovoltammetrie - die „Spektroskopie"des Elektrochemikers", *Angewandte Chemie* **1984**, *96*, 823.

[211] S. Arrhenius, "Über die Dissociationswärme und den Einfluss der Temperatur auf den Dissociationsgrad der Elektrolyte", *Zeitschrift für Physikalische Chemie* **1889**, *4U*, 96.

[212] M. Volmer, A. Weber, "Keimbildung in übersättigten Gebilden", *Zeitschrift für Physikalische Chemie* **1926**, *119U*, 277.

[213] R. M. Cornell, U. Schwertmann, *The iron oxides: structure, properties, reactions, occurrences, and uses*, 2nd, completely rev. and extended ed, Wiley-VCH, Weinheim, **2003**, 664 pp.

[214] R. Vasilic, N. Vasiljevic, N. Dimitrov, "Open circuit stability of underpotentially deposited Pb monolayer on Cu(111)", *Journal of Electroanalytical Chemistry* **2005**, *580*, 203.

[215] J.-W. Yan, J.-M. Wu, Q. Wu, Z.-X. Xie, B.-W. Mao, "Competitive Adsorption and Surface Alloying: Underpotential Deposition of Sn on Sulfate-Covered Cu(111)", *Langmuir* **2003**, *19*, 7948.

[216] J. R. Lagraff, B. J. Cruickshank, A. A. Gewirth, "In-Situ Observation of Oxide Monolayer Formation on Copper Solid-Liquid Interfaces", *MRS Online Proceedings Library* **1994**, *332*, 121.

[217] H. Siegenthaler, K. Jüttner, "Voltammetric investigation of lead adsorption on Cu(111) single crystal substrates", *Journal of Electroanalytical Chemistry and Interfacial Electrochemistry* **1984**, *163*, 327.

[218] E. Murad, "Magnetic properties of microcrystalline iron (III) oxides and related materials as reflected in their Mössbauer spectra", *Physics and Chemistry of Minerals* **1996**, *23*, 248.

[219] W. D. Chemelewski, H.-C. Lee, J.-F. Lin, A. J. Bard, C. B. Mullins, "Amorphous FeOOH Oxygen Evolution Reaction Catalyst for Photoelectrochemical Water Splitting", *Journal of the American Chemical Society* **2014**, *136*, 2843.

[220] J. M. D. Coey in *Iron in Soils and Clay Minerals*, (Eds.: J. W. Stucki, B. A. Goodman, U. Schwertmann), NATO ASI Series, Springer Netherlands, Dordrecht, **1988**, pp. 397–466.

[221] M. Guignard, V. Nazabal, X.-H. Zhang, F. Smektala, A. Moréac, S. Pechev, H. Zeghlache, A. Kudlinski, G. Martinelli, Y. Quiquempois, "Crystalline phase responsible for the permanent second-harmonic generation in chalcogenide glass-ceramics", *Optical Materials* **2007**, *30*, 338.

[222] S. Chen, K. F. Li, G. Li, K. W. Cheah, S. Zhang, "Gigantic electric-field-induced second harmonic generation from an organic conjugated polymer enhanced by a band-edge effect", *Light: Science & Applications* **2019**, *8*, 17.

[223] H. G. Zachmann, A. Jüngel, *Mathematik für Chemiker*, 6th ed., Wiley-VCH, **2007**.

[224] X. Zhao, S. Ong, K. B. Eisenthal, "Polarization of water molecules at a charged interface. Second harmonic studies of charged monolayers at the air/water interface", *Chemical Physics Letters* **1993**, *202*, 513.

[225] M. Chemla, J. F. Dufrêche, I. Darolles, F. Rouelle, D. Devilliers, S. Petitdidier, D. Lévy, "Bias voltage dependent electrochemical impedance spectroscopy of p- and n-type silicon substrates", *Electrochimica Acta* **2005**, *51*, 665.

[226] G. Nogami, "Characterization of Semiconductor Electrodes with a Deep Impurity Level", *Journal of The Electrochemical Society* **1982**, *129*, 2219.

[227] G. Nogami, "Some Aspects of Large Frequency Dispersion of Mott-Schottky Plots in TiO_2 Electrodes", *Journal of The Electrochemical Society* **1985**, *132*, 76.

[228] A. N. Jansen, P. T. Wojcik, P. Agarwal, M. E. Orazem, "Thermally Stimulated Deep-Level Impedance Spectroscopy: Application to an n-GaAs Schottky Diode", *Journal of The Electrochemical Society* **1996**, *143*, 4066.

[229] N. F. Mott, "Note on the contact between a metal and an insulator or semi-conductor", *Mathematical Proceedings of the Cambridge Philosophical Society* **1938**, *34*, 568.

[230] S. Onari, T. Arai, K. Kudo, "Infrared lattice vibrations and dielectric dispersion in α-Fe_2O_3", *Physical Review B* **1977**, *16*, 1717.

[231] K. M. Rosso, D. M. A. Smith, M. Dupuis, "An ab initio model of electron transport in hematite (α-Fe_2O_3) basal planes", *The Journal of Chemical Physics* **2003**, *118*, 6455.

[232] M. Cardona, "Electroreflectance at a Semiconductor-Electrolyte Interface", *Physical Review* **1967**, *154*, 696.

[233] J. Gandia, M. Pujadas, P. Salvador, "Electrolyte electroreflectance", *Journal of Electroanalytical Chemistry and Interfacial Electrochemistry* **1988**, *244*, 69.

[234] A. Hankin, F. E. Bedoya-Lora, J. C. Alexander, A. Regoutz, G. H. Kelsall, "Flat band potential determination: avoiding the pitfalls", *Journal of Materials Chemistry A* **2019**, *7*, 26162.

[235] A. Goossens, "Potential Distribution in Semiconductor Particles", *Journal of The Electrochemical Society* **1996**, *143*, L131.

[236] M. F. Dupont, S. W. Donne, "Charge storage mechanisms in electrochemical capacitors: Effects of electrode properties on performance", *Journal of Power Sources* **2016**, *326*, 613.

[237] F. Le Formal, E. Pastor, S. D. Tilley, C. A. Mesa, S. R. Pendlebury, M. Grätzel, J. R. Durrant, "Rate Law Analysis of Water Oxidation on a Hematite Surface", *Journal of the American Chemical Society* **2015**, *137*, 6629.

[238] Y. Zhang, H. Zhang, A. Liu, C. Chen, W. Song, J. Zhao, "Rate-Limiting O–O Bond Formation Pathways for Water Oxidation on Hematite Photoanode", *Journal of the American Chemical Society* **2018**, *140*, 3264.

[239] C. A. Mesa, L. Francàs, K. R. Yang, P. Garrido-Barros, E. Pastor, Y. Ma, A. Kafizas, T. E. Rosser, M. T. Mayer, E. Reisner, M. Grätzel, V. S. Batista, J. R. Durrant, "Multihole water oxidation catalysis on haematite photoanodes revealed by operando spectroelectrochemistry and DFT", *Nature Chemistry* **2020**, *12*, 82.

[240] J. Li, W. Wan, C. A. Triana, H. Chen, Y. Zhao, C. K. Mavrokefalos, G. R. Patzke, "Reaction kinetics and interplay of two different surface states on hematite photoanodes for water oxidation", *Nature Communications* **2021**, *12*, 255.

[241] C. T. Campbell, "The Degree of Rate Control: A Powerful Tool for Catalysis Research", *ACS Catalysis* **2017**, *7*, 2770.

[242] D. Wang, T. Sheng, J. Chen, H.-F. Wang, P. Hu, "Identifying the key obstacle in photocatalytic oxygen evolution on rutile TiO2", *Nature Catalysis* **2018**, *1*, 291.

[243] D. A. Grave, H. Dotan, Y. Levy, Y. Piekner, B. Scherrer, K. D. Malviya, A. Rothschild, "Heteroepitaxial hematite photoanodes as a model system for solar water splitting", *Journal of Materials Chemistry A* **2016**, *4*, 3052.

[244] O. Stern, "Zur Theorie der elektrolytischen Doppelschicht", *Zeitschrift für Elektrochemie* **1924**, *30*, 508.

[245] K. L. Cheng, "Counterion Triple Layer in Solid/Solution Interface: Stirring and Temperature Effects on pH Measurements", *Journal of Colloid and Interface Science* **2001**, *239*, 385.

[246] K. Syrek, J. Kapusta-Kołodziej, M. Jarosz, G. D. Sulka, "Effect of electrolyte agitation on anodic titanium dioxide (ATO) growth and its photoelectrochemical properties", *Electrochimica Acta* **2015**, *180*, 801.

[247] Y. Ge, X. Xie, J. Roscher, R. Holze, Q. Qu, "How to measure and report the capacity of electrochemical double layers, supercapacitors, and their electrode materials", *Journal of Solid State Electrochemistry* **2020**, *24*, 3215.

[248] G. Paasch, S. Scheinert, "Charge carrier density of organics with Gaussian density of states: Analytical approximation for the Gauss–Fermi integral", *Journal of Applied Physics* **2010**, *107*, 104501.

[249] R. van de Krol, A. Goossens, J. Schoonman, "Erratum: "Mott-Schottky Analysis of Nanometer-Scale Thin-Film Anatase TiO_2" [J. Electrochem. Soc., 144, 1723 (1997)]", *Journal of The Electrochemical Society* **1998**, *145*, 3697.

[250] Y. Shan, Y. Li, D. Huang, Q. Tong, W. Yao, W.-T. Liu, S. Wu, "Stacking symmetry governed second harmonic generation in graphene trilayers", *Science Advances* **2018**, *4*.

[251] E. Willinger, C. Massué, R. Schlögl, M. G. Willinger, "Identifying Key Structural Features of IrO_x Water Splitting Catalysts", *Journal of the American Chemical Society* **2017**, *139*, 12093.

[252] L. J. Frevel, R. Mom, J.-J. Velasco-Vélez, M. Plodinec, A. Knop-Gericke, R. Schlögl, T. E. Jones, "In Situ X-ray Spectroscopy of the Electrochemical Development of Iridium Nanoparticles in Confined Electrolyte", *The Journal of Physical Chemistry C* **2019**, *123*, 9146.

[253] A. Kartouzian, P. Heister, M. Thämer, S. Gerlach, U. Heiz, "In-line reference measurement for surface second harmonic generation spectroscopy", *JOSA B* **2013**, *30*, 541.

[254] J. M. Marmolejos, P. J. Bisson, M. J. Shultz, "Gold as a standard phase reference in complex sum frequency generation measurements", *The Journal of Chemical Physics* **2019**, *150*, 124705.

[255] L. Dalstein, A. Revel, C. Humbert, B. Busson, "Nonlinear optical response of a gold surface in the visible range: A study by two-color sum-frequency generation spectroscopy. I. Experimental determination", *The Journal of Chemical Physics* **2018**, *148*, 134701.

[256] G. Golub, W. Kahan, "Calculating the Singular Values and Pseudo-Inverse of a Matrix", *Journal of the Society for Industrial and Applied Mathematics Series B Numerical Analysis* **1965**, *2*, 205.

[257] N. Pavlycheva, A. Niyazgulyyewa, A. Sakhabutdinov, V. Anfinogentov, O. Morozov, T. Agliullin, B. Valeev, "Hi-Accuracy Method for Spectrum Shift Determination", *Fibers* **2023**, *11*, 60.

[258] S. Cięszczyk, K. Skorupski, M. Wawrzyk, P. Panas, "A Wavelet Derivative Spectrum Length Method of TFBG Sensor Demodulation", *Sensors* **2023**, *23*, 2295.

[259] K. H. Saeed, D.-A. G. Osorio, C. Li, L. Banerji, A. M. Gardner, A. J. Cowan, "Monitoring interfacial electric fields at a hematite electrode during water oxidation", *Chemical Science* **2023**, *14*, 3182.

D Supporting Information

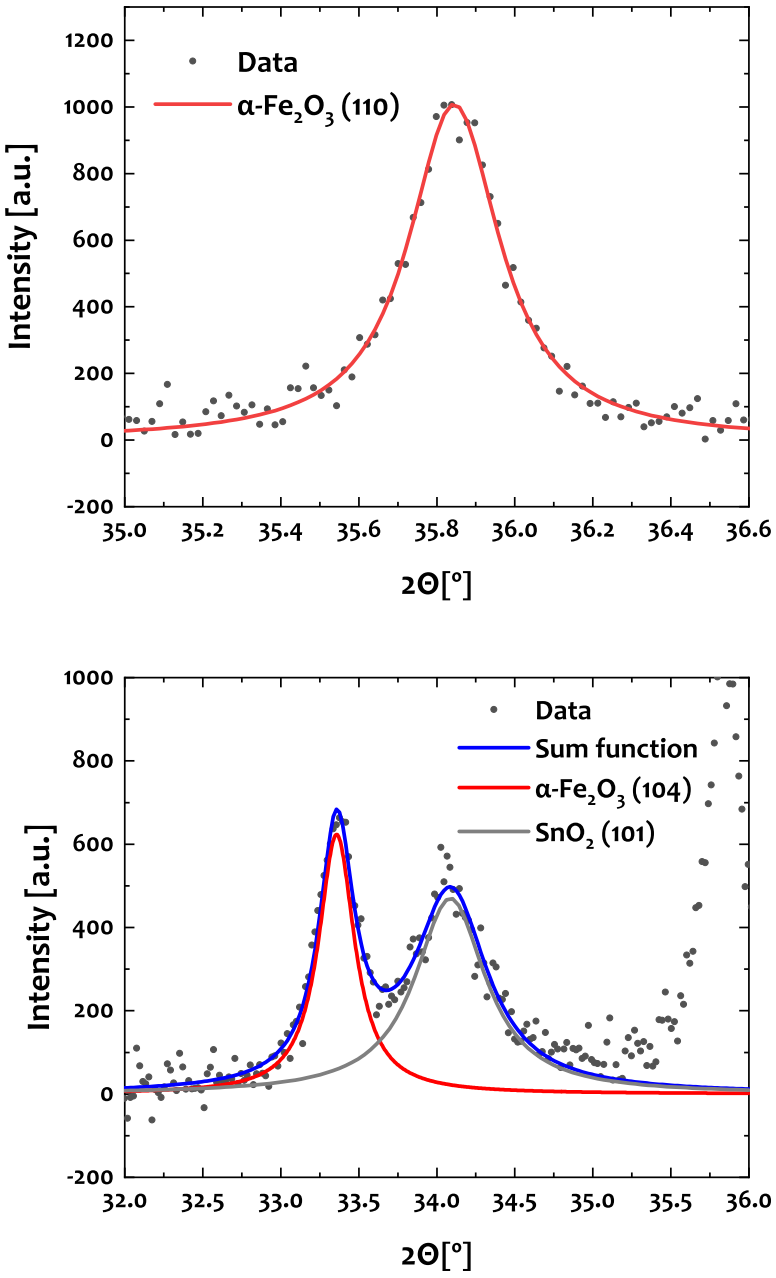

Figure I: Estimation of the crystallite size from the Scherrer equation. A Lorentzian line shape was fit to the (110) reflex at 35.8° and a 2Θ FWHM of 0.284° is obtained. A Lorentzianfit of the (104) reflex from α-Fe_2O_3 at 33.3° in combination with an SnO_2 (101) signal delivered a 2Θ FWHM of 0.280°

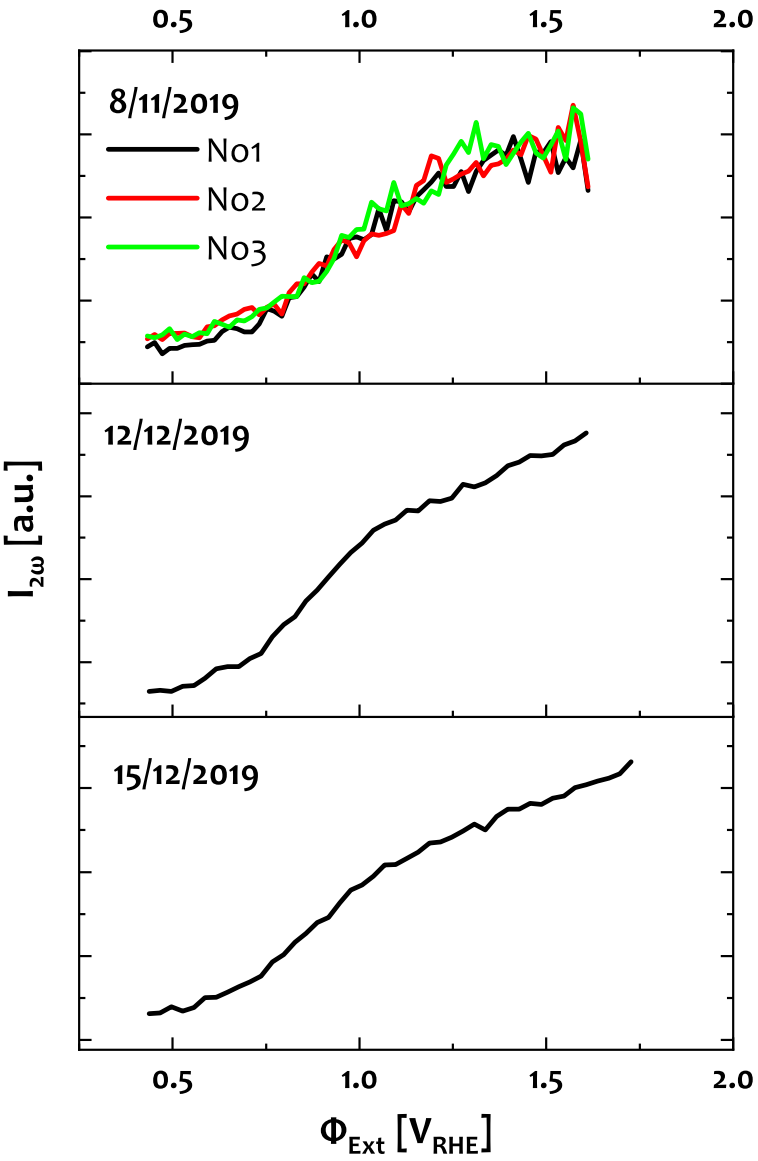

Figure II: Repeatability and stability of SHG spectroscopy under photoelectrochemical control. Potential dependent SHG intensity $I_{2\omega}(\Phi_{\mathrm{Ext}})$ from two samples, at three different days. The upper panel shows a threefold repetition of one sample, the middle and lower panel show the same experiment on another sample at two different days. All graphs exhibit the same potential dependence and therefore confirm a representative and meaningful measurement.

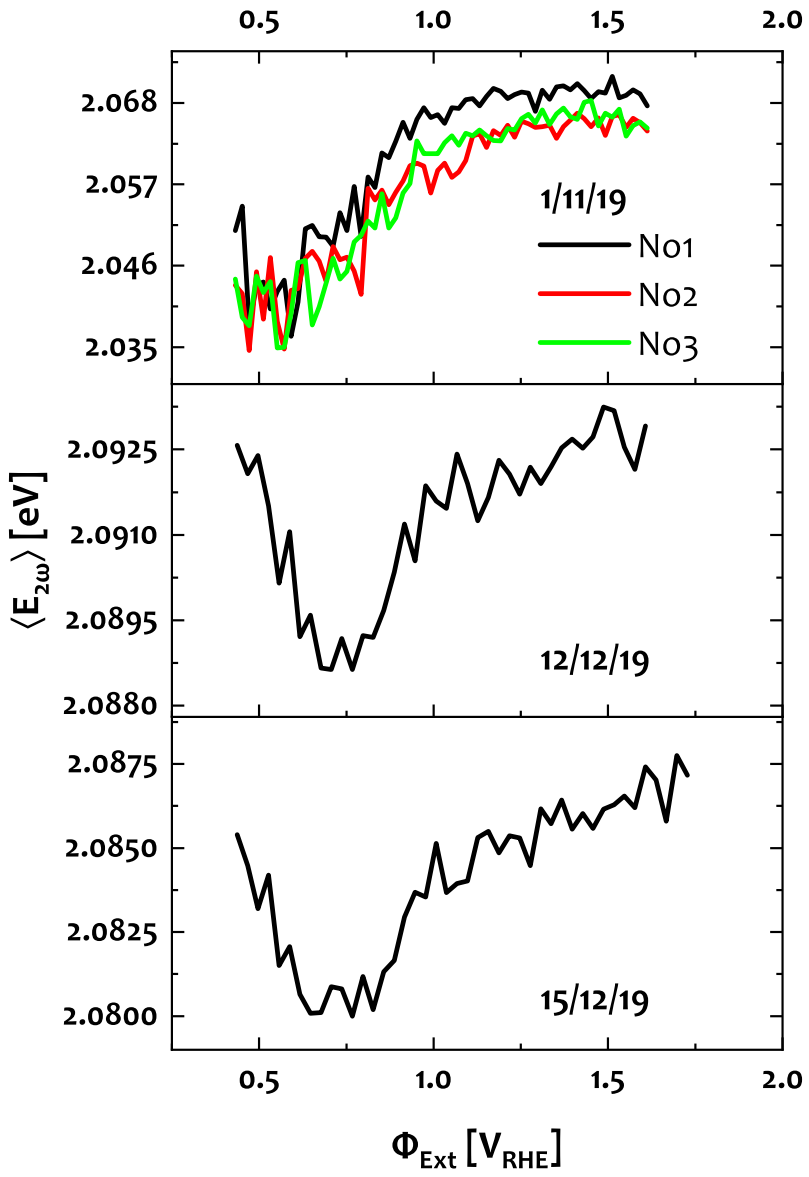

Figure III: Repeatability and stability of SHG spectroscopy under photoelectrochemical control. Potential-dependent SH photon energy expectation value $\langle E_{2\omega} \rangle (\Phi_{\mathrm{Ext}})$ from two samples, at three different days. The upper panel shows a threefold repetition of one sample, the middle and lower panel show the same experiment on another sample at two different days. All graphs exhibit the same potential dependence and therefore confirm a representative and meaningful measurement.

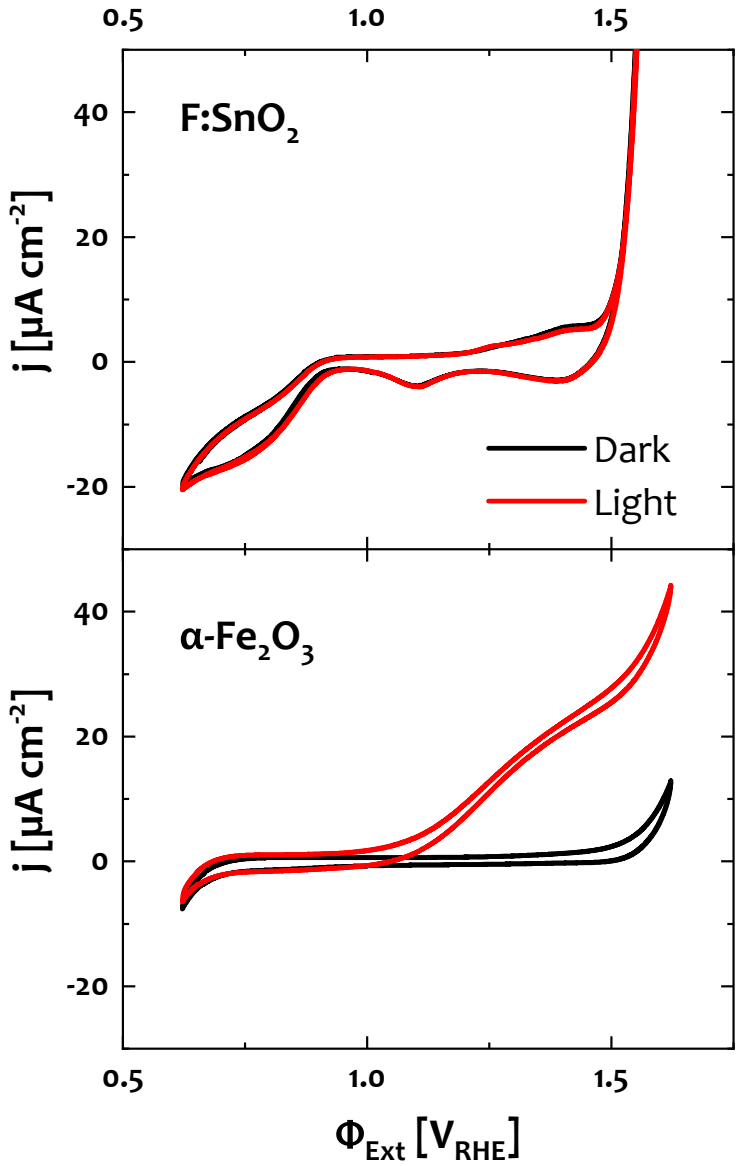

Figure IV: Origin of photoresponse. CV-curves at a scan rate of 10 mV/s from the α-Fe_2O_3 sample compared to the bare F:SnO_2 substrate with and without electrode illumination. While the α-Fe_2O_3 sample shows a clear photocurrent upon illumination, the CV-curve from the bare F:SnO_2 substrate remains unchanged, proving that the entire photoreponse is generated within the α-Fe_2O_3 film on top of the substrate.

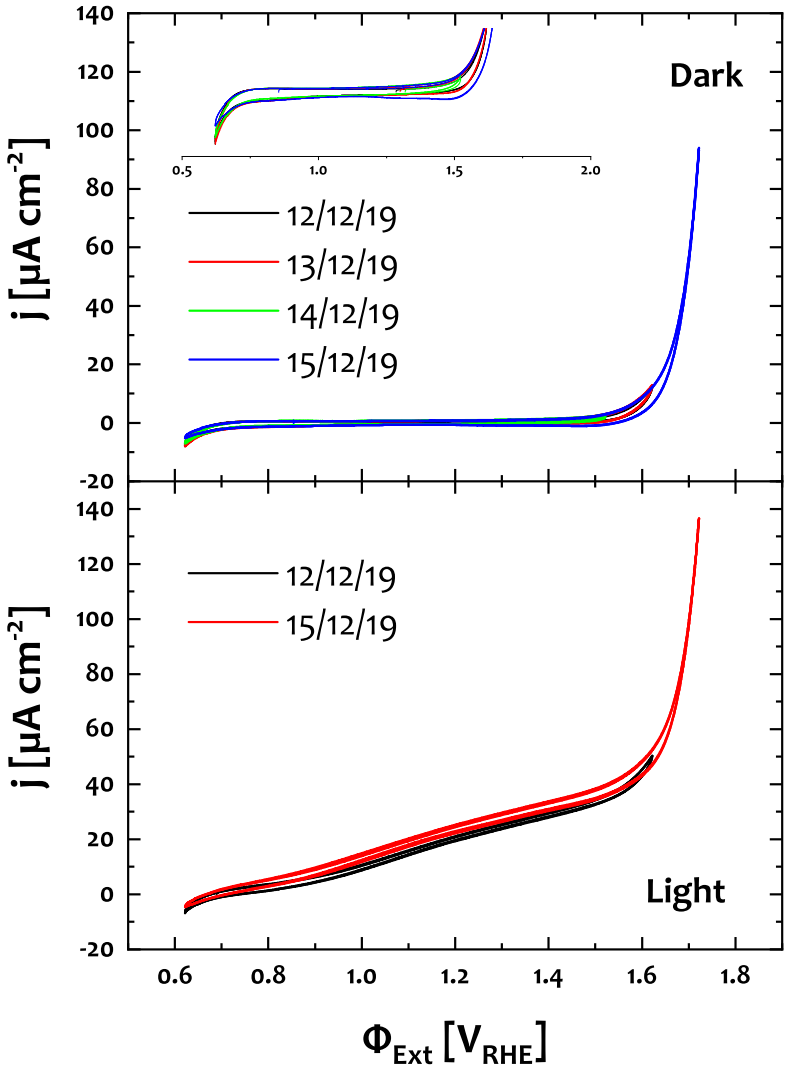

Figure V: Stability of the α-Fe_2O_3 electrode system. Multiple repetition of CV scans were performed at a scan rate of 10 mV/s in the dark (top panel) and under illumination (bottom panel). Each CV curve shows three consecutive cycles. All curves show a typical shape of a photoanode and no significant changes of the CV signal can be found, neither within one measurement, nor between different days of measurement. This demonstrates a stable cell- and sample system and the repeatability of the experiment.

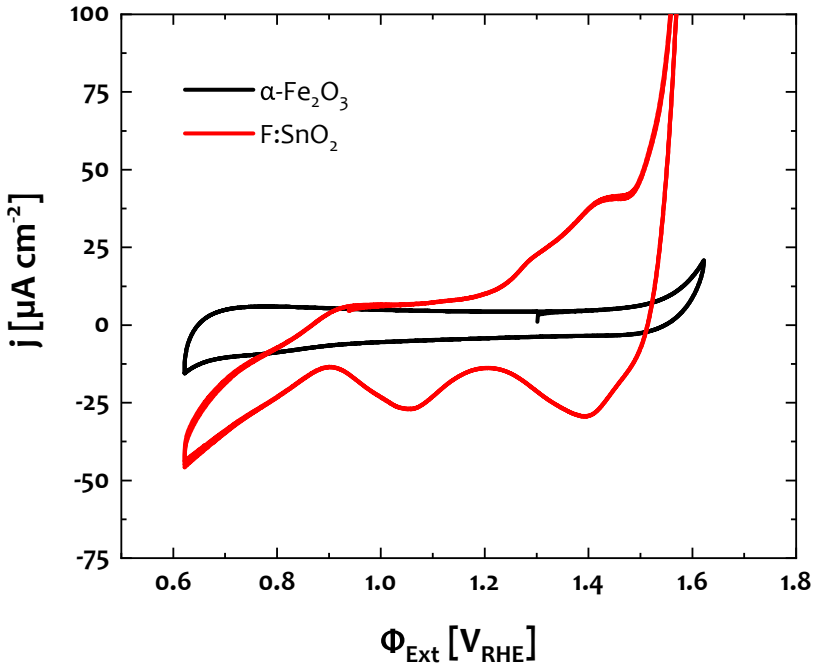

Figure VI: Substrate coverage. Comparison between the CV curves from α-Fe_2O_3 and the underlying bare F:SnO_2 substrate in the dark at scan rates of 100 mV s^{-1}. While the α-Fe_2O_3 shows a quite flat CV response, the F:SnO_2 substrate exhibits a pronounced pattern, which is not present at the α-Fe_2O_3 coated sample system. Therefore, the α-Fe_2O_3 film has covered the F:SnO_2 substrate completely, and any electrochemical response from the sample compound can be ascribed to the α-Fe_2O_3 film and separated from the substrate.

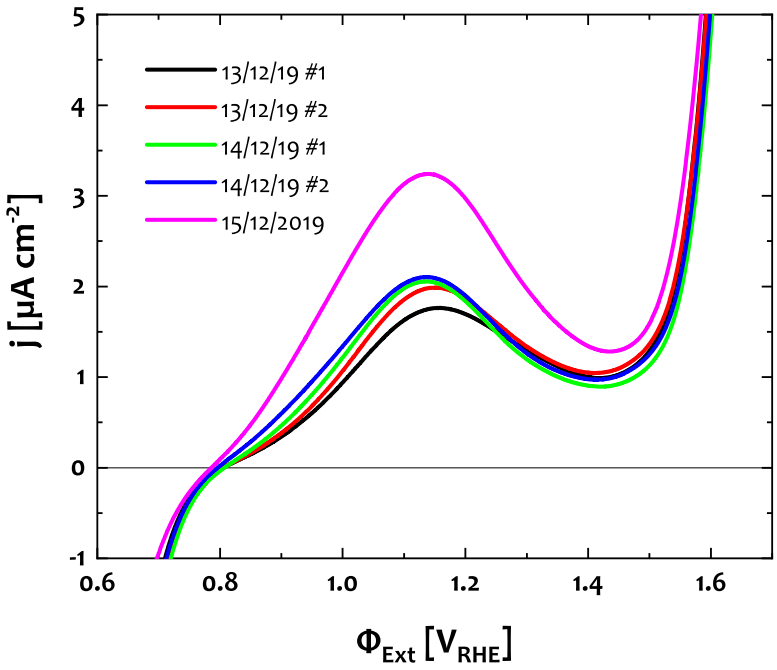

Figure VII: Repeatability and stability of the surface state oxidation wave. Multiple repetitions (#1 and #2) of a static IV scan at a scan rate of 1 mV s^{-1} on two different days showing a steady pronunciation of the signal increasing with time. The signal analysed in Chapter 12 was recorded on December 5th 2019 which is significantly larger than the signal from days before.

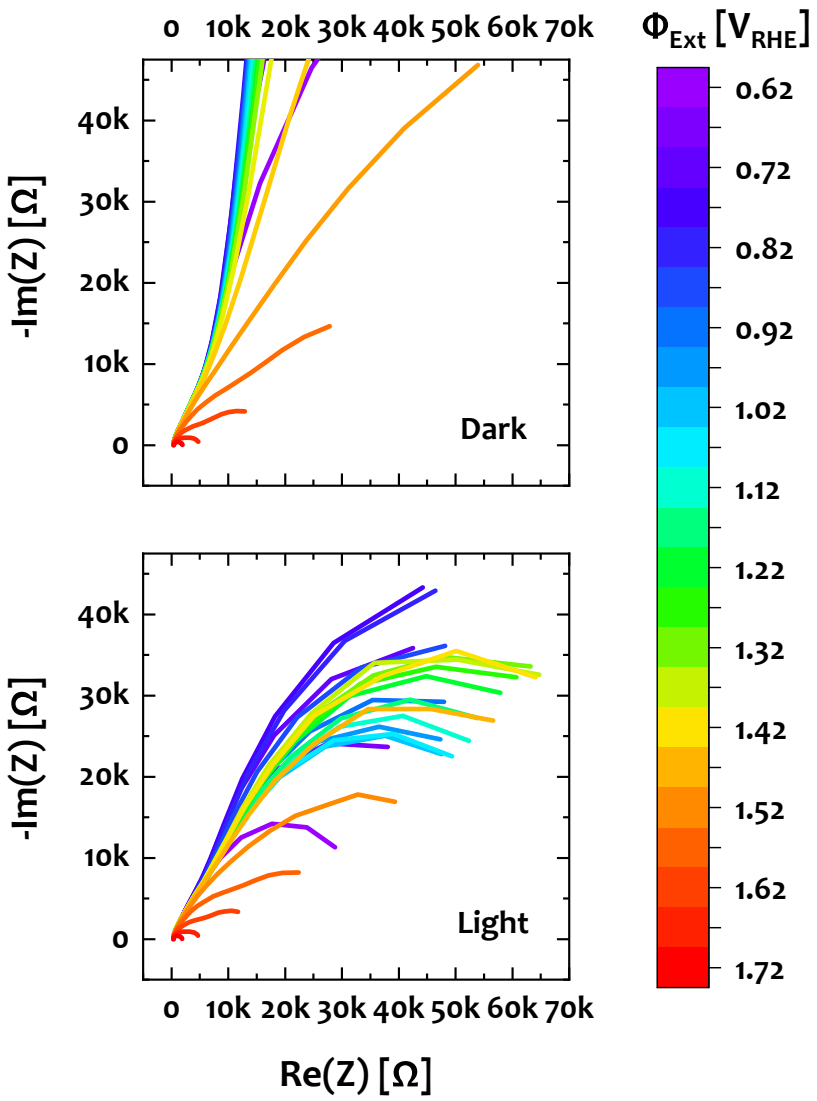

Figure VIII: NYQUIST plots of the impedance spectra of the sample system. The complex impedance was recorded under perturbation of an externally applied potential Φ_{Ext} with an amplitude of 20 mV over a frequency range from 0.1 Hz to 10 000 Hz. Since no pronounced semi circles and a quite vertical, thus capacitive shape were measured in the dark, the analysis of space charge capacitance was performed directly from the imaginary part of the current response.

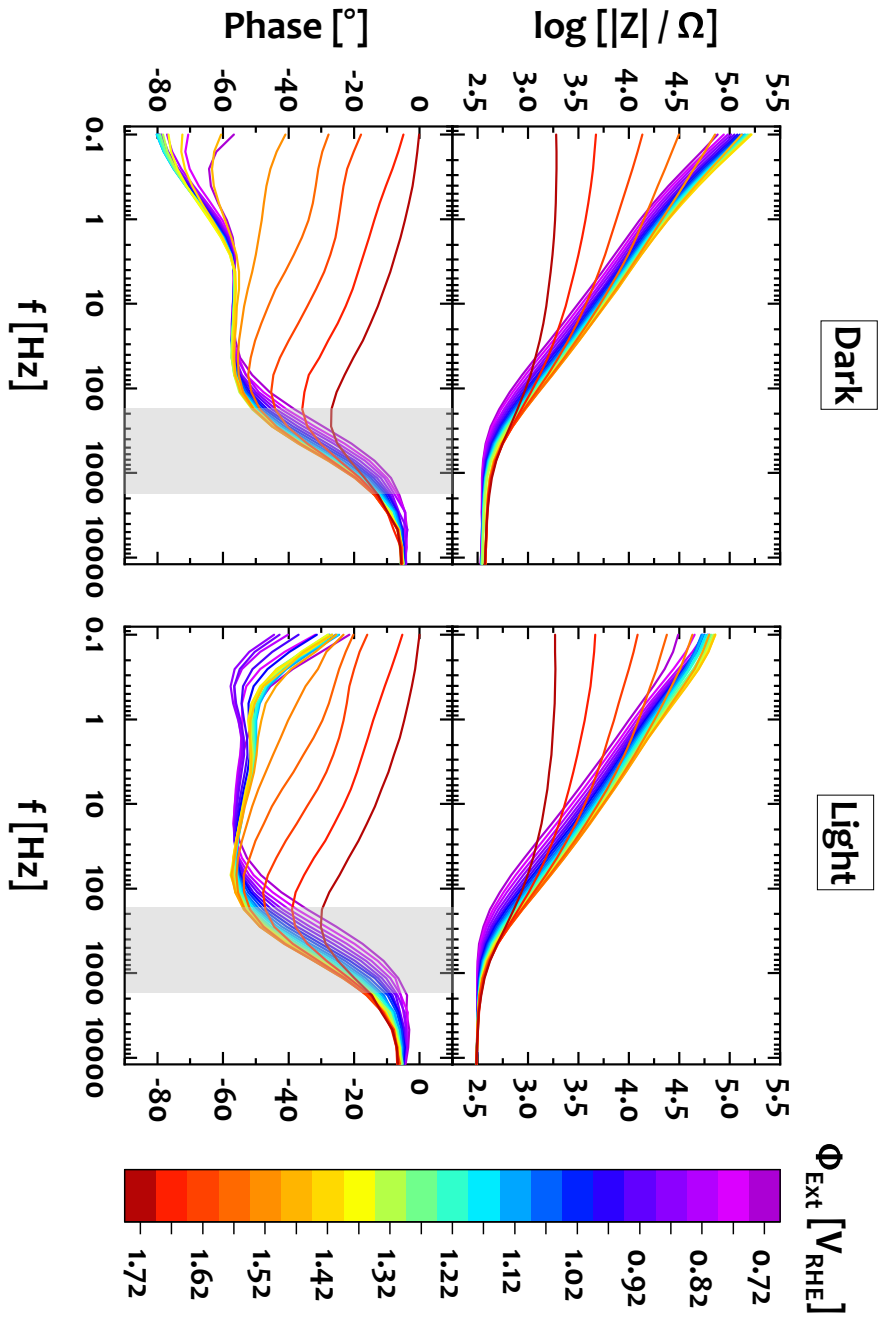

Figure IX: Bode plots of the frequency response of the sample system in the dark and under illumination. The phase angle from 180 Hz to 1800 Hz shows a distinct frequency dependence and was used to calculate $C_{\mathrm{eff}} \approx C_{\mathrm{SC}}$ for the Mott-Schottky-analysis.

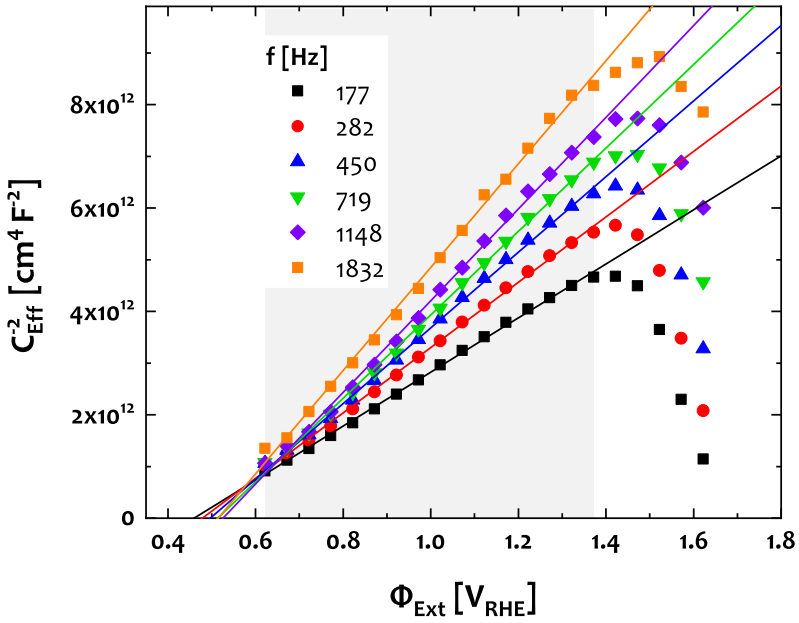

(a) Mott-Schottky plots of C_{Eff} obtained from the imaginary impedance (Eq. 10.3) at perturbation frequencies between 177 Hz and 1832 Hz

f [Hz]	N_{D} [10^{17} cm^{-3}]	φ_{FB} [V_{RHE}]
177	11	0.43
282	8.9	0.45
451	7.7	0.47
719	7.0	0.49
1148	6.4	0.50
1832	5.6	0.49
Average	7.7 ± 1.8	0.47 ± 0.02

(b) Mott-Schottky-analysis of C_{Eff} from the imaginary impedance at perturbation frequencies between 177 Hz and 1832 Hz as shown in Fig. X(a)

Figure X: Mott-Schottky Analysis from imaginary impedance measurements

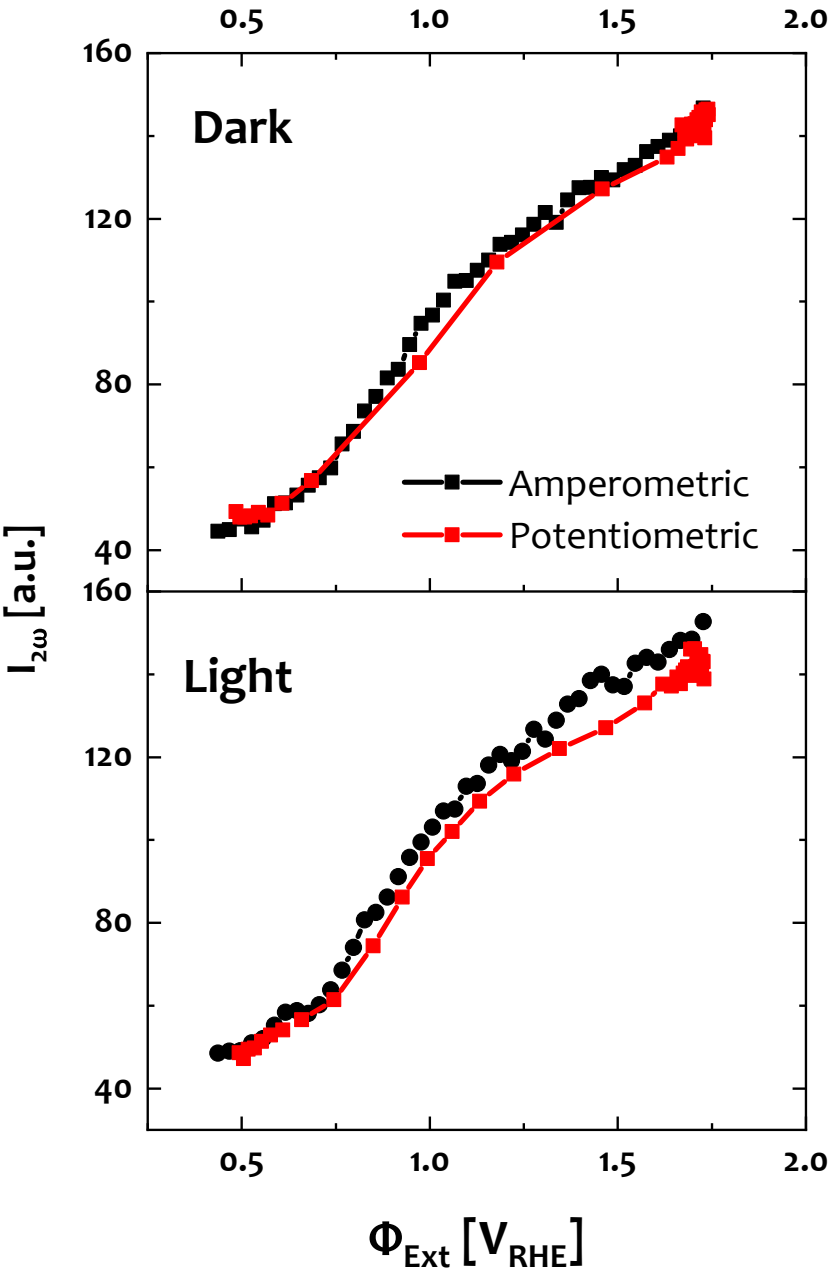

Figure XI: EFISH in two different EC configurations. Projection of the potentiometric SHG response onto the amperometric $I_{2\omega}(\Phi_{\mathrm{Ext}})$ plane. The potential dependent SHG intensity is resembled in two different EC modes confirming an unambiguous relationship between SHG intensity and semiconductor electrode band bending

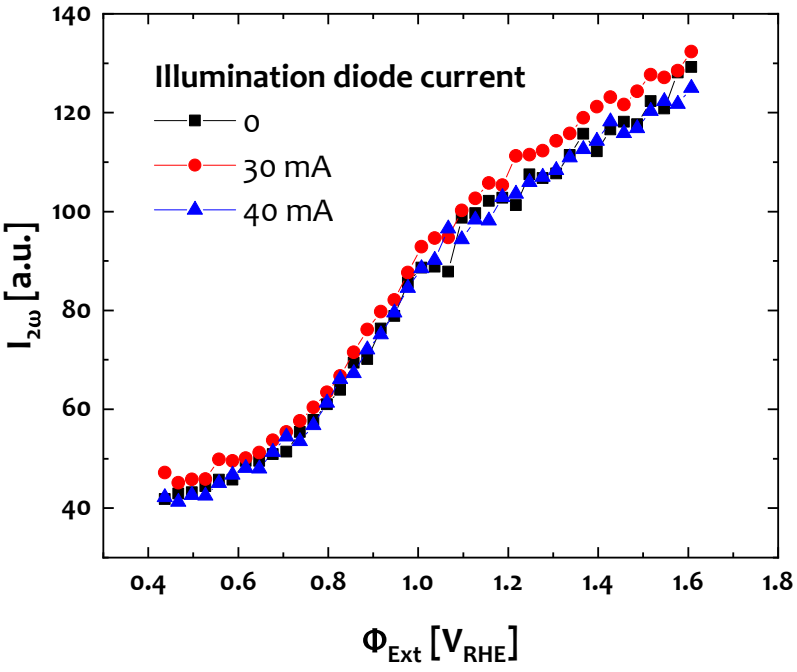

Figure XII: SHG response as function of externally applied potential under varying electrode illumination power in an amperometric setup. A significant change of the SHG response from electrode illumination under these conditions cannot be significantly confirmed, nor excluded.

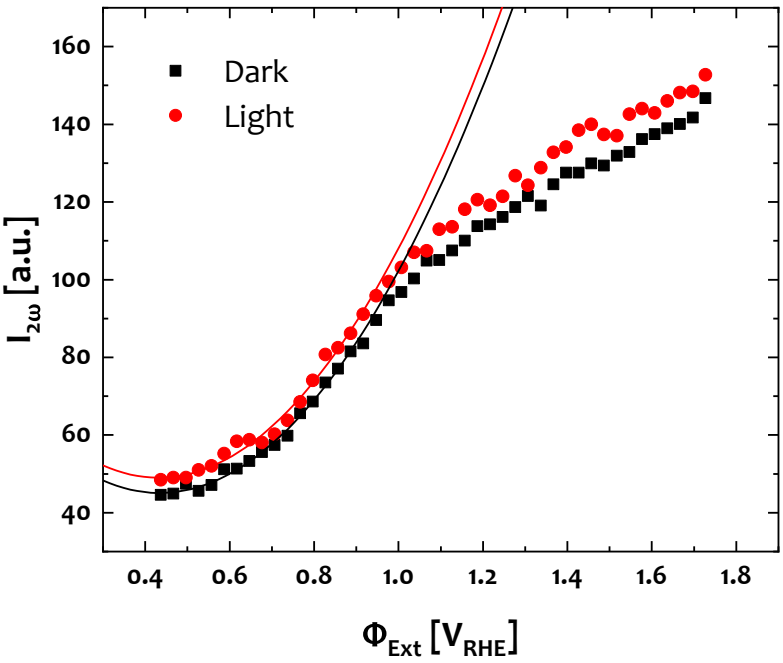

Figure XIII: Quadratic fit of the potential dependent SHG response under gentle depletion conditions to determine φ_{FB} from the vertex of the parabola for the electrode in the dark and under illumination

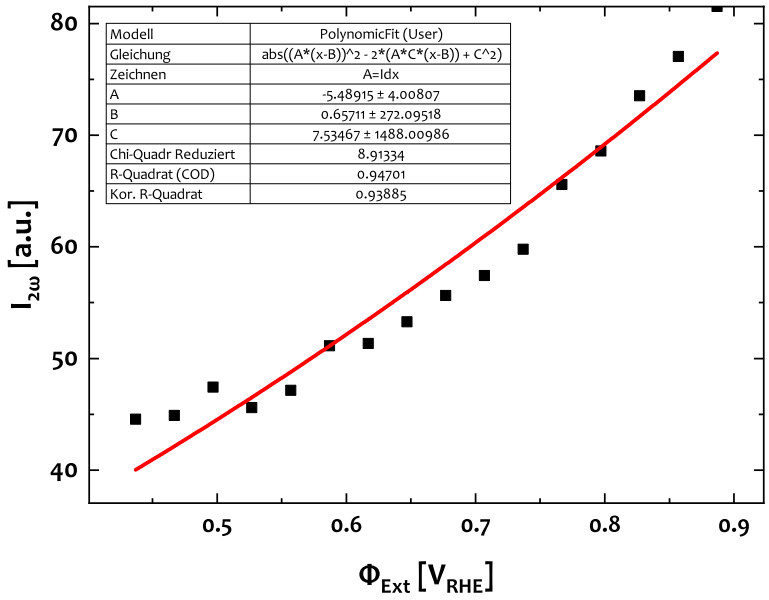

(a) Polynomic fit of the potential dependent SHG response including the second and third order cross-term contribution. The flat-band potential obtained including a linear term at is significantly differing from the corresponding values 0.43 V_{RHE} and 0.47 V_{RHE} as obtained from the quadratic vertex expression Eq. 13.3 and Mott-Schottky analysis, respectively.

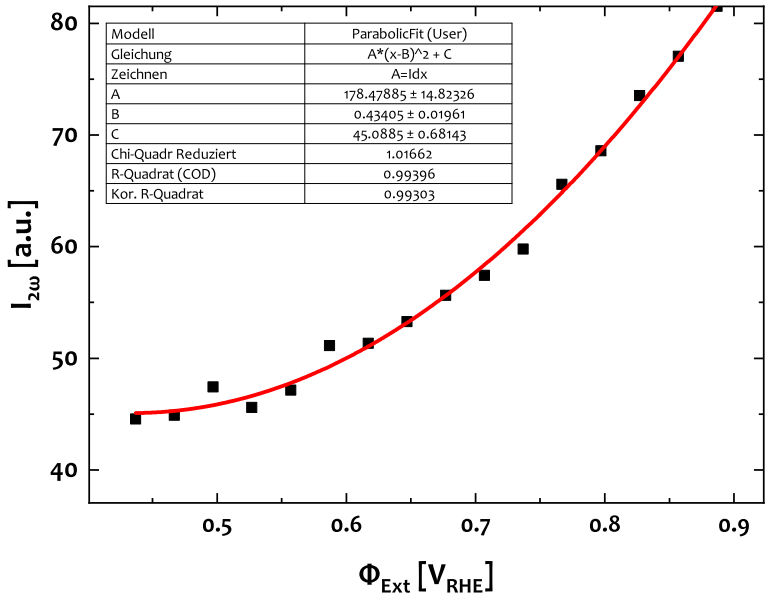

(b) Parabolic fit of the potential dependent SHG response including second and third order cross-term contribution. The flat band potential obtained from a vertex model 0.43 V_{RHE} is in good agreement with the value obtained from Mott-Schottky analysis 0.47 V_{RHE}.

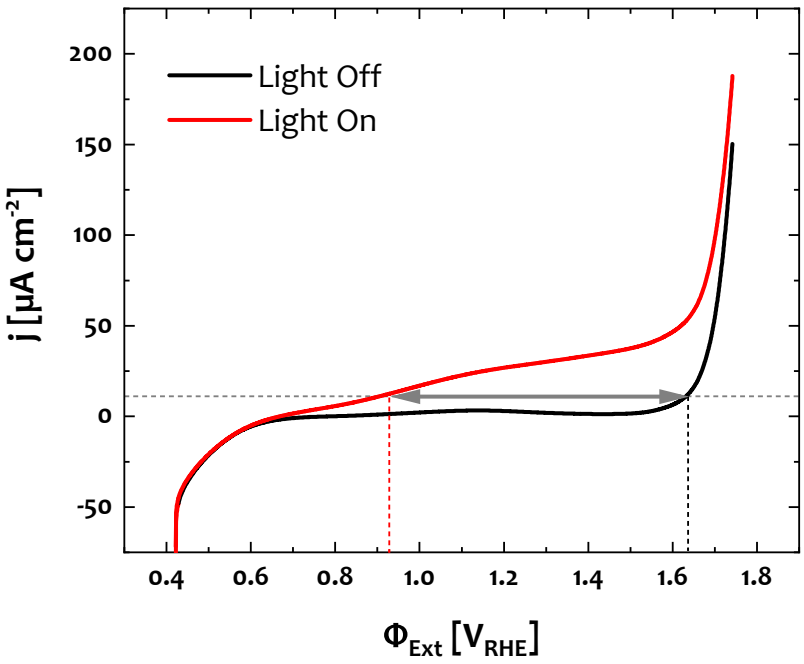

Figure XV: Illustration of the chronopotentiometric measurements on the α-Fe_2O_3 photoanode from its respective IV characteristics. A constant current of 11.1 µA cm^{-2} is imposed to the electrode while the electrode illumination is switched on and off. According to the IV curves one would expect the electrode potential to librate between 0.9 V_{RHE} and 1.6 V_{RHE}.

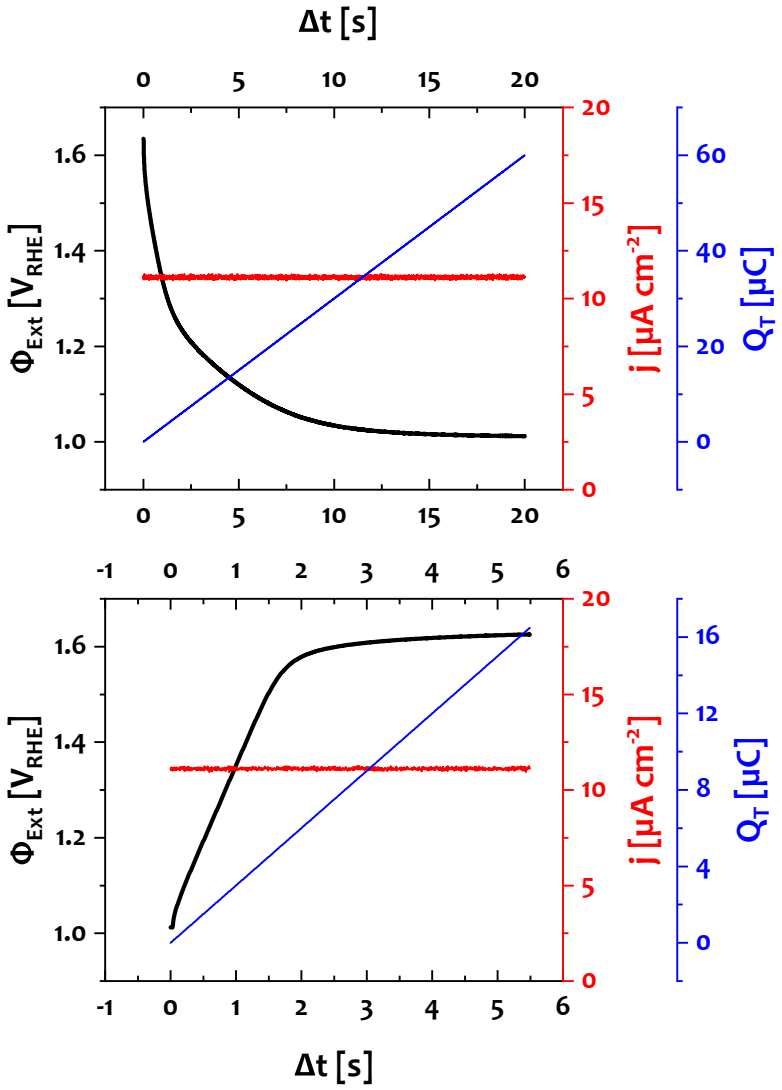

Figure XVI: Quantification of CP data. Time dependent evolution of dark and photovoltage and corresponding cell current and charge. These quantities were used for the determination of a total capacitance C_T.

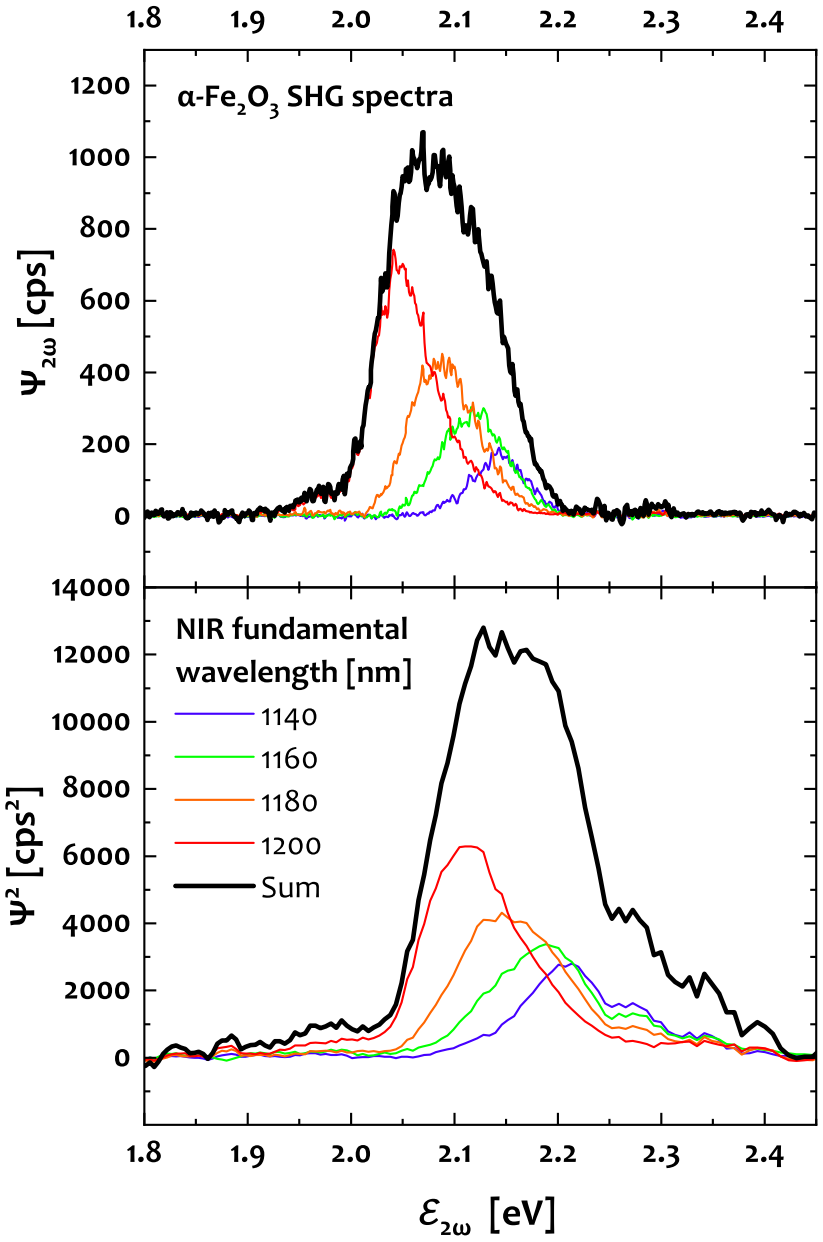

Figure XVII: Raw data for the normalization of the α-Fe_2O_3 SHG response to the NIR fundamental. NIR and SHG spectra were measured at fundamental wavelengths of 1140, 1160, 1180 and 1200 nm and added up to sum spectra

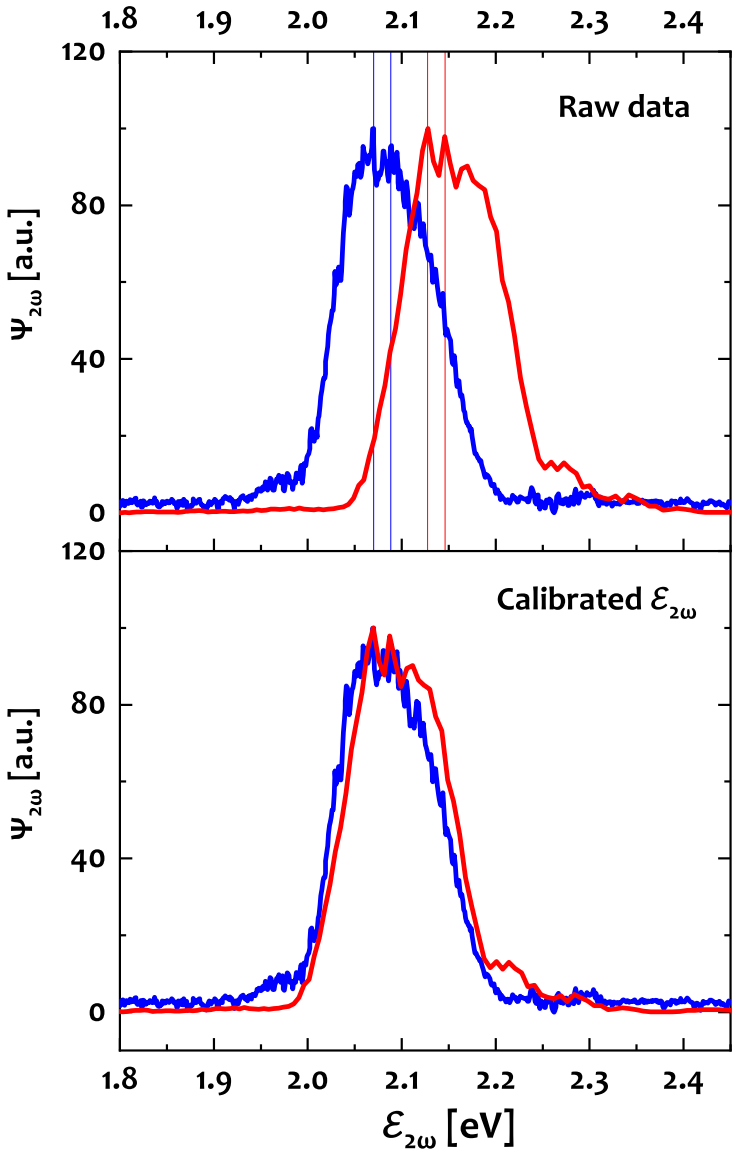

Figure XVIII: Referencing of the squared NIR sum spectra to the calibrated SHG spectrometer scale using two characteristic optical features between both spectra

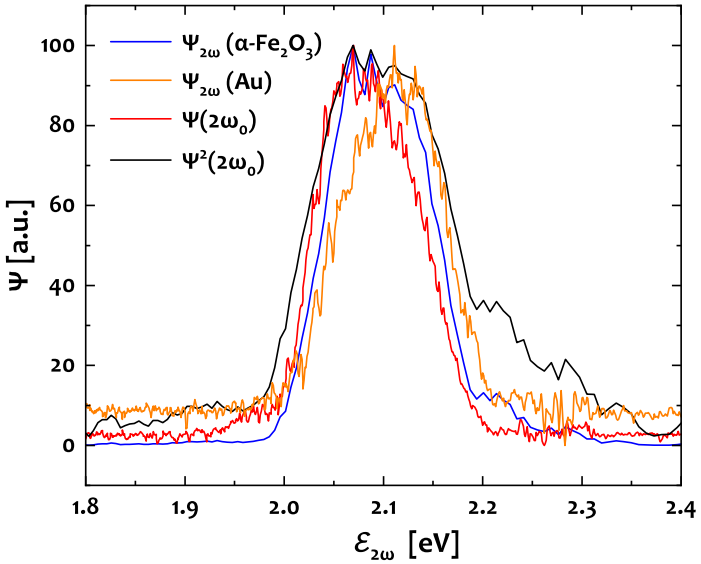

Figure XIX: Comparison between linear and squared fundamental and α-Fe_2O_3 SHG signal line shapes

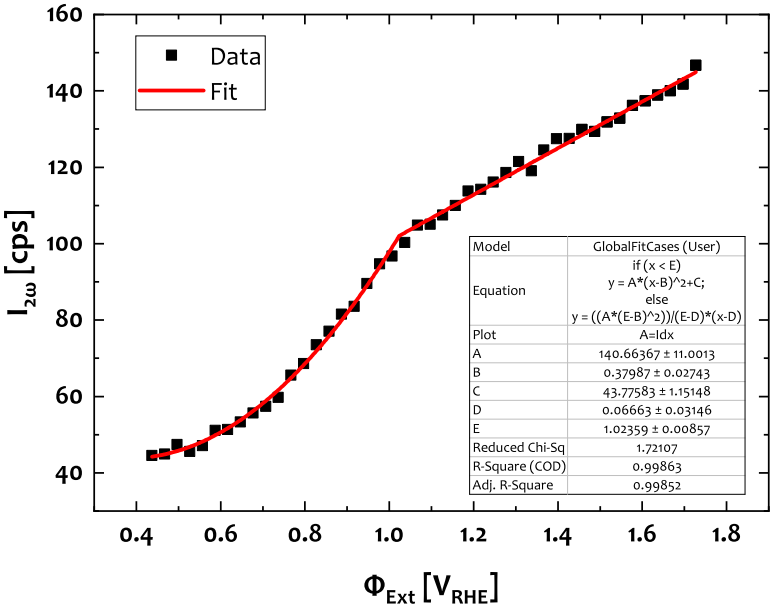

(a) Parameters and statistic quantities of the fit of the potential dependent SHG intensity to the case model presented in Fig. 13.3

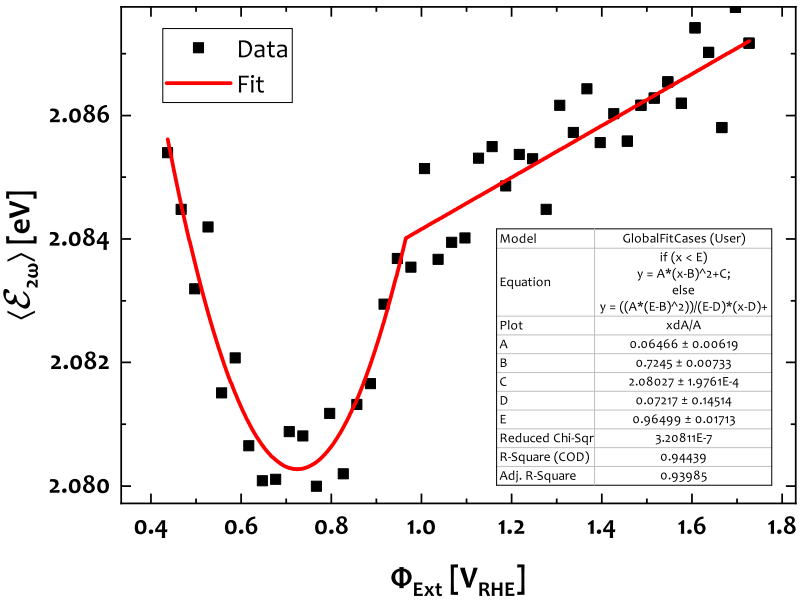

(b) Parameters and statistic quantities of the fit of the potential dependent SHG spectral shift to the model presented in Fig. 13.3

Figure XX: Fit reports of two SHG metrics to a global model as presented in Fig. 13.3

Declaration of authorship

Name: Plescher

First name: Julius Mathias

I declare to the Freie Universität Berlin that I have completed the submitted dissertation independently and without the use of sources and aids other than those indicated. The present thesis is free of plagiarism. I have marked as such all statements that are taken literally or in content from other writings. This dissertation has not been submitted in the same or similar form in any previous doctoral procedure. I agree to have my thesis examined by a plagiarism examination software.

Location, date, signature